Site M0029[1]

Expedition 313 Scientists[2]

Chapter contents

Operations

Transit to Hole M0029A

Preparations for transit to Integrated Ocean Drilling Program (IODP) Hole M0029A commenced at 1455 h on 20 June 2009. This included setting a buoy to mark the location of the casing to be recovered from the seafloor at Hole M0028A. The jack-down procedure began at 1815 h, and the *L/B Kayd* moved off Hole M0028A at 1825 h, arriving at Hole M0029A at 1915 h. The legs were lowered to the seafloor, and preloading of the platform began at 1945 h. The drilling floor was opened up to operations personnel at 0630 h on 21 June to begin setting up generators, powering up containers, and preparing the drilling floor.

Hole M0029A

During the morning of 21 June 2009, the European Consortium for Ocean Research Drilling (ECORD) Science Operator (ESO) and drilling teams prepared the *L/B Kayd* for coring operations in Hole M0029A, and by 1030 h, the casing was ready to be run in (Table T1). The first three core runs had no recovery, and it was suspected that the soft sediment could not break through the microsphere bags. The microsphere bags were changed over to softer sample bags, and this, combined with a slight change in lithology, resulted in core recovery in run four. For the rest of the day, continuous coring was completed to 19 m drilling depth below seafloor (DSF), beyond which a switch was made to conducting a 3 m core run every 9 m. Coring continued to progress well for the rest of the day and through the night into 22 June.

After reaching 55 m DSF by 0530 h on 22 June, preparations were made to set the casing deeper into the seabed. The PQ string was pulled and the casing carefully rotated into the ground. To speed the process up, the *L/B Kayd*'s jacking capability was used to assist in setting the casing. Rapid progress was made until the top drive sprung an oil leak and had to be stripped down. After setting had resumed, the casing was successfully positioned within a clay layer at ~11 m DSF. After reaming back down the hole, coring resumed by midnight and continued into Tuesday, 23 June, alternating with periods of reaming and circulating because of caving sands, to 67.31 m DSF by 0850 h.

At 1155 h on 3 June, operations were halted when the PQ string became stuck and a twist-off of the core bit and reamer occurred.

After tripping the PQ string and fishing the bit and reaming shell back onto deck, a modified PQ outer core barrel and ALN core barrel was made up. The PQ pipe was run back in at 2230 h.

Early on 24 June, the base of the hole (69.36 m DSF) was reached, and coring, with some open-holing, resumed at 76.47 m DSF. However, at 1150 h, sands with mud polymer patches caused the inner and outer core barrels to stick together, resulting in difficulty in rotating, flushing, and lifting the pipe. For the next 3 h, various attempts were made to release the string. The *L/B Kayd* was jacked down, taking the casing with it, allowing access to the PQ joint. Once the PQ was disconnected, the HQ was run to the base of the hole. Seawater was pumped down the HQ string, and at 0400 h on Thursday, 25 June, rotation was reestablished. Six rod stands were removed with difficulty and the hole circulated. The PQ string was reamed to the base of the hole, and the hole was advanced by open-hole drilling to 117 m DSF, where two core runs were made. This was followed by further open-hole drilling to 148 m DSF to the seismic reflection thought to be m1.

Open-hole drilling and spot coring continued throughout 26 June, apart from a short time when operations were suspended because of a lightning storm. By midnight, the hole had advanced to 224 m DSF with nine core runs. At 0100 h on 27 June, drilling operations were suspended for 1.5 h because of another lightning storm. After operations recommenced, open-hole drilling and spot coring continued until 1500 h, by which time the base of the hole was at 257 m DSF. The operation then switched to continuous coring.

Initially, recovery was poor in loose sands, and various bit combinations were tried to improve recovery. However, core recovery generally improved on 28 June, although it was still variable. At midnight, the base of the hole had advanced to 312 m DSF. Coring progressed steadily on 29 June, with recovery between 50% and 114%, reaching 352 m DSF by midnight. By midnight on 30 June, the base of the hole had advanced to 395 m DSF.

On 1 July, coring operations were suspended several times because of lightning storms. However, coring then continued from 395 m DSF with excellent core recovery on a steady basis, reaching the target depth of 754.55 m DSF by 1820 h on 11 July. On completion of coring, the rig floor was prepared for the logging program and the hole was conditioned.

During the day, the vertical seismic profile (VSP) equipment, including the air guns, were prepared and tested. Marine mammal observations began 30 min prior to firing of the air guns, which started at 2050 h. The logging program began with through-pipe VSP from the base of the hole. Just after midnight, a storm approached the platform and the lightning safety procedure was implemented. Through-pipe VSP operations were suspended at 0145 h (at ~200 m DSF). The deck was evacuated, and all personnel remained inside the accommodation module until it was safe to return to the deck at ~0400 h. Because of darkness at that time, it was not possible to restart the air gun, as the VSP permit stipulated start-up during daylight hours only. It was decided to abandon the through-pipe VSP operation and switch to through-pipe natural gamma wireline logging from 755 m DSF. The through-pipe logging operation of the entire hole began at 0510 h and was completed successfully by 1215 h, although the winch motor was running very hot.

The next stage was to pull the pipe back to 600 m DSF and open-hole log the bottom section of the hole. However, the drill pipe was stuck and required significant effort to free it. Alternating pulling pipe with reaming and flushing continued for most of the day without significant improvement in the condition of the hole. As by this time the pipe had been pulled back above the 600 m DSF level, the decision was made to continue the hole conditioning operation while pulling up to the next logging step at 484 m DSF and from there try to log the bottom two sections of the hole. This depth was reached at 2245 h on 12 July.

Logging with the resistivity sonde began at 2350 h and was completed at 0300 h on 13 July, despite an intermittent electro/mechanical fault on the winch. The hole was conditioned, and the sonic sonde was lowered. At 624 m DSF, as the sonde was logging, the power supply to the winch tripped several times, and eventually both the winch motor and control box burned out. The sonde was manually recovered to deck by pulling 600 m of wire up the drill pipe and was back on deck at 0905 h. The winch was removed from the drill floor and replaced with the back-up logging winch that had been used for VSP operations. Logging recommenced at 1110 h, first with the sonic and then with the magnetic susceptibility sonde. Between each logging run, the drill hole was conditioned by circulating mud and rotating the pipes.

At 1925 h, the acoustic imaging sonde was connected to the winch cable on deck. No signal was detected, indicating a faulty tool, cable, or connector. Fault-finding efforts continued until 0100 h on 14 July, with several faults being repaired and the tool replaced. On deployment of the tool at 0100 h, a further fault developed with the winch. Then, fatally, all contact was lost with the tool at 0235 h. The gen-

erator was also causing concern but kept functioning. The tool was retrieved by 0515 h, and fault finding restarted. An earth-leakage fault in the winch cable at the tool-connector end was finally identified. A section of cable was removed, and the end of the cable was reterminated. Once fixed and tested, the log run was successful, finishing at 1800 h.

Before tripping pipe up to the top of the next logging interval, the opportunity was taken to complete the through-pipe VSP that had been aborted on 12 July. Marine mammal observations started at 1700 h, and the top section of the hole (0–200 m DSF) was logged successfully, finishing at 2100 h. Once complete, the drill pipe was tripped back to the top of the next logging interval at 335 m DSF. It was noted that the drill pipes were very tight for the first five double stands.

On 14 July, the supply boat *Sorensen Miller* conducted a postdrill survey around Hole M0028A with side-scan sonar and magnetometer, prior to recovery of the casing at a later date.

On 15 July, tripping of the pipe was completed by 0150 h. The natural gamma sonde was lowered down the hole but was unable to progress very far. It punched through an upper bridge but could not penetrate deeper than 352 m DSF because of a second bridge. Logging was therefore conducted between 335 and 352 m DSF. A reaming operation started at 0825 h and was completed at 1845 h, having encountered a third bridge at 495 m DSF. Following this, the resistivity sonde was lowered down the hole at 1900 h. It was unable to penetrate the bridge at 352 m DSF despite reaming. Further reaming and probing indicated open-hole conditions below 357 m DSF. The decision was taken to ream down beneath both bridges and log the lower part of the scheduled logging interval. However, upon reaming to this depth, the probe revealed that a new bridge had formed at 400 m DSF. Further reaming continued to remove this bridge.

Logging with the resistivity, sonic, and magnetic susceptibility sondes continued until 1205 h on Thursday, 16 July. However, after connecting the acoustic imager sonde to the winch, an electrical problem in either the winch cable or connectors halted operations. Despite tripping pipe back to 352 m DSF to enable time for the repairs to be made, it became obvious that it would not be possible to complete repairs and finish the logging schedule within the remaining time because of transit time and the need to enter Atlantic City, New Jersey (USA), on a high tide. Therefore, at 1425 h on 16 July, the decision was made to stop operations, trip all drill pipe and casing, and prepare the containers for transit back to Atlantic City.

Transit to Atlantic City, New Jersey

The *L/B Kayd* began preparations to depart from Hole M0029A at 0100 h on 17 July 2009, which involved removing all power to the ESO containers, securing the drill floor and equipment, and moving all personnel into the accommodation block. Jacking-down of the platform began at 0200 h, and transit to Atlantic City commenced at 0315 h, with the vessel arriving alongside the Coast Guard Station quayside at 1545 h.

Demobilization of the ESO containers and equipment continued on 17 and 18 July, with the containers being lifted onto the quayside on 18 July. On 19 July, all containers were collected for shipping back to Europe, with the wireline tools being collected on Monday, 20 July. All ESO staff departed on 20 July.

Lithostratigraphy

Figure F1 provides a key to colors and symbols used for figures in this section.

Hole M0029A was drilled in the shallow shelf primarily to sample the thick middle Miocene. Seven lithostratigraphic units are defined (Table T2). Figure F2 illustrates the positions of the lithostratigraphic units on the seismic sections. The basal lithostratigraphic unit of Hole M0029A, Unit VII (756.33–747.27 mbsf, late early Oligocene to early Miocene), is siltstone with glauconite sand and thin-walled articulated shells deposited in a low-energy deep offshore environment. Unit VI (747.27–728.55 mbsf; middle early Miocene [late Aquitanian to early Burdigalian]) is a pale brown clayey silt with intercalated very fine and fine sand beds. These sediments represent a river-dominated offshore (prodelta) environment. Units V–III (728.55–640.51 mbsf; middle early Miocene to early middle Miocene) contain a series of granuliferous coarse quartz and glauconite sand packages separated by bioturbated silt. The sand packages are generally sharp based and fine uphole into silt. The sand is interpreted to represent toe-of-clinoform-slope apron systems deposited during lowered sea level and the silt to represent deep offshore deposition during high sea level. Unit II (640.51–325.12 mbsf; middle Miocene [Langhian]) is divided into several subunits. Subunit IID (640.51–602.25 mbsf) contains two packages with poorly sorted medium to coarse glauconitic sand at the base and bioturbated silt on top. The environment of deposition is interpreted as a toe-of-clinoform-slope apron at the base and deep offshore on top. Subunit IIC (602.25–502.01 mbsf) comprises a monotonous succession of very fine sandy silt and silt deposited in a deep offshore environment below storm wave base. Subunit IIB (502.01–448.49 mbsf) is mostly

sand, and deposition was likely by sediment gravity flow on a clinoform slope, either within a submarine channel or on an intraslope apron. Subunit IIA (448.49–325.12 mbsf) is another monotonous very fine sandy silt and silt with uncommon sand beds representing offshore and river-influenced offshore environments. Unit I (325.12–3.85 mbsf; late Pleistocene–?late Miocene) was not continuously cored. Spot cores attempted to identify major seismic reflectors. Sediments recovered were likely deposited in a range of shelf settings, from shallow marine shoreface to foreshore, coastal plain, and estuarine.

Figure F3 summarizes Units I–VII, and their constituent subunits are described in more detail below. Lithologic descriptions are given according to the order of core numbering, from the top to the base of each lithostratigraphic unit or subunit, whereas interpretations are given in chronologic order, from the base of each unit or subunit uphole.

Unit I

Interval: 313-M0029A-4R-1, 0 cm, to 65R-2, 80 cm
Depth: 3.85–325.12 mbsf
Age: late Pleistocene to late Miocene

Because of difficult coring conditions in sandy sediment, cores in this unit targeted reflectors identified on seismic profiles as post-Langhian unconformities (m4, m3, and m1). No attempt was made to core materials between the reflectors.

Subunit IA

Interval: 313-M0029A-4R-1, 0 cm, to 24R-1, 10 cm
Depth: 3.85–118.56 mbsf

Recovery of this subunit was generally very poor, and many cores had no recovery. Cores 313-M0029A-4R through 8R (3.85–17.27 mbsf) contain interbedded and interlaminated micaceous fine sand and silty clay with shell fragments. Cores 313-M0029A-13R through 15R (40.45–50.16 mbsf) contain medium to coarse micaceous, slightly glauconitic sand. There is a change across a sharp surface (Fig. F4) in Section 313-M0029A-15R, 8 cm, from silty medium to coarse sand above to silty clay below. The contact is lined by pebbles. Brown clay and pale blue clay are found in Cores 313-M0029A-16R and 19R. The clay in Core 313-M0029A-19R has a single pebble at its base. Cores 313-M0029A-20R through 24R contain well-sorted fine sand.

Interpretation

Sediments recovered in Cores 313-M0029A-1R through 24R were likely deposited in a range of shelf settings, including shallow-marine shoreface to foreshore, coastal plain, and estuarine. Poor recovery,

however, prevents detailed environmental analysis. Two potential unconformities are identified in Cores 313-M0029A-19R and 15R (Fig. F4) based on the clays possibly representing soil environments, although this interpretation is tentative because of coring gaps and sporadic disturbed cores. The upper succession is Pleistocene in age, based on Zone NN21 in Core 313-M0029A-7R. The lower succession, between Cores 313-M0029A-16R and 19R (~50–65 mbsf) is also suggested to be Pleistocene in age.

Subunit IB

Interval: 313-M0029A-25R-1, 0 cm, to 30R-1, 94 cm
Depth: 145.91–160.81 mbsf

Cores 313-M0029A-25R through 30R targeted reflector m1 in an attempt to better date and determine its sedimentological character. Core 313-M0029A-25R recovered medium sand with granules that graded down to clay and fine sand in Core 313-M0029A-26R. Core 313-M0029A-27R was empty. Below, Cores 313-M0029A-28R through 30R contained beds ranging from fine sand to clayey silt with organic matter and wood, including a gravel layer at Section 313-M0029A-29R-1, 17 cm.

Interpretation

These unsorted, coarse-grained sands with granules interbedded with clay and silty clays are interpreted as coastal plain deposits with possible intervening channels. The gravel bed is a candidate to represent the unconformity and reflector m1.

Subunit IC

Interval: 313-M0029A-33R-1, 0 cm, to 35R-2, 8 cm
Depth: 188.61–195.12 mbsf

Cores 313-M0029A-31R through 35R targeted reflector m3 in an attempt to better date and determine the sedimentological character of the seismic reflector. Cores 313-M0029A-31R and 32R recovered no sediment. Cores 313-M0029A-33R and 34R contain deeply weathered clay and silty clay with large (>10 cm) pieces of wood. Below the clay is medium sand (Core 313-M0029A-35R).

Interpretation

The deeply weathered clay (Cores 313-M0029A-33R and 34R) may represent separate paleosols (Fig. F5). They are interpreted to represent an unconformity and reflector m3.

Subunit ID

Interval: 313-M0029A-36R-1, 0 cm, to 41R-3, 8 cm
Depth: 219.11–235.97 mbsf

Cores 313-M0029A-36R through 41R targeted reflector m4 in an attempt to better date and determine its sedimentological character. Medium to coarse sand in Core 313-M0029A-36R with some shell debris changed to very fine sand and sandy clay with sand granules, woody organic matter, and no fauna in Core 313-M0029A-37R. At the bottom of the succession in Core 313-M0029A-40R was clay and silty sand, and at the bottom of the succession in Core 313-M0029A-41R was fine-grained sand rich in plant debris.

Interpretation

The coarsening-upward succession could represent an interdistributary bay to crevasse splay facies succession passing probably upward to marine deposits as indicated by the presence of reworked shell debris. No clear sharp contact attributable to an unconformity and reflector m4 was identified, except by the presence of coarse granules.

Subunit IE

Interval: 313-M0029A-44R-1, 0 cm, to 65R-2, 80 cm

Depth: 261.81–325.12 mbsf

The top of the succession (Cores 313-M0029A-44R through 51R) is moderately sorted medium and fine sand barren of shells. A change in Core 313-M0029A-51R to interbedded medium/fine sand and silty clay below lies above a sharp contact with a clean gravel below in Core 313-M0029A-54R (293 mbsf). The underlying succession is sand prone with granules, shell fragments, mica, and significant amounts of plant debris to an abrupt bioturbated contact at the base of the succession (Section 313-M0029A-65R-2, 80 cm).

Interpretation

The basal bioturbated contact of silty fine sand above clay (Fig. F6) also marks an abrupt downhole increase in hardness and is interpreted as an unconformity. The overlying succession (Core 313-M0029A-61R to Section 56R-1; 312–295 mbsf) coarsens uphole from silty very fine sand to medium sand, indicating a change from a shoreface–offshore transition to a shoreface setting. The significant amount of mica, plant debris, and organic-rich burrow fills suggests a strong fluvial influence. Gravel in Section 313-M0029A-54R-CC (293 mbsf) and the distinctive overlying interbedded succession of sharp-topped and sharp-based blue-gray clay layers with well-sorted medium sands is interpreted as representing beach/backbeach coastal plain environments (Fig. F7). The cores above Core 313-M0029A-51R to the top of the subunit (Core 313-M0029A-41R) are

generally fine- and medium-grained sand without shell fragments, which might be an incised valley fill given the blocky character of the gamma log. The base of this interpreted valley fill (~286 mbsf) may be a candidate for an unconformity and sequence boundary.

Unit II

Interval: 313-M0029A-65R-2, 80 cm, to 175R-1, 50 cm

Depth: 325.12–640.51 mbsf

Age: middle Miocene (Langhian)

Subunit IIA

Interval: 313-M0029A-65R-2, 80 cm, to 108R-1, 63 cm

Depth: 325.12–448.49 mbsf

Subunit IIA$_1$

Interval: 313-M0029A-65R-2, 80 cm, to 72R-1, 49 cm

Depth: 325.12–343.81 mbsf

Sediments in Subunit IIA$_1$ are dominated by silty clay with occasional thin, sharp-based fine sand beds (convex-up laminae; e.g., interval 313-M0029A-68R-1, 24–30 cm); finely dispersed organic material; and pyrite. A carbonate-cemented siltstone with its base at 49 cm in Section 313-M0029A-72R-1 separates silty clays above from muddy bioturbated fine sand below.

Interpretation

The base of the carbonate-cemented siltstone (Section 313-M0029A-72R-1, 49 cm) marks a deepening in environment of deposition. The overlying section was deposited in shoreface–offshore transition and offshore environments.

Subunit IIA$_2$

Interval: 313-M0029A-72R-1, 49 cm, to 83R-2, 99 cm

Depth: 343.81–377.15 mbsf

Sections 313-M0029A-72R-1, 49 cm, through 73R-3 (343.81–349.70 mbsf) are muddy and silty very fine and fine sand becoming silty clay below. Section 313-M0029A-75R-1 (353.31 mbsf) is silty clay. The succession coarsens downhole to medium sand, with many large shells in Sections 313-M0029A-76R-2 and 76R-3 (355.84–356.44 mbsf). The section then fines downhole to clayey silt rich in plant debris with common *Turritella* and rare thin-shelled bivalves (Section 313-M0029A-81R-2; 371.17 mbsf). The succession coarsens downhole to fine sand in Section 313-M0029A-83R-2 (376.16 mbsf). These

successions are interrupted by three normally graded beds:

1. Interval 313-M0029A-79R-2, 50–90 cm (364.46–364.86 mbsf): 40 cm thick sharp-based bed that grades from a gravelly sand to a poorly sorted coarse sand (Fig. F8);
2. Interval 313-M0029A-82R-1, 53–90 cm (372.36–372.73 mbsf): fine sand with 3% granules that grades normally to a fine to coarse silty sand;
3. Interval 313-M0029A-83R-2, 0–99 cm (376.16–377.15 mbsf): medium sand with coarse sand and granules that grades normally to a fine sand.

Interpretation

This subunit represents river-influenced predominantly offshore environments at the base (Sections 313-M0029A-83R-2, 99 cm, through 78R-2; 377.15–360.94 mbsf), with river-influenced shoreface–offshore transition environments on top (Sections 313-M0029A-78R-1 through 75R-1; 360.94–353.31 mbsf). Deposition was punctuated by coarser graded sand beds (intervals 313-M0029A-83R-2, 0–99 cm [376.16–377.15 mbsf]; 82R-1, 53–90 cm [372.36–372.73 mbsf]; and 79R-2, 50–90 cm [364.46–364.86 mbsf]) that represent either individual turbidity current deposits of coarser material and/or episodes of lowered sea level.

Subunit IIA$_3$

Interval: 313-M0029A-83R-2, 99 cm, to 108R-1, 63 cm

Depth: 337.15–448.49 mbsf

From Section 313-M0029A-84R-1 (377.71 mbsf) to Section 313-M0029A-107R-1, 35 cm (448.49 mbsf), the succession is overall silt and silty clay with plant debris and mica along with beds that alternate in degree of lamination and bioturbation (*Chondrites*). This interval includes a few thin (centimeter thick) sand beds. In Section 313-M0029A-94R-1, a downhole coarsening from silty clay to sandy silt is separated by a sharp bioturbated erosion surface from silty clay below. The base of Section 313-M0029A-107R-2, 127 cm, has a faint surface across which the silt contains rare glauconite grains. Core 313-M0029A-108R is slightly glauconitic silt on top, and glauconite grains increase in size and number downsection.

Interpretation

The section represents deposition in the outer limits of the shoreface–offshore transition zone or the shallowest depths of the offshore.

Subunit IIB

Interval: 313-M0029A-108R-1, 63 cm, to 126R-2, 80 cm

Depth: 448.49–502.01 mbsf

Subunit IIB$_1$

Interval: 313-M0029A-108R-1, 63 cm, to 118R-1, 25 cm

Depth: 448.49–478.61 mbsf

Subunit IIB$_1$ increases in glauconite concentration and grain size from silt to silty sand with granules down to an inclined surface at Section 313-M0029A-108R-1, 124 cm (449.00 mbsf), which truncates the underlying clayey silt. Sections 313-M0029A-108R-2 through 111R-CC (448.49–460.52 mbsf) are overall poorly sorted slightly shelly silt. A 60 cm thick fine sand succession with cross-bedsets occurs in Section 313-M0029A-110R-2 (Fig. F9). In Cores 313-M0029A-112R through 118R, the section coarsens downhole from silty fine sand to poorly sorted slightly glauconitic medium sand. A bioturbated surface in Section 313-M0029A-118R-1, 25 cm (478.61 mbsf), separates medium sand above from siltstone below.

Interpretation

The bioturbated basal contact is interpreted as a sequence boundary. The overlying poorly sorted and immature coarse sediments likely represent debris flow and turbidity current deposits on a clinoform slope, possibly in a channelized context (e.g., erosion surface at Section 313-M0029A-108R-1, 124 cm).

Subunit IIB$_2$

Interval: 313-M0029A-118R-1, 25 cm, to 126R-2, 80 cm

Depth: 478.61–502.01 mbsf

The top part of Subunit IIB$_2$ is siltstone. Sediments between Sections 313-M0029A-120R-1 and 126R-2 (478.61–502.01 mbsf) contain two packages that irregularly fine downhole. Medium sand with coarse to very coarse grains (Core 313-M0029A-120R; 481.41 mbsf) fines downhole to clayey silt to Section 313-M0029A-122R-2, 52 cm (489.54 mbsf). Cores 313-M0029A-121R through 122R (484.46–487.6 mbsf) contain numerous sharp-based erosive sand beds that grade normally to sandy silt, commonly with parallel and cross-lamination and plant debris near the bed top. The second fining-downward package is found between Sections 313-M0029A-122R-2, 52 cm, and 126R-2, 80 cm (489.54–502.01 mbsf). Sediments in this interval contain a variety of sedimentary structures, including parallel and cross-lamination, possible ripple lamination, and contorted and convolute lamination.

Interpretation

The poorly sorted but well-stratified nature of the sediments and the lack of storm-related sedimentary

structures suggest sedimentation took place below the mean storm wave base. Normal grading cross-stratification style suggests rapid deposition by turbidity currents. The environment of deposition is likely a clinoform slope with sediment gravity flow, either within a submarine channel or intraslope apron environment.

Subunit IIC

Interval: 313-M0029A-126R-2, 80 cm, to 161R-2, 37 cm

Depth: 502.01–602.25 mbsf

Sections 313-M0029A-126R-2, 80 cm, to 161R-2, 37 cm, is a largely monotonous succession of very fine sandy silt and silt. At the top (Cores 313-M0029A-127R and 128R), sporadic centimeter-scale very fine sand beds contain faint laminae, and *Teichichnus* burrows decrease in thickness downhole (Fig. F10). Beginning in Core 313-M0029A-129R, the deposits become homogeneous, slightly micaceous very fine sandy silt with rare thin-walled shells, *Teichichnus* burrows, and plant debris. There are several ~20 cm thick heavily bioturbated intervals with burrow infills containing glauconite sand, quartz sand, shell debris, and occasional granules. This lithology continues to the bottom of Core 313-M0029A-159R. In Sections 313-M0029A-160R-1 to 161R-2, 37 cm (597.31–602.33 mbsf), silt deposition is interrupted by sharp-based beds (3–14 cm thick) of medium sand that grades normally to silty very fine sand. At the base of the unit, sandy silt overlies muddy to granuliferous medium sand assigned to Subunit IID.

Interpretation

Sediments in Subunit IIC were deposited in a deep offshore environment below mean storm wave base. The intervals with glauconite-filled burrows might represent periods of lower sedimentation rates. The graded beds are interpreted as dilute turbidity current deposits.

Subunit IID

Interval: 313-M0029A-161R-2, 37 cm, to 175R-1, 50 cm

Depth: 602.25–640.51 mbsf

This subunit contains two similar glauconite sand packages that fine uphole to silts at the top. A silt below Section 313-M0029A-167R-2, 42 cm, is used as the basis for dividing the subunit into Subunits IID_1 and IID_2.

Subunit IID$_1$

Interval: 313-M0029A-161R-2, 37 cm, to 167R-2, 42 cm

Depth: 602.25–620.59 mbsf

Section 313-M0029A-161R-2, 37 cm, to 163R-2, 40 cm (602.23–608.37 mbsf), are dominantly muddy glauconite sand, and the amount of glauconite and quartz increases downhole. Beds of glauconitic sandy mud indicate the presence of original stratification. Shell fragments are scattered throughout, and quartz granules have a patchy green coating, but no plant debris or mica are observed. Physical structures include subparallel to cross-lamination, and some laminae have a more chaotic and crosscutting pattern. In Sections 313-M0029A-163R-2, 40 cm, to 167R-2, 42 cm (608.37–620.59 mbsf), glauconite (from 30%–40% to ~5%) and mud decrease downhole. In Core 313-M0029A-165R-2 (614.1–615.66 mbsf), there is a concentration of thin-walled shells in poorly sorted sand and an isolated and articulated thin-walled shell. Quartz grains and granules become increasingly well rounded downhole through this unit. There are more cemented horizons, and light and dark green glauconite grains are observed. In Section 313-M0029A-167R-2, 42 cm (620.59 mbsf), there is an abrupt and bioturbated surface of coarse-grained glauconitic sand on brown clayey silt. The burrows are horizontal and vertical and filled with coarse glauconite and quartz sand.

Interpretation

The deeply bioturbated surface in Section 313-M0029A-167R-2, 42 cm (620.59 mbsf), marks an abrupt increase in the supply of coarse sediment. This surface is a candidate unconformity or a correlative conformity and is interpreted as a sequence boundary. The overlying poorly sorted sand, glauconitic sand, and muddy sand are interpreted as sediment gravity flow deposits. The preservation of delicate thin-walled shells suggests deposition by cohesive laminar flow deposits (debrites). The common crosscutting concave-upward laminae may indicate dewatering of saturated turbidites soon after deposition or could be a bioturbation fabric (*Teichichnus* type). Some remnants of tractional structures and weak normal grading support the interpretation of turbidity current deposits. The environment of deposition is interpreted as a toe-of-slope apron system. The succession increases in mud content and gradually decreases in quartz and glauconite sand content in Section 313-M0029A-161R-2, indicating a progressive abandonment of downslope transport.

Subunit IID$_2$

Interval: 313-M0029A-167R-2, 42 cm, to 175R-1, 50 cm

Depth: 620.59–640.51 mbsf

Brown clayey silt is found below an abrupt and bioturbated surface in Section 313-M0029A-167R-2, 42

cm (620.59 mbsf). The clayey silt contains many thin-walled shells. In Core 313-M0029A-168R (621.71 mbsf), the succession changes to bioturbated glauconite-bearing silt, which coarsens downhole into poorly sorted glauconitic medium to coarse sand. Cemented medium-grade glauconite sandstone is present in Core 313-M0029A-172R. Variably cemented glauconite sand continues from Core 313-M0029A-173R to the top of Core 175R. Thick-walled shells occur throughout this interval but show signs of severe dissolution. Glauconite grains are coarse and fragmented. Silty coarse glauconitic sand abruptly changes to bioturbated glauconitic silt and silt in Section 313-M0029A-175R-1, 50 cm.

Interpretation

The abrupt grain size increase across the basal surface indicates an increase in energy and can be interpreted as a sequence boundary. The floating very coarse sand grains and granules in silt suggest deposition of debris flows, though bioturbation at several levels indicates that the individual deposits must have been thin. Glauconite sand appears in pulses uphole, becoming dominant in coarse cemented units in Core 313-M0029A-175R and above. There are no physical sedimentary structures preserved in the coarse sandstones (or burrows in the most coarse beds), and the depositional process is unclear. The most likely explanation is multiple sediment gravity flow deposits in a toe-of-slope apron setting.

Unit III

Interval: 313-M0029A-175R-1, 50 cm, to 179R-2, 28 cm
Depth: 640.51–650.13 mbsf
Age: early middle to late early Miocene (early Langhian to late Burdigalian)

This unit was poorly recovered at Site M0029. Unit III begins with glauconitic siltstone. Several large vertical burrows and *Teichichinus* are identified in the upper 70 cm. Siltstone decreases in glauconite content downhole and is largely confined to burrows. Glauconite grains are coarse and fragmented. Thick-walled shells occur but show signs of severe dissolution. Glauconite and quartz sand, including quartz granules, increase toward the base of Unit III to a sharp surface in Section 313-M0029A-179R-2, 28 cm (650.13 mbsf).

Interpretation

The abrupt influx of sand at the base of Unit III on a bioturbated contact may be interpreted as an unconformity at the fringe of a toe-of-slope fan or at a sediment bypass surface. The overlying siltstone is interpreted as a deep offshore setting.

Unit IV

Interval: 313-M0029A-179R-2, 28 cm, to 183R-2, 101 cm
Depth: 650.13–663.88 mbsf
Age: middle early Miocene (middle Burdigalian)

Core 313-M0029A-179R is bioturbated silt with glauconite sand–filled *Thalassinoides* burrows at the top, and the sediment passes down into intensely bioturbated silt with floating coarse and very coarse quartz sand grains. The succession is dominantly siltstone with dispersed plant debris, sand-filled burrows, and rare thin-walled shells. The succession gradually coarsens downhole and increases in glauconite and quartz sand through Core 313-M0029A-183R (661.36–664.29 mbsf).

Interpretation

The fining- and thinning-upward trend at the base of Unit IV is interpreted to represent reduction in sand supply to a toe-of-slope setting in response to updip transgression. The sedimentary expression of this at the lower clinoform break in slope is a return to silt and clay deposition with coarse-grained material stored on the topsets of clinothems. Floating coarse grains in silt suggest a cohesive mud flow depositional process, and bioturbation indicates that the mud flow deposits must have been thin. There is a possible unconformity at the top of the unit.

Unit V

Interval: 313-M0029A-183R-2, 101 cm, to 208R-1, 9 cm
Depth: 663.88–728.55 mbsf
Age: middle early Miocene (early to middle Burdigalian)

Subunit VA

Interval: 313-M0029A-183R-2, 101 cm, to 189R-2, 15 cm
Depth: 663.88–675.06 mbsf

This succession begins in brown bioturbated silt with traces of plant debris, and grain size gradually increases downhole in glauconite and quartz sand through Core 313-M0029A-183R (661.36–664.29 mbsf) through silty medium glauconitic sand to coarse sandstone with many subangular granules, very coarse quartz sand grains, and articulated shells and well-preserved benthic foraminifers. The proportion of glauconite varies. From Core 313-M0029A-184R to Section 313-M0029A-189R-2, 15 cm (664.41–675.06 mbsf), the succession is coarse grained with poorly sorted medium glauconite sand with quartz and silty glauconitic sand, with shell fragments, benthic foraminifers, and an articulated

shell. Bed stratification is poorly preserved. Physical structures are rare, although convolute and subparallel laminations were observed. In Section 313-M0029A-189R-2, 15 cm (675.06 mbsf), an abrupt and bioturbated contact between medium and fine silty glauconitic sand above and silty clay below exhibits glauconite and quartz sand in burrows. Concretions are distinctive, as they contain quartz grains with a shattered fabric, although quartz grains are pristine outside the cemented areas.

Interpretation

The sharp-based sandstone in Section 313-M0029A-189R-1, 15 cm, is interpreted to be an unconformity, with the overlying coarse-grained unit an apron system that extended seaward of the lower clinoform break in slope. The main depositional processes in operation are inferred to be debris flows, although evidence of more sedimentary structures and bed stratification toward the top suggests the presence of turbidity current deposits. The top of this coarse-grained package is not sharp; rather, there is a gradational fining and thinning of beds uphole, indicating a sediment supply response to transgression.

Subunit VB

Interval: 313-M0029A-189R-1, 15 cm, to 196R-1, 93 cm
Depth: 673.61–695.84 mbsf

Below a bioturbated contact in Section 313-M0029A-189R-1, 15 cm (673.61 mbsf), silty clay contains glauconitic and quartz sand–filled burrows. The silty clay has rare benthic foraminifers and thin-walled shells, along with a trace of mica and plant debris. Silty clay continues through Section 313-M0029A-192R-2 (675.06 mbsf), where there are patches and beds of glauconite sandy mud and muddy sand with glauconite concentrated in burrows but with no observed quartz grains associated with the glauconite. Core 313-M0029A-193R-1 and 193R-2 both contain burrowed erosion surfaces. Below the surfaces, brown silt continues with dispersed very fine mica and traces of fine shell debris. Glauconite-filled burrows are concentrated in the top 16 cm of Section 313-M0029A-194R-2, where the glauconite is fine sand sized and occasionally forms larger aggregates. The base of the unit is placed at the base of Section 313-M0029A-196R-1, 93 cm (695.84 mbsf), below which there is gradational change to glauconitic sandy silt.

Interpretation

Silty clay is interpreted as a deep offshore environment. The absence of quartz grains with the glauconite may indicate that the glauconite is forming in

situ. Alternatively, glauconite concentrations may represent submarine fan/apron deposits that were remobilized down the clinoform slope from source areas with no quartz. The two erosion surfaces in Core 313-M0029A-193R likely represent significant sequence stratigraphic surfaces.

Subunit VC

Interval: 313-M0029A-196R-1, 93 cm, to 199R-CC, 11 cm
Depth: 695.84–707.17 mbsf

Sections 313-M0029A-196R-1, 93 cm, to 199R-CC, 11 cm (695.84–707.17 mbsf), contain glauconitic sandy silt and silty glauconite sand and sandstone with 5% quartz, including floating quartz granules. Glauconite granules are pale green (immature), whereas the smaller glauconite grains are almost black (mature). The amount of quartz decreases down through the cores to 10% in Core 313-M0029A-199R. Interbeds of fine sand and silt are observed near the base of the subunit together with ripple-scale cross-lamination that could be spreiten and, as such, the result of burrowing rather than physical processes. Grain size abruptly decreases between Sections 313-M0029A-199R-2 and 200R-1 from quartzose fine sand above to siltstone below.

Interpretation

The abrupt grain size increase at the base of Subunit VC from siltstone to sand is interpreted as a sequence boundary. The silty glauconite sand with quartz-rich intervals and granules in Cores 313-M0029A-199R through 197R is interpreted to be a series of debrites in an apron system seaward of the toe-of-clinoform slope.

Subunit VD

Interval: 313-M0029A-199R-CC, 11 cm, to 205R-2, 75 cm
Depth: 707.17–721.74 mbsf

Subunit VD is predominantly silt with varying amounts of glauconitic sand and rare ripple-scale cross-lamination. Glauconite is commonly concentrated in burrows together with rare shell fragments and benthic foraminifers. Granules of pale green and subangular glauconite are observed with fine sand grains of dark green glauconite. In interval 313-M0029A-205R-1, 79–82 cm (720.10–720.13 mbsf), a fine to medium glauconite and quartz sand forms a weakly normally graded bed.

Interpretation

The silt is interpreted as a deep offshore deposit, whereas the glauconite patches and beds are inter-

preted to be an in situ accumulation. The base of the unit includes more sand grains and a normally graded sand bed, which indicates a component of downslope transport of clastic sediment via turbidity currents.

Subunit VE

Interval: 313-M0029A-205R-2, 75 cm, to 208R-1, 9 cm

Depth: 721.74–728.55 mbsf

This succession begins in poorly sorted sand beds interbedded with sandy silt. Overall, the succession coarsens downhole to muddy medium sand with clay laminae and normal grading in discrete 2–5 cm thick beds. The coarse component is increasingly well sorted and well rounded downhole, and glauconite also increases downhole to an abrupt and bioturbated base in Section 313-M0029A-208R-1, 9 cm (728.55 mbsf).

Interpretation

The abrupt bioturbated boundary in Section 313-M0029A-208R-1, 9 cm (728.55 mbsf) (Fig. F11), is interpreted as an unconformity, and the overlying coarse-grained glauconitic is interpreted as having been deposited from downslope sediment gravity flow. Discrete 2–5 cm thick graded sand beds separated by clay laminae are interpreted as turbidites.

Unit VI

Interval: 313-M0029A-208R-1, 9 cm, to 214R-1, 52 cm

Depth: 728.55–747.27 mbsf

Age: middle early Miocene (late Aquitanian to early Burdigalian)

The Unit VI succession is a pale brown (tan colored) clayey silt with intercalated very fine and fine sand beds. There are several nodules in the upper part of this succession that fizz mildly with hydrochloric acid. The nodules commonly have deformed laminae above and below, with truncated laminae above. This interval has alternating units of interlaminated and bioturbated clayey silt with sand. In the interlaminated units, sharp-based sand beds are commonly rich in mica and plant debris and are normal and/or inverse graded. Parallel lamination, along with rare cross-ripple lamination, is observed in sand beds. There are common *Taenidium* burrows and also *Chondrites, Planolites,* and *Teichichnus*. A change in color around Section 313-M0029A-212R-2, 119 cm (744.76 mbsf), marks a transition from pale clayey silt to dark brown siltstone with rare shell fragments, trace plant debris and mica, a loss of lamination/bedding, and a decrease in clay content. Core recovery is poor at the base of the unit, although a very fine sandstone is found in Core 313-M0029A-214R.

Interpretation

The base of the unit is taken to be below the glauconitic very fine sandstone recovered in Core 313-M0029A-214R. The overlying succession fines and becomes paler uphole into an interlaminated unit interpreted as river-dominated offshore (prodelta) deposits with sediment gravity flow deposits, possibly flood events. Deformed laminae around the nodule demonstrate precompactional carbonate precipitation, and truncation of deformed laminae above the nodules indicate that nodule growth took place just below the water/sediment interface. A more glauconitic unit is identified on well logs (K/Th ratio), and with the rock pieces recovered in Core 313-M0029A-214R, an unconformity may be inferred at 745.90 mbsf.

Unit VII

Interval: 313-M0029A-214R-1, 52 cm, to 217R-CC, 11 cm

Depth: 747.27–756.33 mbsf

Age: early Miocene (early Aquitanian)

Section 313-M0029A-214R-1, 52 cm, through Core 217R (747.27–756.33 mbsf) is siltstone with glauconite sand grains, thin-walled articulated shells, trace mica, and plant debris.

Interpretation

The succession is interpreted as a low-energy deep offshore environment.

Conclusions

Miocene clinoforms in Hole M0029A were cored in a more seaward position than in Holes M0028A and M0027A. Sedimentary packages summarized here correspond well with sequences resolved by seismic stratigraphy (see "Stratigraphic correlation"). Unit VI shows evidence for development of open-shelf, shallow-water dysoxia in the form of weak or absent bioturbation, millimeter-laminated bedsets, and pyrite precipitation. We developed a facies model for deepwater toe-of-slope sequences from observations from Unit V to Subunit IID. Above a basal surface interpreted as a sequence boundary, sediment gravity flow deposits represent lowstand. The section fines uphole during transgression and highstand to offshore bioturbated silt. The majority of the section consists of silt deposited in offshore environments, including in situ glauconite. These fine-grained sediments are fossiliferous. Coarse-grained intraslope units within the silt-prone Unit II are either turbidite

lobes or channel fills. Spot coring may have identified Pleistocene sequences.

Smear slides

Analysis of 56 smear slides from Hole M0029A shows variations and general trends in the relative abundance of sand, silt, and clay (see "Site M0029 smear slides" in "Core descriptions"). Sand, silt, and clay composition curves broadly correspond to major lithostratigraphic units (Fig. F12). Silty sediments dominate; therefore, siliceous and calcareous microfossils such as diatoms, silicoflagellates, sponge spicules, and nannoplankton are common in Hole M0029A (absent in Subunit IE and Unit VI). Photomicrographs of typical smear slides are shown in Figures F13, F14, F15, and F16.

Paleontology

Pleistocene and middle and lower Miocene sections were identified from calcareous nannofossils, planktonic foraminifers, and dinocysts (Fig. F17) and integrated with Sr isotope stratigraphy to establish a chronostratigraphic framework for Hole M0029A (Fig. F18). There is generally good agreement among the ages obtained from different planktonic microfossil groups, which is particularly important in this hole because Sr isotope ages above ~480 mbsf (younger than 15 Ma) have substantial scatter due to possible reworking and the low rate of increase in global Sr isotope values (see "Chronology"). Microfossils are also more abundant in this hole, allowing for age refinements within the lower Miocene section that is barren of planktonic microfossils in previous holes. As in previous holes, reworked Paleogene material occurs throughout the Miocene section, although it is more concentrated in the lower Miocene, making age assignments somewhat difficult in certain intervals.

Paleobathymetric estimates in Hole M0029A are based on benthic foraminifer occurrences, which indicate that paleodepths fluctuated from the outer neritic zone (100–200 m) to the inner neritic zone (0–50 m). Benthic foraminifer biofacies changes indicate that paleobathymetric fluctuations occur within a sequence stratigraphic framework, with several sequences showing a shallowing-upward succession and one showing a deepening-upward succession. Benthic foraminifer water depth estimates and palynological estimates of proximity to shoreline show excellent agreement. Palynological data support previous reconstructions of a warm, humid early Neogene climate.

Biostratigraphy

Calcareous nannofossils

A total of 79 samples from Hole M0029A were examined for calcareous nannofossil biostratigraphy. Sample spacing was generally one sample every three cores (~10 m), with fewer samples taken from sandy or disturbed intervals. In addition, more samples were taken near the bottom of the hole to increase the biostratigraphic resolution. The total abundance of calcareous nannofossils within samples ranged from barren to very abundant. There were significantly fewer barren horizons in Hole M0029A compared to the two previous holes, and, in general, abundances were also greater at this site, allowing for better age control. Most samples contained moderately to moderately well preserved calcareous nannofossils, although increasingly poorer preservation occurs near the bottom of the hole. Members of the Noelaerhabdaceae family dominate most of the assemblages throughout the hole, although a few horizons characterized by lower overall abundances contain primarily discoasters and *Coccolithus pelagicus.*

Horizons recovered in Hole M0029A contain Pleistocene and middle and lower Miocene assemblages (Table T3; Fig. F19). Two samples from the uppermost part of the hole (Samples 313-M0029A-5R-1, 34.5 cm, and 7R-1, 25 cm; 7.245–13.25 mbsf) are assigned to Martini's (1971) Zone NN21 based on the presence of *Emiliania huxleyi,* indicating an age of <250 ka for the youngest sediments in this hole. Samples from Cores 313-M0029A-13R through 47R (40.56–289.38 mbsf) are barren of calcareous nannofossils, and no age is assigned to this interval.

Age assignments for Cores 313-M0029A-53R through 68R (289.38–332.15 mbsf) are tentative because of the lack of biostratigraphic marker taxa. Sample 313-M0029A-53R-1, 12 cm (289.38 mbsf), contains an abundant assemblage characteristic of the middle Miocene but no age-diagnostic taxa. *Coccolithus miopelagicus,* whose last occurrence (LO) falls within Zone NN8 at 11.0 Ma, occurs in Sample 313-M0029A-54R-1, 10 cm (292.41 mbsf). The biostratigraphic marker taxon for the base of Zone NN7, *Discoaster kugleri,* is not found in any samples in this hole. This species' entire range falls within Zone NN7 (11.5–11.8 Ma), so its absence could indicate that the horizons in Cores 313-M0029A-53R through 68R (289.38–332.15 mbsf) are either upper Zone NN7 (11.0–11.5 Ma) or older than the first occurrence (FO) of *D. kugleri* (>11.8 Ma); thus, these sediments are assigned to undifferentiated Zone NN6/NN7.

Calcidiscus premacintyrei, a secondary marker taxon with a LO within Zone NN6 (12.65 Ma) is found in Sample 313-M0029A-70R-2, 13 cm (339.69 mbsf). The horizons from this sample to Sample 313-M0029A-74R-1, 147 cm (351.13 mbsf), are therefore assigned to Zone NN6 based on the presence of *C. premacintyrei* and the absence of *Sphenolithus heteromorphus.* Further work should indicate if the overlying sediments assigned to undifferentiated Zone NN6/NN7 are in fact all older than Zone NN7.

The LO of *S. heteromorphus* (13.6 Ma), which marks the top of Zone NN5, occurs in Sample 313-M0029A-78R-1, 147 cm (360.88 mbsf). It is not apparent if this represents the actual extinction horizon of this species or if there is an unconformity present that truncates the range of the species. *Cyclicargolithus floridanus,* whose LO falls within Zone NN6 at 13.19 Ma, is only questionably present above the LO of *S. heteromorphus* at this site but consistently present below, which could indicate that some of Zone NN6 and possibly Zone NN5 is missing. The interval from Sample 313-M0029A-78R-1, 147 cm, to 134R-1, 16 cm (360.88–524.27 mbsf), is assigned to Zone NN5 based on the presence of *S. heteromorphus* and the absence of *Helicosphaera ampliaperta.*

The LO of *H. ampliaperta* (15.6 Ma), which marks the top of Zone NN4, occurs in Sample 313-M0029A-137R-2, 147 cm (533.19 mbsf). The interval from this sample to Sample 313-M0029A-192R-1, 23 cm (682.94 mbsf) is assigned to Zone NN4 based on the co-occurrence of *H. ampliaperta* and *S. heteromorphus* and the absence of *Sphenolithus belemnos.* Zone NN4 is particularly long (15.6–18.3 Ma), with very few secondary biostratigraphic events to further divide it. The last common occurrence (LcO) of *Discoaster deflandrei* (16.2 Ma) is found in Sample 313-M0029A-164R-2, 145 cm (612.46 mbsf). The FO of *Discoaster petaliformis* is thought to predate the LcO of *D. deflandrei;* however, in this hole the two events are found in the same sample, which could indicate a small unconformity within Zone NN4 or reworking. This interpretation is further confirmed by the presence of debris flows in this interval (see "Lithostratigraphy").

Sample 313-M0029A-194R-1, 22 cm (689.03 mbsf), contains a poorly to moderately preserved assemblage of calcareous nannofossils with a characteristic lower Miocene assemblage but no age-diagnostic taxa and is therefore not assigned to a zone. Sample 313-M0029A-197R-1, 20 cm (698.16 mbsf), contains *S. belemnos,* the LO of which marks the top of Zone NN3 (18.3 Ma). This species is not found in any other samples from Hole M0029A. The total range of *S. belemnos* is restricted to Zone NN3, so this sample can be assigned an age of 18.3–19.2 Ma (within Zone NN3). The next sample examined (Sample 313-M0029A-199R-1, 132.5 cm; 705.385 mbsf) contains few poorly to moderately preserved calcareous nannofossils with no age-diagnostic taxa and therefore cannot be assigned an age. Sample 313-M0029A-202R-1, 50 cm (712.28 mbsf), is tentatively assigned to undifferentiated lower Zone NN3/NN2 based on the absence of *S. belemnos.* The top of Zone NN2 is marked by the LO of *Triquetrorhabdulus carinatus* (19.6 Ma). This species is rare in lower Miocene sediments from the previous sites, so its absence in the sample from Core 313-M0029A-202R does not exclude the possibility that the sediments are assignable to Zone NN2.

The LO of *T. carinatus* is found in Sample 313-M0029A-205R-1, 30 cm (719.61 mbsf). Thus, sediments from this sample to the bottom of the hole (Sample 313-M0029A-217R-CC, 11–13 cm; 719.61–756.35 mbsf) are assigned to Zone NN2. Furthermore, the scarcity of *Helicosphaera euphratis* in these sediments suggests that they are younger than the crossover in abundance of *Helicosphaera carteri* with *H. euphratis,* a secondary event within Zone NN2 dated to ~21.5 Ma. Therefore, the age of the sediments at the bottom of the hole is probably <21.5 Ma based on calcareous nannofossils.

Planktonic foraminifers

A total of 102 samples between Samples 313-M0029A-21R-CC, 0–3 cm, and 217R-CC, 11–13 cm (85.61–756.33 mbsf), were examined for planktonic foraminifers; of these, 72 are barren (Table **T4;** Fig. **F20**). Planktonic foraminifer results indicate that sediments recovered from Hole M0029A are of early–middle Miocene age. The samples contain a Miocene assemblage consisting of *Globigerina praebulloides, Globoquadrina baroemoenensis, Paragloborotalia mayeri, Globigerinoides quadrilobatus, Globigerinoides triloba, Globorotalia praescitula, Globigerina woodi, Catapsydrax parvulus, Globorotalia continuosa, Globorotaloides suteri, Globoquadrina dehiscens, Sphaeroidinellopsis disjuncta, Fohsella peripheroronda, Globorotalia archeomenardii,* and *Praeorbulina sicana.*

Most samples between Cores 313-M0029A-21R and 64R (85.61–322.20 mbsf) are barren of planktonic foraminifers. Two samples (313-M0029A-67R-CC, 0–2 cm, and 68R-1, 145–150 cm; 331.84 and 333.41 mbsf) are assigned to middle Miocene undifferentiated Zone M10–M11/N13–N14 based on the presence of *P. mayeri* (LO 11.4 Ma) in the latter sample and the absence of any members of the *Fohsella foshi* spp. group (LO 11.9 Ma) in either sample. Another barren interval occurs between Samples 313-M0029A-70R-CC, 0–2 cm, and 78R-CC, 0–3 cm (341.04–362.49 mbsf), so these samples are unzoned.

F. peripheroronda (LO 13.8 Ma) occurs in Sample 313-M0029A-81R-CC, 0–2 cm (371.83 mbsf), and *G. archeomenardii* (LO 13.9 Ma) is found in the next sample examined (82R-CC, 13–15 cm; 374.31 mbsf). The LOs of these species fall with Zone M7/N10. The interval from Sample 81R-CC, 0–2 cm, to 135R-CC, 0–2 cm (371.83–528.20 mbsf), is therefore assigned to Zone M7/N10 based on the presence of these species and absence of *P. sicana,* a secondary marker for the base of Zone M7/N10 (14.8 Ma).

The LO of *P. sicana* (14.8 Ma) occurs in Sample 313-M0029A-137R-CC, 14–16 cm (533.70 mbsf), indicating Zone M6/N9 or older. The FO of this species marks the base of Zone M5/N8 (16.4 Ma) and the lower/middle Miocene boundary; this event is found in Sample 313-M0029A-167R-2, 151–153 cm (621.68 mbsf). Thus, the interval between these two samples (533.70–621.68 mbsf) is assigned to undifferentiated Zone M5–M6/N8–N9. A possible secondary event occurs within this interval in Sample 313-M0029A-150R-2, 149–151 cm (569.80 mbsf): the FO of *G. archeomenardii.* Kennett and Srinivasan (1983) indicate that this event occurs within uppermost Zone M5/N8, suggesting that the Zone M5–M6/N8–N9 boundary occurs somewhere above 569.80 mbsf. However, this taxon has not been calibrated well to the timescale, and it should be used as a datum level with caution.

The interval from Sample 313-M0029A-169R-CC, 9–11 cm (626.54 mbsf), to 176R-CC, 30–32 cm (644.26 mbsf), is assigned to lower Miocene undifferentiated Zone M3–M4/N6–N7 based on the presence of *G. praescitula* (FO 18.5 Ma) and the absence of *P. sicana* (FO 16.4 Ma). Most samples below this are barren, making it difficult to assign a zone, although *C. parvulus* is present in Sample 313-M0029A-195R-CC, 10–12 cm. The FO of this species is a secondary marker for the M3–M4/N6–N7 boundary and could therefore indicate that the interval above belongs to Zone M4/N7. In addition, Eocene foraminifer *Turborotalia cerroazulensis* (LO 33.8 Ma) co-occurs with Miocene taxa near the bottom of the hole (Sample 313-M0029A-214R-1, 51–53 cm; 747.73 cm), indicating that it is reworked.

Dinocysts

A total of 35 samples between Cores 313-M0029A-28R and 217R (156.18–756.33 mbsf) were examined for dinocysts (Table **T5;** Fig. **F21**). Dinocysts are extremely sparse in Samples 313-M0029A-28R-CC, 14–17 cm, to 40R-CC, 12–14 cm (156.18–231.99 mbsf), and those present are long-ranging taxa; thus, these sediments were not zoned.

Samples 313-M0029A-41R-CC, 8–10 cm, to 54R-CC, 14–16 cm (235.97–292.75 mbsf), are assigned to un-

differentiated dinocyst Zones DN6–DN8 (13.3–8.7 Ma) based on the presence of *Habibacysta tectata, Selenopemphix dionaeacysta,* and *Cyclopsiella granosa* (Fig. **F21;** Table **T5**). The presence of *Cordosphaeridium minimum* and *Cerebrocysta poulsenii* together with *H. tectata, S. dionaeacysta,* and *C. granosa* constrains Samples 313-M0029A-64R-CC through 69R-CC (322.20–337.89 mbsf) to between dinocyst Zone DN6 and the lower part of Zone DN8 (13.3–10.7 Ma). A similar flora, containing *C. minimum, H. tectata,* and *C. granosa* but lacking *S. dionaeacysta* and containing rare *Systematophora placacantha,* whose LO marks the top of Zone DN5 (~13.2 Ma), allows the age of Sample 313-M0029A-73R-CC (349.70 mbsf) to be constrained to the upper part of Zone DN5 (~14.2–13.2 Ma; early Serravallian). Samples 313-M0029A-77R-CC, 18–20 cm, to 119R-CC, 10–12 cm (361.51–385.91 mbsf) can be assigned to the lower part of Zone DN5 because of the co-occurrence of *Trinovantedinium papulum* and abundant *Apteodinium tectatum* together with other dinocysts characteristic of the middle Miocene, such as *Labyrinthodinium truncatum truncatum* and *H. tectata.* De Verteuil and Norris (1996) placed the LO of *A. tectatum* in the same horizon as the FO of *H. tectata* (~14.2 Ma); however, *H. tectata* has been noted in slightly older sediments at other sites in this study. The same has been noted in the North Sea Miocene sequence (Munsterman and Brinkhuis, 2004; Dybkjaer and Piasecki, 2008).

The interval between Samples 313-M0029A-124R-2, 133–135 cm, and 148R-CC (496.45–563.84 mbsf) is tentatively assigned to lower Zone DN5 to DN4. The marker taxon for the base of Zone DN5 (LO of *Distatodinium paradoxum*) is only present in much older samples in this hole; thus, the LO of *Cousteaudinium aubryae* can be used to approximate this boundary. This event occurs in Sample 313-M0029A-158R-CC, 20–22 cm (592.78 mbsf); however, because this is a secondary event that is not as well calibrated, these samples are assigned to undifferentiated lower Zone DN5 to DN4. Species characteristic of this interval include *A. tectatum, S. placacantha,* and *Labyrinthodinium truncatum modicum.* Samples 313-M0029A-158R-CC, 20–22 cm, and 169R-CC, 9–11 cm (592.78–626.54 mbsf), are tentatively assigned to Zone DN4 based on the co-occurrence of *C. aubryae* and *L. truncatum modicum.* The base of Zone DN4 is marked by the FO of *L. truncatum modicum,* which occurs in Sample 313-M0029A-169R-CC, 9–11 cm (626.54 mbsf). The interval between this sample and Sample 313-M0029A-198R-CC (703.76 mbsf) is assigned to Zone DN3 based on the co-occurrence of *Lingulodinium multivirgatum* and *Sumatradinium druggii,* together with *A. tectatum, Apteodinium spiridoides,* and *C. aubryae.*

The LO of *Exochosphaeridium insigne* marks the top of Zone DN2 and occurs in Sample 313-M0029A-201R-CC (711.48). The interval from this sample to Sample 313-M0029A-212R-CC, 22–25 cm (743.79 mbsf), is assigned to Zone DN2, which spans 22.2–19.2 Ma (late Aquitanian–early Burdigalian) based on the presence of this taxon, together with *Sumatradinium hamulatum, Sumatradinium soucouyantiae, Tityrosphaeridium cantharellum,* and *D. paradoxum.* The presence of *E. insigne* in Samples 313-M0029A-201R-CC and 205R-CC, 13–15 cm, restricts the interval from 711.48 to 722.80 mbsf to the upper part of Zone DN2. The presence of taxa such as *Distatodinium biffii* and *Stoveracysta conerae* suggests reworking of Paleogene sediments in Samples 313-M0029A-208R-CC, 14–16 cm (703.65 mbsf), and 209R-CC (731.51 mbsf). The presence of *Cribroperidinium tenuitabulatum* and *Caligodinium amiculum* together with common *T. cantharellum* allows Sample 313-M0029A-217R-CC, 11–13 cm (756.33 mbsf), to be assigned to Zone DN1 (uppermost Chattian–Aquitanian) by comparison to dinocyst flora in Hole M0027A, although definitive markers for this zone are absent, other than *Homotryblium vallum.* This age assignment is tentative, considering the clear evidence of reworking in this sample.

Paleoenvironment

Benthic foraminifers

Benthic foraminifers were examined from 104 core catcher samples and samples from within cores from Samples 313-M0029A-21R-CC, 0–3 cm (85.61 mbsf), to 217R-CC, 11–13 cm (756.33 mbsf) (Fig. **F22;** Table **T6**). Benthic foraminifer abundances ranged from absent to abundant, and preservation ranged from poor to excellent. Poorly preserved specimens likely were reworked and were not used in paleodepth estimates.

Paleobathymetric estimates based on benthic foraminifer occurrences indicate that paleodepths fluctuated from the outer neritic zone (100–200 m) to the inner neritic zone (0–50 m). Barren intervals occur throughout the section and may indicate nearshore/nonmarine environments, substantial downslope transport, or dissolution. The low-resolution sampling interval did not bracket all lithologic changes, and the sampling interval varied throughout the hole. Stratigraphic biofacies distributions may be related to substrate (finer grained versus sandier sediments), changes in sediment input, and/or organics/dysoxia, which often correspond to bathymetry. Preliminary results presented here suggest that benthic foraminifer biofacies changes in Hole M0029A indicate that paleobathymetric fluctuations occur within a sequence stratigraphic framework, with several sequences showing a shallowing-upward succession and one showing a deepening-upward succession. Detailed, higher resolution postcruise studies will elaborate on this.

The base of the uppermost shallowing-upward succession occurs in middle Miocene (Serravalian) sediments above seismic reflector m4.2, which is identified near the bottom of Core 313-M0029A-71R (343.64 mbsf) (Fig. **F22**). Samples in and above Sample 313-M0029A-56R-CC, 15–17 cm (295.49 mbsf), were barren or contained only one or two specimens of foraminifers; no paleodepths could be determined for these samples (Fig. **F22**). Below this, sparse foraminifers in Sample 313-M0029A-58R-CC, 7–8 cm (303.16 mbsf), may indicate a 25–50 m paleodepth, with *Buliminella gracilis* dominating the underlying sample (Sample 313-M0029A-60R-CC, 0–3 cm; 310.49 mbsf), indicating slightly greater depths of 50–75 m. Paleodepths were deeper in the three samples below this one (Samples 313-M0029A-67R-CC, 0–2 cm [331.84 mbsf], to 70R-CC, 0–2 cm [341.04 mbsf]), as indicated by abundant *Uvigerina juncea* and *Bolivina tectiformis,* along with *Nonionella pizarrensis/Nonionella miocenica stella, Hanzawaia concentrica/Hanzawaia hughesi,* and other taxa. These samples overlie reflector m4.2, which appears to be a sequence boundary (see **"Stratigraphic correlation"**).

Below this, a second shallowing-upward succession within the middle neritic zone (50–100 m) occurs from the base of Core 313-M0029A-71R (343.64 mbsf) through Sample 313-M0029A-108R-1, 124–128 cm (451.22 mbsf), above the placement of seismic sequence m5 (478.61 mbsf) (see **"Stratigraphic correlation"**). *B. gracilis* and *U. juncea* are excellent depth markers that were identified in this section (Fig. **F22;** Table **T6**). Samples containing more abundant *B. gracilis* indicate slightly shallower paleodepths (50–80 m) than samples containing more abundant *U. juncea* (75–100 m), based on faunal studies from New Jersey coastal plain boreholes (Miller et al., 1997). Other rare to common species found in these faunas characterized by *Buliminella-Uvigerina* typically include *Bolivina paula, B. tectiformis, Bulimina mexicana, Fissurina* spp., *H. concentrica/H. hughesi, Lenticulina* spp., *Marginulina* sp., *N. pizarrensis/N. miocenica stella, Pararotalia* sp., *Quinqueloculina* sp., polymorphinids, and *Stilostomella* spp.

In contrast to the overlying units, benthic foraminifer assemblages indicate an overall deepening-upward succession in Samples 313-M0029A-156R-CC, 0–3 cm, to 119R-CC, 10–12 cm (588.19–479.85 mbsf), with fluctuations superimposed on this trend (Fig. **F22**). This section overlies seismic sequence

boundary m5.2, placed at ~602 mbsf (see "Stratigraphic correlation"). With several exceptions, most samples in Samples 313-M0029A-119R-CC, 10–12 cm (479.85 mbsf), to 137R-CC, 14–16 cm (533.70 mbsf), contain faunas that indicate depths >100 m, in the outer neritic zone (100–200 m). These samples typically have faunas similar to those described above for the middle neritic zone but with additional species (or increased abundances) in rare to common numbers that result in higher diversity and indicate deeper paleodepths, such as *B. mexicana, Cassidulina* spp., *Cibicidoides pachyderma, Cibicidoides* spp., *Hanzawaia mantaensis,* miliolids, *Nonion* sp., *Oridorsalis* sp., polymorphinids, and *Rectuvigerina lamelata.* Paleowater depths in the lower part of the interval are consistently shallower than above, with faunas characterized by varying abundances of *B. gracilis* and *U. juncea,* indicating variations within the middle neritic zone (50–100 m) in Samples 313-M0029A-145R-CC, 0–4 cm (556.35 mbsf), through 156R-CC, 0–3 cm (588.19 mbsf) (Fig. F22).

The large number of seismic sequence boundaries (see "Stratigraphic correlation") below Sample 313-M0029A-156R-CC, 0–3 cm (588.19 mbsf), to the bottom of the hole makes it difficult to identify trends in the paleodepth estimates relative to seismic reflectors (Fig. F22). Most samples are barren between Samples 313-M0029A-158R-CC, 20–22 cm, and 173R-CC, 153–156 cm (592.78–636.76 mbsf); this may indicate very shallow water environments or downslope transport. The exception in this interval is Sample 313-M0029A-167R-2, 151–153 cm (621.68 mbsf), which contains a well-preserved assemblage characterized by *B. paula, B. tectiformis,* and *B. gracilis,* with rarer specimens of *U. juncea, Globocassidulina subglobosa,* and *Cassidulina laevigata,* indicating a paleodepth of 50–75 m.

Deeper water assemblages were identified below this, with lower middle neritic (~75–100 m) faunas in Samples 313-M0029A-176R-CC, 30–32 cm, to 192R-CC, 15–17 cm (644.26–686.21 mbsf), including *B. gracilis* and *U. juncea,* with *N. pizarrensis/N. miocenica stella, H. concentrica/H. hughesi, Lenticulina* spp., *C. pachyderma,* and agglutinated foraminifers. Sample 313-M0029A-178R-CC, 0–3 cm (652.52 mbsf), also includes common specimens of *Chilostomella* sp. and *Fursenkoina* spp., which may indicate low-oxygen pore water conditions. The deepest part of the section is in the lower part of the interval, with benthic foraminifers indicating a paleodepth >100 m for Sample 313-M0029A-195R-CC, 10–12 cm (695.19 mbsf).

Below a barren interval (Samples 313-M0029A-198R-CC, 0–4 cm [703.76 mbsf], to 210R-3, 25–27 cm [737.81 mbsf]), two samples contain faunas that in-

dicate paleowater depths >100 m (Samples 214R-1, 51–53 cm [747.73 mbsf], and 217R-1, 0–4 cm [752.86 mbsf]). These faunas include *Bigenerina* sp., *Bolivina* spp., *B. gracilis, C. pachyderma, Cibicidoides crebbsi, Fissurina* spp., *Gyroidinoides* spp., *H. mantaensis, Lenticulina* spp., *Oridorsalis* sp., *Plectofrondicularia* sp., polymorphinids, and *U. juncea.* The lowermost sample examined, Sample 313-M0029A-217R-CC, 11–13 cm (756.33 mbsf), is dominated by *U. juncea,* with *B. gracilis, Plectofrondicularia* sp., and polymorphinids, indicating 75–100 m paleodepth.

Terrestrial palynomorphs and palynofacies

Sediments from 24 core catcher samples from Samples 313-M0029A-28R-CC, 14–17 cm, to 217R-CC, 11–13 cm (156.18–756.35 mbsf), were analyzed for palynomorphs (Table T5; Fig. F23). Palynomorph preservation was generally good enough to assign specimens to major groups, although pollen identification was often hampered by pyrite accumulations inside pollen grains (Table T7). Frequent pollen types (e.g., oak, hickory, and linden pollen) were sometimes determined to genus level in order to identify dominant vegetation types. In the following, the total content of nonsaccate pollen and pollen with small sacci is used as a reference sum (thus, combined non/small-saccate pollen is always 100%), and percentages of other palynomorphs are related to this sum. Ages mentioned are in accordance with the preliminary age model based on organic-walled dinoflagellate cysts (dinocysts).

Serravalian to early Tortonian (~150 to ~340 mbsf)

The five samples analyzed for the interval between ~150 and ~340 mbsf are characterized by generally low numbers of marine palynomorphs (Fig. F23). In combination with the also relatively low amount of bisaccate pollen, this points to a short distance between Hole M0029A and the shoreline and probably also to relatively shallow water depths. The increase in bisaccate pollen in Sample 313-M0029A-64R-CC (322.20 mbsf) is probably related to a shift in hinterland vegetation, although increased percentages in marine palynomorphs could indicate an increase in distance to the shoreline. Pollen from herbs, sedges, and grasses are relatively frequent and indicate the presence of open landscapes. Among nonsaccate tree pollen, those from (probably) shrublike oaks are most frequent. One sample (313-M0029A-38R-CC, 16–18 cm; 226.51 mbsf) contains a relatively high amount of hickory pollen (>12%), but in general, hickory was probably not as widespread during this interval as during the preceding intervals (Fig. F24; see below).

Late Langhian to early Serravalian (~340 to ~480 mbsf)

In the six samples examined from this interval, there is a generally higher percentage of marine palynomorphs compared to samples from ~150 to ~340 mbsf, pointing to a longer distance between Hole M0029A and the coast. One peak in bisaccate pollen (Sample 313-M0029A-111R-CC, 14–17 cm; 460.49 mbsf) is probably related to shifts in hinterland vegetation rather than directly to changes in the hole to shoreline distance because it is coeval with relatively low contents of marine palynomorphs. The time interval represented in the samples between ~340 and ~480 mbsf probably witnessed a spreading of grasses. Sample 313-M0029A-119R-CC, 10–12 cm (479.85 mbsf), may reflect a medium-term cooling event because the pollen data indicate on one hand the spreading of mountainous pines, herbs, and shrublike oaks and on the other the retreat of other tree taxa, with the latter adapted to more humid conditions. The hinterland was probably dominated by oak and hickory-oak forests.

Latest Burdigalian to earliest Serravalian (~500 to ~625 mbsf)

The interval from Samples 313-M0029A-124R-2, 133–135 cm, to 169R-CC, 9–11 cm (496.45–626.54 mbsf), is represented by five analyzed samples. It is characterized by relatively low numbers of marine palynomorphs, pointing to generally shorter distances between Hole M0029A and the shoreline. Comparatively low abundances of herb, shrublike oak, and hickory pollen paired with higher amounts of broad-leaf tree pollen indicate a very humid interval.

Aquitanian to Burdigalian (~625 to ~760 mbsf)

The interval from Sample 313-M0029A-176R-CC, 30–32 cm (644.26 mbsf), to the bottom of the hole (Core 217R; 756.35 mbsf) is characterized by generally higher amounts of bisaccate pollen and increasing percentages of dinocysts (downcore to ~725 mbsf). This points to increased water depth and distance between the shoreline and Hole M0029A in the lower portion of this interval. Sample 313-M0029A-180R-CC, 11–13 cm (655.30 mbsf), contains unusually high amounts of elm and beech pollen, which may point to a medium-term shift in forest assemblages. This could have been caused by slightly increased humidity because pollen of probably shrublike oaks and herbs decrease in the same sample.

Samples from Cores 313-M0029A-208R and 209R (730.65–735.07 mbsf) contain especially high numbers of dinocysts and foraminifer test linings, along with the highest content of bisaccate pollen in analyzed samples from Hole M0029A. This suggests a longer distance between Hole M0029A and the shoreline compared to all other analyzed intervals.

These same samples plus a sample from Core 313-M0029A-212R (743.79 mbsf) contain relatively high amounts of hemlock pollen, with pollen of both eastern and western American species. The presence of western hemlock species in combination with lower amounts of hickory pollen indicates moister and slightly cooler conditions during the time interval reflected in these three samples. For the remainder of the early Burdigalian to the late Aquitanian, hickory-oak forests dominated the vegetation of the hinterland. An especially high amount of hickory pollen is found in Sample 313-M0029A-212R-CC, 22–25 cm (743.79 mbsf), at the onset of the interval of hemlock presence. These high percentages (~20%) indicate the dominance of hickory at that time because hickory pollen is generally underrepresented compared to oak and bisaccate pollen.

Geochemistry

Interstitial water

Like Holes M0027A and M0028A, Hole M0029A displays alternating layers of fresher and saltier water within the upper part of the hole (Table T8; Fig. F25). Unlike earlier holes, however, Hole M0029A contains an increasingly saline brine from 345 mbsf to the deepest sample at 748 mbsf, in which chloride concentration reaches 995 mM, nearly twice the concentration in seawater. Brine was also just barely penetrated near the bottom of Hole M0028A from 627 to 664 mbsf. From 0 to 330 mbsf in Hole M0029A, there are seven relatively fresh layers, with minimum chloride concentrations from 19 to 313 mM, alternating with saltier layers with maximum concentrations from 373 to 509 mM. We were able to define these many layers in spite of the fact that the upper 200 mbsf was the only spot cored in this hole. Excluding brine in the lower half of the hole, the average chloride concentration in these alternating layers, weighted by depth interval, is 314 mM, nearly identical to the 309 mM calculated for Hole M0028A, indicating that, overall, 40% of the pore water in the upper half of the hole is fresh. The deepest layer of fresher water, at 315–324 mbsf, is shallower in Hole M0029A than in the other two holes. Brine in the bottom half of Hole M0029A approaches an asymptotic composition of ~1000 mM chloride, indistinguishable from similar asymptotic brine concentrations measured during Ocean Drilling Program (ODP) Leg 150 at Sites 902, 903, 904,

and 906 farther offshore, from the upper slope at a water depth of 445 mbsl to the mid-slope at 1123 mbsl (Mountain, Miller, Blum, et al., 1994). Such convex-upward, asymptotic depth profiles for a non-reactive species like chloride are typical of one-dimensional advective-diffusive profiles that suggest upwelling of pore water, which in this case is a brine.

As in Holes M0027A and M0028A, most of the major and minor ions in the seawater closely mimic the depth profile for chloride (Figs. F25, F26). Ratios of these ions to chloride can therefore reveal the composition of waters from different sources within the upper half of the hole and the composition of the brine within the lower half. As in earlier holes, fresher and saltier layers each have distinctive, perhaps unique, compositions. Of the seven layers of fresher water in the upper half of the hole, for example, five have lower Na/Cl than seawater and two have higher Na/Cl. These same five layers have higher K/Cl than seawater, but the other two do not. The upper four layers have higher Br/Cl than seawater and the lower three do not. Some layers have higher Mg/Cl than seawater and some lower, whereas still others have similar ratios to seawater. All the fresher layers have higher Ca/Cl than seawater, but some are much higher than others. All layers of fresher water have a different pH from the adjacent salty layers and, although most are higher, at least one, at 277–286 mbsf, is much lower. It remains to be seen whether these compositions can be correlated laterally with compositionally similar layers in the other two holes. As brine becomes more concentrated with depth in Hole M0029A, Na, K, and Mg decrease relative to chloride and Br, Li, B, Ca, and Sr increase. Many of these changes in elemental ratio to chloride are approximately linear with depth. The directions of change are generally consistent with those seen in Holes M0027A and M0028A but are much more definitive because the changes are so much larger in the saltier brine in Hole M0029A.

Based on the ratio of sulfate to chloride, sulfate has been selectively reduced within freshwater layers, as was the case in Holes M0027A and M0028A. Alternatively, fresher waters have a source of sulfate independent of chloride (i.e., not seawater). Saltier layers all have sulfate to chloride ratios near that of seawater. Unlike the other holes, there is not a large increase in either alkalinity or ammonium within any of these layers, fresh or salty, nor was H_2S detected at any depth. Below the depth of the deepest freshened layer, sulfate drops to low concentrations, mostly <1 mM, presumably because of microbial sulfate reduction during oxidation of organic matter. Total sulfur (TS) in the sediment ranges as high as 4.2 wt% over this interval and pyrite as high as 5%–6% (Fig. F27).

As expected, alkalinity, ammonium, phosphorus, and Ba increase greatly over the interval in which sulfate decreases. The distribution of apatite in the sediment is also greatly affected. Alkalinity then begins a slow decrease toward the bottom of the hole, as Ca increases and $CaCO_3$ precipitates in response. Increases in ammonium and Ba slow over this interval until they, too, decrease again near the bottom of the hole. Phosphorus undergoes this increase and then decreases over a much shorter depth interval, presumably because it is released by oxidation of organic matter and then is quickly reprecipitated as apatite (Fig. F27).

Like Holes M0027A and M0028A, Hole M0029A shows a large chemical anomaly in a single interval, comprising large peaks in Mn, Fe, Si, B, Li, and K. This time, the usual peaks in Ca and Sr are quite muted, if present at all, and there is no prominent low in Na/Cl. There is, however, an extreme low in pH, as there was in Hole M0028A. The anomalous interval in Hole M0029A is at 277–286 mbsf, shallower than the similar anomalies at 394 and 407 msbf in, respectively, Holes M0027A and M0028A. It also occurs in a layer that is not particularly salty, unlike the earlier cases. The cause of this single anomaly in each of the three holes remains unknown.

Sediment chemistry and mineralogy

Sediment samples were analyzed for total carbon (TC), total organic carbon (TOC), and TS concentrations. Total inorganic carbon (TIC) was calculated as the difference between TC and TOC (Table T9). Bulk sample X-ray diffraction (XRD) data were produced for the same samples (Table T10). The upper part of Hole M0029A was spot-cored, and sampling was sparse for these analyses; only three samples were measured above the deepest freshwater layer at 330 mbsf, at 7, 16, and 50 mbsf. We are thus unable to infer the effects of fresh versus salty layers as was done for Holes M0027A and M0028A. Instead, the samples document the effect of increasing salinity with depth from 330 mbsf to the bottom of the hole.

The uppermost sample at 7 mbsf is relatively rich in TIC and carbonate minerals and poor in TOC and TS (Figs. F27 and F28). The next deepest sample at 17 mbsf has the highest quartz concentration measured in Hole M0029A, 70%, and lies at the top of the first salty layer. The sample at 552 mbsf has the highest concentrations of TOC, TS, and pyrite measured in any sample recovered during Expedition 313. As in Holes M0027 and M0028A, TS correlates very well with pyrite as measured by XRD (Fig. F27). As noted above, apatite varies systematically with dissolved phorphorus, and siderite correlates with apatite, as it

did in Holes M0027A and M0028A (Fig. F28). As dissolved Ca and Ca/Cl increase with depth in brine, alkalinity decreases steadily below 379 mbsf (Fig. F26), indicating precipitation of $CaCO_3$, mainly as calcite (Fig. F28). TIC is relatively high and variable over this depth interval, reaching a maximum concentration of 1.6 wt% at 696 mbsf, nearly the same depth at which alkalinity peaks within the general decline, at 690 mbsf.

As in Holes M0027A and M0028A, quartz dominates the mineralogy of the sediment in Hole M0029A, ranging in concentration from 37% to 70% in analyzed samples (mean = 59%) (Table T10; Fig. F29). Other minerals that exceed 6% are, in order, plagioclase, kaolinite, other clay minerals, and calcite.

Physical properties

The focus of this section is to provide a description of the petrophysical data sets collected on cores from Hole M0029A and their significant characteristics and variations, as well as concentrating in more detail on a number of interesting aspects. Some measurements display variation primarily associated with depositional changes, whereas other measurements are controlled more by postdepositional factors such as the degree of cementation, porosity, and the type of interstitial water. In addition, the combined integration of the core and logging petrophysical data sets allows calibration of core data with in situ borehole properties and provides an assessment of the precise depth from which core was collected in the borehole.

Whole-core measurements were acquired on a multisensor core logger (MSCL): gamma density, *P*-wave velocity, noncontact electrical resistivity, and magnetic susceptibility. Thermal conductivity and natural gamma radiation (NGR) measurements were taken on whole cores prior to the commencement of the Onshore Science Party (see "Physical properties" in the "Methods" chapter). Density, porosity, and *P*-wave velocity were measured and calculated from, on average, one sample in every core section. Figure F30 provides an overview of the data acquired. A synthesis of all downhole and physical property data from this site can be found at the end of "Downhole measurements."

Density and porosity
Gamma density and wet bulk density

Gamma density in Hole M0029A is more variable than in Hole M0027A but less variable than in Hole M0028A. Outliers outside the 1.5 to 2.9 g/cm³ interval are not considered below (Figs. F31, F32). Wet bulk density calculated from wet and dry weight and dry volume of samples from cores varies between 1.65 and 2.25 g/cm³, with a few high values from the sampled cemented beds (2.7 and 2.9 g/cm³).

Repeat measurements with resaturation of sediment before measurement indicate that the density of samples may be overestimated by up to 5%. Despite this uncertainty, there is fair correspondence between gamma density and wet bulk density; however, there is greater scatter than is found Holes M0027A and M0028A. Detailed comparison of gamma density and wet bulk density for Hole M0029A shows wet bulk density measurements that were probably entered for the wrong core section in the data files. Based on written data sheets, it was possible to correct some of these errors. For gamma density, tops and ends of cores often show reduced densities. This problem is a result of fractured/disturbed core extremities. In the case of short sections, the problem seems persistent. No attempt has been made here to correct for this, except through numerical high-pass filtering. It is recommended in the future that short Section 2s or 3s be removed in the gamma density data set if values are lower than the average of the core.

Density varies downhole with intervals of lower densities (~1.85 g/cm³) and higher densities (~2.1 g/cm³) (Fig. F31). These variations broadly correspond to different bulk lithologies: respectively, clay- to silt-rich intervals and sand, glauconite, or cemented intervals, as in Holes M0027A and M0028A. These variations are more frequent and show higher amplitude from 600 m to the base of the hole, enriched with coarse-grained glauconitic quartz sand horizons. This correspondence to lithology is particularly clear when investigated in combination with porosity (see below).

Calculated porosity

Calculated porosity, here referred to as porosity, is derived from the difference between wet and dry weights and dry volume of selected sediment samples (see "Physical properties" in the "Methods" chapter). Some core liners had little drill fluid in them. As a result, sediments with high permeability may have been drained of water during the storage and handling. Porosity may therefore be underestimated, particularly that of sands. Based on repeated measurements, we estimate that the porosity of sands may be underestimated by ~10%, perhaps up to 19%. Clays and silt sediments have relatively little permeability and are not expected to have drained as much. Calculated porosity values vary from 27% to 58%.

Stratigraphically, porosity varies with intervals of low porosity (~40%) and intervals with high porosity

(~45%–55%). This variation corresponds to bulk lithology (Fig. F31). Clay- to silt-rich sediments in general have higher porosity than sand, glauconite, or cemented sediments.

The porosity of clay and silt intervals decreases with depth. The same tendency is observable for sand-rich intervals. Porosity reductions broadly follow the exponential decrease in porosity of sands, silts, and clays that has been observed from a number of passive margins and derived analytically (Sclater and Christi, 1980; Bahr et al., 2001). High-amplitude, high-frequency variations are common in the lower part of the hole from 620 m downhole and are characterized by coarse-grained quartz glauconitic intervals.

Combined density and porosity as a stratigraphic tool

As in Hole M0027A, there is a significant inverse variation between porosity and density in samples from Hole M0029A (Fig. F33). The different lithologies of Hole M0029A fall close to a mixing line between rock (zero porosity and density of 2.7 g/cm³) and saltwater (100% porosity and density of 1.027 g/cm³). Sand sediments and the majority of clay and silt samples plot close to the mixing line between rock and saltwater. Glauconite-rich sediments clearly plot above the mixing line at higher densities, most likely influenced by mature glauconite with a density of 2.9 g/cm³ as opposed to ~2.65 for quartz. A significant portion of the silt and clay samples plot below the line and have relatively reduced densities, which could be interpreted as organic matter and other low-density minerals (Rider, 2006).

Downhole, there are differences between gamma density and density measured on samples. Gamma density corresponds to the main lithology variation in the hole and is a bit more variable than bulk wet density (Fig. F34A, F34B, F34C, F34D). There is little separation between density and porosity curves when plotted on inverted scales.

A number of packages of gradual overall increasing density and decreasing porosity can be delineated based on the average "log motif" of gamma density and sample-based density and porosity (Fig. F34A, F34B, F34C, F34D). In lithostratigraphic Unit I and Subunit IIA above 430 mbsf, the packages in general are separated by an abrupt density decrease and a porosity increase stratigraphically uphole. These packages correspond to large-scale coarsening-upward successions ending in abrupt fining (horizontal arrows; Fig. F34A, F34B) (see "Paleontology"). Subpackages of coarsening uphole sediments can be seen. In Subunits IIB and IIC, thicker fining-upward packages are present (Fig. F34B, F34C, F34D). Below Unit II, the log motif is inverted compared to that in the top of Unit I and II. An abrupt density increase and porosity decrease are followed by a more gradual density decrease and porosity increase, stratigraphically uphole. This pattern mimics fining-upward successions.

Significant boundaries based on the averaged log motif can be identified at several places. Many of the abrupt density shifts correspond to surfaces or intervals with a shift in other petrophysical parameters and wireline logs (Table T11). Such surfaces often correspond to important surfaces, as determined by sedimentology and stratigraphic correlators (see "Lithostratigraphy" and "Stratigraphic correlation"). Intervals with abundant organic phytoclasts seem to have densities reduced relative to porosity.

P-wave velocity

P-wave velocity was measured on both the MSCL and discrete samples. Additionally, sonic logs were obtained between 720 and 404 m wireline log depth below seafloor (WSF) (see "Downhole measurements") (Fig. F35). These three sets of velocity measurements generally correlate well with each other, as well as with density data. Core recovery in the upper ~320 mbsf was sparse in the unconsolidated sediments of Unit I, and suitable samples for discrete velocity measurements were correspondingly few. MSCL velocity measurements are also mostly lacking between ~400 and ~620 mbsf (see "Physical properties" in the "Methods" chapter), except for the occasional particularly consolidated intervals. The lack of accurate MSCL velocity measurements in that section of the hole is thought to be due to the presence of gas (methane) resulting in small bubbles forming in the core liner fluid and preventing signal transmission between the transducers. Confirmation of this awaits postexpedition analysis of the headspace gas collected.

The highest discrete velocities obtained were on cemented intervals or concretions, for example at 343 mbsf in the siltstone of Unit II (just below Subunit IIA₂), where a velocity of 5600 m/s corresponds to a clear increase in MSCL density, MSCL velocity, and conductivity logs (Fig. F35). With the exception of this siltstone bed, MSCL velocities are low (<1800 m/s) throughout Unit II (as are most of the discrete velocity measurements) and in Unit I (where obtained). Velocities are slightly higher in Subunit IIA₂, where the change in lithology from sands to silts and clays enabled more data to be collected. Around 479 mbsf there is a claystone interval just above a gap in core recovery. At the base of this level, MSCL density and all velocities display a clear increase. The sonic

log indicates that the maximum peak is within the gap. Around 602 mbsf (Subunit IID_1), velocities increase in the sonic log with correspondingly higher core velocities (where obtained), especially in the center of this section at ~612 mbsf. In the glauconite-rich coarse cemented intervals toward the base of Subunit IID_2 (see "Lithostratigraphy"), velocities increase. Between ~668 and 674 mbsf, a further increase in velocity is apparent (up to 3500 m/s in the samples measured). Discrete velocities from ~574 mbsf (in Subunit VB) are fairly constant and not high (<2500 m/s), although more variation is evident in both MSCL and sonic velocity logs. Only discrete velocities and very few MSCL velocities were acquired from 728 mbsf to the base of the hole; they display variation with a particularly high value measured on a cemented nodule bed at 734 mbsf.

Magnetic susceptibility

MSCL magnetic susceptibility was measured at 1 cm intervals and illustrates high-resolution changes in lithology related to variations in the magnetic minerals and/or their sizes. The 5 cm resolution downhole trends associated with lithological units and stratigraphic surfaces are described in "Downhole measurements." Core measurements and log measurements correlate extremely well, although absolute values are different.

Electrical resistivity

As in Hole M0027A, electrical resistivity is affected by core liner saturation with drilling fluids. Short Section 3s are not considered here because of their low core liner saturation, although the removal of this effect has been attempted by high-pass filtering (Figs. F31, F34).

Resistivity is highly variable throughout the hole (Figs. F34, F35), from low values of ~0.3 Ωm to high values of 6 Ωm. High resistivity is encountered in a number of cemented levels. Above ~280 mbsf, resistivity is ~1 Ωm. Below ~280 mbsf, resistivity is ~0.7 Ωm with thin intervals of higher resistivity in cemented levels. Variability is high, between ~400 and 535 mbsf and below 630 mbsf, respectively, from the lower part of Subunit IIA through the upper part of Subunit IIC and from the lower part of Subunit IID to the base of the hole.

In the latter interval, the larger resistivity variations are bounded by cemented beds (see correlation with sonic log in Fig. F35) and possibly pyrite-rich horizons that sharply differ from the smooth increase in chlorinity with depth.

Digital linescans and color reflectance

All cores from Hole M0029A were measured using an X-ray fluorescence (XRF) digital linescan system with data recorded at a resolution of 0.068 mm as both images and red-green-blue (RGB) values down the core centerline. All suitable cores were also scanned for color reflectance. These data may reflect changes in such factors as glauconite or iron content by analysis of a specific wavelength or a*/b* ratios. The quality of the core section shows a significant effect on the scattering of the data (see "Physical properties" in the "Methods" chapter).

Thermal conductivity

The few thermal conductivity measurements downhole to 300 mbsf (Fig. F36) show high values (>2 W/[m·K]) in sand with seawater chlorinity levels and low values (1.5–1.8 W/[m·K]) in clays with low-chlorinity water (see "Geochemistry"). Below 300 mbsf, variations are smooth and decrease downhole. Clay layers (380–460 and 530–600 mbsf) show low and subconstant thermal conductivity values. Thermal conductivity increases in glauconitic intervals, possibly in relation to changes in porosity. In contrast to Holes M0027A and M0028A, thermal conductivity does not clearly correlate with chlorinity (see "Downhole measurements").

Natural gamma radiation and core-log correlation

All cores were measured for NGR (Fig. F35). These data are equivalent to the downhole total gamma ray log; although absolute values are different, trends are parallel. Gamma ray trends and characteristics are described in "Downhole measurements." Correlations between the MSCL-NGR and downhole total gamma ray (TGR) are excellent, with only minor (<1 m and usually <0.6 m) vertical offsets in any interval. The match is better where there is both good core recovery and distinctive peaks in both data sets.

The correlation between core depths and logging data can be evaluated using several petrophysical data sets, notably NGR measurements, but magnetic susceptibility is also very useful. Toward the base of the hole, we applied a depth correction to several cores (see "Stratigraphic correlation"). Magnetic susceptibility measurements on both core and logs are also useful at this site in assessing correlation.

Petrophysical surfaces and intervals

Important surfaces and intervals are identified based on pronounced or sharp changes in trends in one or

more of the petrophysical values. Many abrupt shifts correspond to surfaces or intervals with trend changes in wireline logs. A preliminary summary of the most important surfaces or intervals is given in Table **T11.** Some surfaces and intervals correspond to important surfaces, as determined from sedimentology and/or seismic data (see **"Lithostratigraphy"** and **"Stratigraphic correlation"**).

A synthesis of petrophysical data together with downhole logs and derived quantities of each lithostratigraphic unit are presented at the end of **"Downhole measurements."**

Paleomagnetism

Discrete sample measurements

A total of 511 samples from Hole M0029A were measured in the pass-through magnetometer. Sequences of finer grained sediments (silt and clay) were targeted for sampling at varying resolution, from one sample every 20 cm to one sample every meter, depending on grain size and predicted accumulation rates. In addition, some coarser grained sequences were sampled at one sample per section. Natural remanent magnetization (NRM) and the remanence after sequential alternating-field (AF) demagnetization up to 15 or 60 mT was measured for all samples.

Remanent magnetization

Similar to Holes M0027A and M0028A, the primary magnetization in Hole M0029A is mostly carried by a low-coercivity component, with demagnetization also indicating the presence of a high-coercivity magnetic mineral. The initial NRM moment of the sediments is typically weak, on the order of 10^{-10} to 10^{-8} Am^2, except for a clay-rich horizon in Cores 313-M0029A-210R and 211R (~734–740 mbsf), which exhibits stronger magnetic moments, on the order of 10^{-8} Am^2 (Fig. **F37**).

Just as for the lower half of Hole M0028A, we decided to limit the demagnetization procedure to a maximum alternating field of 15 mT (except for cores) to preserve the signal for more detailed and careful treatment after the science party. Magnetic remanence from Hole M0029A sediments generally follows a semistraight trajectory after successive AF demagnetization up to 15 mT, indicating that a single component is being demagnetized. However, this component often does not trend toward the origin, suggesting the presence of a second higher coercivity component that is not demagnetized. As in Holes M0027A and M0028A, inclination data show prevailing normal polarity, suggesting that the first component is a viscous overprint.

Magnetostratigraphy

The low level of AF demagnetization means that, in many cases, it is impossible to isolate a characteristic remanent magnetization (ChRM) for the sediments. Preliminary polarity interpretations were made for Cores 313-M0029A-61R through 73R (~310–349 mbsf) (Fig. **F38**) and 208R through 217R (~728–756 mbsf) (Fig. **F39**), which are characterized by slightly elevated magnetic susceptibility values, in addition to stronger NRM moments in the latter case. Preliminary polarity interpretations were also made for Cores 313-M0029A-74R through 160R (~350–600 mbsf), but at this stage we were not able to isolate any apparent reversal boundaries. All interpretations were based on inclination data after 15 mT AF demagnetization (up to 60 mT between 325.02 and 332.58 mbsf) and by studying the trajectory of the NRM in orthogonal Zijderveld plots. In this section, we present preliminary age estimates (Table **T12**) for each reversal boundary based on the constraints given by Sr isotope ages and biohorizons (Figs. **F38, F39**).

For Cores 313-M0029A-61R through 73R (~310–349 mbsf), the first reversal boundary (from normal to reversed polarity [N/R]) between 331.11 and 330.91 mbsf is tentatively identified as the onset of Chron C5AAr (Fig. **F38**). The next reversal boundary (R/N) between 327.95 and 327.53 mbsf is identified as the onset of Chron C5AAn.

A thick zone of normal polarity between ~370 and 470 mbsf may represent Chrons C5Acn through C5ADN, dating the upper surface above sequence m5 as ~14.6 Ma (Fig. **F40**).

For Cores 313-M0029A-208R through 217R (~728–756 mbsf), a reversal boundary (N/R) between 733.49 and 733.29 mbsf is identified as the onset of Chron C6An.1r. A thick normal magnetozone to ~747 mbsf may be wholly or in part Chron C6An.2n.

Downhole measurements

The focus in this section is to provide a description of the downhole data sets collected in Hole M0029A and their most significant characteristics. A few examples of log trends and boundaries where trends in MSCL core measurements are equivalent to borehole measurements are discussed in this section. Some variations depend mostly on lithology, whereas some are controlled by postdepositional factors such as the degree of cementation, diagenesis, and the type of interstitial water formation. Integration of core and logging petrophysical data allows calibration of core data with in situ borehole properties and provides an assessment of the precise depth below

the seafloor. These correlations are briefly described in "Physical properties." At the end of the chapter, a synthesis of petrophysical data, downhole, and derived quantities are presented for each lithostratigraphic unit.

Downhole measurements in Hole M0029A

In Hole M0029A, 1923 m of wireline logging data was acquired, in addition to VSP measurements (see Tables T7 and T8 in the "Methods" chapter). Spectral gamma logs were acquired through the steel drill pipe down to 757 m WSF.

Two overlapping sections of open hole were logged in Hole M0029A, from 729 to 483 m WSF (lower section) and from 491 to 403 m WSF (middle section), as well as a small upper section between 348 and 322 m. In the lower interval in open hole, acoustic, conductivity, sonic, and magnetic susceptibility logs were run. In the middle interval, conductivity, magnetic susceptibility, and sonic logs were acquired, and in the upper section, open-hole spectral gamma and conductivity logs were collected. VSP measurements through the drill pipe were acquired at 3.05 m spacing from 753 to 207 m WSF and then on a second run from 226 to 13 m WSF. Figure F41 provides an overview of downhole measurements for Hole M0029A (see "Core-seismic-log synthesis").

In all figures, downhole geophysical data and images are plotted in meters below present-day seafloor based on the wireline scale (WSF), and, where appropriate, boundaries between lithostratigraphic units (Units I–VII; see "Lithostratigraphy") are indicated to facilitate comparison with other chapters.

Spectral gamma ray logs

Spectral gamma ray logs allow continuous characterization of the entire borehole because they mainly depend on lithology. As in Hole M0027A and M0028A, the TGR signal from the downhole probe and the NGR measurements run on whole cores correlate very well, in some cases allowing accurate repositioning of core depth below seafloor (see "Stratigraphic correlation").

Total gamma ray counts in Unit I (see "Lithostratigraphy") display high variability (Fig. F41). TGR values around 40 counts per second (cps) correspond to sand, whereas excursions to higher values (above 100 cps) correlate to clays, as observed in the recovered cores. From the top of Unit II to 600 m WSF, TGR values are around 170 cps, with several lows corresponding to coarser intervals (479.20, 490.90, and 497.62 m WSF) and two peaks around 560 and

565 m WSF corresponding to increased Th content. The lower part of Unit II is characterized by a drastic increase in K content related to glauconite-rich sand packages. These sands are also clearly evidenced by some peaks in magnetic susceptibility and higher density. Glauconite-rich sands are also observed in the units below, at the bottom of Unit V. The transition to the tan-colored clayey silt of Unit VI is not clearly expressed in the total gamma counts. However, as for Unit VI in Hole M0028A, this unit is characterized by a clear increase in Th content and low K and U.

The gamma ray record in Hole M0029A can be interpreted using the same guidelines used in Holes M0027A and M0028A ("Downhole measurements" in the "Site M0027" chapter and "Downhole measurements" in the "Site M0028" chapter), based on TGR (ASGRcgs) (Fig. F41); concentrations of K, U, and Th; and their ratios. TGR and elemental composition allow continuous lithological interpretation, which can be precisely tied to core observations and extended to unrecovered intervals.

Here we propose, as a preliminary attempt, an interpretation of the upper part of the hole (0–320 m WSF) (Fig. F42) where coring was sparse (see "Lithostratigraphy" and "Stratigraphic correlation" for comparison). The interpretation of log data suggests the presence of silt and clay in the upper part of Hole M0029A (0–53 m WSF) and mainly sand downhole, containing clay intervals at different levels. Several sharp contacts between sands and clays (43.5, 53, 154, 182, 220, 250, 287, and 293 m WSF) are observed. The sand may be glauconitic in the upper part of the hole, with glauconite content decreasing to 104.5 mbsf. The presence of glauconite is possibly detected in the 182–191.5 m WSF interval. Glauconite was not observed in the recovered cores (see "Lithostratigraphy"), but it might occur between 10 and 20 m WSF, as inferred from high magnetic susceptibility and a Th/K ratio <0.05. An XRD result at 7.28 mbsf supports this, as a relatively high amount of glauconite is indicated compared to cores from lower in the hole.

Variations in the Th/K ratio indicate that the glauconite content decreases in the sand near the clay intervals. This pattern is observed in the 0–100 m WSF interval (12, 43–53, 57.5, and 68 m WSF clayey intervals) (Fig. F42). In Figure F42, clay intervals are underlined in light gray and organic matter–rich intervals are underlined in dark gray. In clay intervals, Th/K ratios are close to 0.1, whereas in glauconitic sands, Th/K ratios are <0.05 and decrease on both sides (above and below) of clay layers (arrows in Fig.

F42) and could be interpreted as resulting from diagenetic chemical diffusion processes at clay/sand boundaries.

Organic matter can be tentatively identified by peaks in U that do not encompass changes in K. It is noteworthy that organic matter content seems to increase downhole, with occurrences in sands at different levels. In Unit I, small peaks were encountered at 75, 83, 268–269, 274.5–278, 289, and 293–304 m WSF. A slight increase in organic matter occurs downhole in the 344–400 m WSF interval. Systematically higher values of U, compared to Th, from 470 m WSF downhole can be interpreted as better preservation of organic matter, especially in the glauconitic units. U content is particularly high at 560 and 564 mbsf, at the boundary between high- and lower density sediments (see "Physical properties"). From 600 to 700 m WSF, there is alternation of glauconitic sands and clays that are slightly depleted in Th and enriched in K and U.

One of the most striking features can be observed at the upper and lower boundaries of lithostratigraphic Unit VI (728.5–742 m WSF). Unit VI itself is characterized in the gamma ray record by depleted K and U and by increased Th when compared to the adjacent unit (Fig. F35). K and Th contents are highest in the center of the unit and decrease slightly toward the edges. Glauconite can be identified in correspondence of the upper and lower boundary by K and U peaks and low Th content.

Below 320 m WSF, lithologies inferred from the gamma ray logs are in good agreement with core observations (see "Lithostratigraphy"). Several sedimentary sequences can also be predicted from gradual changes in gamma ray measurements, coarsening either uphole (222–227, 267–287, 304–314 m WSF, and slightly between 344 and 400 mbsf) or downhole (231.5–236, 248–250, 287–293, and 314–318 m WSF).

Magnetic susceptibility logs

Magnetic susceptibility is commonly a clear indicator of lithological variations. In all holes, magnetic susceptibility signals from the wireline measurements (EM51 probe) and MSCL on whole cores correlate very well, in some cases allowing very accurate repositioning of core depth below seafloor. As the magnetic susceptibility wireline log in Hole M0029A begins at 404 m WSF in Subunit IIA (see "Lithostratigraphy"), further description of magnetic susceptibility throughout the borehole can be found in "Physical properties." In general, magnetic susceptibility trends correlate with glauconite occurrence throughout, with the exception of the tan clays of Unit VI (Figs. F41, F43). The magnetic susceptibility curve correlates also very well with K content (related to glauconite), density, and P-wave velocity. It anticorrelates with conductivity and, to a lower degree, with discrete porosity. In more detail, from the beginning of the lower logged interval at 404 m WSF, magnetic susceptibility is low and drastically increases at 602 m WSF (top of Subunit IID_1). Below this unit (Fig. F41), magnetic susceptibility fluctuates from very high values to intervals of lower values but always at a higher base level than that found above 602 m WSF. Lower values correspond to siltstone levels apparently poor in glauconite, whereas higher values tie to cemented glauconitic-rich intervals (also high velocities on the sonic and low conductivity values; see below). Consistently high magnetic susceptibility intervals are observed between 634 and 640, 666 and 674, and 698 and 705 m WSF, each of which represents glauconite estimates of at least 60% in part of each interval. From 720 m WSF to the end of the log at 730 m WSF, values are low with a slight increase downhole.

Acoustic image logs

The ABI40 was run at a resolution of 288 ppt in the lower part of Hole M0029A between 657 and 483 m WSF. Acoustic amplitude and traveltime images provide a gauge of the induration and texture of the borehole walls. Lithological changes and potential impedance contrasts can be identified in several places, despite the fact that the tool was not centralized in the hole. For example, lithologic unit boundaries are clearly evidenced on the acoustic images at 620.42 and 650.13 m WSF, correlating with the Subunit IID_1–IID_2 and Unit IV–V transitions, respectively. In Figure F43, a sharp contact is clearly observed on both the amplitude and acoustic images at the base of a submarine fan/apron corresponding to the lower part of Subunit IID_1 (see "Lithostratigraphy"). The transition between Subunits IIC and IID_1 is also marked by a change in borehole diameter that is more irregular and locally smaller in the very fine sandy silt and silt forming Subunit IIC. Slight changes in the amplitude image reflect locally some changes in lithologies, such as the occurrence of glauconite-rich sands between 607.52 and 608.45 m WSF (e.g., Core 313-M0029A-163R).

Sonic velocity logs

Sonic velocity logs were obtained from 720 to 404 m WSF in open hole (Subunit IIA_3 through Unit V). Velocity measurements from whole cores and discrete samples are described in "Physical properties" in the "Methods" chapter. All velocity measurement trends generally correlate relatively well with each other as well as with the core density data. In Hole

M0029A, 2PSA *P*-wave velocities gradually increase from 404 to 602 m and become more irregular deeper, with alternating high and low values (Fig. **F41**). In more detail, sonic velocities are generally low (<1750 m/s) until 449 m WSF, where a small peak corresponds to a sand layer (interpreted as a sequence boundary; see **"Lithostratigraphy"**). Below this, velocities remain slightly higher (Subunit IIB$_1$) until decreasing over ~10 m to 479 m WSF, where there is a sharp increase in a siltstone horizon. The sonic log indicates that the maximum occurs within a core recovery gap. Velocities downhole of this gap are slightly variable but become more consistent around 502 m WSF as the lithology becomes finer grained. A major change occurs at 602 m WSF (Subunit IID$_1$) (Fig. **F43**) with correspondingly higher core velocities (where obtained). This interval from 602 to 643 m WSF is characterized by variable, often high (>2400 m/s) velocities correlating with more indurated intervals, especially in the glauconite-rich coarse cemented intervals toward the base of Subunit IID$_2$ (see **"Lithostratigraphy"**). Notable peaks occur at 612, 624, 640, and 634–642 m WSF (Fig. **F43**), generally fitting conductivity lows, increased densities, and impedances (Fig. **F44**). Between ~668 and 674 m WSF, a further increase in velocity is apparent (Fig. **F45**). Between ~695 and 707 m WSF, a broad raised velocity peak corresponds to an elevated K/Th ratio and higher magnetic susceptibility. Only discrete velocities and a very few MSCL velocities were acquired from 720 m WSF to the base of the hole (see **"Physical properties"**).

Conductivity logs

Conductivity in the borehole is influenced by a variety of aspects, including lithology, pore water content, and salinity. In Hole M0029A where data were acquired, the conductivity signal globally increases toward 600 m WSF and becomes highly variable below (Fig. **F41**). It is generally anticorrelated with density core values (Fig. **F44**). A small interval was logged close to the top of Unit II from 334.37 to 347.87 m WSF. In this interval, conductivity shows drastic changes in the signal, passing from high values peaking from 344.60 to 344.16 m WSF to lower values below. This peak fits with a cemented fine-grained horizon possibly developed at the transition between saltier pore waters above and less salty pore water below (Fig. **F36**).

In the rest of the hole, from 403 m WSF downhole, conductivity increases relatively constantly to 601.20 m WSF, with several lows related to coarser intervals also evidenced by small peaks in the sonic curves (e.g., 479.20, 490.90, and 497.62 m WSF). At 601.20 m WSF, a drastic change is observed when entering a coarse-grained interval associated with a debris flow apron (Subunit IID; see **"Lithostratigraphy"**). In this interval, several conductivity lows correlate with glauconitic levels, evidenced by high values in the magnetic susceptibility signal, or with indurated intervals also evidenced by sonic peaks and density increase (Fig. **F43**). Conductivity then increases at the transition between Units II and III, when entering siltstones. A succession of high-value intervals (644–661, 675–682, and 709–715 m WSF) and low-value intervals characterize Units III–V (Fig. **F45**). The highest values correspond to siltstone levels poor in glauconite (low susceptibility), whereas low values tie to cemented glauconite-rich intervals (high magnetic susceptibility, high velocities on the sonic log, and high densities measured from whole cores).

In contrast to Holes M0027A and M0028A, there is no clear evidence for correlation between chlorinity variations from interstitial waters and conductivity variations in Hole M0029A (Fig. **F36;** see **"Geochemistry"**). However, the absolute values of conductivity are greater in this hole, which correlates with the significantly higher chlorinity values (Fig. **F36**). This correlation ties in with lower average resistivity values measured on the MSCL (see **"Physical properties"**) compared to Sites M0027 and M0028.

Vertical seismic profiling

VSP data were acquired through pipe for the entire borehole (753 m WSF uphole) in two stages, but none were acquired in open hole at this site (Fig. **F46**). Downgoing waves were picked and time-depth relationships calculated. The resultant time-depth curve can be used to calibrate the time to depth of the seismic reflection profile.

Example of multilog interpretation

Petrophysical and downhole measurements can provide evidence for sequence boundaries. Figure **F43** is a compilation of several parameters between 596 and 626 m WSF, containing two sedimentary transitions between lithologic Subunits IIC and IID$_1$ and Subunits IID$_1$ and IID$_2$ (see **"Lithostratigraphy"**). As evidenced from the figure, data measured on the whole cores (MSCL data) match the wireline signal relatively well. Some slight shifts in core depth are, however, evidenced locally by comparing magnetic susceptibility peaks from the downhole probe (EM51) and from the MSCL (e.g., 607.5–608.4 and 625.35 m WSF). A sharp change in the acoustic signals is clearly observed on the ABI40 images at 620.42 m WSF (wavy yellow line). It marks the abrupt transition between sandy siltstones below and glauconitic sands above (Section 313-M0029A-167R-2). This fa-

cies change was observed at 620.52 mbsf in the cores (see "Lithostratigraphy"). At the same depth, petrophysical data evidence an increase in density and a slight increase in resistivity when passing from Subunit IID_2 to Subunit IID_1. The magnetic susceptibility signal also increases at this transition, reflecting the presence of glauconite in the sands located above. These sands are 18 m thick (from 602.10 to 620.40 m WSF). They are locally characterized by high TGR counts (602.10–608.30, 612–617, and 618.6–625.35 m WSF), reflecting enrichment in glauconite content. These intervals are also associated with increased magnetic susceptibility. In some places, the sonic shows peaks (607, 611.9, and 612.9 m WSF) correlating with cemented levels associated with low conductivities. At the top of the sands (dotted yellow line), the total gamma count drastically decreases when entering the glauconite-free silt unit located above 602.10 m WSF. The absence of glauconite is also testified by an increased Th/K ratio. This transition is also associated with a decrease in density and a slight increase in resistivity.

Downhole log and physical property integration

This section combines results of logging and physical property measurements with the main characteristics of the lithostratigraphic units. A brief summary shows links between key petrophysical intervals (Table T11) and stratigraphic surfaces (Fig. F44A, F44B, F44C, F44D, F44E, F44F, F44G, F44H). All depths are given in meters below seafloor and ignore small differences that may exist between core (mbsf) and log (m WSF) depths. More details can be found in "Physical properties" or above. Numerical data are accessible online; see "Publisher's notes" for links to the database.

Lithostratigraphic Unit VII

Unit VII is characterized by relatively high TGR that corresponds to clayey silt to silt with two lows at 754 and 750 mbsf. It shows relatively high U content, possibly due to the presence of organic matter, and an increase in magnetic susceptibility at the top.

The transition to Unit VI is not clearly marked on the gamma ray logs. It fits a low in magnetic susceptibility, a low in density, and an increase in porosity, although the few measurement points do not allow clear characterization of this boundary.

Lithostratigraphic Unit VI

TGR in Unit VI shows an overall serrated shape, high Th content, and low amounts of K and U. Magnetic susceptibility is high and highly variable, reflecting the presence of magnetic minerals except glauconite,

as indicated by the high Th/K ratio. The estimated clay volume is also high. Clay volumes and Th content increase at the base of the unit and decrease at the top. The lower part of this unit is different (from the unit lower boundary to 744 mbsf), as it is rich in K and U and depleted in Th and clay. According to the low Th/K ratio, this interval should be rich in glauconite, but the lack of magnetic susceptibility measurements prevent any conclusion. The above observations suggest that despite the poor core recovery, an important change occurs at 744 mbsf close to the m5.8 boundary. Chlorinity (Fig. F36) shows high values, reflecting high concentrations.

The transition to Unit V shows no change in TGR but an increase in K content; a sharp increase in magnetic susceptibility; and a decrease in Th, clay volume, and porosity. The transition is characterized by the appearance of glauconite in the sands of Unit V above.

Lithostratigraphic Unit V

TGR in Unit V is highly variable, serrated, and of medium value. Two large K-rich intervals at 708–695 and 674–666 mbsf and the succession of small peaks between 688 and 682 mbsf clearly correlate with high magnetic susceptibility, sonic velocity, and impedance values and low Th/K ratios, conductivity, and porosities. They reflect glauconite-rich sandy intervals. In contrast to Site M0027, the trend of conductivity in Unit V does not correlate with measured chlorinity, which is relatively constant and high in this interval (Figs. F36, F44). Conductivity is highly related to variations in porosity and magnetic susceptibility, suggesting that the electric signal is essentially carried by the matrix when passing through the formation and/or is very sensitive to variations in pore water volumes. However, in this unit, as well as in Units IV and III above, a line passing through the highest values of conductivity measured in the fine-grained intervals follows the chlorinity curve trend.

The transition to Unit IV is smooth. It is marked by an increase in K and Th contents, reaching a maximum a few meters above the boundary, and by a small peak in magnetic susceptibility.

Lithostratigraphic Unit IV

The TGR curve in Unit IV is relatively flat with a smooth bow shape with depressed areas at the base and top that are slightly enriched in K, reflecting the presence of glauconite, as also evidence by increased magnetic susceptibility. Sonic velocity, conductivity, porosity, and density signals show relatively constant values, except, again, at the lower and upper boundaries of the unit.

The transition to Unit III is marked by a peak in magnetic susceptibility just below the boundary and a peak in density just above. It also fits with a peak in sonic velocity, correlating with a low in conductivity. This boundary is visible on the acoustic image by a change in wall texture and an increase in caliper diameter above the boundary.

Lithostratigraphic Unit III

The TGR curve of Unit III is relatively flat, except at the lower and upper limits. The lowermost meter is slightly enriched in glauconite, as evidenced by increased K content, high magnetic susceptibility, and a low Th/K ratio. This interval is also marked by high sonic, high density, high magnetic sucsceptibility and low conductivity compared to the formation above, suggesting possible slight induration. Sonic, conductivity, porosity, and density signals also show relatively constant values, except at the boundaries. The remainder of Unit III is relatively homogeneous up to 644 mbsf, where a strong peak in P-wave velocity fits with a density peak, a conductivity low, and a diminution of the hole diameter, just above an unnamed sequence boundary (between surfaces m5.3 and m5.6).

At the transition to Unit II, we observe an increase in K content and magnetic susceptibility across the boundary. A small peak in sonic is also evidenced, just at the base of a small increase in density. Borehole diameter is slightly reduced at the boundary.

Lithostratigraphic Unit II

The TGR curve in Unit II shows a bow to serrated shape with intermediate values in the sand/silt intervals observed from the base of the unit to 602 mbsf and a flatish, serrated shape with intermediate to low values in the overall clayey silt above 602 mbsf to the top of the unit. Some intermediate sandy units (500–450 and 360–340 mbsf) are weakly expressed by irregular trends in the TGR curve. Below 602 mbsf, Unit II is rich in K. The K curve correlates with the magnetic susceptibility and sonic signals, and the low Th/K ratio attests to the presence of glauconite (except around 622 mbsf). The conductivity curve correlates with the porosity trend and mirrors density and sonic variations.

Above 602 mbsf, conductivity curve trends better correlate to the chlorinity curve, which is anticorrelated to density compared to the rest of the hole below. Sediments are almost glauconite free, as evidenced by high Th/K ratios, except between 500–495 and 480–469 mbsf in sand intervals with high density and sonic and low conductivity.

Above 469 mbsf, the TGR curve trend is much more regular compared to the formation below. The density curve decreases from 481 to 407 mbsf, reaching a minimum and increasing again toward 343 mbsf, where a peak is observed. This peak marks a clear petrophysical and geophysical boundary, as it correlates with a peak in conductivity and in P-wave velocity, a porosity low, and a clear low on the TGR curve and spectral elements. This interval fits with a cemented horizon observed in cores. A subhorizontal quartz vein was observed in Core 313-M0029A-71R (345.60 mbsf) in a cemented horizon, possibly related to overpressure. A sharp decrease in chlorinity at 346 mbsf suggests the 342–346 mbsf interval may act as a diffusion barrier to upgoing pore water (Fig. **F36**).

A number of petrophysical boundaries were recognized in Unit II. Most of the surfaces that correlate to sequence seismic boundaries show high densities and velocities. This explains the high impedance contrast at the origin of these high-amplitude seismic reflectors. Surface m5.2 does not fit this scheme and should possibly be placed a little bit lower in the section (612 mbsf) at a sharp impedance contrast.

The boundary with Unit I is characterized by a small TGR low and an increase in density. A porosity low is observed just above the transition.

Lithostratigraphic Unit I

The TGR curve of Unit I shows, from base to top, two bow-shaped serrated trends in intermediate values, a thick boxcar-shaped trend in low values, and a set of irregular to bell-shaped trends in intermediate values ending up in another boxcar-shaped trend in low values. These trends with overall low values correspond to sandy material to sand and clay alternations deposited in a range of settings from shelf (gradational bell shape) to shoreface, foreshore (boxcar shape), and coastal plain (irregular to bell shape).

Chlorinity curve shape is much more irregular in Unit I compared to the diffusive-advective profile it displays in the sedimentary units below (see **"Geochemistry"**). Comparisons between the TGR and chlorinity curves suggest that the higher chlorinities have been measured in low-TGR intervals, whereas the lowest chlorinities are encountered in higher TGR intervals (Fig. **F36**). This suggests that, as for Holes M0027A and M0028A, saltier water is stored in coarse-grained levels, whereas fresher water is observed in finer grained intervals.

Several petrophysical boundaries were picked in Unit I, but poor core recovery prevented any good correlation with seismic and sedimentary surfaces.

Stratigraphic surfaces and correlation with petrophysical intervals

Table T11 lists key petrophysical surfaces and intervals recognized in Hole M0029A. Many of these petrophysical horizons relate to stratigraphic surfaces (see penultimate column in Table T11), although small differences in depth are attributed to differences in picks of the surfaces (i.e., at the start of an increase in a parameter value or at the peak of the change). Petrophysical surfaces and intervals are defined using the full suite of logs and petrophysical parameters, chosen where more than one property displays a significant change. Surface m4 is located just below a TGR peak, although it is not identified as a petrophysical surface. Surface m4.3 is the only surface that does not match logging and petrophysical data. All parameters in this interval show minimal variation. Surface m5.2 may be better located lower (see "Unit III"). Surface m5.3 is an example of a surface that is particularly clear, with a kick in most petrophysical parameters. Some petrophysical surfaces/intervals do not clearly correlate with stratigraphic surfaces or lithostratigraphic units/subunits between 490 and 580 mbsf within Subunit IIC. This unit is characterized by a high degree of variability. Some surfaces are related to cemented horizons (see notes in last column of Table T11), whereas others illustrate minor sedimentological changes within lithostratigraphic units.

Stratigraphic correlation

Seismic sequence identifications

Seismic sequence identification through the *Oceanus* 270 (Oc270) and *Cape Hatteras* 0698 (CH0698) seismic grids guided Hole M0029A site selection and the spot cores taken in the upper 250 mbsf of the hole. The drill site location lies at the crossing of dip CH0698 profile 307 common depth point (CDP) 10997 and strike CH0698 profile 310 CDP 4613 (Fig. F7 in the "Expedition 313 summary" chapter; Fig. F48). CH0698 profile 307 samples the same trend as the regional Oc270 profile 529, which is close to Hole M0029A, with CDP 3640 on Oc270 profile 529 also locating the site (Fig. F48). Time-depth correlations were based on semblance velocity data from Oc270 (see "Stratigraphic correlation" in the "Methods" chapter).

Hole M0029A is the farthest offshore of the three Expedition 313 holes and samples the thickest section of middle Miocene sediments. Seismic reflectors traced (with difficulty) from Holes M0027A and M0028A guided the selection of spot cores within the uppermost 100 mbsf of Hole M0029A. Pleisto-cene surfaces, including marine isotope Chron (MIC) 6/5e, MIC 4/3c, MIC 3b/3a, and MIC 2/1 (Carey et al., 2005), were penetrated during drilling, but their correlation to Expedition 313 cores will have to be done in subsequent analyses. Middle Miocene seismic sequence surfaces m1, m3, and m4 remain difficult to trace to this location because of both the hummocky to chaotic seismic facies that must be traversed and the distance between their corresponding clinoform structures and Hole M0029A.

Below surface m4, five new seismic surfaces have been identified (Figs. F47, F48; see Table T10 in the "Methods" chapter), though not all are interpreted as seismic sequence boundaries. The highest and youngest of the five reflectors, m4.1, is a high-amplitude continuous surface reflector marking the base of a seismic facies defined by low- to moderate-amplitude discontinuous subparallel reflectors. The nature of reflector m4.1 is not clearly defined within the Oc270 or CH0698 grids, though there are indications of a possible seismic sequence defining reflector terminations. The next seismic surface predicted, m4.2, is clearly tied to a clinoform structure on CH0698 profile 21 and is thought to be a seismic sequence, though a similar seismic geometry is not suggested on Oc270 profile 529. Two lower surfaces selected because of their moderate- to high-amplitude nature are m4.3 and m4.4. Neither surface can be defined as a seismic sequence boundary, but they do suggest the possibility of being flooding surfaces because of limited downlap reflector terminations. Seismic facies between these three surfaces, m4.2, m4.3, and m4.4, are similar with low to moderate amplitude and a parallel to subparallel pattern. The lowest new reflector, m4.5, is a moderate- to high-amplitude continuous reflector with onlapping reflectors. This limited information indicates the possibility that m4.5 may be a seismic sequence boundary.

Below m4.5 is a 30 ms interval of low- to moderate-amplitude parallel reflectors before reaching moderate- to strong-amplitude seismic sequence surface m5 (Fig. F47). Sequence m5.2 can be divided into two different seismic facies at 655 ms. Moderate-amplitude, discontinuous parallel reflectors that display downlapping terminations define the upper seismic facies. The lower facies is also marked by downlapping terminations, but all reflectors are noticeably weaker. High-amplitude continuous seismic sequence boundary m5.2 marks the base of this clinoform toe.

The next four seismic sequence surfaces, m5.3, m5.4, m5.45, and m5.47, are moderate-amplitude, continuous reflectors that average 15 ms separation between them (Fig. F47, F48). In Hole M0029A, there

are indications of limited small-scale strata-bound faulting at this depth in both Oc270 and CH0698 data (Fig. F47). Displacement shows normal offset and probably relates to dewatering structures and compaction within fine-grained sediment (Dewhurst et al., 1999; Gay et al., 2004). Indications of these compaction structures continue down through the last three seismic sequence surfaces sampled at Hole M0029A, m5.6, m5.7, and m5.8. These deep surfaces are difficult to trace as they lose amplitude and descend into depths of decreased seismic resolution.

Core-seismic sequence boundary integration

The Pleistocene to upper middle Miocene section was spot-cored in Hole M0029A, and the hole bottomed in the lower Miocene. A clay/sand contact between Sections 313-M0029A-7R-2 and 8R-1 (14.63–16.05 mbsf) may mark the base of the youngest Pleistocene sequence (Fig. F49) indicated on Geopulse seismic profiles and correlated to marine isotope Chron 3 (Sheridan et al., 2000; Carey et al., 2005). A surface was encountered at Section 313-M0029A-15R-1, 8 cm (49.68 mbsf), where medium-coarse poorly sorted sands overlie clay; this may be the base of the Pleistocene (Fig. F50). This depth agrees closely with the base of the Pleistocene using Geopulse reflectors from Carey et al. (2005) and applying the time-depth conversion used in this volume.

Seismic sequence boundary m1 (predicted depth of 152–153 mbsf) may have been recovered in interval 313-M0029A-28R-3, 49–98 cm (~155.5–156 mbsf), where there is a weathered clayey silt associated with the approximate level of the reflector (Fig. F51). This clay appears to be associated with the high downhole gamma values at 156.24 mbsf.

Seismic sequence boundary m3 (predicted depth of 190–195 mbsf) could be placed at the base of Section 313-M0029A-34R-1 (193.17 mbsf). The section consists of wood over weathered silty clay with roots interpreted as a paleosol; these overlie very fine sands in Section 34R-2 (193.17 mbsf) (Fig. F52). There is a large gamma log kick (Fig. F51) in both the downhole TGR and core NGR logs and a large MSCL density increase at 192.74 mbsf (Section 313-M0029A-34R-1, 107 cm), though the significance of the latter cannot be confirmed because of spot coring.

Seismic sequence boundary m4 (predicted depth of 225–235 mbsf) may have been captured in Section 313-M0029A-40R-1, 39 cm (231.7 mbsf), where a woody clay (possible paleosol) overlies silty fine sand. This is a level of major downhole increase in both the downhole TGR and core NGR logs (Fig. F51).

Hole M0029A penetrated a 240 m thick section between seismic sequences m4 and m5 (Fig. F53). Five reflections were traced through this package (R1–R5 counting downsection; see "Seismic sequence identifications"), with two likely sequence boundaries (m4.2 and m4.4) and three other surfaces (m4.1, m4.3, and m4.5). Reflector m4.1 (predicted depth of 325–330 mbsf) appears to correlate with a contact of silty glauconite fine sand over a 10 cm thick contact zone with silty clay in interval 313-M0029A-65R-2, 80–90 cm (325.13–325.23 mbsf). Core observations (see "Lithostratigraphy") identify this as a candidate sequence boundary.

A contact that was sampled as sequence boundary but is likely a burrowed flooding surface occurs at the top of Section 313-M0029A-71R-1 (341.11 mbsf). This surface has sand-filled burrows into clay and is immediately above the predicted depth of reflector m4.2 (345–350 mbsf).

Seismic reflector m4.2 appears to be a sequence boundary in Sections 313-M0029A-72R-1, 64 cm, to 72R-1, 87 cm (343.24–343.89 mbsf). It consists of an indurated contact of clays over claystones over muddy fine sand. This likely correlation of reflector m4.2 (predicted depth = 345–350 mbsf) is associated with a very large density contrast and downhole gamma log minimum (Fig. F53). Core observations (see "Lithostratigraphy") identify this as a candidate sequence boundary.

The predicted level of reflector m4.3 (350–360 mbsf) is associated with a burrowed surface of sands over silty clay in Section 313-M0029A-74R-1, ~14 cm (350.4 mbsf). MSCL density shows a large contrast in Section 313-M0029A-75R-1 (Fig. F53), where there is a sharp contact of silty clay over fine sand at 35 cm (353.66 mbsf). The significance of this surface remains uncertain but appears to be a facies change from sands above to clays below.

The predicted level of reflector m4.4 (390–400 mbsf) appears to be a clayey zone with nodules in Section 313-M0029A-89R-1 (393–394 mbsf) in an otherwise monotonous succession. However, MSCL density data (Fig. F53) show a sharp contrast in Sections 313-M0029A-89R-2, 66 cm, 89R-2, 74 cm, 90R-1, 49 cm, and 90R-1, 106 cm. This appears to be a flooding surface because it comprises some of the finest sediments of the sequence and is sandwiched between samples with the greatest paleodepth (>100 mbsf in Sample 313-M0029A-82R-CC and 75–80 mbsf in Sample 92R-CC).

The sequence boundary noted in interval 313-M0029A-108R-1, 124–128 cm (449.1–449.14 mbsf) is a dramatic, burrowed, and irregular surface separating glauconitic silty sand above from siliceous silt below (Fig. F54). This sequence boundary noted in

the core occurs at the depth predicted for reflector m4.5 at 445–455 mbsf. It is a general maximum in MSCL density (Fig. F55). Core observations (see "Lithostratigraphy") identify a candidate sequence boundary at 449.1 mbsf.

There is a major contact in Section 313-M0029A-118R-1, 25 cm (478.61 cm), to the top of Core 313-M0029A-20R (481.41 mbsf) (Fig. F56), which occurs at the level predicted for seismic sequence m5 (Fig. F55). A sandy silt to silty sand is intensely burrowed with clay in interval 313-M0029A-118R-1, 25–61 cm. There is an indurated zone and concretions in Sections 313-M0029A-18R-1, 61 cm (478.97), to 19R-1, 25 cm (479.75 mbsf). There is a coring gap to the top of Section 313-M0029A-20R-1, where two indurated fragments (cavings) occur above medium sand. Section 313-M0029A-19R-CC (479.82 mbsf) has sands and a deeper water (>100 m) benthic foraminifer assemblage similar to those in Core 20R and below. The main density contrasts are associated with the top of indurated zones in Sections 313-M0029A-18R-1, 61 cm (478.93 mbsf), 18R-1, 90 cm (479.25 mbsf), and 19R-1, 23 cm (479.73 mbsf), which contribute to the impedance contrast that causes reflection m5 in this corehole (predicted depth = 475–482 mbsf, with best estimate of 479 mbsf). A downhole log velocity peak occurs at 480.2 mbsf, which suggests that the reflector should be placed in the gap. Precise placement of the sequence boundary may be revealed by thin sections. Of note is the fact that this sequence boundary is seismically and paleontologically a "correlative conformity" with outer neritic shelf facies (>100 m) below and middle neritic shelf facies above. Core observations (see "Lithostratigraphy") identify a candidate sequence boundary at 478.61 mbsf.

Seismic sequence boundary m5.2 (predicted depth of 590–600 mbsf) was encountered in Section 313-M0029A-161R-2, 37 cm (602.25 mbsf) (Fig. F57), at a change from sandy silt to glauconitic sand below (Fig. F58); glauconites contain a series of six graded beds within the section. This level is a downhole change to glauconite and large increases in MCSL density and downhole TGR and spectral K logs (Fig. F57). However, core observations (see "Lithostratigraphy") place a transgressive surface at 602.25 mbsf and a candidate sequence boundary at ~621 mbsf. Further studies are needed to resolve this difference.

Seismic sequence boundary m5.3 (predicted depth of 638–642 mbsf) is best placed at Section 313-M0029A-176R-1, 13 cm (643.19 mbsf) (Fig. F57), at a change from glauconite sands to silt (Fig. F59). This is a level with a sharp MSCL density peak and is the preferred placement of the seismic sequence boundary. However, there are two other candidate placements of the

sequence boundary in the cores. First, a contact in interval 313-M0029A-175R-1, 50–120 cm (640.51–641.2 mbsf), fits a model for these toe-of-slope deposits with basal glauconite sands and upper clays/silts. This level is associated with decreasing density values, but caution must be taken in interpreting these because of possible core disturbance. Core observations place a candidate sequence boundary at 640.51 mbsf (see "Lithostratigraphy"). Second, Section 313-M0029A-171R-2, 57 cm (634.43 mbsf), at a downhole change from glauconitic quartz sand to glauconite sand, is the top of a major downhole increase in gamma log values (driven by K values, indicative of glauconite in this case) and is likely a facies change. A secondary spectral K peak occurs at the level of the preferred sequence boundary at 643.19 mbsf.

Placement of seismic sequence boundary m5.4 (predicted depth of 658–670 mbsf) is problematic (Fig. F57). The best placement from a core-seismic perspective is in Section 313-M0029A-183R-1, 112 cm (662.48 mbsf), at a contact between clays above and glauconite-quartz sands below (Fig. F60). This is associated with a large downhole increase in both MSCL density values and sonic velocities, suggesting that this is the best placement of the seismic sequence boundary. However, there are nine core contacts encompassing the four seismic sequence boundaries, m5.3 through m5.47, in Hole M0029A, and these thin (11–19 m) sequences cannot be correlated to seismic sequences boundaries for certain considering the seismic resolution of 5 m. The successions in this toe-of-slope setting of sequence m5.3–m5.4 appear to display a pattern of basal transported glauconite sands grading up to silts/clays. Given this, it is possible to place the core sequence boundary in Section 313-M0029A-179R-1, 23 cm (648.68 mbsf), at a change from glauconite above to clay below at a modest density peak; this is where core observations place a candidate sequence boundary and interpret 662.37 mbsf as a transgressive surface (see "Lithostratigraphy").

Seismic sequence boundary m5.45 (predicted depth of 670–690 mbsf) is best placed in Section 313-M0029A-193R-2, 73 cm (673.71 mbsf), at the base of a glauconite bed on clay (Fig. F61). This is at a major downhole decrease in MSCL density values. This level is interpreted as a candidate sequence boundary based on core observations (see "Lithostratigraphy").

Seismic sequence boundary m5.47 (predicted depth of 685–690 mbsf) is in Section 313-M0029A-193R-2, 60 cm (688.0 mbsf), with glauconite sand on silt. This is the base of a density peak (Fig. F57). Two other contacts occur immediately above this: (1) Sec-

tion 313-M0029A-192R-2, 11 cm (685.34 mbsf), has clay on glauconite and a density increase; and (2) Section 192R-1, 46 cm (683.16 mbsf), is the top of the glauconite and the downhole start of a density high that peaks just above 687.88 mbsf (Fig. F62). Core observations do not recognize a candidate sequence boundary near the level predicted for m5.47 but place a maximum flooding surface (MFS) near this level. Further studies are needed to resolve this difference.

Seismic sequence boundary m5.6 (predicted depth of 700–716 mbsf) occurs in a coring gap between the base of Section 313-M0029A-200R-1 (707.56 mbsf) in glauconite sand and the top of Core 201R (710.16 mbsf) in clay/claystone. The clays below are lower density than the sands above (Fig. F63). There is a major upsection TGR increase across the coring gap that is due to higher U values shown in the spectral gamma ray. Core observations place a candidate sequence boundary near this level.

Seismic sequence boundary m5.7 (predicted depth of 735–743 mbsf) occurs as a dramatic erosional surface in interval 313-M0029A-208R-1, 9–11 cm (728.56 mbsf) (Fig. F63). The surface marks a contact between glauconite sand above and tan clay below (Fig. F64). Burrowing across the contact is extensive, with burrows down to >30 cm below. There is a marked downsection decrease in MSCL density and magnetic susceptibility values associated with the contact. A TGR peak occurs above the contact (~726.3 mbsf). NGR core data show this same peak at 726.69–727.0 mbsf, suggesting a core shift of Cores 313-M0029A-207R and 208R up by ~40 cm (based on lining up the troughs because the peak is not fully sampled). The downhole spectral gamma log shows a distinct peak at 727.33 mbsf, immediately above the sequence boundary. The underlying sequence m5.8 consists of tan clays as in Hole M0028A. Core observations place a candidate sequence boundary at 728.56 mbsf (see "Lithostratigraphy").

It is not clear that Hole M0029A penetrated seismic sequence boundary m5.8 (predicted depth of 750–755 mbsf or below the corehole total depth) (Fig. F63). There are several possible placements, considering two major coring gaps. The first coring gap goes from Section 313-M0029A-213R-1, 28 cm (743.97 mbsf), to the top of Section 215R-1 (746.96 mbsf). The placement of the 53 cm of Section 313-M0029A-214R-1 is uncertain but appears to be at the top of the gap. Clays from Section 313-M0029A-212R-2, 120 cm, through Section 213R-1 are darker and have higher velocities measured on the core, suggesting that this may be the source of the impedance contrast. Large downhole TGR and K gamma peaks occur in the gap that separates glauconitic clay

above from clay below. This suggests possibly placing reflector m5.8 at the base of the TGR peak (~746 mbsf). No MSCL density contrast is apparent on either side of the coring gap.

Another coring gap separates Core 313-M0029A-215R from Core 217R (750–752.86 msbf). It is possible that the sequence boundary is in the coring gap. The third possibility is that a sequence boundary occurs associated with an increase in downhole TGR values at 753.8 mbsf, though NGR values place it in the core at 753.22 mbsf (Section 313-M0029A-217R-1, 36 cm; note 44 m uphole shift in core). Section 313-M0029A-217R-1, ~36 cm, and below contains thin wisps of glauconite sand. Again, there is no major density contrast associated with the cores recovered in either at 753.22 mbsf or across the coring gap.

An acoustic impedance log was computed for Hole M0029A following the Onshore Science Party to aid in core-seismic integration. The impedance log was constructed in two ways using MSCL bulk densities; velocities were taken both from MSCL velocity logs and downhole sonic logs. The resultant acoustic impedance logs are complementary because no sonic logs were available for the upper part of the hole and MSCL sonic quality was poor and the data were spotty for the middle part; only the lower part of the hole had overlapping sonic and MSCL acoustic impedance records. Impedance records shown on the synthesis figures (Figs. F49, F51, F53, F55, F57, F63) allow evaluation of seismic-core correlation made by other means: (1) we first predicted depth based on the velocity-depth function (Table T13), and (2) we then slightly adjusted our predicted depths based on core surfaces, downhole log, and MSCL changes. Adding the acoustic impedance logs as we did after the fact provides a reasonably independent means of testing our core-seismic integration.

The impedance log in the top 330 m (Figs. F49, F51, F53) and core-log-seismic integration is hampered by spot coring. Below this, acoustic logs are very helpful. Reflector m4.2 is associated with a large impedance contrast at 343 mbsf and seismic evidence for a clinoform rollover (see "Seismic sequence identifications"); core observations suggest that it is a candidate sequence boundary. Reflector m4.3 was placed slightly (~2 m) above a decrease in acoustic impedance. This reflector has been interpreted as flooding surface because of downlap (see "Seismic sequence identifications") and an NGR peak (see "Core-seismic-log synthesis") but was not identified as such by core observations (see "Lithostratigraphy"). Similarly, reflector m4.4 occurs directly on a downhole decrease in impedance and is associated with seismic downlap and interpreted as a flooding

surface but was not identified as such by core observations. Further study of both surfaces is needed.

Both reflectors m4.5 and m5 have major acoustic impedance peaks precisely at the levels predicted (449.1 and 478.61 mbsf, respectively) and have been interpreted as candidate sequence boundaries based on core observations (see "Lithostratigraphy") and seismic criteria. Similarly, reflectors m5.2 (602.25 mbsf), m5.3 (641.2 mbsf), m5.4 (662.37 mbsf), and m5.45 (673.71 mbsf) are associated with large acoustic impedance contrasts within <1 m of where they are predicted, though core observations interpret the surfaces associated with m5.2 and m5.4 as transgressive surfaces. Interestingly, the impedance log does not identify a clear placement of reflector m5.47 because both possible locations (683.66 and 687.87 mbsf) are associated with impedance contrasts. The upper level is a downhole increase in acoustic impedance (as are most sequence boundaries at Site M0029), whereas the lower level is a downhole decrease in impedance. We favor placing the sequence boundary at the lower surface (687.87 mbsf) where deeper water glauconite sands lie on offshore silts. Core observations do not identify either as a candidate sequence boundary but place a transgressive surface in between at ~685 mbsf (see "Lithostratigraphy"). Further study of the interval from 683 to 690 mbsf is needed.

The placement of reflector m6 (707.86–710.16 mbsf) is associated with the largest decrease in acoustic impedance noted at this site, though the impedance record cannot place the precise location of the source of the reflector within 3 m. The acoustic impedance record associated with reflector m5.8 suffers from poor recovery and the lack of a sonic record, but there is a strong hint of a contrast at ~753 mbsf.

Core-seismic-log synthesis

Figures F49, F51, F53, F55, F57, and F63 summarize the ties between sequence boundaries, sediment facies, and chronostratigraphy developed in Hole M0029A. (These figures are combined in Fig. F65.) The figures illustrate the same information as those for Holes M0027A and M0028A and are discussed below, emphasizing the relations among core sequences, logs, and seismic facies within the lithostratigraphic framework.

Lithostratigraphic Unit I (3.85–325.12 mbsf)

The upper ~50 mbsf of Hole M0029A is Pleistocene, according to the biostratigraphic information at this site and estimates based on previous study of the New Jersey shelf (Carey et al., 2005). It belongs to the upper part of lithostratigraphic Subunit IA (see "Lithostratigraphy"), but it is sedimentologically poorly constrained because of the discontinuous and low recovery.

A gamma ray peak at ~10 mbsf correlates with a fine-grained interval in Cores 313-M0029A-6R and 7R. Otherwise, both above this depth and below, the log character is consistent with a moderately uniform deposit of coarse-grained sediment. Pleistocene deposits (from fluvial to shoreface environment) (Fig. F49) overlie a discontinuity tentatively placed at 46.68 mbsf (Section 313-M0029A-15R-1, 8 cm) and correspond to a significant time hiatus (Pleistocene–Pliocene).

Only spot cores were obtained from the base of the Pleistocene to the top of Subunit IE at 261.81 mbsf. Several peaks in TGR values (>150 cps) are observed at 50–53, 58, 68–69, 126, and 135–138 mbsf. Cores at 50–53 and 68–69 mbsf were nonmarine silty clays thought to be paleosols. This suggests that several other sharp gamma spikes of similar character but lacking cores could be paleosols as well. In general, sediments of Unit I were deposited in a range of shelf settings (shoreface to foreshore, coastal plain, and estuarine).

The boundaries between lithostratigraphic Subunits IB, IC, and ID cannot be clearly established (see "Lithostratigraphy"), and the succession was only spot cored (Fig. F51). Nonetheless, Subunit IB was assigned to a fluvial–deltaic–shoreface environment (high content of organic matter and wood debris, or seen also in the high concentration of U and Th), and Subunit IC (lower delta plain sediments) contains paleosols at 193.17 mbsf that correspond to reflector m3. There is no time constraint for this unconformity in Hole M0029A. Similarly, reflector m4 is poorly constrained in age (Serravalian–Tortonian according to dinocyst biostratigraphy). By contrast, the predicted depth to reflectors m1, m3, and m4 occur near or close to (within 5 m) the tops of fine-grained intervals within the overall sand-prone Unit I indicated by gamma log values (Fig. F51).

This thick interval (Subunits IB, IC, and ID) is seismically characterized by a homogeneous facies with discontinuous reflectors. The oscillations of gamma ray values within Subunit IE correlate with lithology, but the enrichment in U concentration between 293 and 304 mbsf can be attributed to an increase in organic matter (see "Downhole measurements").

Lithostratigraphic Unit II (325.12–641.21 mbsf)

Lithostratigraphic Unit II is almost fully recovered, as illustrated in Figure F53. The contact between lithostratigraphic Units I and II is placed at 325.13 mbsf within the predicted depth interval for seismic

reflector m4.1 (325–330 mbsf). The associated lithological boundary occurs in interval 313-M0029A-65R-2, 80–90 cm (see "Core-seismic sequence boundary integration"). This surface is a candidate sequence boundary based on core observations (see "Lithostratigraphy").

The seismic prediction for reflector m4.2 is between 341 and 350 mbsf. The sequence boundary associated with this reflector is described at 343.24–343.89 mbsf (Sections 313-M0029A-71R-R, 64 cm, to 72R-1, 57 cm) and corresponds to a major kick in bulk density and a minimum in gamma ray values. This sequence boundary is placed within the predicted depth interval based on velocity function, and it marks the transition between lithostratigraphic Subunits IIA$_1$ and IIA$_2$ (offshore clay and silt). The associated MFS is placed at 341.11 mbsf (top of Section 313-M0029A-71R-1), corresponding to a burrowed surface (see "Core-seismic sequence boundary integration") immediately above the predicted depth for reflector m4.2 (Fig. F53). Middle Miocene age has been assigned to this surface based on nannoplankton (NN6–NN7) and dinocyst (DN6–DN8) biostratigraphy. It marks the passage from a seismic facies characterized by discontinuous reflectors (Subunits IE and IIA$_1$) to a facies characterized by semitransparent reflectors downhole (Fig. F53). It is possibly related to gradual lithological change between lithostratigraphic Units I and II.

The predicted depth of reflector m4.3 is between 350 and 360 mbsf. This interval contains a surface described at 350.4 mbsf (Section 313-M0029A-74R-1, 14 cm) and is interpreted as a facies change at the top of a flooding interval. Paleodepth indications are consistent with the interpretation (see "Paleontology"), and it is positioned at the top of the gamma ray kick, within Subunit IIA$_2$.

The contact between lithostratigraphic Subunits IIA$_2$ and IIA$_3$ falls into the interval bounded by m4.3 and m4.4, an interval with remarkably uniform gamma log character despite changes in lithology (Fig. F53). There are clear changes in density that may be responsible for the weak and discontinuous reflectors that onlap a clinoform front and correspond to generally silty clay with occasional graded intervals in an offshore setting. The predicted depth for seismic reflector m4.4 is between 390 and 400 mbsf (Fig. F53), and it matches well with an associated surface described in Section 313-M0029A-89R-1 (393–394 mbsf). This surface is associated with a flooding surface (likely the MFS, given benthic foraminifer paleodepth estimates), and it falls in an interval containing carbonate nodules (see "Core-seismic sequence boundary integration").

Seismic reflectors m4.5 and m5 bracket lithostratigraphic Subunit IIB$_1$ (Fig. F55) and are positioned at 445–455 and 475–482 mbsf, respectively, according to the prediction based on the velocity function used during Expedition 313. Both predictions are in accordance with the sedimentological facies (see "Lithostratigraphy"). The sequence boundary m4.5 transition between lithostratigraphic Subunits IIA$_3$ (offshore clay/silt) and IIB$_1$ (clinoform slope apron) is described at 449.1 mbsf (Section 313-M0029A-108R-1, 124 cm) as a surface separating glauconitic silt from siliceous silt (see "Lithostratigraphy"). No particular expression in the well log data is observed, whereas a peak in bulk sediment density is found at this level.

Sequence boundary m5 is placed at 478.61 mbsf (Section 313-M0029A-118R-1, 25 cm), corresponding to an indurated silt bed (Fig. F55). A change of seismic facies occurs at this surface. Reflectors above m5 commonly onlap the m5 clinoform; those below m5 downlap deeper surfaces, building seaward as toe-of-clinoform deposits. The seismic reflection is most likely caused by a high impedance contrast related to high density values in the cemented zone.

The predicted depth range for seismic reflector m5.2 is between 590 and 600 mbsf, slightly shallower than a surface described in the core (Section 313-M0029A-161R-2, 37 cm; 602.25 mbsf) and interpreted as an MFS (see "Lithostratigraphy") and a major density contrast. Further studies are needed to resolve the interpretation of sequence boundaries versus MFSs. This reflector is at the contact between lithostratigraphic Subunits IIC and IID (offshore silt overlying partially cemented glauconite sand, toe-of-slope apron of Subunits IID$_1$ and IID$_2$).

Lithostratigraphic Unit III (640.51–650.13 mbsf)

The predicted depth interval for sequence boundary m5.3 is at 638–642 mbsf. Three possible surfaces (640.5, 643.4, and 649.7 mbsf) in the core could be associated with this seismic reflector (see "Core-seismic sequence boundary integration"). The best tie is at 643.19 mbsf, relying on the sediment physical properties (significant density peak and an increase in the gamma ray values, associated with K that reveal the presence of glauconite). Several boundaries in physical properties were recognized between 634 and 643 mbsf that will help to better define the placement of reflector m5.3, which is poorly constrained in age. Seismic reflectors m5.3 and m5.4 delineate lithostratigraphic Unit III, which was poorly recovered and interpreted as deposited in a deep offshore environment, as indicated by paleodepth indication (75–100 m) given by benthic foraminifers (see "Paleontology").

Lithostratigraphic Unit IV (650.13–663.88 mbsf)

The best placement for sequence boundary m5.4 is at 662.37 mbsf (Section 313-M0029A-183R-1, 102 cm) (Fig. F57). This position matches the predicted depth range (658–670 mbsf). Nonetheless, other surfaces are observed in the cores and large variations in density are present and could be associated with the seismic reflector (see "Core-seismic sequence boundary integration"). Refinement of core-seismic-log correlation will possibly clarify the position of reflector m5.4 in the sedimentary record. Nonetheless, the two surfaces described in cores (649.68 and 622.37 mbsf) bound the lithostratigraphic Unit IV, characterized by fine-grained, indurated sediments of offshore environments (75–100 mbsf, as shown by benthic foraminifers).

Lithostratigraphic Unit V (663.88–728.55 mbsf)

Sequence boundary m5.45 is predicted at 670–680 mbsf (Fig. F57). The associated sedimentary surface (contact between Subunits VA [offshore setting] and VB [debrite apron]) is placed within this interval (Section 313-M0029A-193R-2, 73 cm; 673.71 mbsf) at the base of the increasing bulk sediment density based on MSCL measurements.

Sequence boundary m5.47 falls within lithostratigraphic Subunit VB in the depth range predicted from the velocity function (685–690 mbsf). The surface that correlates with this seismic reflector is tentatively positioned in Section 313-M0029A-193R-2, 60 cm, at ~688 mbsf, corresponding to a density peak (Fig. F57). Several peaks in density and in gamma ray values are observed below the position of m5.47, mainly occurring at glauconite-rich horizons. Seismic facies belonging to lithostratigraphic Units II, III, IV, and V are characterized by strong parallel reflectors (Fig. F57).

Sequence boundary m5.6, predicted between 700 and 716 mbsf, is placed in a core gap between 707.56 and 710.16 mbsf (Fig. F63). This correlates with a significant peak in gamma ray values (>250 cps) due to high K concentration. It indicates the presence of glauconite-rich sand found at the top of Core 313-M0029A-201R (710.16 mbsf; lithostratigraphic Subunit VC, composed of silty glauconitic sand deposited as a series of debrites). Surface m5.6 as detected in the core encompasses the depth interval calculated on function velocity. Surface m5.6 has reasonably good age constraints because it falls within the interval where nannofossil Zone NN3 was identified for the first time.

Lithostratigraphic Unit VI (728.55–747.27 mbsf)

The surface corresponding to sequence boundary m5.7 is positioned at 728.56 mbsf, considerably higher (~7–15 m) than the predicted depths (735–743 mbsf) (Fig. F63). However, the sedimentological expression of this discontinuity appears spectacular on the sedimentary record (burrowed contact between glauconite sand and clay; see "Core-seismic sequence boundary integration"). This surface marks the transition between lithostratigraphic Units V and VI (see "Lithostratigraphy"). Sediments below this surface consist of banded clays and claystones, reflecting a river-influenced offshore delta environment (see "Lithostratigraphy") barren of microfossil content. Banded clays lie in sequence m5.8 as they do in Hole M0028A.

Lithostratigraphic Unit VII (747.27–756.33 mbsf)

The contact between lithostratigraphic Units VI and VII is possibly marked by seismic reflector m5.8. The predicted depth for sequence boundary m5.8 is placed between 750 and 755 mbsf, near the bottom of Hole M0029A (Fig. F63). Several sedimentary surfaces observed in the cores can be associated with this reflection. The upper one is higher than the predicted depth at 746 mbsf (between Sections 313-M0029A-213R-1 and 215R-1) at the peak of gamma ray values corresponding to glauconitic clays. The interval between 750 and 752.86 mbsf across the coring gap, or at 753.22 mbsf at the top of a horizon showing a significant decrease in gamma ray values (possibly the base of a coarse-grained interval), might encompass sequence boundary m5.8. These two horizons match well the predicted depths; nonetheless, only the refinement of biostratigraphic, core, and seismic correlations can clarify the position and the age of this surface.

In summary, lithostratigraphic Unit I from 0 to 280 mbsf is poorly recovered, resulting in difficult correlation between seismic reflections and sedimentary surfaces.

Prominent peaks in NGR/TGR values and concentrations of K, U, and Th allowed placing the base of the Pleistocene and reflectors m1, m3, and m4, whereas density contrast was used to define reflectors m4.1, m4.3, and m4.4 within lithostratigraphic Unit II. These reflectors are interpreted as MFSs (burrowed surfaces, indurated, or with nodules). The correlation between seismic reflectors and core observation for the interval between reflectors m4.1 and m4.4 is problematic (Fig. F53); further revision in interpretation will be needed.

Reflectors m4.5 and m5 (lithostratigraphic Unit II) coincide perfectly with surfaces observed in the core, and they are well defined by density contrasts.

Correlation of seismic reflectors m5.3, m5.4, and m5.8 is still under discussion; additional bio- and

chronostratigraphic data are necessary to clarify the position of these surfaces.

Chronology

The Pleistocene to upper middle Miocene section was spot-cored in Hole M0029A, and the hole bottomed in the lower Miocene. Chronology for the lower middle to lower Miocene in Hole M0029A was obtained by integrating the following on an age-depth diagram (Fig. F18):

1. Biostratigraphy provided by calcareous nannofossil, planktonic foraminifer, and dinocyst data. Zonal durations are plotted using tables provided in "Paleontology," along with select datum levels (first and last occurrences).

2. Sr isotopic ages and associated age errors.

3. Placement of sequence boundaries and other stratal surfaces (Table T13).

4. The timescale of Berggren et al. (1995; BKSA95).

Surfaces were picked as seismic sequence boundaries in two-way traveltime (Table T13) and converted to depth and predicted core (Table T13) using a velocity function (see "Stratigraphic correlation" in the "Methods" chapter for discussion of criteria used to define seismic sequence boundaries and the derivation of the time to depth conversion of seismic data). In figures, features are presented as follows:

• If unsampled by cores, the reflector is indicated with a gray shaded zone.

• If identified in a core, the surface identified by the science party was plotted as a solid red line for sequence boundaries and a dashed line where uncertain or where there was more than one possible core surface for a given seismic sequence boundary (see "Stratigraphic correlation").

• A few prominent (but not all) features interpreted as MFSs identified in the cores (see "Stratigraphic correlation") are indicated with a green line.

• A visual best fit sedimentation rate line (uncorrected for postdepositional compaction) was estimated for each sequence and an age error assigned to each.

Pleistocene sequences in Hole M0029A were identified on Geopulse seismic profiles and interpreted as representing MIC 3 (Sheridan et al., 2000; Carey et al., 2005). Calcareous nannofossils suggest that the uppermost Pleistocene sequence (above 14.63 mbsf) is upper Pleistocene (Zone NN21; < 250 ka). There are no other age constraints on ?Pleistocene sequences above ~156 mbsf.

There are no age constraints on seismic sequence boundaries m1 (156.24 mbsf), m3 (193.17 mbsf),

and m4 (231 mbsf) in Hole M0029A except regional correlations (11.5, 12.8, and 13.6 Ma, respectively) (Miller et al., 1998). A tentative seismic sequence termed m4.2 (231–341.11 mbsf) is poorly dated. It is assigned to calcareous nannoplankton Zones NN6–NN7, with definite Zone NN6 (12.6–13.6 Ma) at its base. It is assigned to dinocyst Zones DN6–DN8 (younger than ~13.2 Ma) and planktonic foraminifer Zone N14 or older (>11.4 Ma). Sr isotope ages for this section show considerable scatter (11.6–14.2 Ma), which is not surprising considering the large age error for this portion of the Sr age regression (±1.17 m.y.). The average value of the five points in this sequence is 12.8 Ma (with an error of better than ±0.8 m.y. considering number of analyses q > 3) (Oslick et al., 1994), which is concordant with a basal age of 13.2 Ma based on nannofossils and a possible extrapolated age as old as 13.6 Ma (Fig. F18). The errors on the age of this sequence are large, and further studies should refine them.

The underlying tentative seismic sequence termed m4.5 (343.24–449.1 msbf) is also poorly dated. It is assigned to dinocyst Zones DN6–DN8 (<13.2 Ma) at the top and DN5 (13.2–15.1 Ma) below 349.70 mbsf and to Zone NN6 at the top (11.8–13.6 Ma) and Zone NN5 (13.6–15.6 Ma) below 360.88 mbsf. The highest occurrence of *F. peripheroronda* in Sample 313-M0029A-81R-CC, 0–2 cm (371.83 mbsf), helps constrain the minimum estimate for this sequence; this datum level is ~13.8 Ma on BKSA95 and the 2004 geologic timescale (Gradstein, 2004), although Shackleton et al. (1999) suggest that this taxon ranges to Zone N10 (M7). Sr isotope values show considerable scatter in this sequence with ages of 13.3–16.4 Ma. Considering the tight grouping of Sr isotopes ages >15 Ma in underlying sequences, biostratigraphic constraints, and superposition, ages older than 15 Ma are interpreted as reworked and indicated with red on Figure F18. The remaining five Sr isotope ages, which are from the upper part of the sequence, average 13.8 Ma ± 0.8 m.y. Thus, data are consistent with an age estimate of 13.5–14.6 Ma for the sequence.

Seismic sequence m5 (449.1–478.61 mbsf) is assigned to calcareous nannofossil Zone NN5 (13.6–15.6 Ma) and to dinocyst Zone DN5 (13.2–15.1 Ma). The last occurrence of *P. sicana* in Sample 313-M0029A-108R-CC, 0–5 cm (451.22 mbsf), has an age of 14.8 Ma according to BKSA95 (this taxon may range into Zone N10 according to Shackleton et al. [1999], who provide a GTS2004 calibration of 13.73 Ma [13.7 Ma on BKSA95]). Five Sr isotope ages >15 Ma are rejected; the remaining three (14.4, 13.5, and 14.7 Ma ± 1.17 m.y.), together with the biostratigraphic constraints, are consistent with an age as-

signment of seismic sequence m5 to 14.6–15.4 Ma, with a possible basal age of 15.0–15.4 Ma. However, the calibration of *P. sicanus* would allow this sequence to be significantly younger (~14 Ma).

The age of seismic sequence m5.2 (478.61–602.25 mbsf) is well constrained as 15.6–16.1/16.2 Ma. This sequence has excellent agreement among nannofossil (Zones NN4 and NN5), dinocyst (Zones DN4–DN5), and planktonic foraminifer (Zone N8/M5) zones. The tightly constrained Sr isotopic age estimates (12 points between 15.5 and 16.3 Ma, with two potential outliers of 16.7 and 16.6 Ma) are in excellent agreement with the biostratigraphic age estimates. Of note is the placement of the Zone NN4/NN5 boundary (15.6 Ma) in the middle of this sequence in this hole and in Hole M0028A, but its placement in Sequence m5.3 at Hole M0027A suggests a premature/depressed last occurrence in the updip site.

The age of seismic sequence m5.3 (602.25–640.51 mbsf) is only broadly constrained by calcareous nannofossils and dinocysts to Zone NN4 and upper Zones DN3–DN4, respectively, and one Sr isotope age of 16.9 Ma ± 0.6 m.y. However, the last common occurrence of nannofossil *D. deflandrei* (16.2 Ma) can be used as a datum level, suggesting that this sequence is ~16.2–16.9 Ma.

The ages of seismic sequences m5.4, m5.45, and m5.47 cannot be precisely estimated because they are assigned to Zone NN4 below the last common occurrence of *D. deflandrei* (16.2–18.3 Ma) and dinocyst Zone DN3 or older (>16.7 Ma). There are no current Sr isotope age estimates, but subsequent work should constrain the ages of these sequences.

Seismic sequence m5.6 (687.87–707.56/710.16 mbsf) has reasonable age constraints in Hole M0029A versus the updip sites. Here, for the only time, Zone NN3 (18.3–19.6 Ma; note that the BKSA95 timescale dashed the base of the zone at 19.1 Ma, but it should be 19.6 Ma) was identified, remarkably consistent with the sole Sr isotope age of 18.3 Ma ± 0.6 m.y. The sequence also contains *S. belemnos,* which further constrains its age to 18.3–19.2 Ma. Further Sr isotope studies should constrain the basal age of the sequence (?18.5 Ma based on extrapolation of sedimentation rates).

Seismic sequence m5.7 (707.56/710.16–728.56 mbsf) is assigned to calcareous nannofossil Zone NN2 (19.6–23.2 Ma), although it is likely younger than 21.5 Ma based on nannofossil datum levels (ratio of *H. carteri/H. euphratis*). It is assigned to the younger part of Zone DN2 (19 to ~20.2 Ma). The best estimate is thus 19.6–20.2 Ma. Further work should help define the precise age of this sequence.

Seismic sequence m5.8 (728.56–746/750 mbsf) is assigned to the mid-upper part of Zone NN2 (older than 19.6 and younger than 21.5 Ma) and dinocyst zone DN2 (19–22.2 Ma). It has a Sr isotope age estimate of 21.0 Ma ± 0.6 m.y., suggesting that the sequence is 20.4–21.6 Ma. Further work should help define the precise age of this sequence.

We may have penetrated seismic sequence m6 below 746/750–752.8/753.22 mbsf. Dinocysts suggest that the base of Hole M0029A is in Zone DN1 (>22.2 Ma); however, nannofossils suggest that the base of Hole M0029A was younger than 21.5 Ma, remarkably consistent with a Sr isotope age of 21.3 Ma ± 0.6 m.y. These ages are more consistent with assignment to sequence m5.8 based on regional correlations.

Sedimentation rates are difficult to estimate in Hole M0029A from the preliminary age constraints. Average sedimentation rates shown on Figure **F18** are ~80 m/m.y. Sedimentation rates during deposition of the targeted m5.2 sequence in a position near its greatest thickness were higher: the ~123 m of this sequence was deposited in 0.7 m.y., with sedimentation rates of ~176 m/m.y. Sedimentation rates in the m4.5 and m4.2 sequences were high (>80 m/m.y) and may have approached the sedimentation rates in sequence m5.2.

References

Bahr, D.B., Hutton, E.W.H., Syvitski, J.P.M., and Pratson, L.F., 2001. Exponential approximations to compacted sediment porosity profiles. *Comp. Geosci.,* 27(6):691–700. **doi:10.1016/S0098-3004(00)00140-0**

Berggren, W.A., Kent, D.V., Swisher, C.C., III, and Aubry, M.-P., 1995. A revised Cenozoic geochronology and chronostratigraphy. *In* Berggren, W.A., Kent, D.V., Aubry, M.-P., and Hardenbol, J. (Eds.), *Geochronology, Time Scales and Global Stratigraphic Correlation.* Spec. Publ.—SEPM (Soc. Sediment. Geol.), 54:129–212.

Cande, S.C., and Kent, D.V., 1995. Revised calibration of the geomagnetic polarity timescale for the Late Cretaceous and Cenozoic. *J. Geophys. Res., [Solid Earth],* 100(B4):6093–6095. **doi:10.1029/94JB03098**

Carey, J.S., Sheridan, R.E., Ashley, G.M., and Uptegrove, J., 2005. Glacially-influenced late Pleistocene stratigraphy of a passive margin: New Jersey's record of the North American ice sheet. *Mar. Geol.,* 218(1–4):155–173 **doi:10.1016/j.margeo.2005.04.006**

de Verteuil, L., and Norris, G., 1996. Miocene dinoflagellate stratigraphy and systematics of Maryland and Virginia. *Micropaleontology,* 42(Suppl.). **doi:10.2307/1485926**

Dewhurst, D.N., Cartwright, J.A., and Lonergan, L., 1999. The development of polygonal fault systems by syneresis of colloidal sediments. *Mar. Pet. Geol.,* 16(8):793–810. **doi:10.1016/S0264-8172(99)00035-5**

Dybkjær, K., 2004. Morphological and abundance variations in *Homotryblium*-cyst assemblages related to depositional environments: uppermost Oligocene–lower Miocene, Jylland, Denmark. *Palaeogeogr., Palaeoclimatol., Palaeoecol.,* 206(1–2):41– 58. doi:10.1016/j.palaeo.2003.12.021

Gay, A., Lopez, M., Cochonat, P., and Sermondadaz, G., 2004. Polygonal faults-furrows system related to early stages of compaction—upper Miocene to recent sediments of the Lower Congo Basin. *Basin Res.,* 16(1):101–116. doi:10.1111/j.1365-2117.2003.00224.x

Gradstein, F.M., 2004. Introduction. *In* Gradstein, F.M., Ogg, J.G., and Smith, A. (Eds.), *A Geologic Time Scale 2004:* Cambridge (Cambridge Univ. Press), 3–19. http://cambridge.org/uk/catalogue/catalogue.asp?isbn=9780521781428

Kennett, J.P., and Srinivasan, M.S., 1983. *Neogene Planktonic Foraminifera: A Phylogenetic Atlas:* Stroudsburg, PA (Hutchinson Ross).

Martini, E., 1971. Standard Tertiary and Quaternary calcareous nannoplankton zonation. *Proc. Int. Conf. Planktonic Microfossils,* 2:739–785.

Miller, K.G., Mountain, G.S., Browning, J.V., Kominz, M., Sugarman, P.J., Christie-Blick, N., Katz, M.E., and Wright, J.D., 1998. Cenozoic global sea level, sequences, and the New Jersey transect: results from coastal plain and continental slope drilling. *Rev. Geophys.,* 36(4):569–602. doi:10.1029/98RG01624

Miller, K.G., Rufolo, S., Sugarman, P.J., Pekar, S.F., Browning, J.V., and Gwynn, D.W., 1997. Early to middle Miocene sequences, systems tracts, and benthic foraminiferal biofacies, New Jersey coastal plain. *In* Miller, K.G., and Snyder, S.W. (Eds.), *Proc. ODP, Sci. Results,* 150X: College Station, TX (Ocean Drilling Program), 169–186. doi:10.2973/odp.proc.sr.150X.313.1997

Mountain, G.S., Miller, K.G., Blum, P., et al., 1994. *Proc. ODP, Init. Repts.,* 150: College Station, TX (Ocean Drilling Program). doi:10.2973/odp.proc.ir.150.1994

Munsterman, D.K., and Brinkhuis, H., 2004. A southern North Sea Miocene dinoflagellate cyst zonation. *Geol. Mijnbouw,* 83(4):267–285. http://www.njgonline.nl/publish/articles/000060/article.pdf

Oslick, J.S., Miller, K.G., Feigenson, M.D., and Wright, J.D., 1994. Oligocene–Miocene strontium isotopes: stratigraphic revisions and correlations to an inferred glacio-eustatic record. *Paleoceanography,* 9(3):427–443. doi:10.1029/94PA00249

Rider, M., 2006. *The Geological Interpretation of Well Logs* (2nd ed.): Sutherland, Scotland (Whittles).

Sclater, J.G., and Christie, P.A.F., 1980. Continental stretching: an explanation of the post-mid-Cretaceous subsidence of the central North Sea basin. *J. Geophys. Res., [Solid Earth],* 85(B7):3711–3739. doi:10.1029/JB085iB07p03711

Shackleton, N.J., Crowhurst, S.J., Weedon, G.P., and Laskar, J., 1999. Astronomical calibration of Oligocene–Miocene time. *In* Shackleton N.J., McCave, I.N., and Graham, P.W. (Eds.), *Astronomical (Milankovitch) Calibration of the Geological Time-Scale.* Philos. Trans. R. Soc., Ser. A., 357(1757):1907–1929. doi:10.1098/rsta.1999.0407

Sheridan, R.E., Ashley, G.M., Miller, K.G., Waldner, J.S., Hall, D.W., and Uptegrove, J., 2000. Offshore-onshore correlation of upper Pleistocene strata, New Jersey coastal plain to continental shelf and slope. *Sediment. Geol.,* 134(1–2):197–207. doi:10.1016/S0037-0738(00)00020-8

Figure F1. Symbols and colors used in "Lithostratigraphy" and "Stratigraphic correlation" figures for Hole M0029A.

Clay	Coarse/medium sand	Organic-rich sediment
Silt	> Sand	Bioclastic horizon
Very fine/fine sand	Glauconite (>25%)	X X Indurated/nodule

∧	Fining-upward interval	p	Pyrite		Echinoids
∇	Coarsening-upward interval	g	Glauconite		Shell fragments
↑	Normal grading		Cross laminae	△	Shell debris
↓	Reverse grading		Wedge-planar laminae		Articulated shell
	Burrow		Scour		Foraminifers
	Hummocky cross stratification		Horizontal lamination		Gastropods
	Swaley cross stratification		Convoluted bedding	wd	Organic matter
		≀	Bioturbation	C.D.	Core disturbance

m.5.4	Predicted depth range for seismic reflection
MIC4	Surface picked in the core
m.3	Surface based on log data

Surface boundary   Maximum flooding surface

Transgressive surface   Flooding surface

SF = shoreface   OFF = offshore   dOFF = distal offshore   SOT = shoreface-offshore transition

Figure F2. Location of Hole M0029A on seismic line 529, showing lithostratigraphic units in color on a background with seismic reflectors.
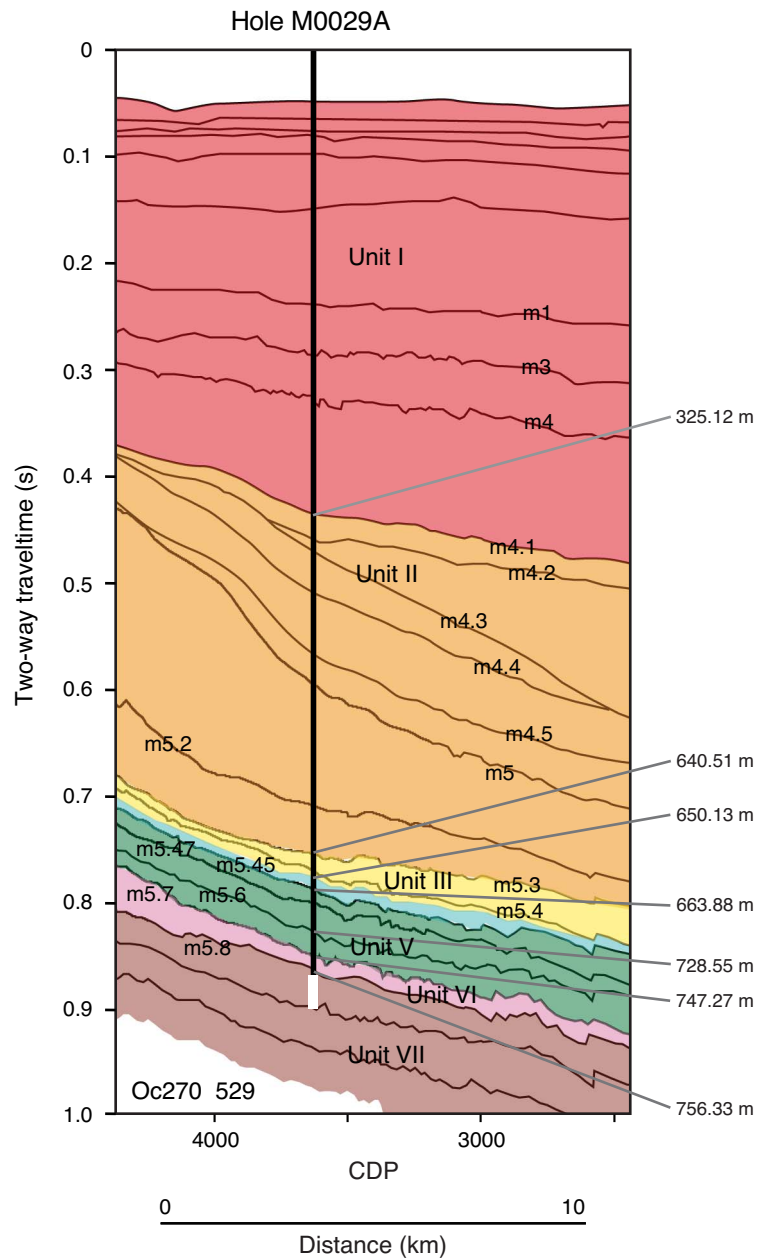
Figure F3. Summary sedimentary logs of lithostratigraphic units and subunits identified in Hole M0029A, from the top of Unit I to the top of Unit VII. vf = very fine, f = fine, m = medium, c = coarse. See Figure **F1** for lithology legend. **A.** 0–280 mbsf. (**Continued on next page.**)
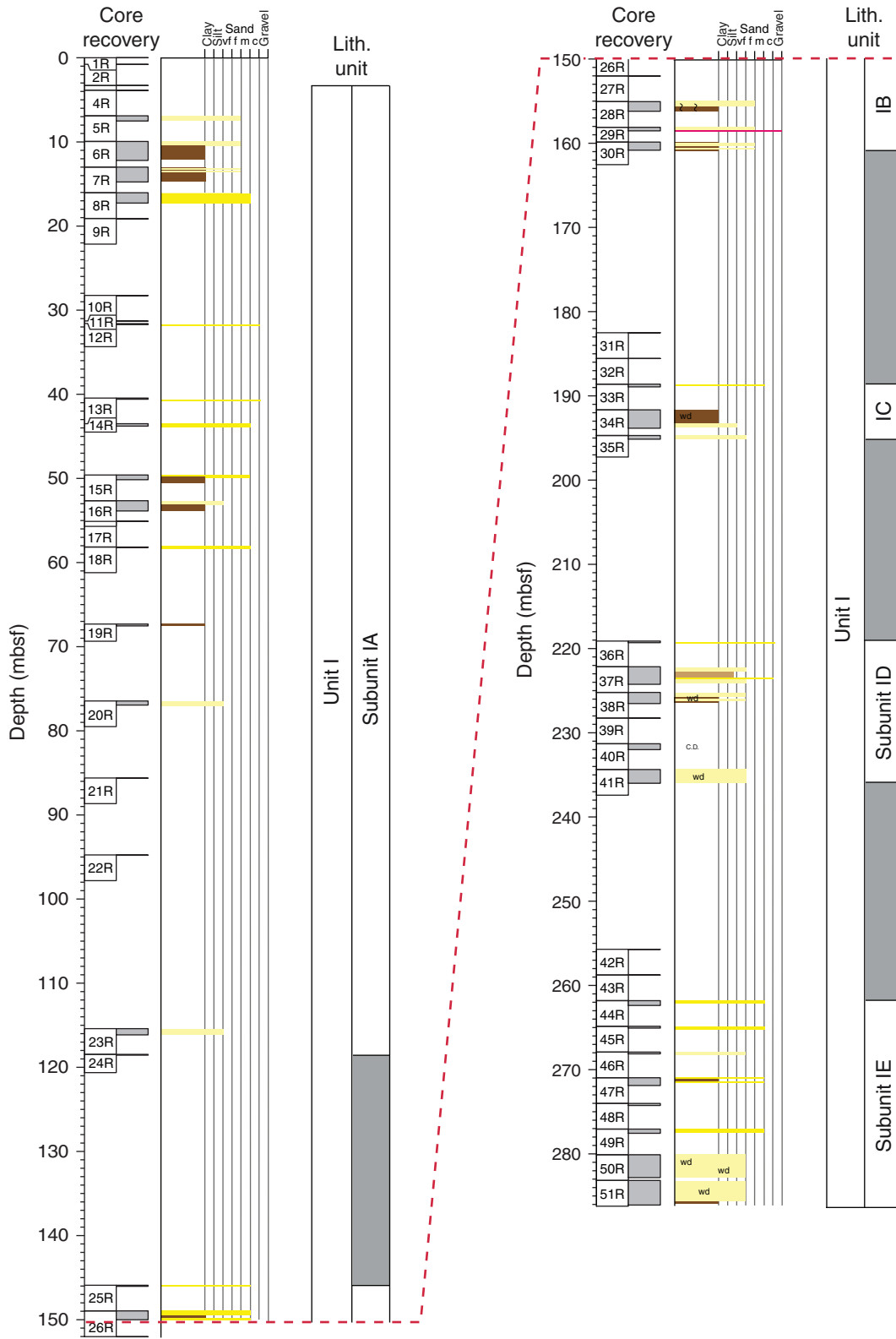
Figure F3 (continued). B. 280–750 mbsf.
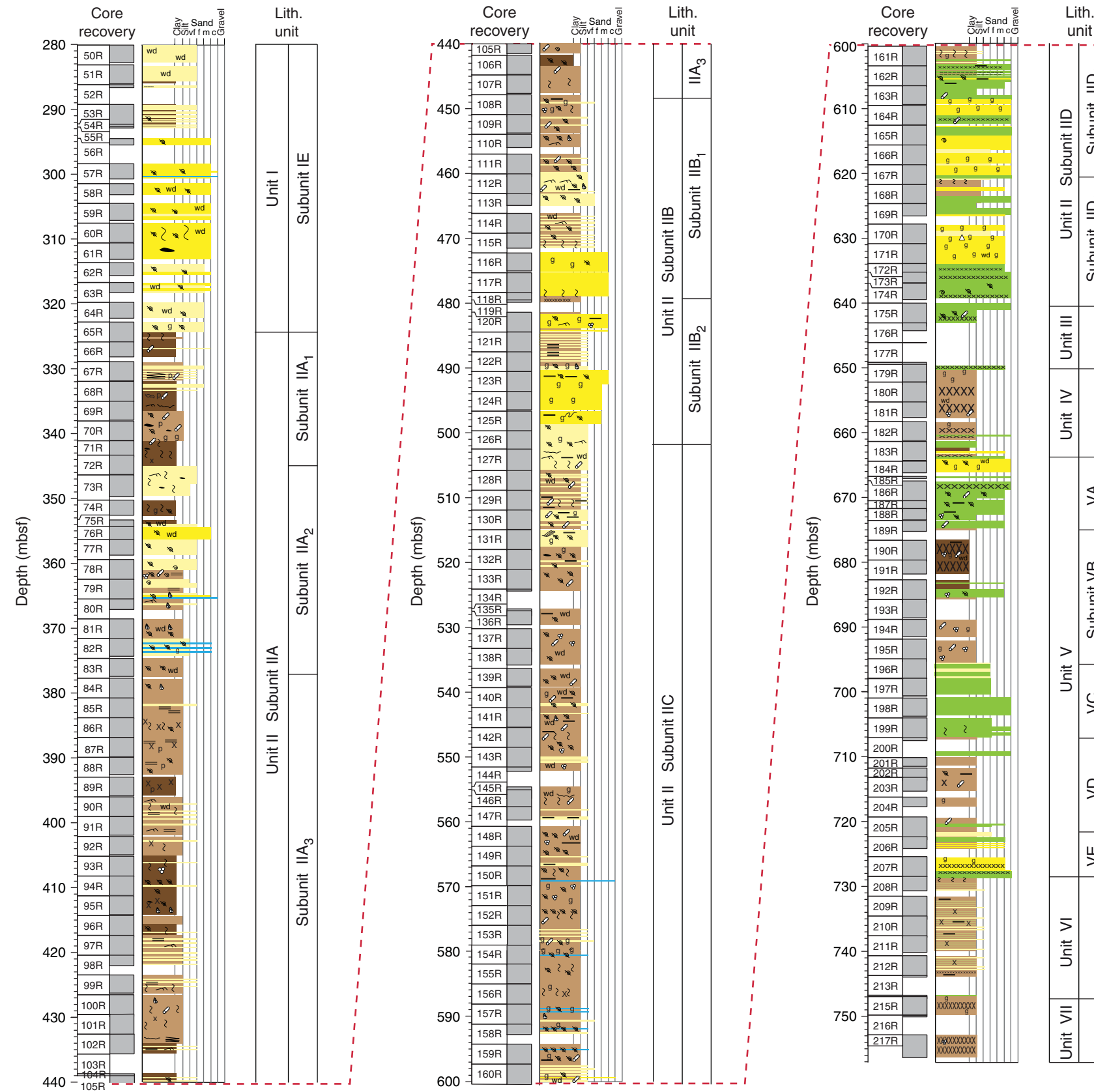
Figure F4. Core photograph of medium to coarse sand with basal gravel at 8 cm above light blue clay (interval 313-M0029A-15R-1, 0–22 cm). Gravel contact is interpreted as an unconformity separating unnamed Pleistocene sequences.
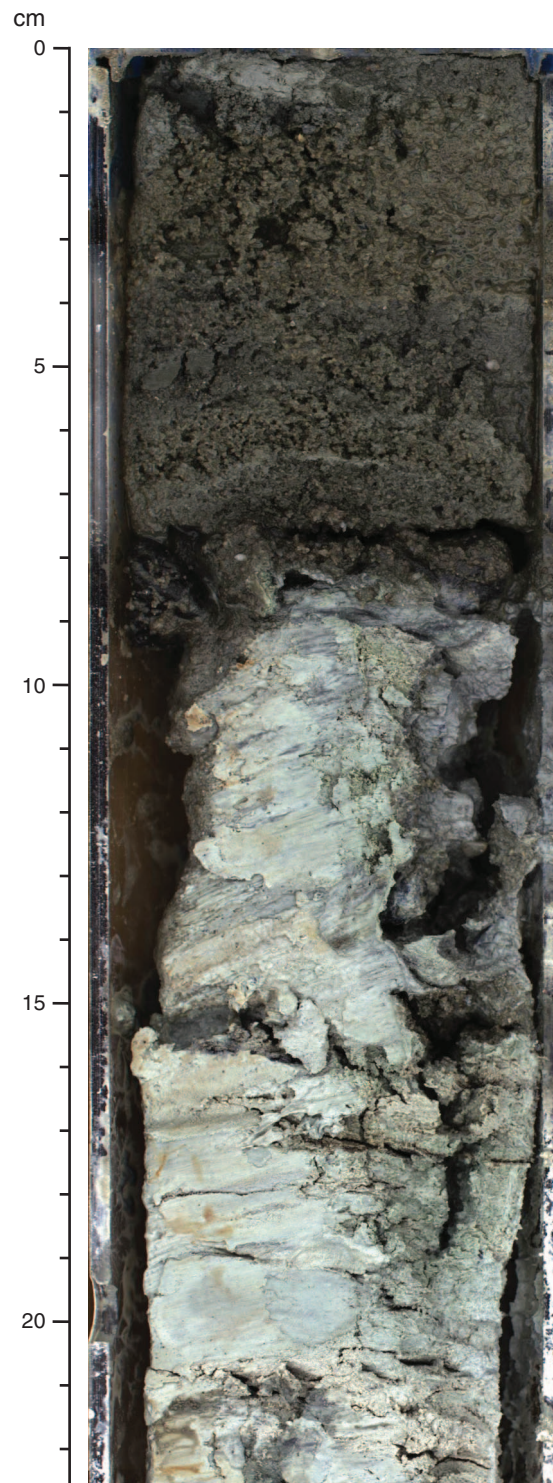
Figure F5. Core photograph of clay with large pieces of wood, in situ roots, and silty clay, possibly deposited in a lower delta plain environment and developed as a paleosol (Section 313-M0029A-34R-1, 9–140 cm).
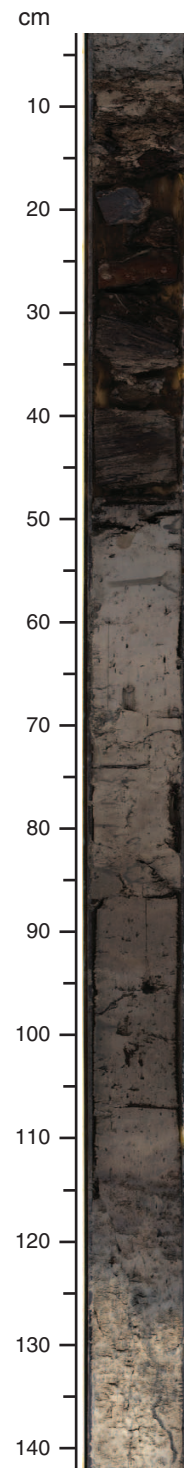
Figure F6. Core photograph of an unconformity separating dark gray silty sand above from stiff silty clay below across an abrupt and deeply bioturbated contact (interval 313-M0029A-65R-2, 71–119 cm).

Figure F7. Core photograph of bioturbated shelly fine sand interbedded with silty clay possibly deposited in lagoonal and barrier beach environments (interval 313-M0029A-53R-2, 20–80 cm).
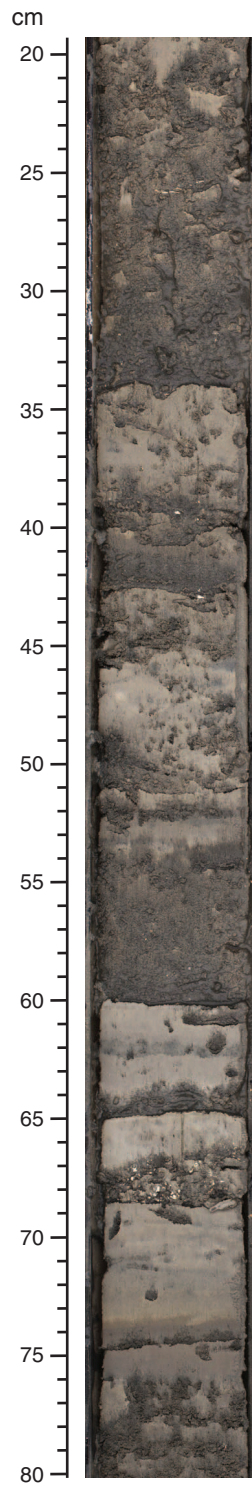
Figure F8. Core photograph of a 40 cm thick sharp-based, normally graded bed that coarsens down from poorly sorted coarse sand at the top to gravely sand at the base (interval 313-M0029A-79R-2, 50–92 cm). See also numerous gastropods, bivalves, and shell fragments. Deposits are part of a larger package of sediment interpreted as sediment gravity flow of coarse material into deep quiet waters possibly shed from upslope rollover positions during periods of relative sea level lowering.

Figure F9. Core photograph of high-angle cross-bedding in slightly shelly, silty very fine sand indicative of bedform migration in a deep marine setting (interval 313-M0029A-110R-2, 50–80 cm).
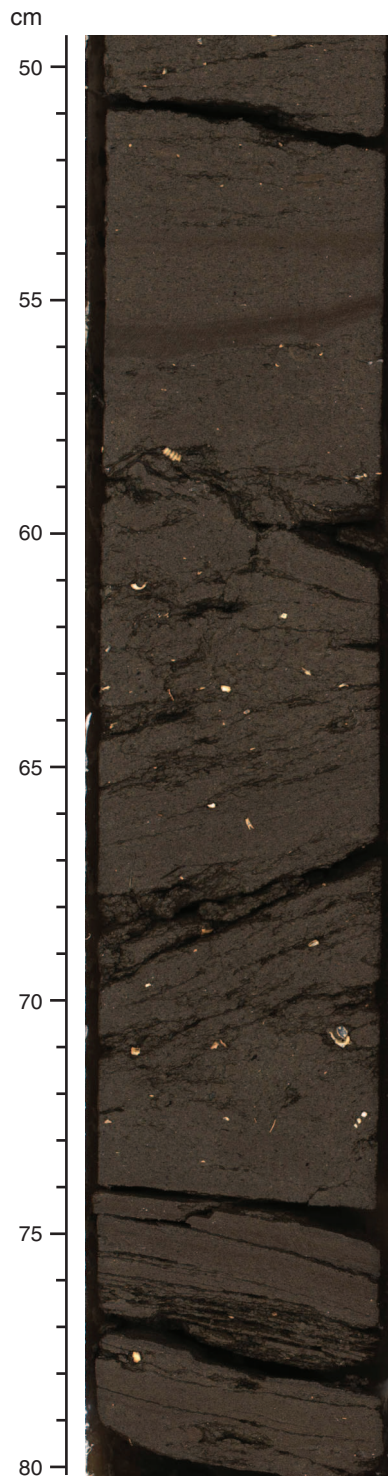
Figure F10. Core photograph of *Teichichnus* burrow at 42 cm in silty very fine sand (interval 313-M0029A-127R-2, 40–45 cm). Burrow's length and width are 1.5 cm each.

Figure F11. Core photograph of sharp contact (at 9 cm) between dark green-brown glauconite sandstone above and pale brown clayey silt below (interval 313-M0029A-208R-1, 0–36 cm). Glauconite sand fills *Thalassinoides* burrows in the underlying clayey silt. This surface is interpreted as an unconformity.

Figure F12. Percentages of sand, silt, and clay based on smear slides from Hole M0029A. Silt content exceeds 40% on average, higher than in Holes M0027A and M0028A.
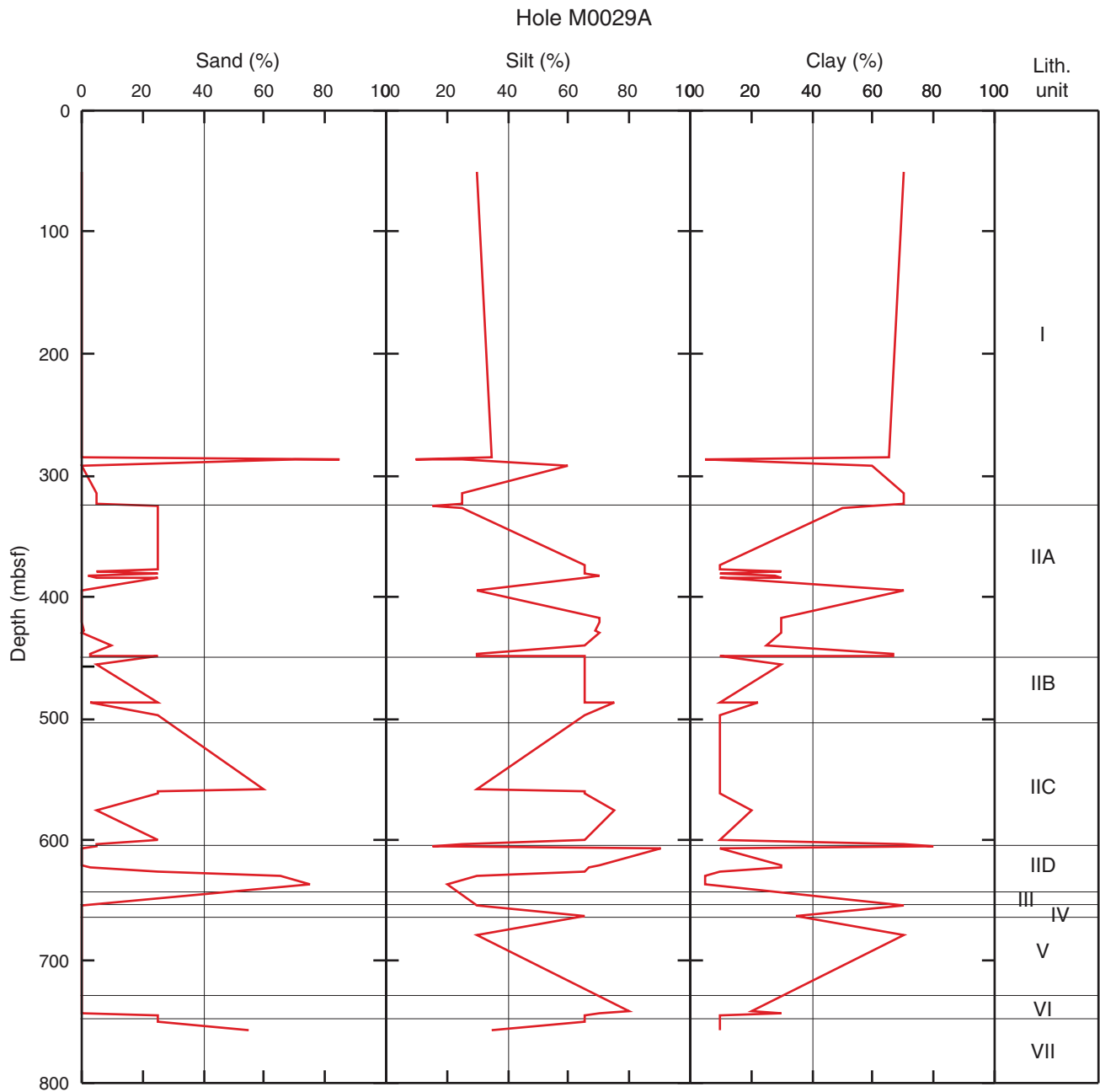
Figure F13. Photomicrograph of calcareous silty clay with silt-sized quartz, large numbers of diatoms, silico-flagellates and sponge spicules, and scattered framboidal pyrite grains, which are common in Unit II (Sample 313-M0029A-108R-1, 33 cm; Subunit IIA). Photo under cross-polarized light is 0.7 mm in width.
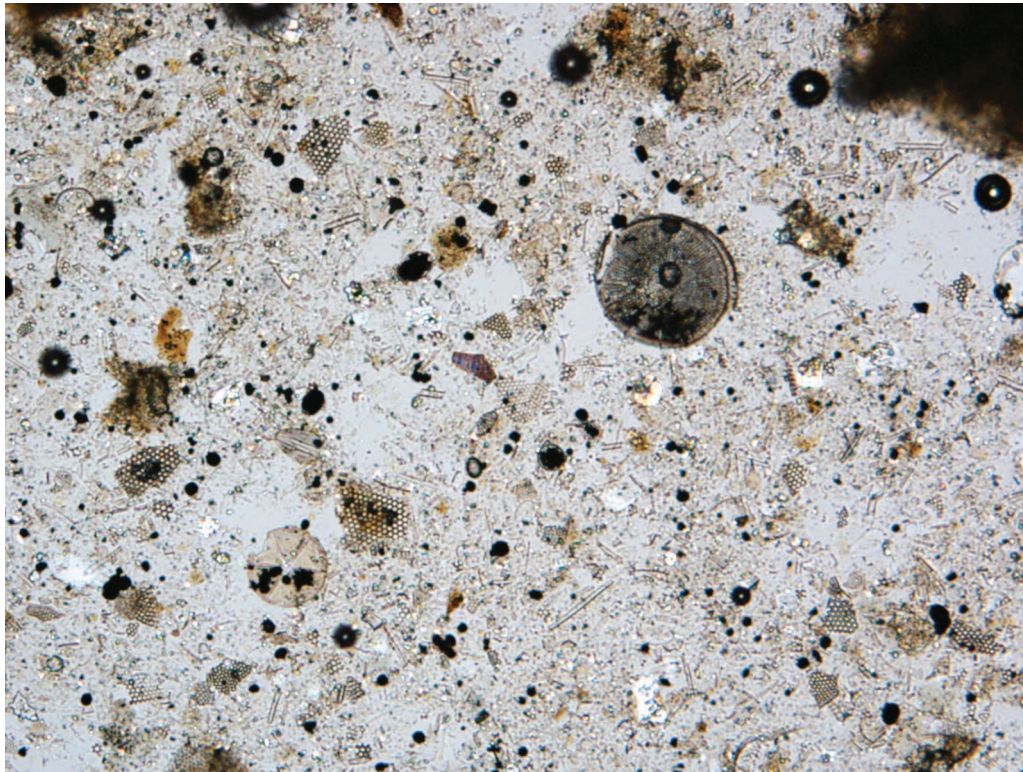
Figure F14. Photomicrograph of silt with medium sand grain (lower right) and several glauconite grains (Sample 313-M0029A-170R-1, 144 cm; Subunit IID). Framboidal pyrite, diatom, and sponge spicules are also scattered. Photo under cross-polarized light is 0.7 mm in width.
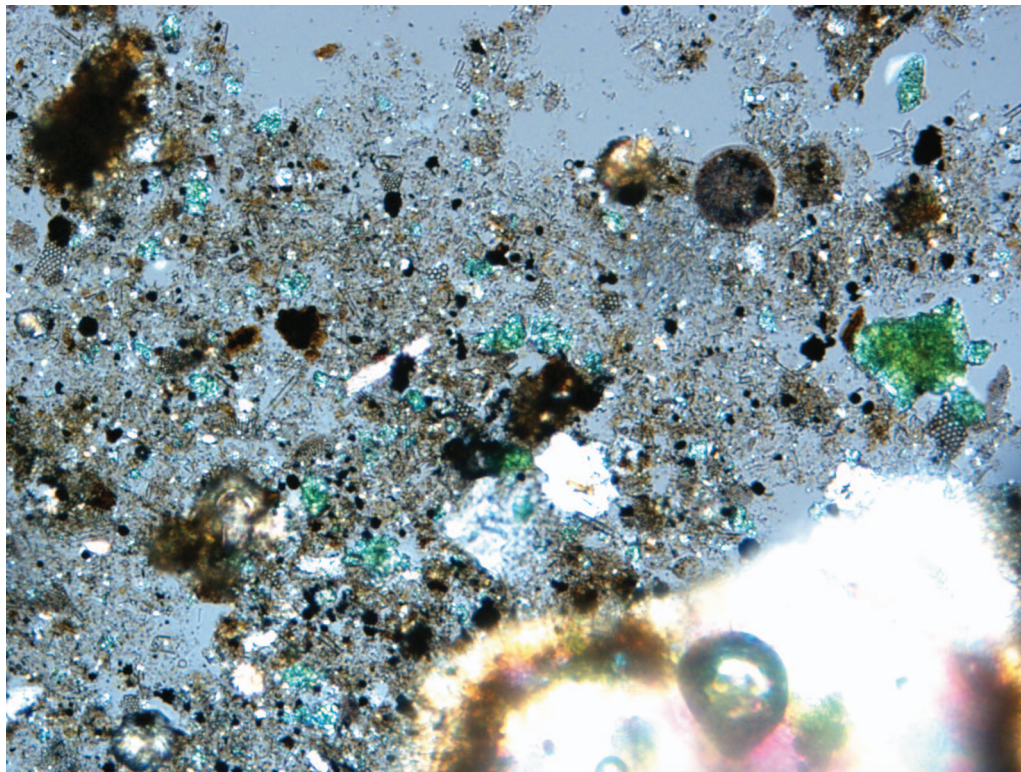
Figure F15. Photomicrographs of calcareous silty clay with quartz (right large grain); glauconite of various sizes from fine silt to fine sand and some opaque minerals (Sample 313-M0029A-162R-1, 105 cm; Unit IID). Calcite grains matrix is much scattered. Photos are 0.7 mm (700 µm) in width. A. Plane-polarized light. B. Cross-polarized light.
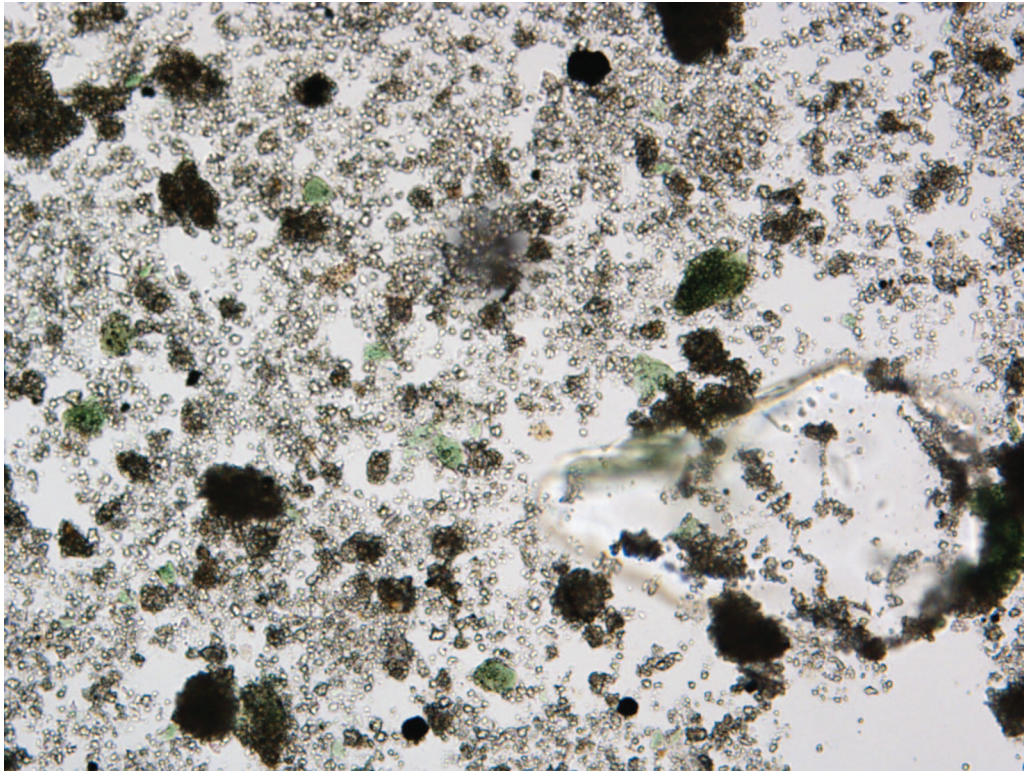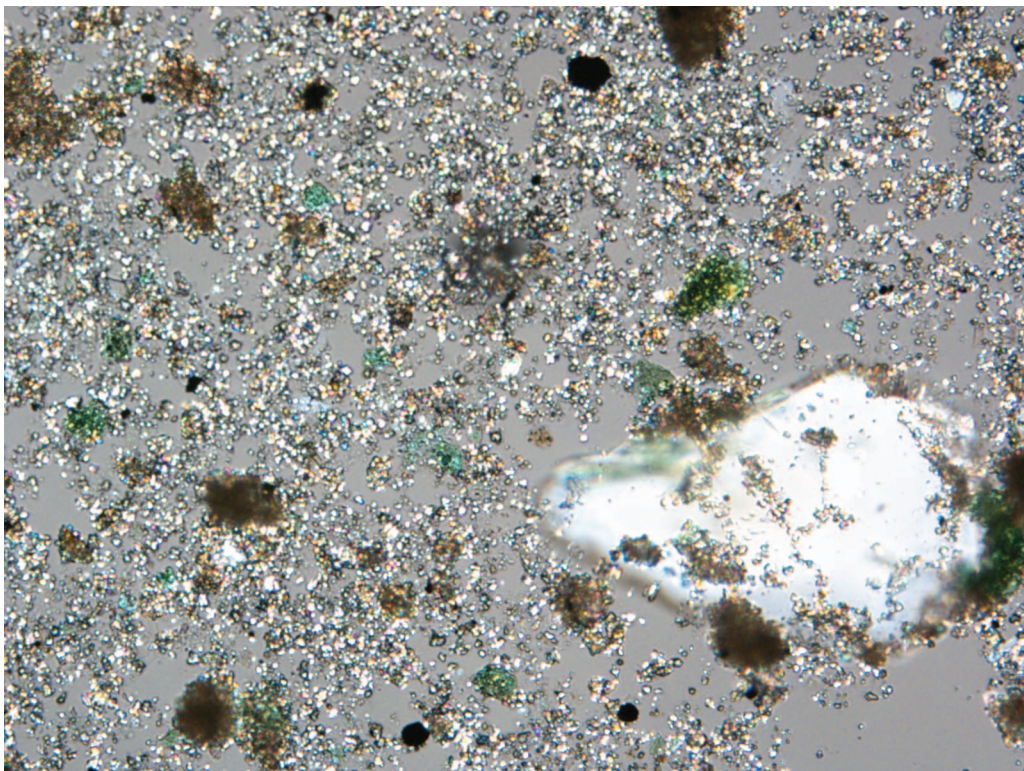
Figure F16. Photomicrograph of sandy clayey silt with angular very fine quartz sand, aggregates, and individual grains, which are common in Unit VI, and some glauconite grains (Sample 313-M0029A-208R-1, 14 cm; Unit VI). Siliceous microfossils are absent, but nannofossils are common in Unit VI. Photo under crossed nicols is 0.7 mm in width.
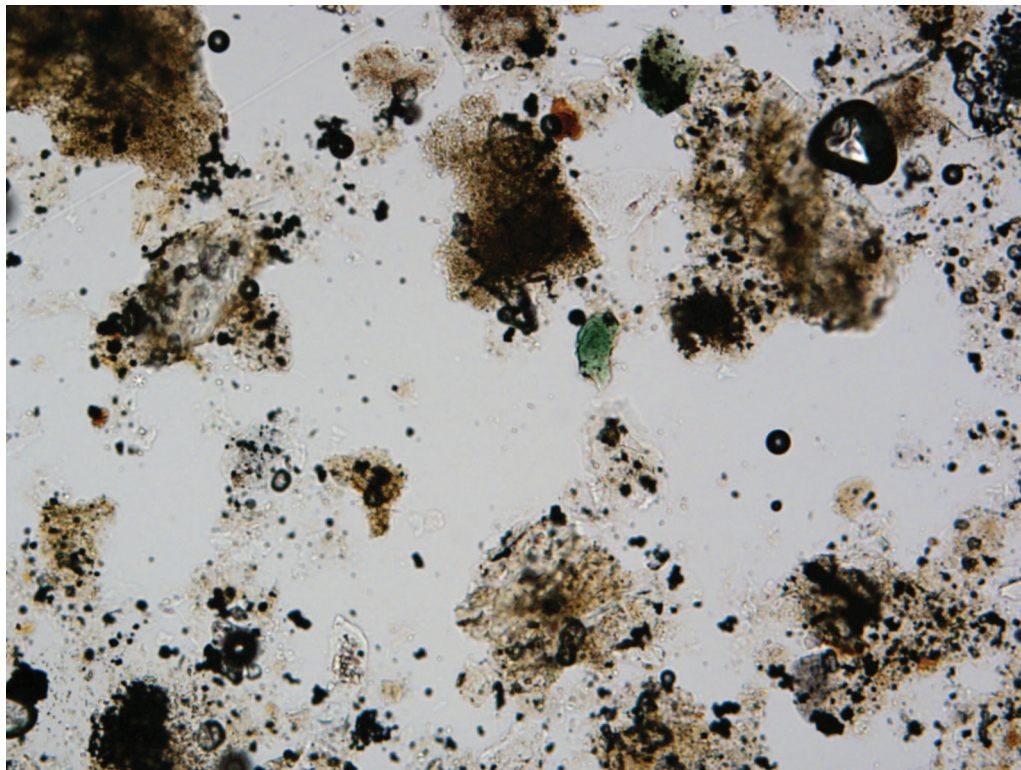
Figure F17. Biostratigraphic summary interpreted from calcareous nannofossils, planktonic foraminifers, and dinocysts, showing Miocene stages. See Figure F12 in the "Methods" chapter for an explanation of the datums used. Zone boundaries are drawn diagonally to indicate uncertainty in zonation between samples because of either the absence of sampling between points or the absence of age-diagnostic taxa. Zonal boundaries are correlated to the geologic timescale. Dashed lines indicate some uncertainty in age assignments. The geologic timescale is that of Berggren et al. (1995), based on the geomagnetic polarity timescale of Cande and Kent (1995). See Figure F4 in the "Methods" chapter for lithology legend. (**Figure shown on next page.**)

Figure F17 (continued). (Caption shown on previous page.)
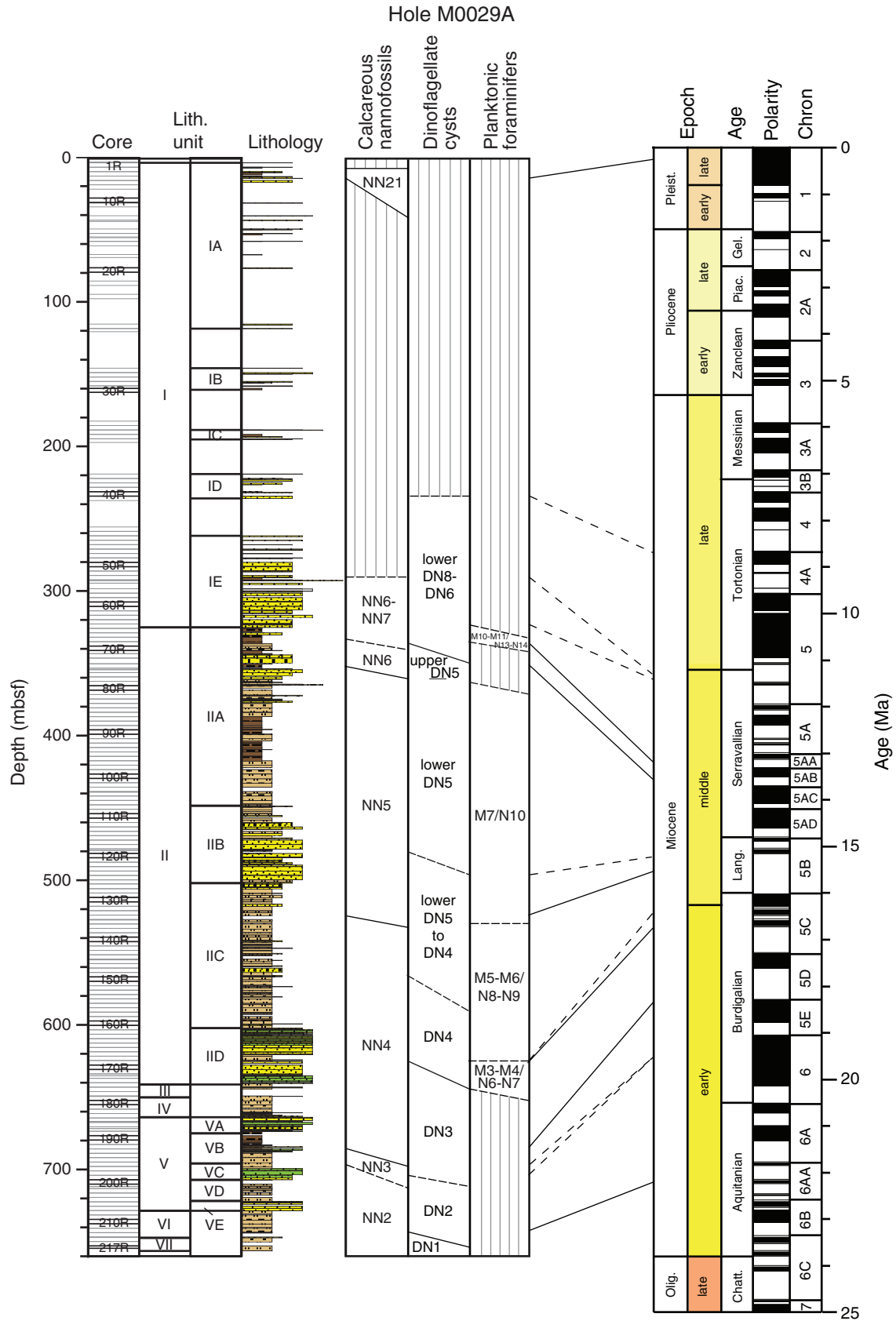
Figure F18. Age-depth plot showing core recovery (every fifth core shaded), the timescale of Berggren et al. (1995), calcareous nannoplankton zones (light blue bars), planktonic foraminifer zones (dark blue bars), and dinocyst zones (green bars). Select highest/last occurrences (x) are shown for nannoplanktons, foraminifers, and dinocysts. Sr isotopic ages are shown as circles with errors of ±0.6 m.y. (older than 15.2 Ma) and ±1.17 m.y. (younger than 15.2 Ma). Red Sr isotope ages are interpreted as reworked. Horizontal lines for sequence boundaries (red) and tentative sequence boundaries (dashed red) lines are labeled with their corresponding depths. Horizontal green lines = flooding surfaces. Planktonic foraminifer zones from Berggren et al. (1995), nannofossil zone from Martini (1971), and dinocyst zones from de Verteuil and Norris (1996). Geomagnetic polarity timescale from Cande and Kent (1995).
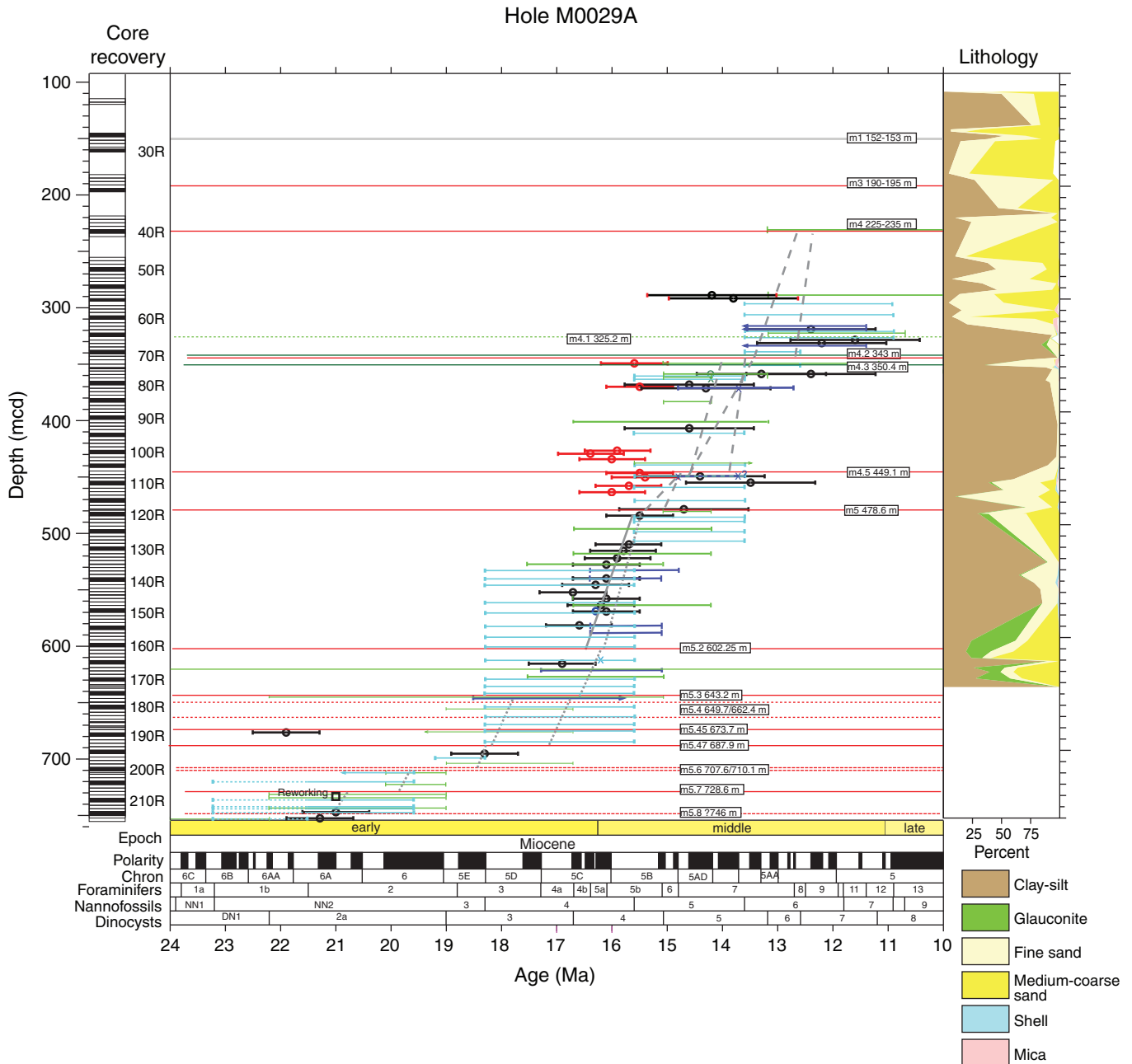
Figure F19. Distribution of biostratigraphically important calcareous nannofossil taxa in Hole M0029A. Thickness of distribution line indicates relative abundance of species. Zonal assignments (Martini, 1971) are given, with approximate age indicated. Red lines = sequence boundaries, green lines = major flooding surfaces. See Figure F4 in the "Methods" chapter for lithology legend.

Figure F20. Planktonic foraminifer stratigraphic distributions in Hole M0029A. Red lines = sequence boundaries, green lines = major flooding surfaces. See Figure F4 in the "Methods" chapter for lithology legend.
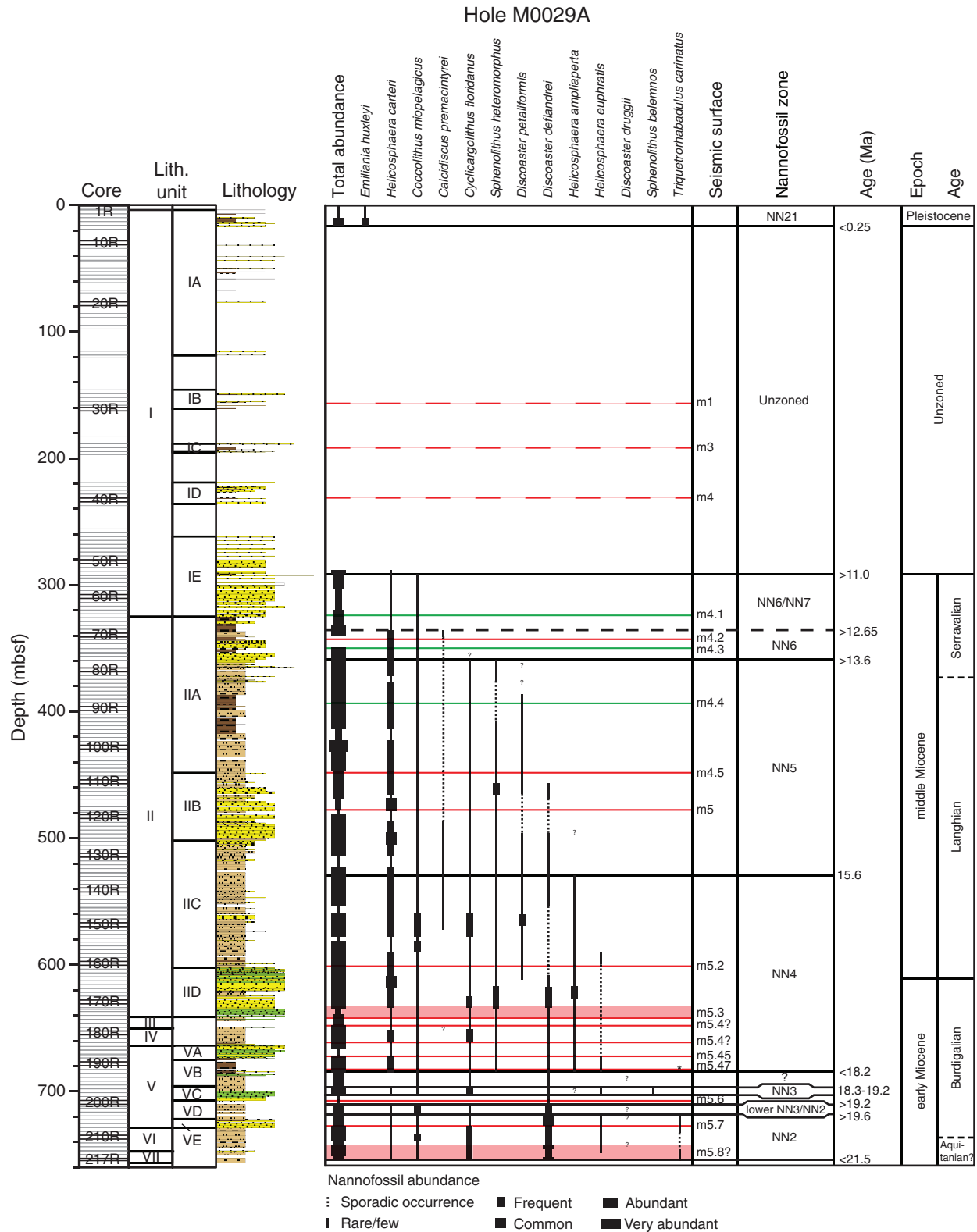
Figure F21. Stratigraphic distribution of age-diagnostic dinocyst taxa in Hole M0029A, with the Miocene zoned following de Verteuil and Norris (1996). Zone boundaries are drawn diagonally to indicate uncertainty in zonation between samples, because of either the absence of sampling between points or of age-diagnostic taxa. Red lines = sequence boundaries, green lines = major flooding surfaces. See Figure F4 in the "Methods" chapter for lithology legend.
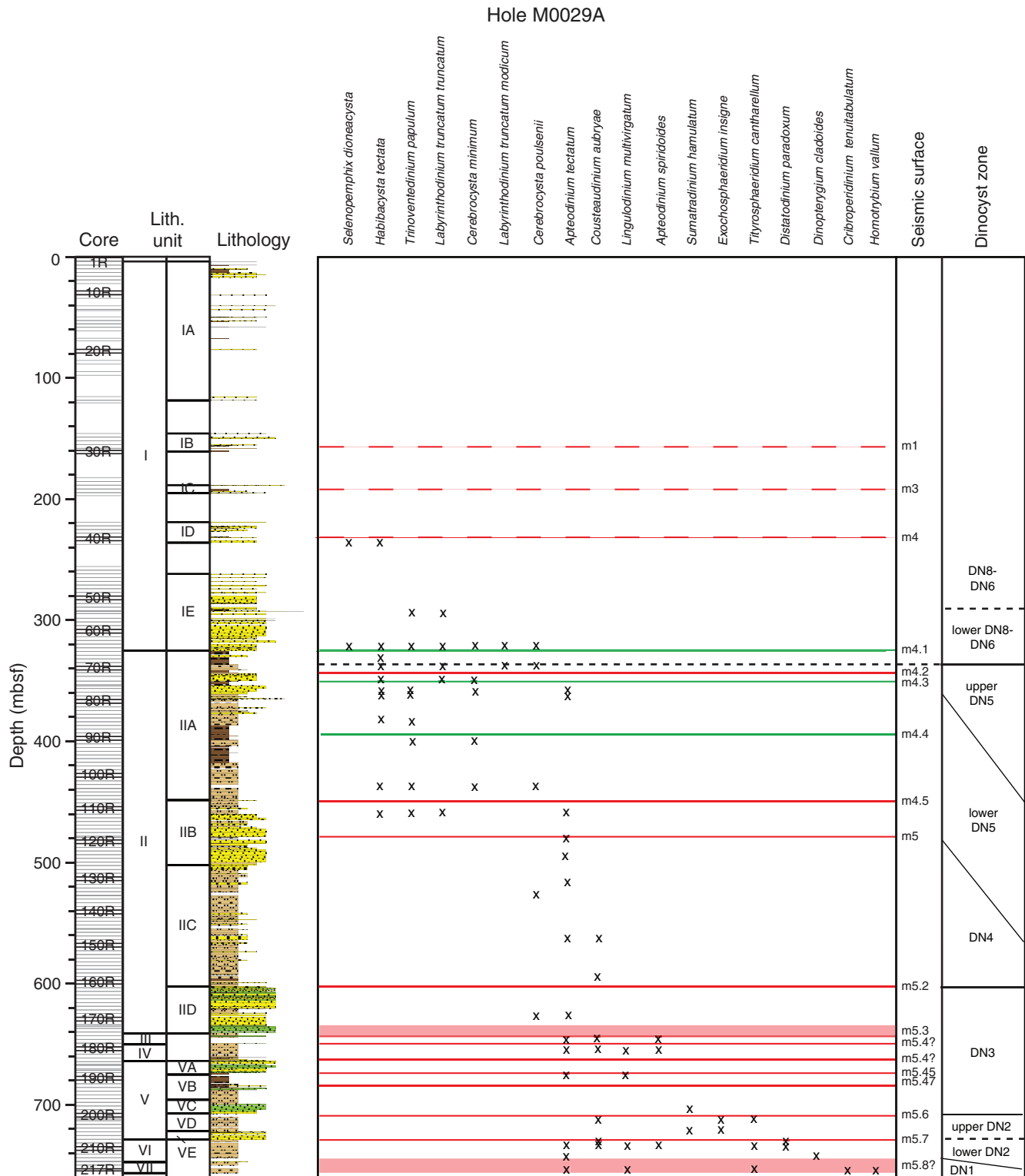
Figure F22. Benthic foraminifer paleobathymetric estimates. ? = barren samples or samples with too few specimens to determine a paleodepth. Arrows = depths deeper than 100 m (mostly likely shallower than ~200 m). Red lines = sequence boundaries, green lines = major flooding surfaces. See Figure F4 in the "Methods" chapter for lithology legend.
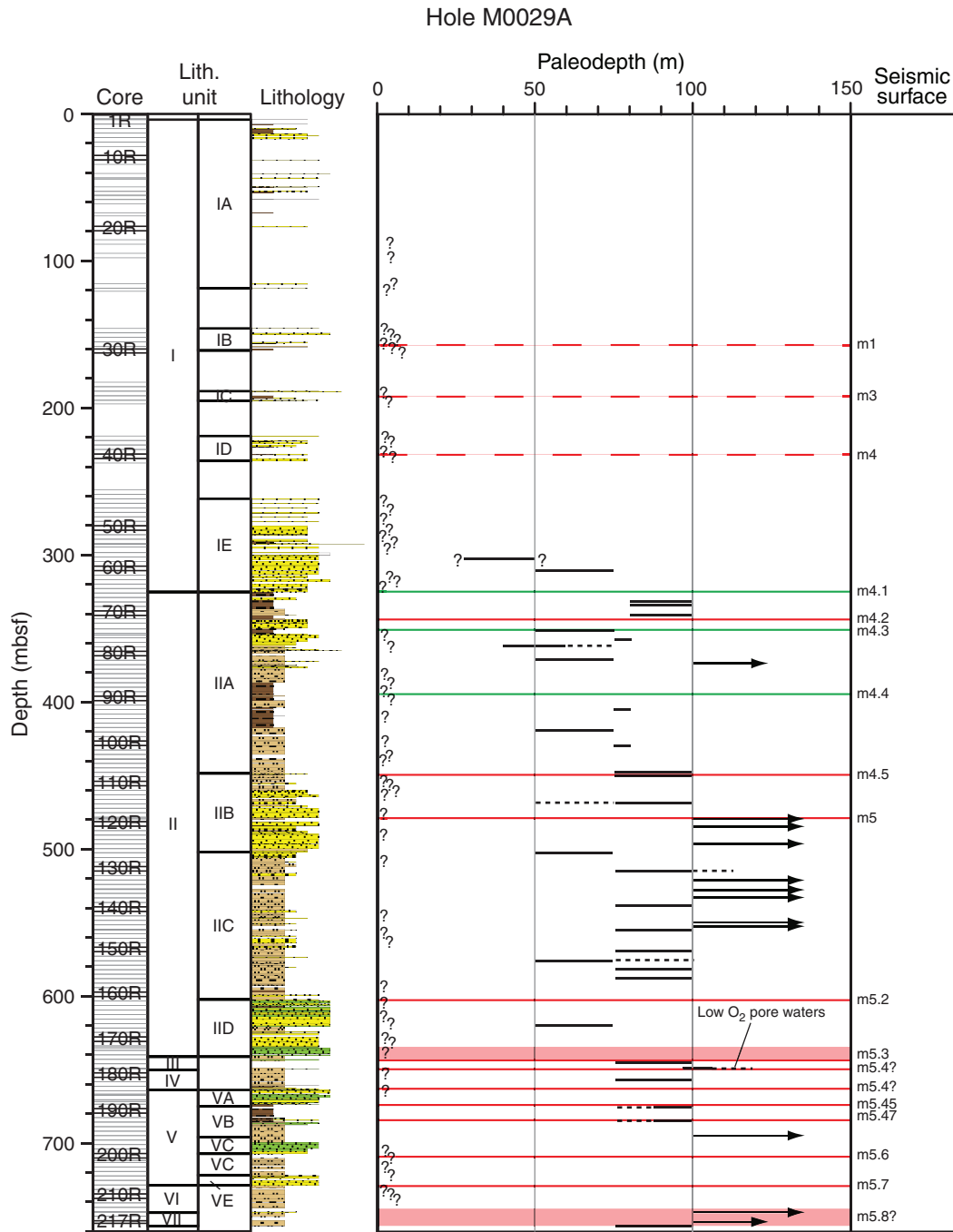
Figure F23. Palynomorph diagram and relationship between terrestrial and marine palynomorphs, Hole M0029A. Reference sum for percentages is total amount of nonsaccate pollen (nonsaccate herb, arboreal, sedge, and grass pollen, as well as unidentified nonsaccate pollen). Orange bar = interval of extraordinarily high content of elm pollen, green bar = interval of relatively high contents of hemlock pollen from both west- and east-American species.
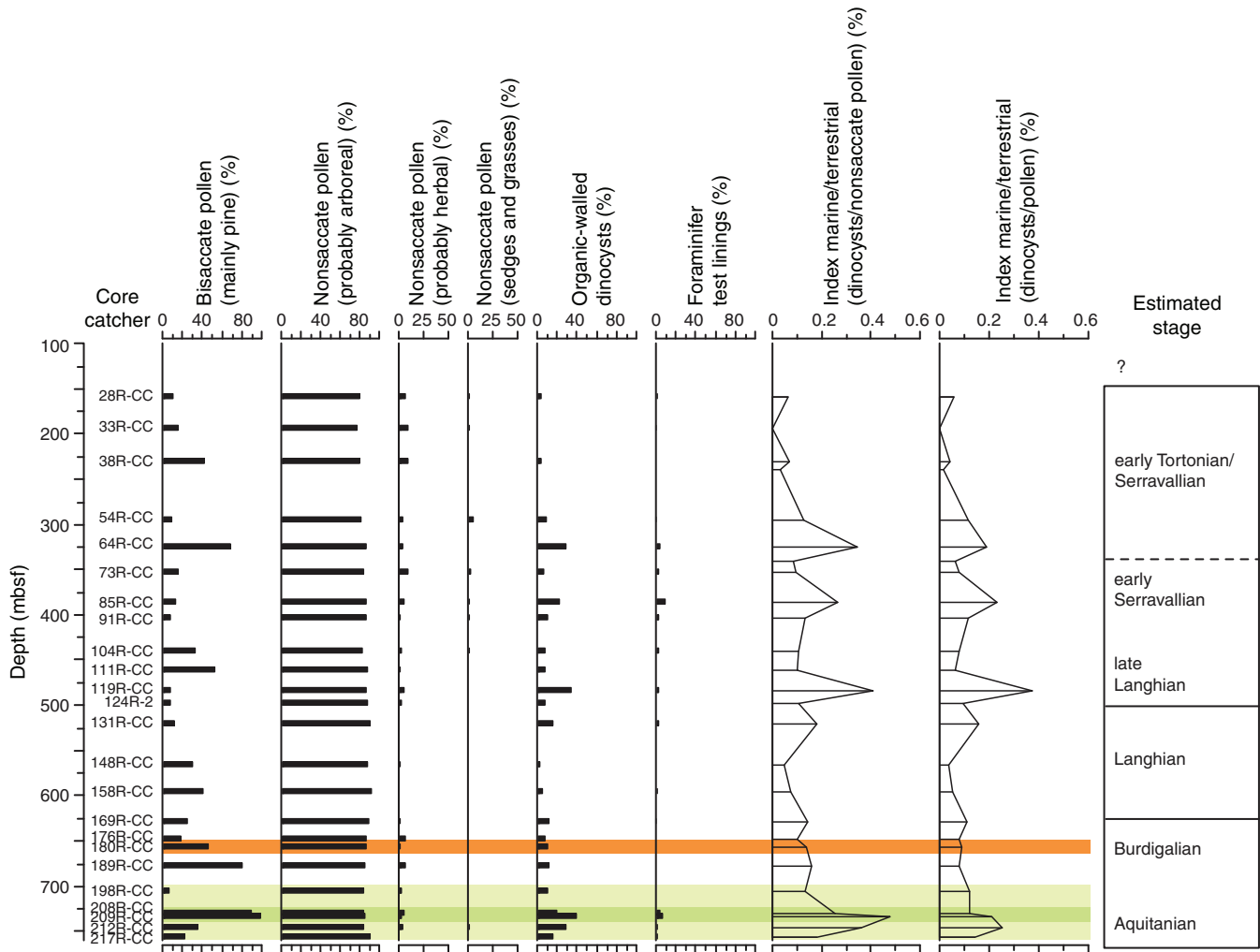
Figure F24. Simplified sketches based on sample analyses for Hole M0029A, showing hinterland and coastal ecology during the Serravallian, the early Serravallian–late Langhian, the early Burdigalian, and the early Burdigalian–late Aquitanian. Gray trees = pines producing bisaccate pollen, green trees = trees producing nonsaccate pollen or pollen with small sacci, blue-green conifers = hemlock, light green trees = hickory, dark green trees = other trees (mainly oak). Gray triangles = transport potential of bisaccate pollen, green triangles = nonsaccate pollen transport potential, blue-green triangle = transport potential of hemlock pollen (pollen with small sacci). Red flowers = herbs producing nonsaccate pollen, excluding monoporate pollen; yellow tussocks = grasses. Spirals = foraminifer test linings, Cyan symbols = dinocysts. Size of yellow sun is proportional to estimated temperatures, size of rain cloud = moisture availability/humidity. Percentages of palynomorphs are displayed on the right. In some cases, an average value for several neighboring samples is shown. Reference sum is the total amount of nonsaccate pollen and pollen with small sacci. Light green bars = hickory pollen, blue-green bars = hemlock pollen, dark green bars = pollen probably related to oaks and other broad-leaved trees, yellow bars = pollen of grasses (Poacea), red bars = herbal pollen. Gaps between green, red, and yellow bars = nonsaccate pollen that could not be assigned to the three main groups (pollen grains of aquatic plants, pollen filled with pyrite, and pollen of morphogroups/families containing both herbal and arboreal taxa). (**Figure shown on next page.**)

Figure F24 (continued). (Caption shown on previous page.)
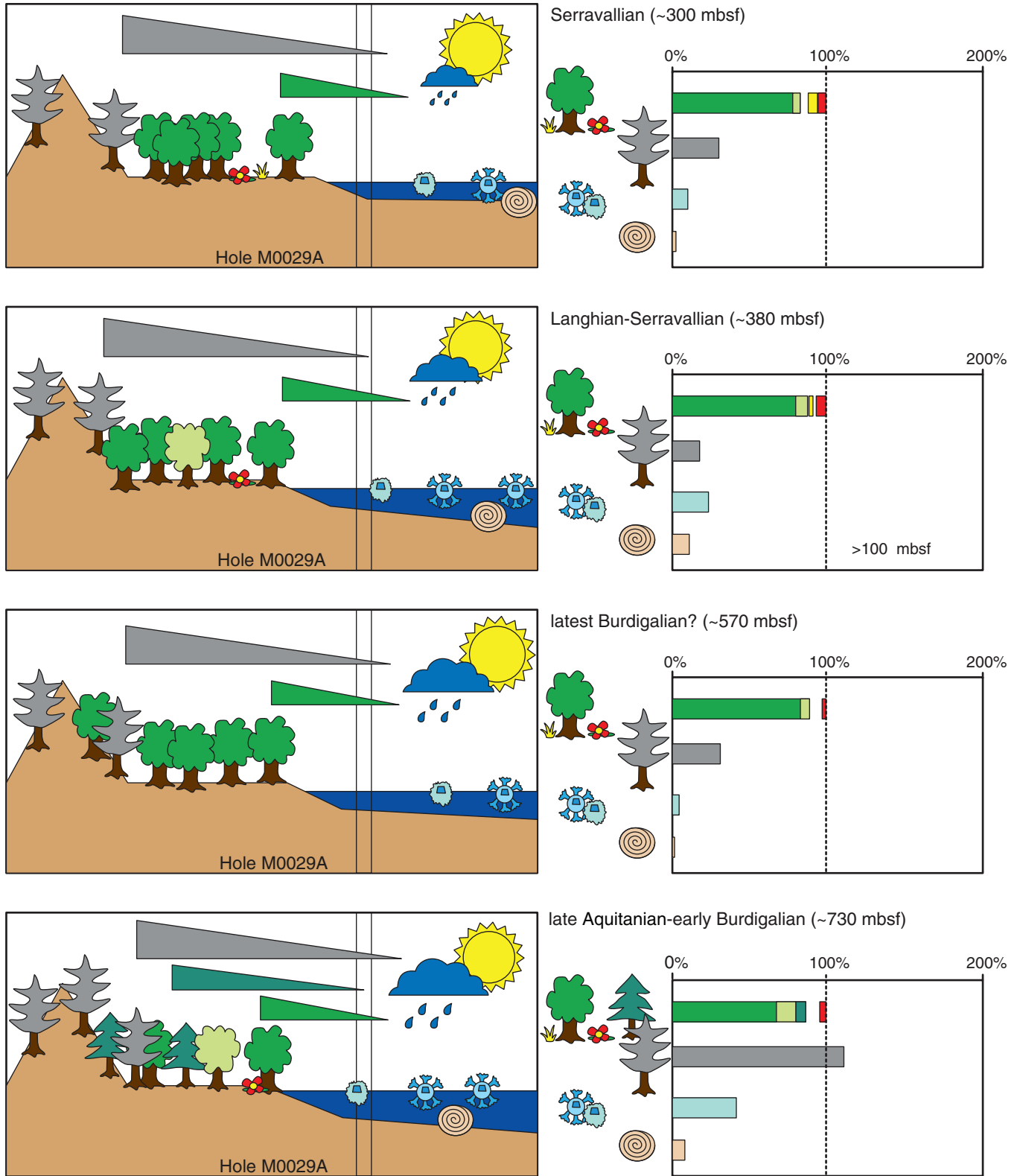
Figure F25. Composition-depth profiles of interstitial water, Hole M0029A. Vertical lines designate value calculated for present-day bottom seawater, which has a chloride concentration of ~524 mM. Horizontal color bands denote discrete freshwater (blue), salty (pink), and briny (yellow) layers of interstitial water.
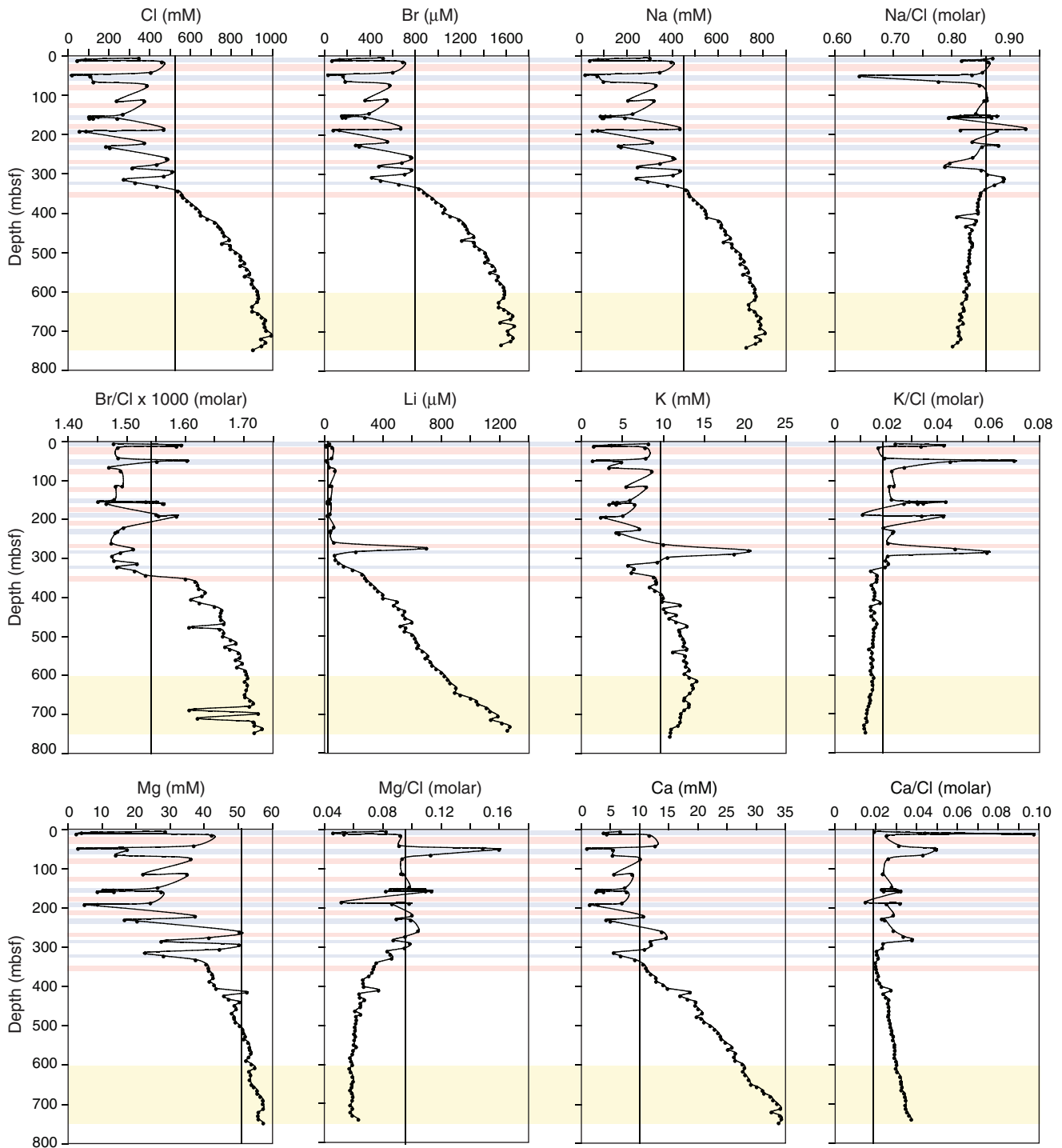
Figure F26. Composition-depth profiles of interstitial water, Hole M0029A. Vertical lines designate value calculated for present-day bottom seawater, which has a chloride concentration of ~524 mM. Horizontal color bands denote discrete freshwater (blue), salty (pink), and briny (yellow) layers of interstitial water.
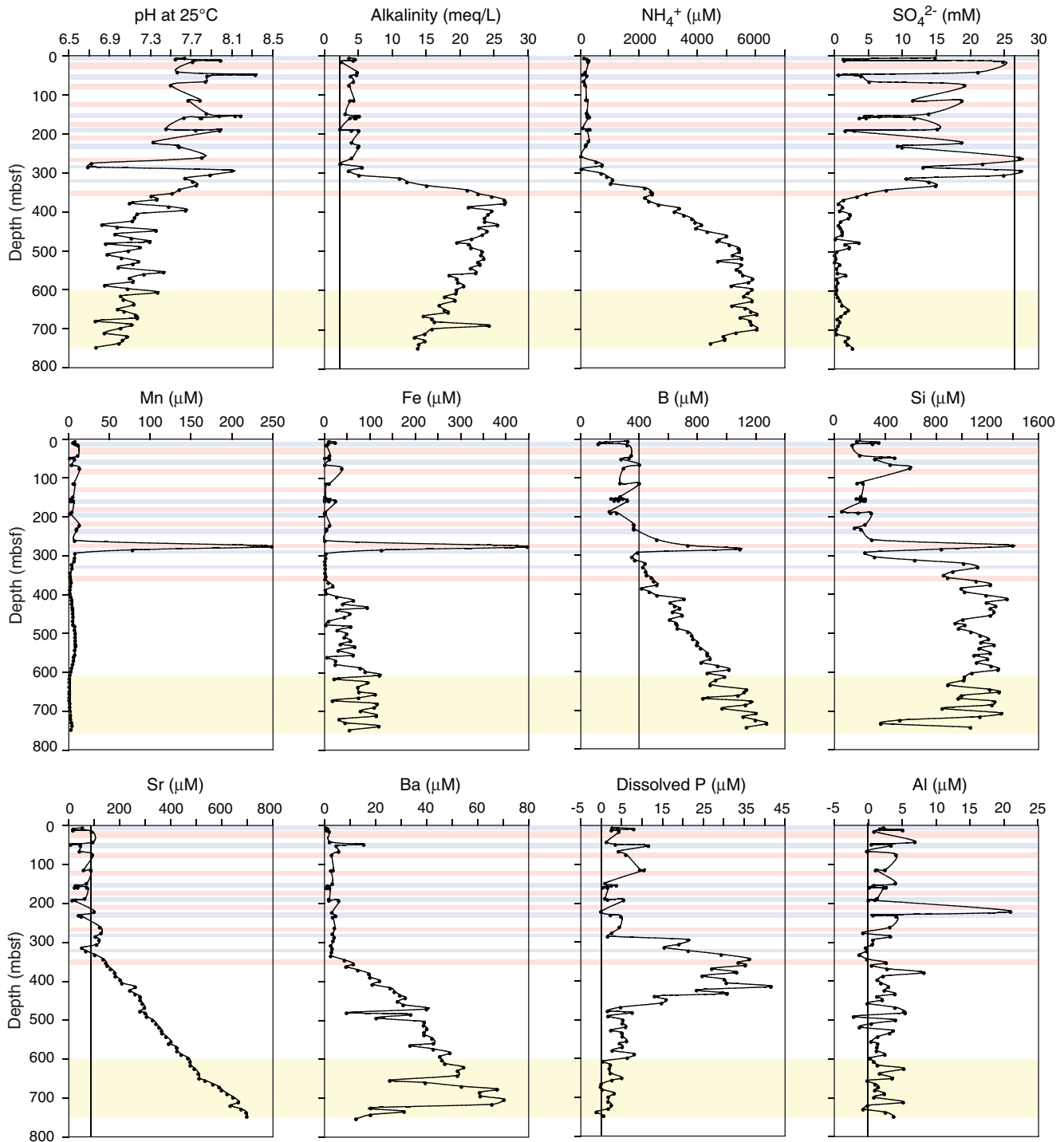
Figure F27. Composition-depth profiles of sediment chemistry and mineralogy compared with interstitial water chemistry, Hole M0029A. Upper row: total carbon (TC), total organic carbon (TOC), total inorganic (carbonate) carbon (TIC), and total sulfur (TS) concentrations in sediment. Lower row: sulfate/chloride and total phosphorus in interstitial water and concentrations of apatite and pyrite from XRD. Horizontal color bands denote discrete freshwater (blue), salty (pink), and briny (yellow) layers of interstitial water.
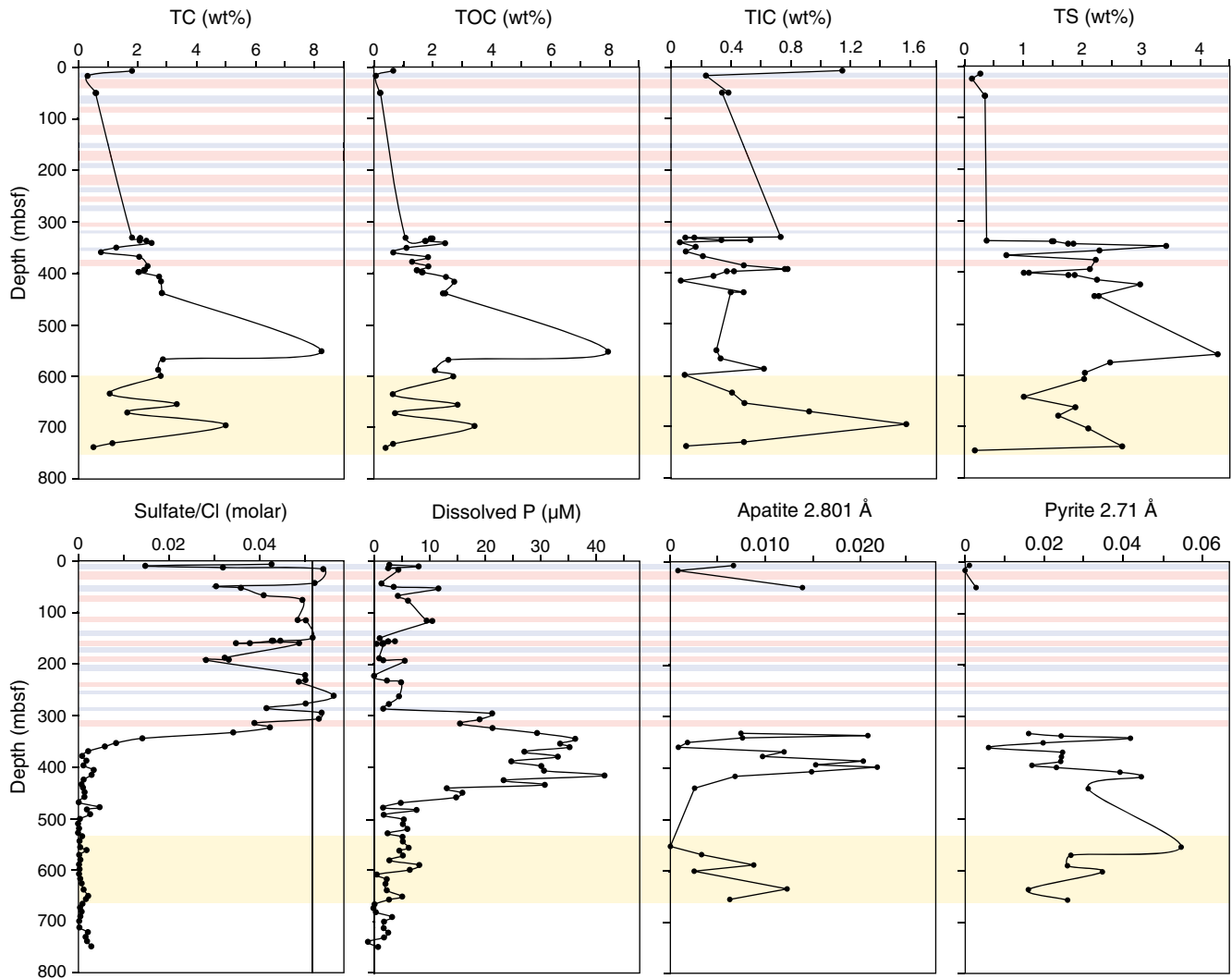
Figure F28. Composition-depth profiles of mineral content in sediment, Hole M0029A, as the ratio of intensity of the specified XRD peak(s) to total intensity of all peaks. Horizontal color bands denote discrete freshwater (blue), salty (pink), and briny (yellow) layers of interstitial water.
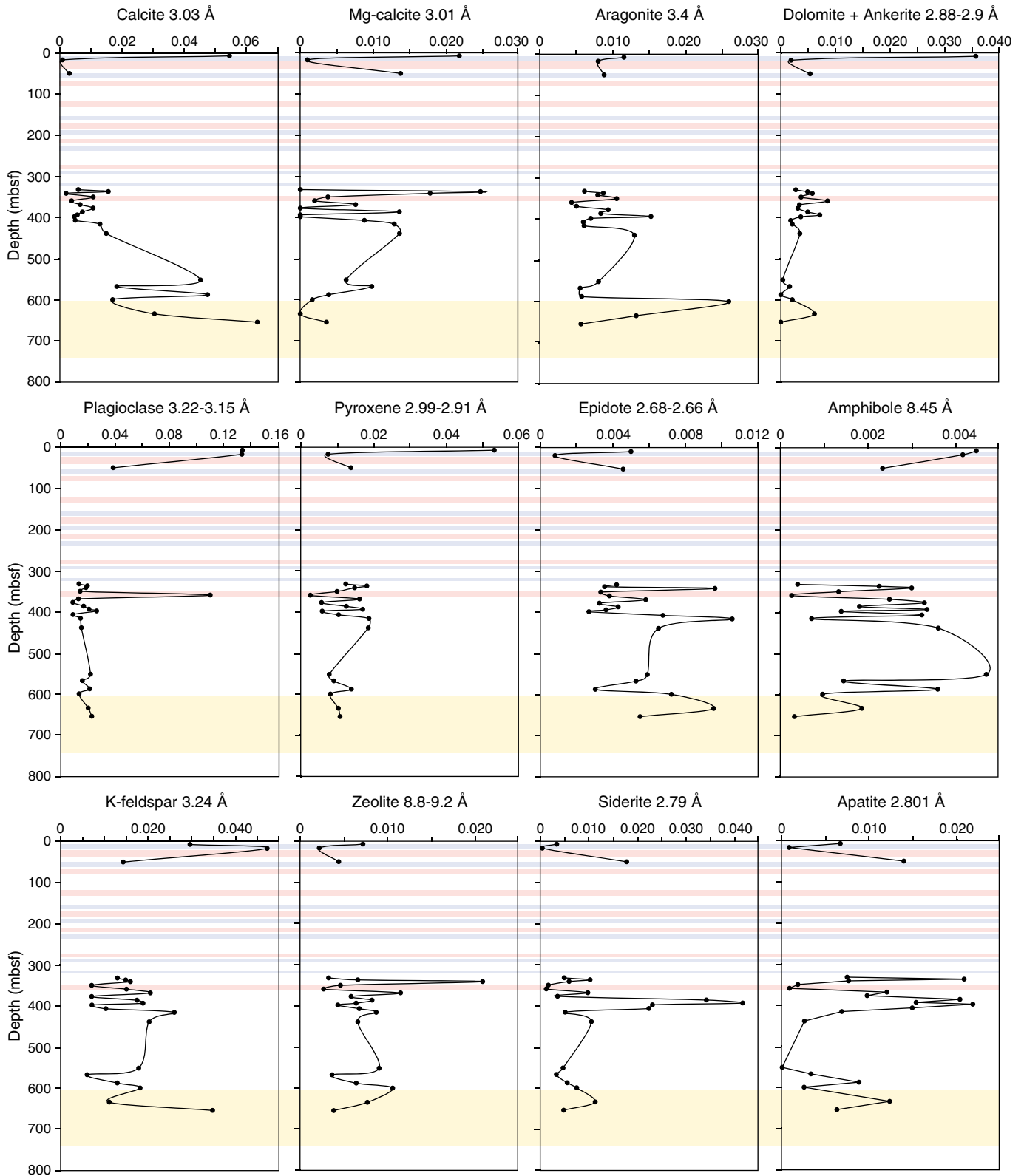
Figure F29. Composition-depth profiles of mineral content in sediment, Hole M0029A, as the ratio of intensity of the specified XRD peak(s) to total intensity of all peaks. Horizontal color bands denote discrete freshwater (blue), salty (pink), and briny (yellow) layers of interstitial water.
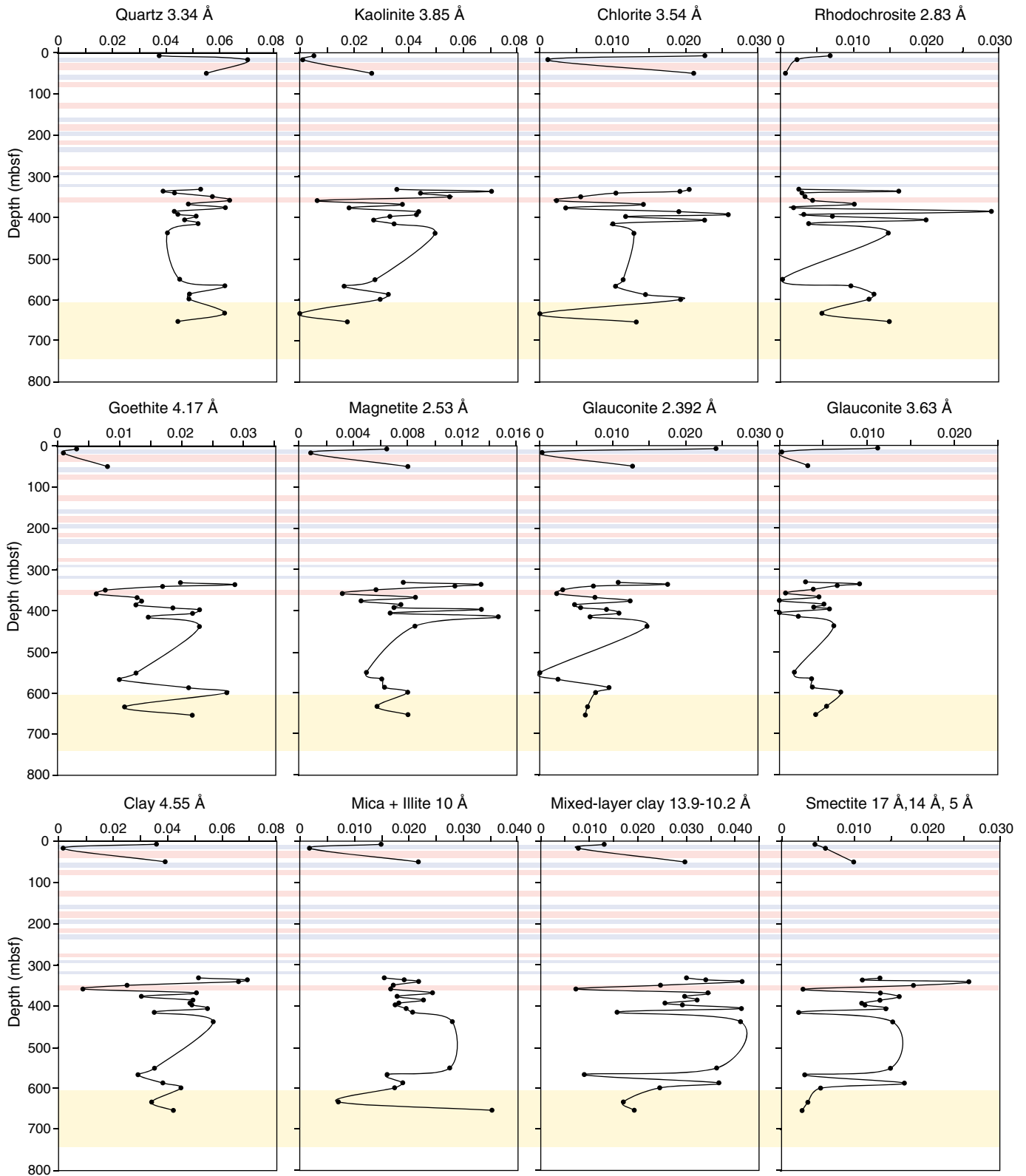
Figure F30. Overview of data acquired from multisensor core logger (MSCL) and sample measurements (in gray), Hole M0029A. From MSCL: natural gamma radiation (NGR), *P*-wave velocity, discrete *P*-wave, gamma density, magnetic susceptibility, noncontact electrical resistivity. From sample measurements: water content, wet bulk density, grain density, porosity, void ratio, and thermal conductivity.
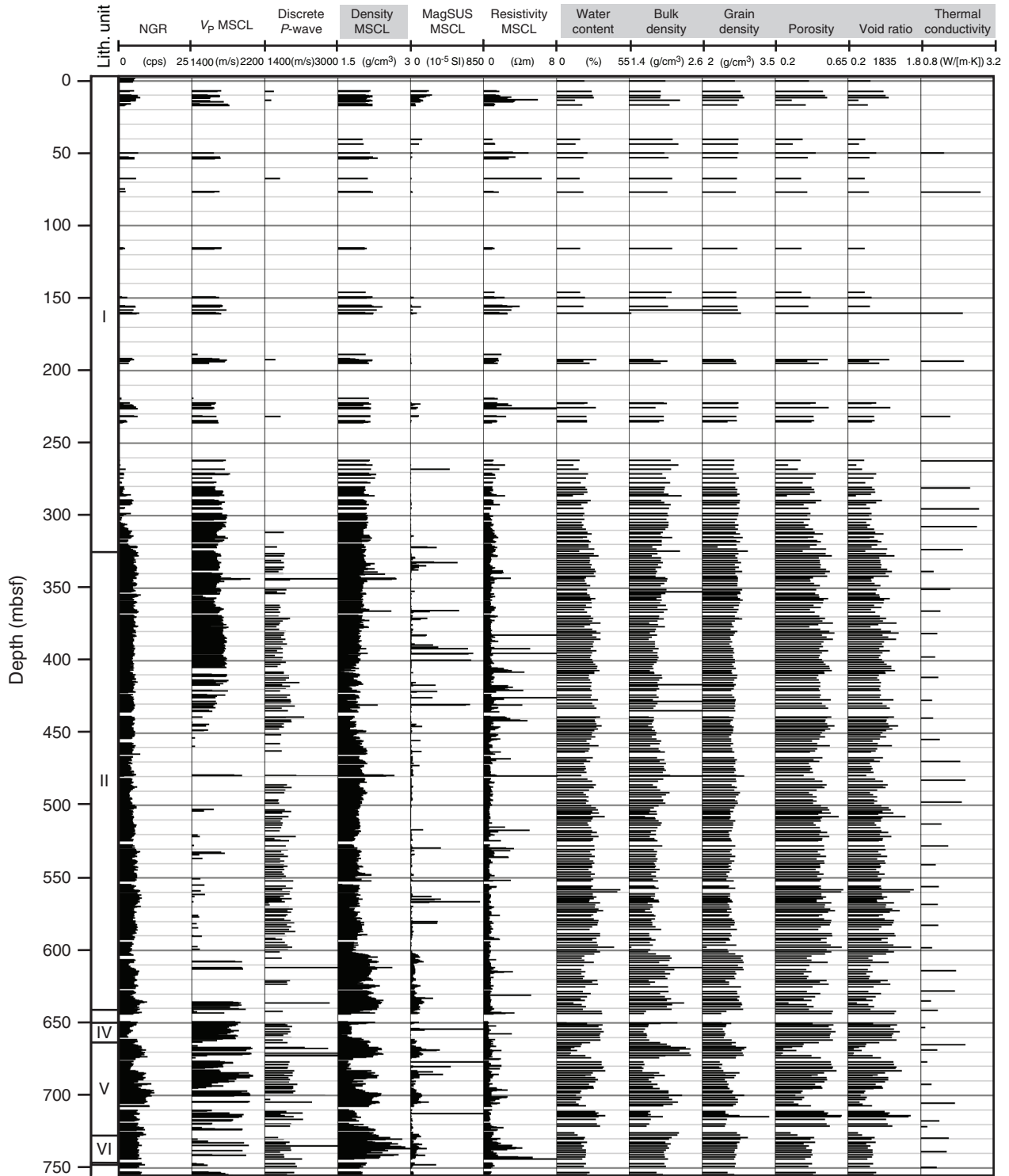
Figure F31. Gamma density, wet bulk density, porosity, and resistivity compared with lithology in Hole M0029A. **A.** Gamma density from the MSCL (black line) and wet bulk density from section samples (red crosses). **B.** Porosity from section samples (red crosses) and high-pass filtered porosity (black line). Mean porosity reduction of sands (blue line) and clay (green line) derived from global averages on different passive margins (Sclater and Christie, 1980; Bahr et al., 2001). **C.** Resistivity from the MSCL. Thin black line = unfiltered, red line = filtered (see text). Vertical black line at 1.3 Ωm = average clay-silt resistivity with low-chlorinity pore water. Note how porosity reduction in clay and silt-rich intervals follows reduction of global averages. See Figure **F4** in the "Methods" chapter for lithology legend.
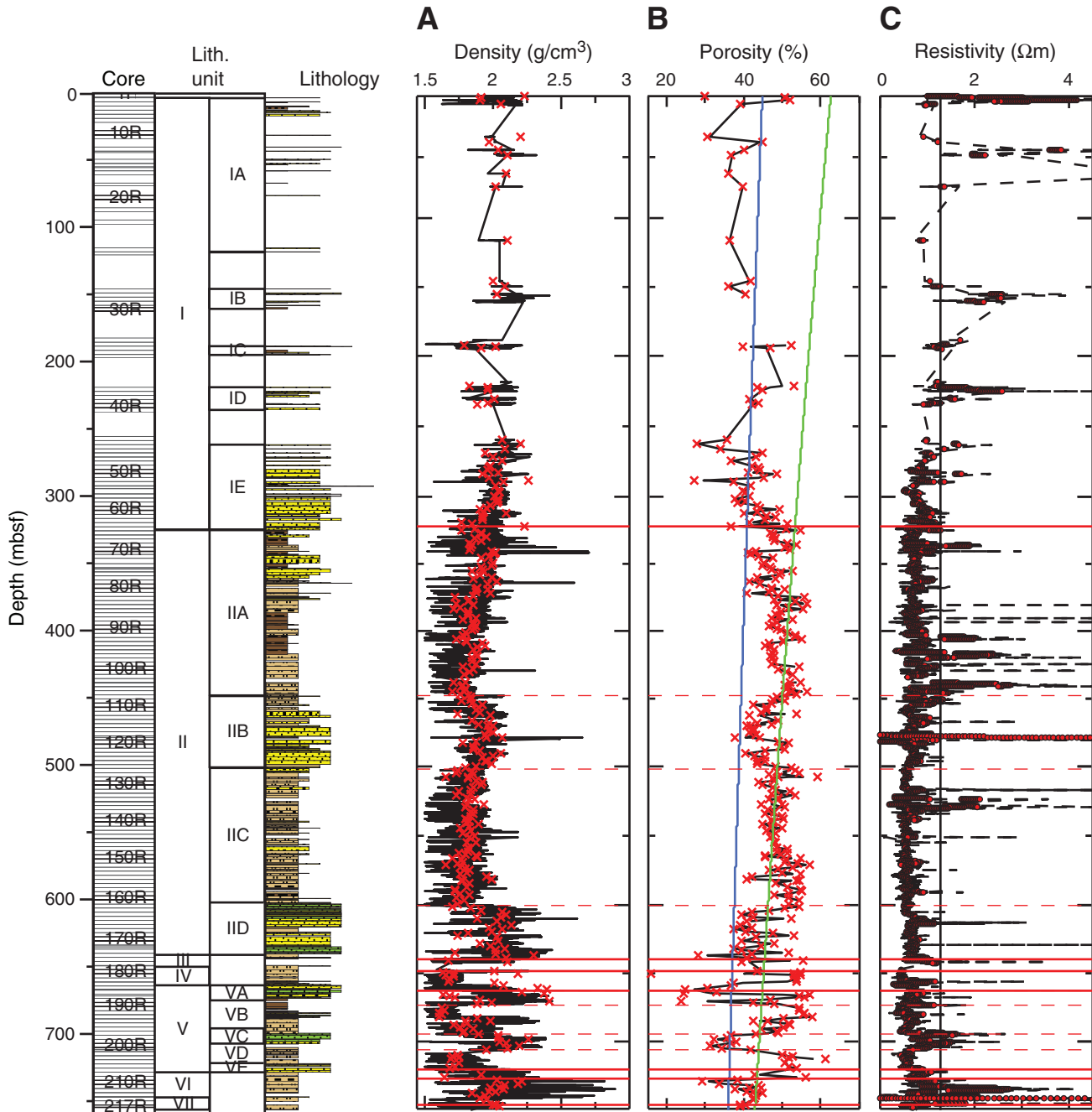
Figure F32. Cross-plot of gamma density and wet bulk density, Hole M0029A. Calculated wet bulk density from core samples is, in general, lower than gamma density. MSCL = multisensor core logger, GRA = gamma ray attenuation.
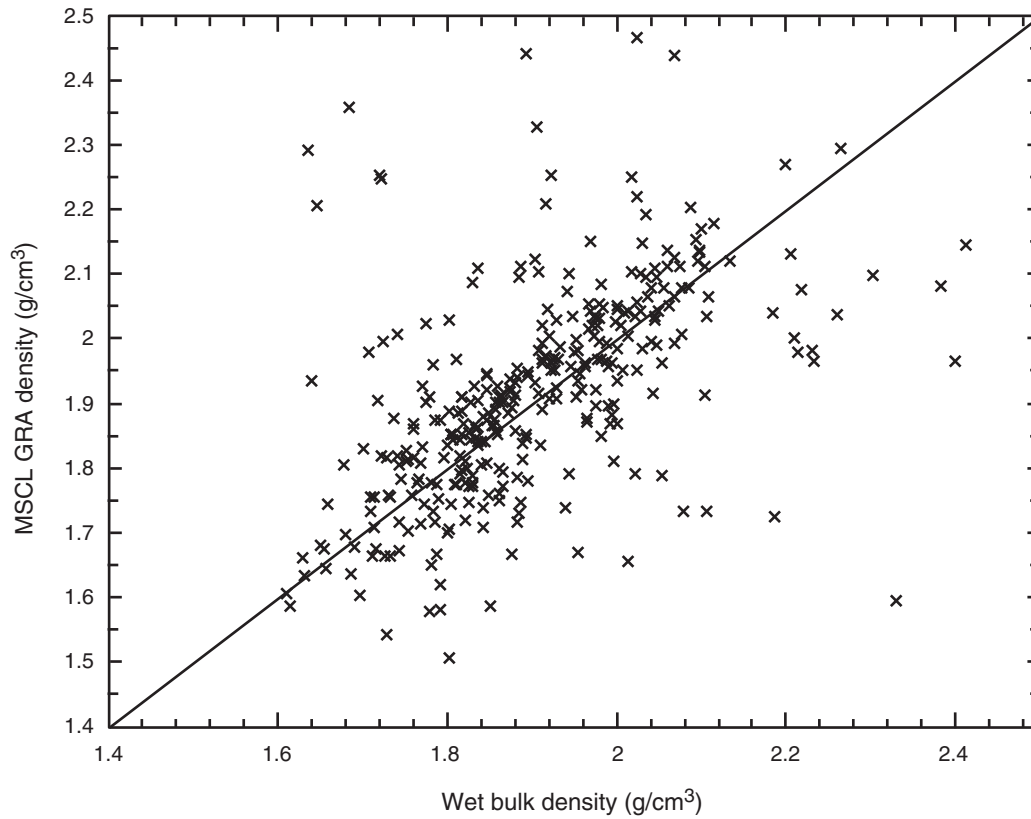
Figure F33. Cross-plot of wet bulk density and porosity from section samples, Hole M0029A. Diagonal line is mixing line between rock (zero porosity and density of 2.7 g/cm^3) and saltwater (100% porosity and density of 1.024 g/cm^3). Note how glauconite containing samples consistently falls to right of mixing line with greater density.
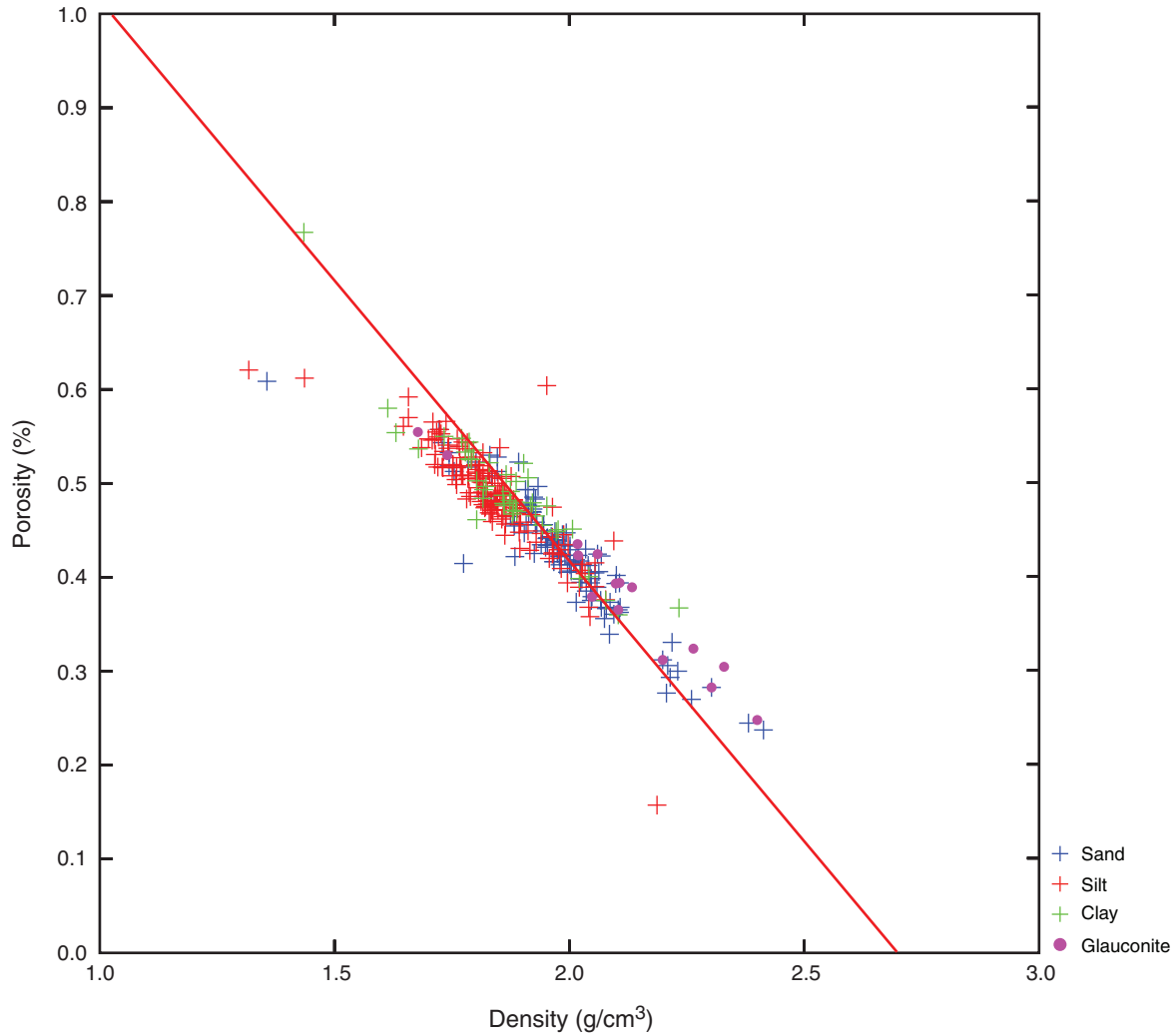
Figure F34. High-pass filtered density and porosity compared with lithology, Hole M0029A. Bulk wet density from samples (black line) overlain on filtered gamma density (thin black line) and original gamma density (gray). Note porosity (red line) increases to left. Overall packages with increasing density and decreasing porosity (diagonal arrows) have a tendency to end with a sharp decrease in density and increase in porosity (horizontal arrow). These sharp shifts to the left correspond to grain size decreases as determined from lithology and may represent flooding surfaces and/or sequence boundaries. Horizontal red lines = lithologic boundaries. See Figure **F4** in the "Methods" chapter for lithology legend. (**Figure shown on next page.**) (**Continued on next four pages.**)

Figure F34 (continued). A. 280–360 mbsf. (**Continued on next page.**)
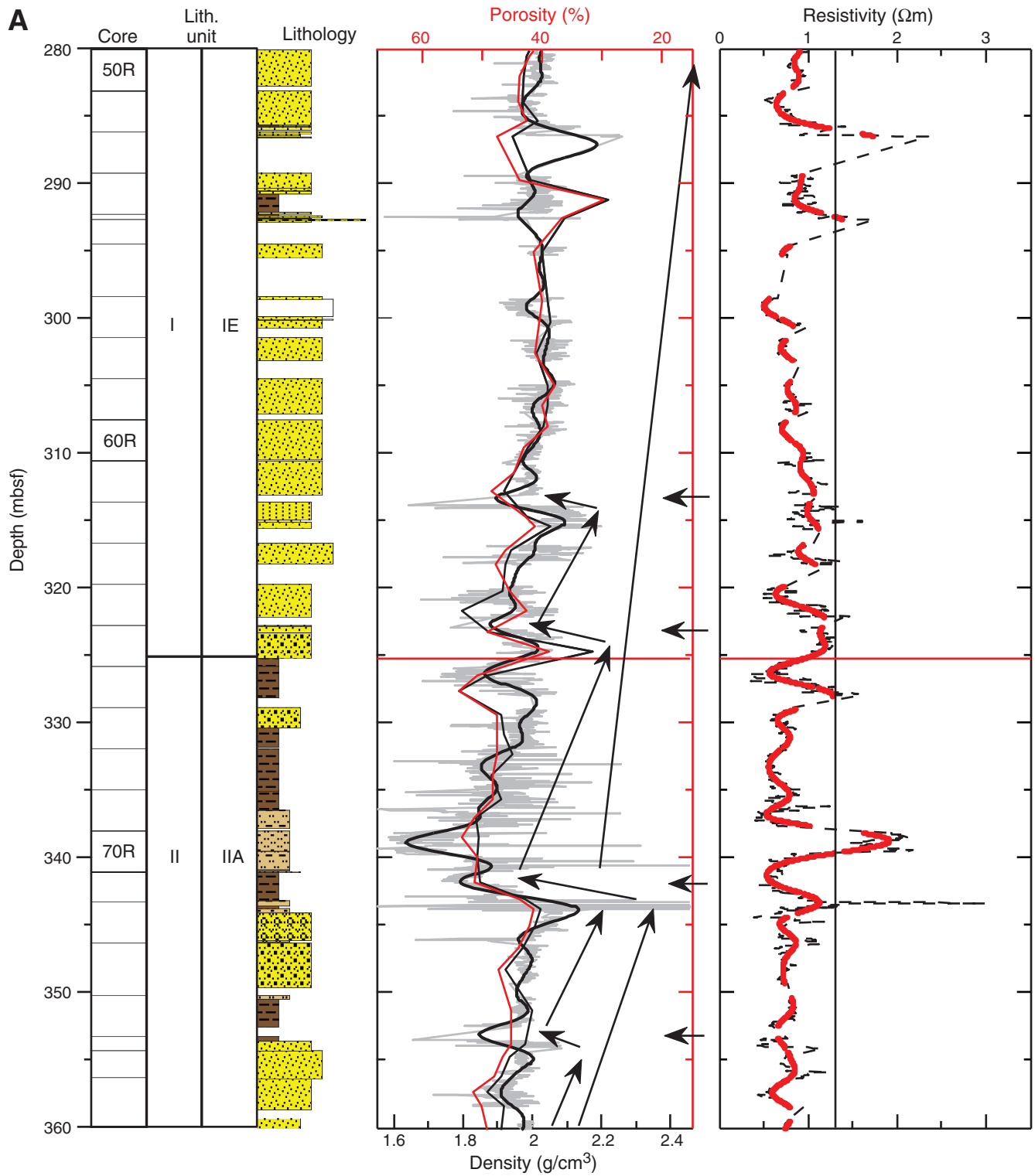
Figure F34 (continued). B. 335–500 mbsf. (**Continued on next page.**)
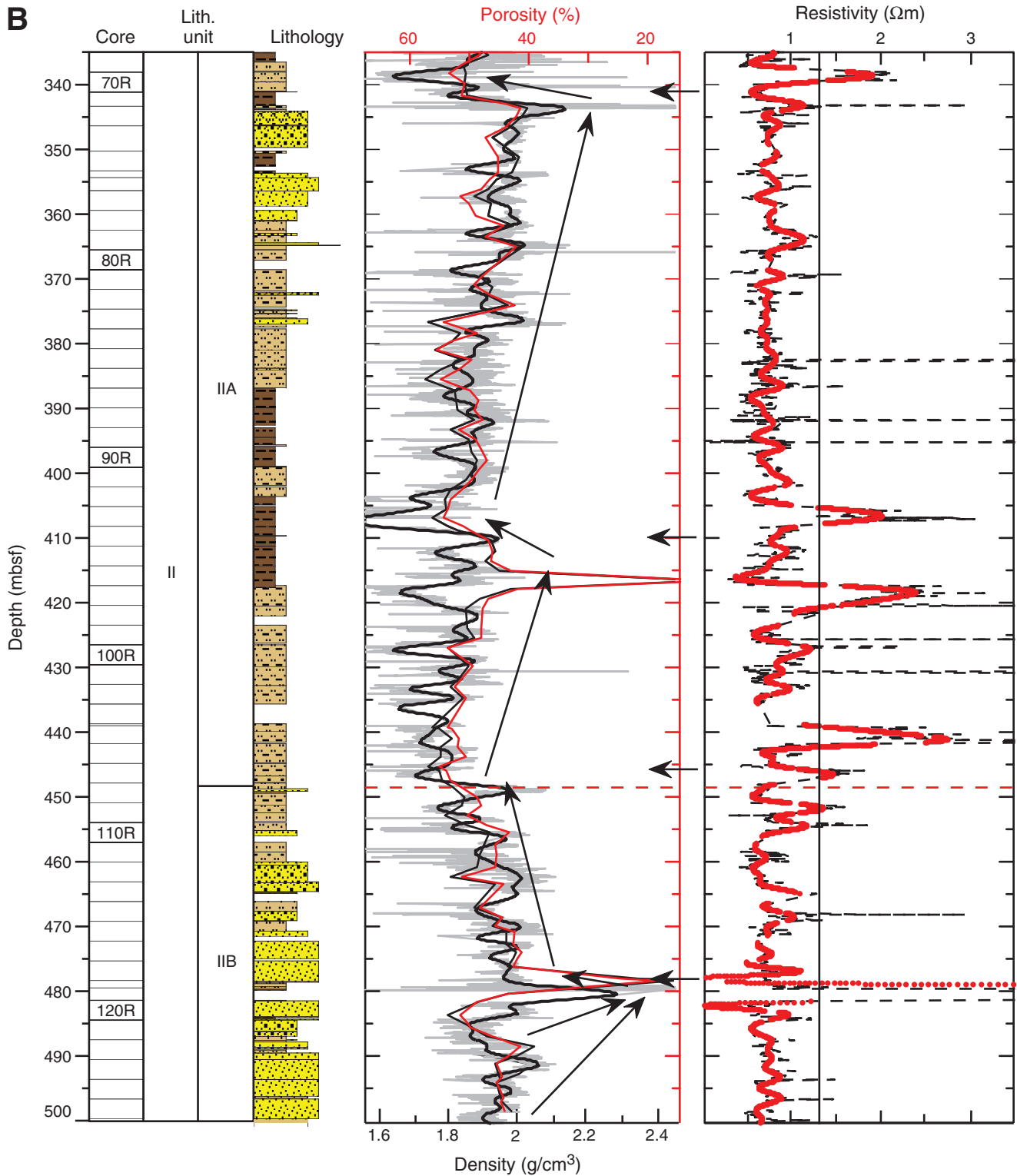
Figure F34 (continued). C. 470–610 mbsf. (**Continued on next page.**)
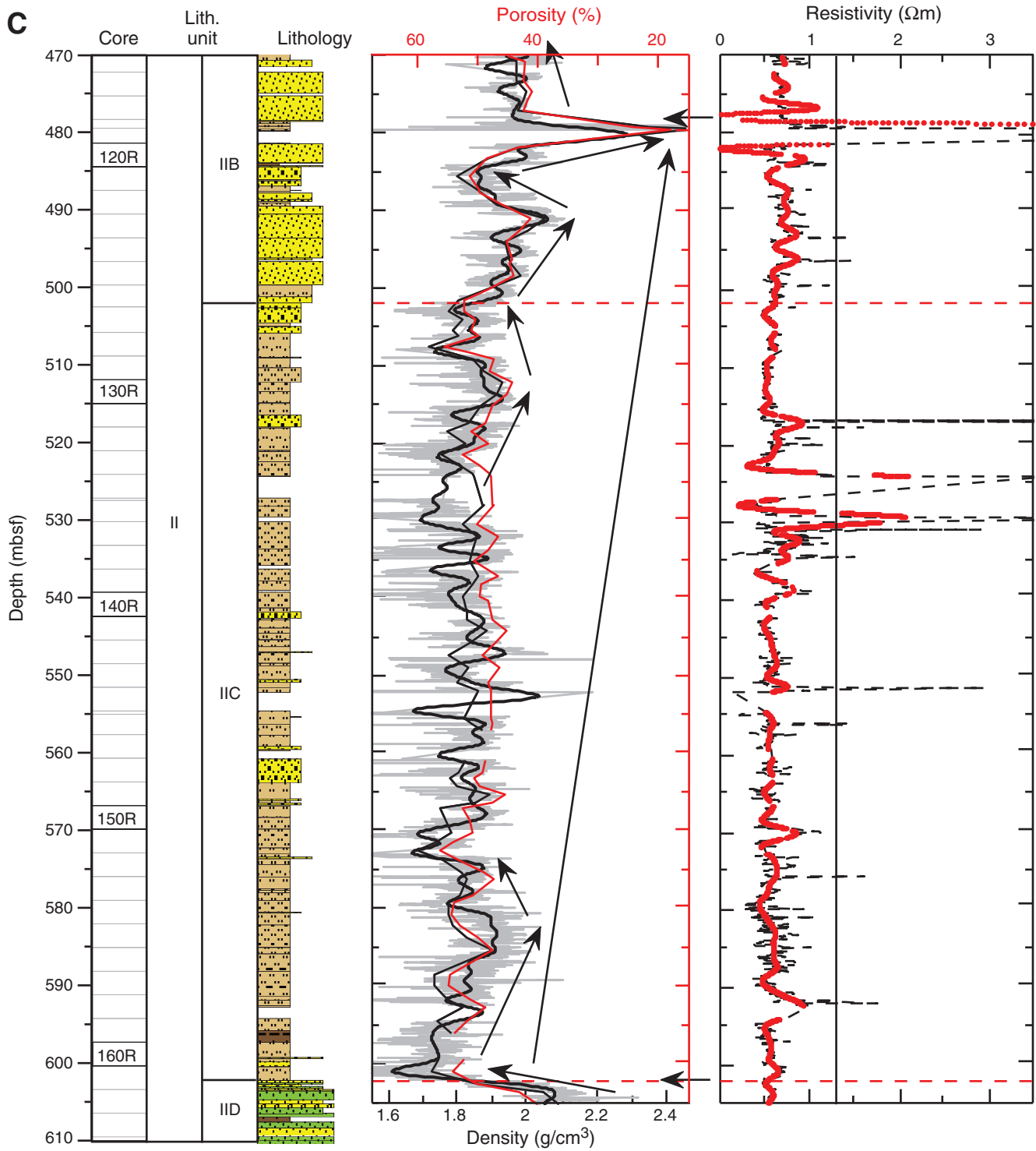
Figure F34 (continued). D. 585–785 mbsf.
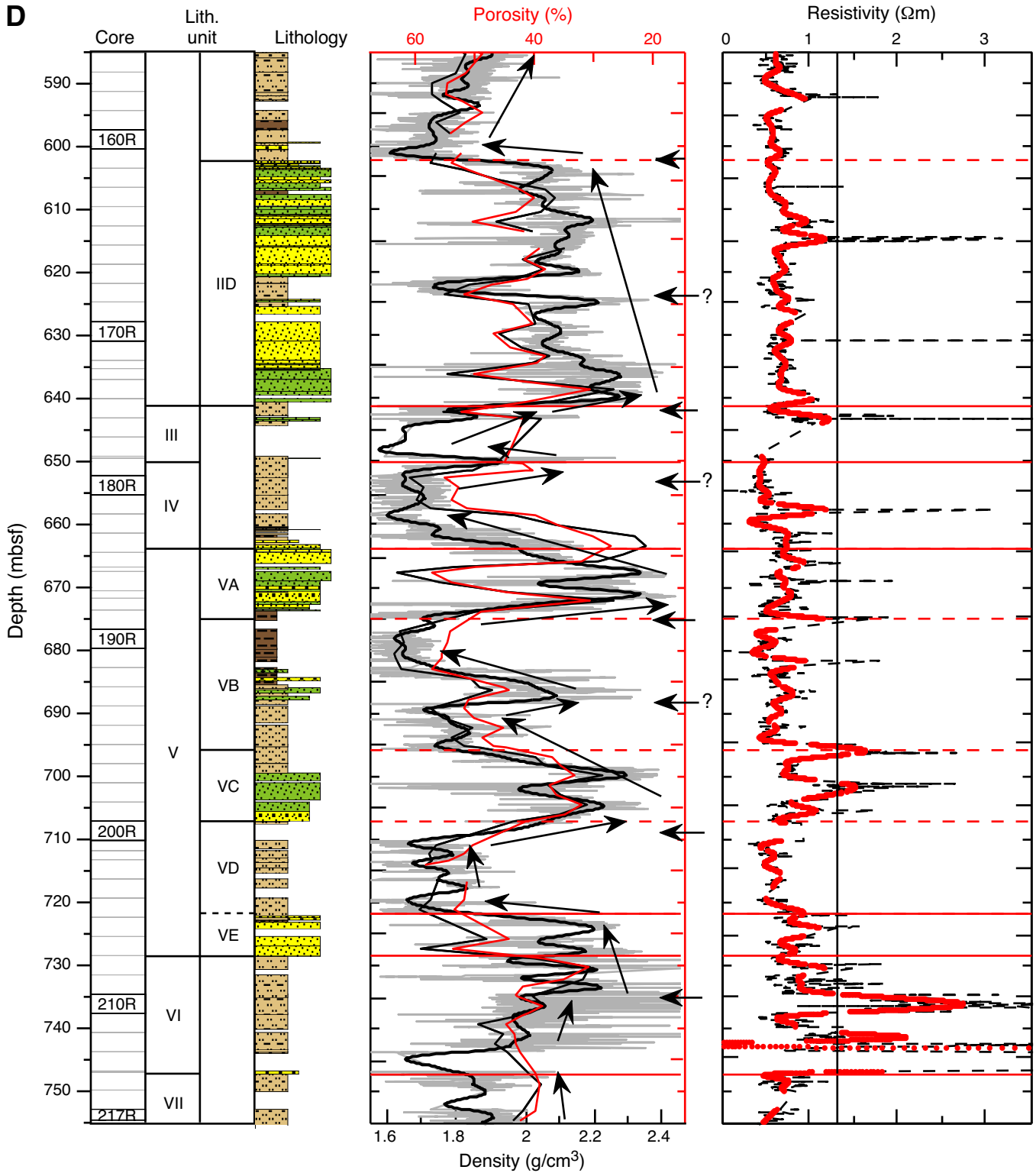
Figure F35. U/K and Th/K ratio on logarithmic scale vs. depth, Hole M0029A. Cemented levels, organic matter, and glauconite-rich levels observed by sedimentologists are indicated.
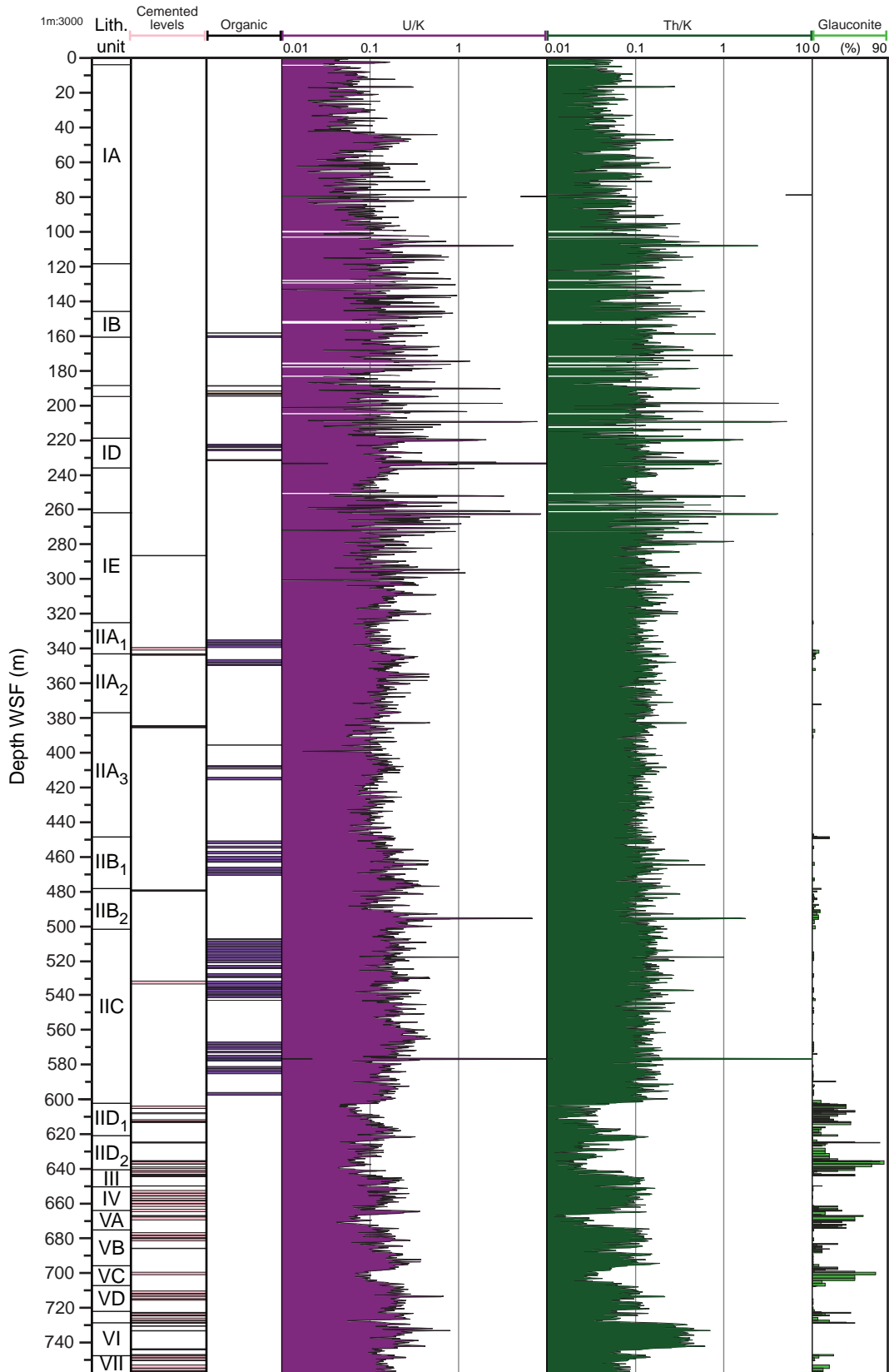
Figure F36. Petrophysical and downhole log data across the m5.3 boundary in Hole M0029A, together with MSCL gamma ray density and *P*-wave velocity. Normalized amplitude and traveltime acoustic images (ABI40 ampl and ABI40 TT), hole diameter (AcCal), total gamma ray through pipe (ASGRcgs), downhole magnetic susceptibility (EM51), whole core natural gamma radiation (NGR), and magnetic susceptibility (MagSus MSCL). A composite of line scan images is shown alongside core depth and whole core measurement have been shifted down by 0.40 m to match the wireline depth.
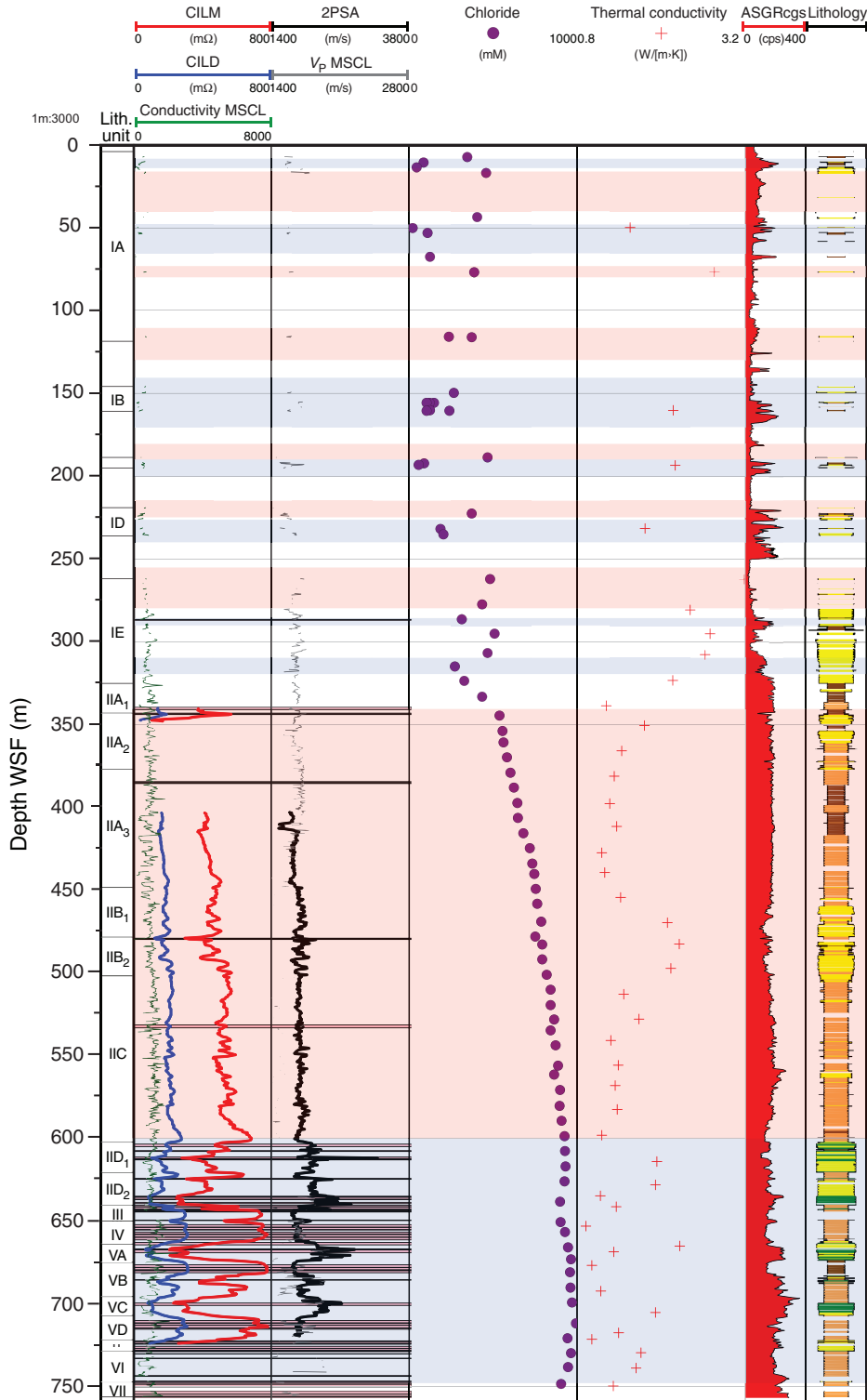
Figure F37. Inclination and magnetic moment data for Hole M0029A for initial NRM (black) and after 15 and 30 mT alternating field demagnetization (blue and red, respectively). MSCL magnetic susceptibility (MS) is also shown for reference.
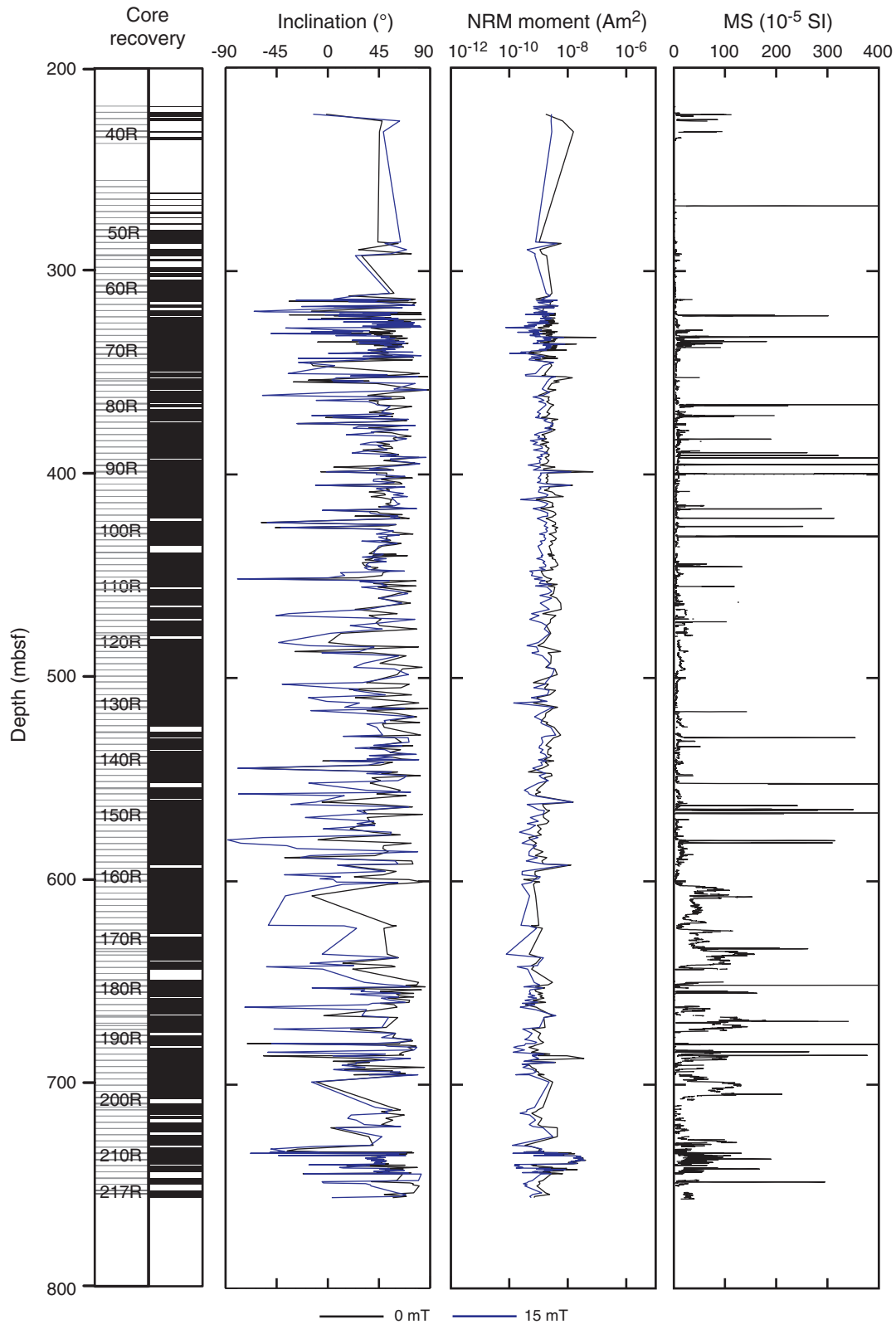
Figure F38. Preliminary magnetostratigraphic interpretation, Cores 313-M0029A-61R through 73R. Inclination data of initial NRM (black) and at 15 mT (blue). Magnetic polarity timescale from Cande and Kent (1995). Solid lines = preliminary tie points.
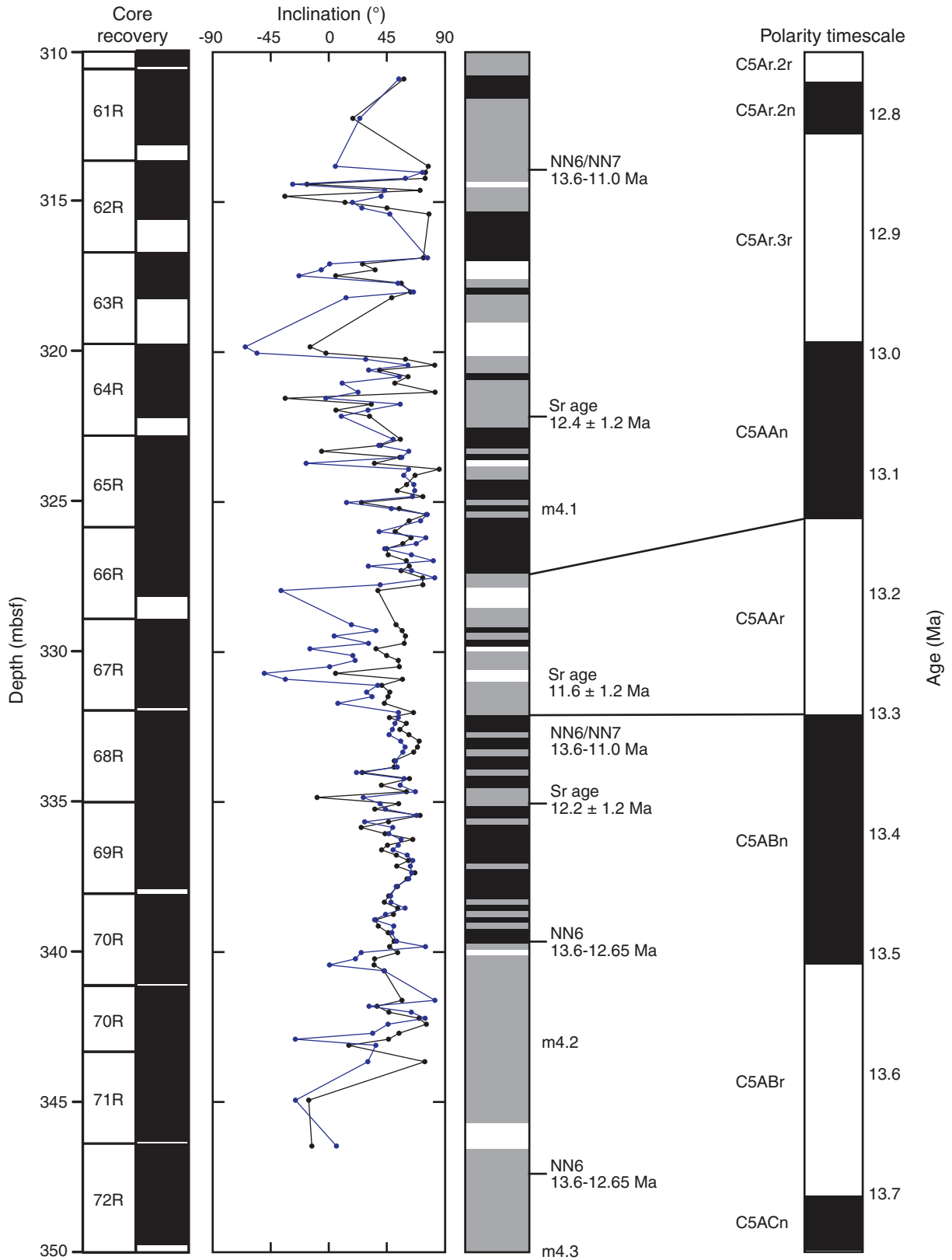
Figure F39. Preliminary magnetostratigraphic interpretation for Cores 313-M0029A-208R through 217R. Inclination data of the initial NRM (black) and at 15 mT (blue). Magnetic polarity timescale from Cande and Kent (1995). Solid lines = preliminary tie points.
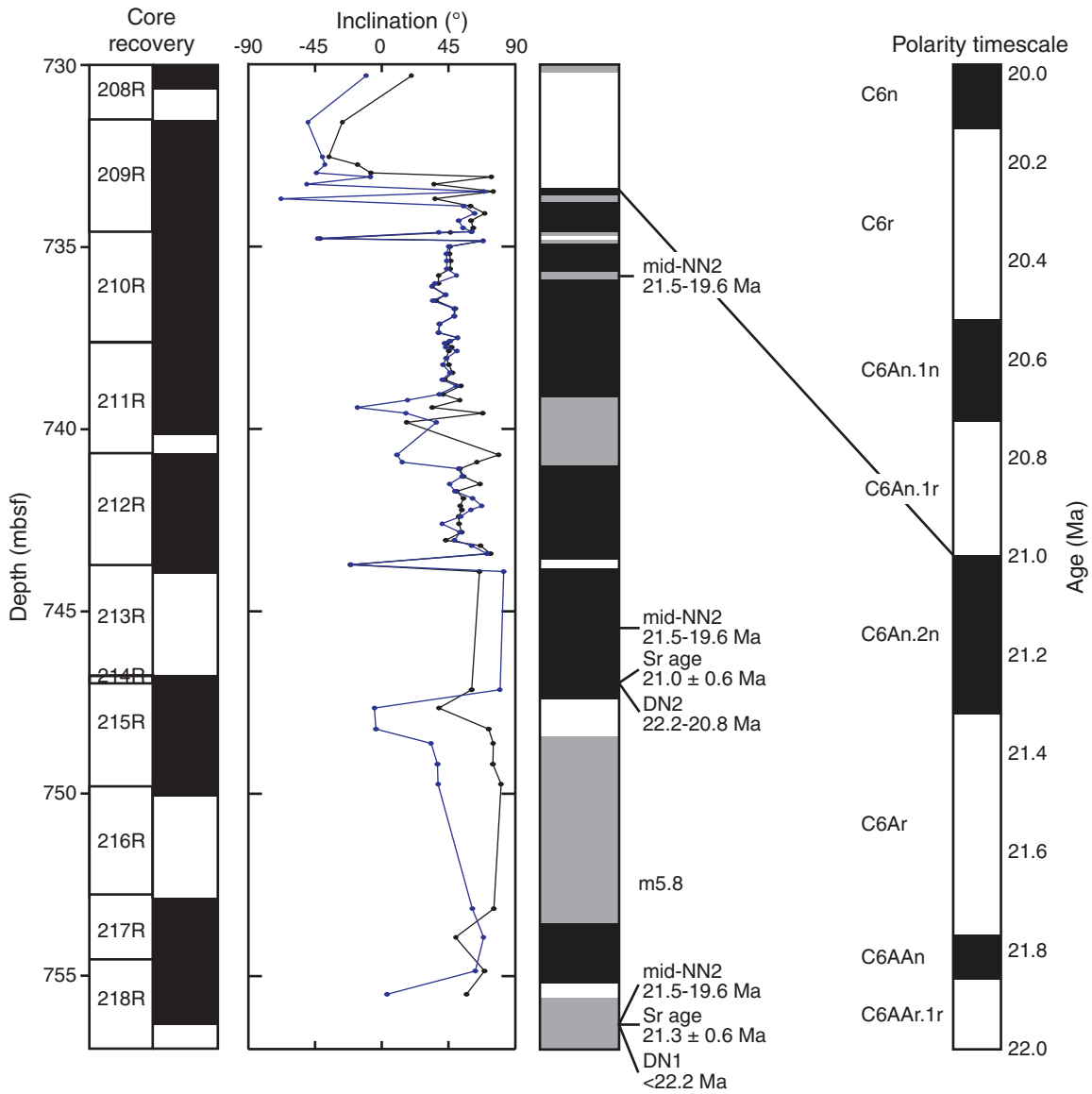
Figure F40. Preliminary magnetostratigraphic interpretation, Cores 313-M0029A-74R through 160R. Inclination data of initial NRM (black) and at 15 mT (blue). Magnetic polarity timescale from Cande and Kent (1995). Solid lines = tie points for tentative interpretations of reversal boundaries.
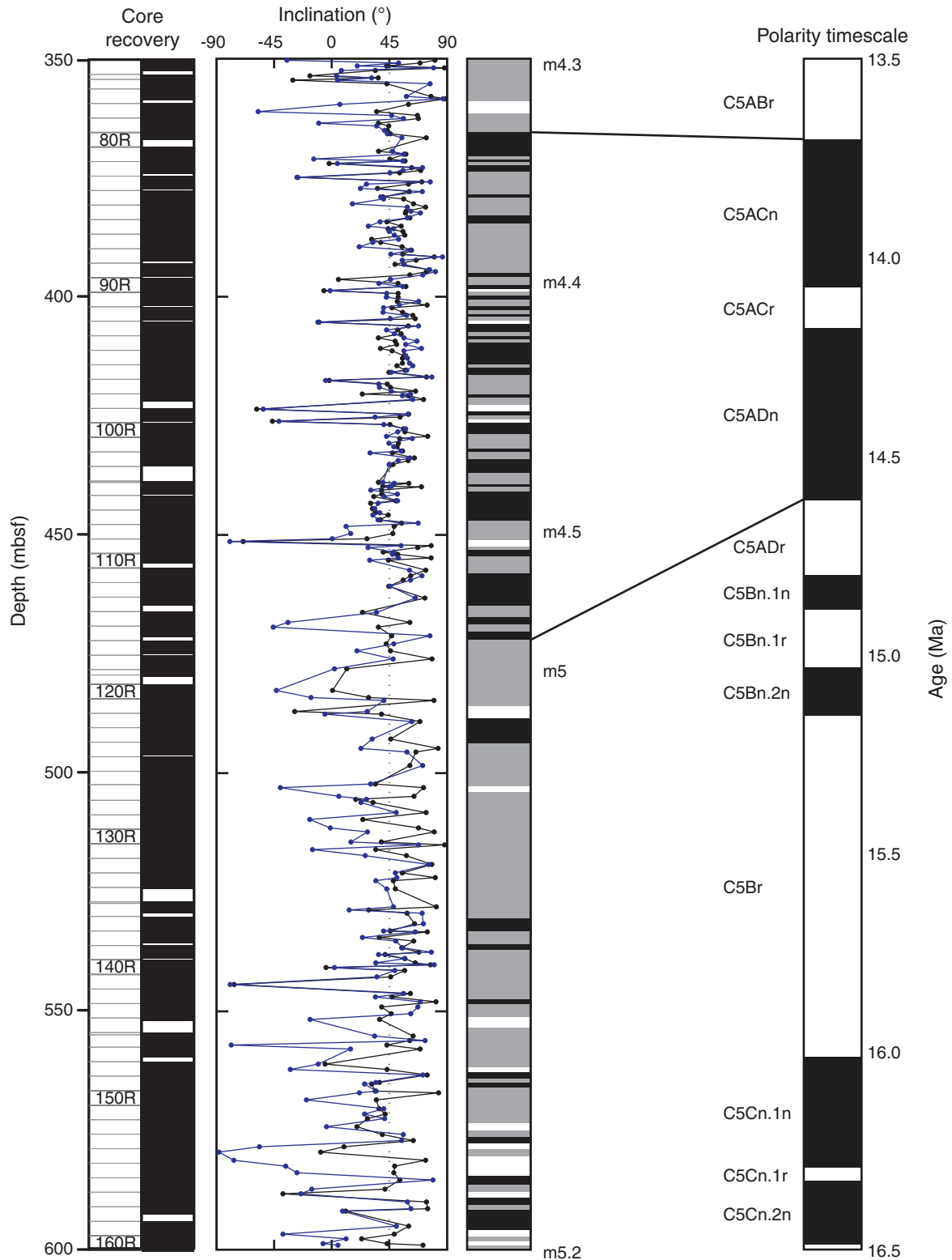
Figure F41. Composite of downhole logging data, Hole M0029A. Normalized amplitude and traveltime acoustic images (ABI40 ampl and ABI40 TT), hole diameter (AcCal), total and spectral gamma ray through pipe (AGSRcgs), conductivity (DIL45), *P*-wave sonic (2PSA), and magnetic susceptibility (EM51). See Figure F4 in the "Methods" chapter for lithology legend.
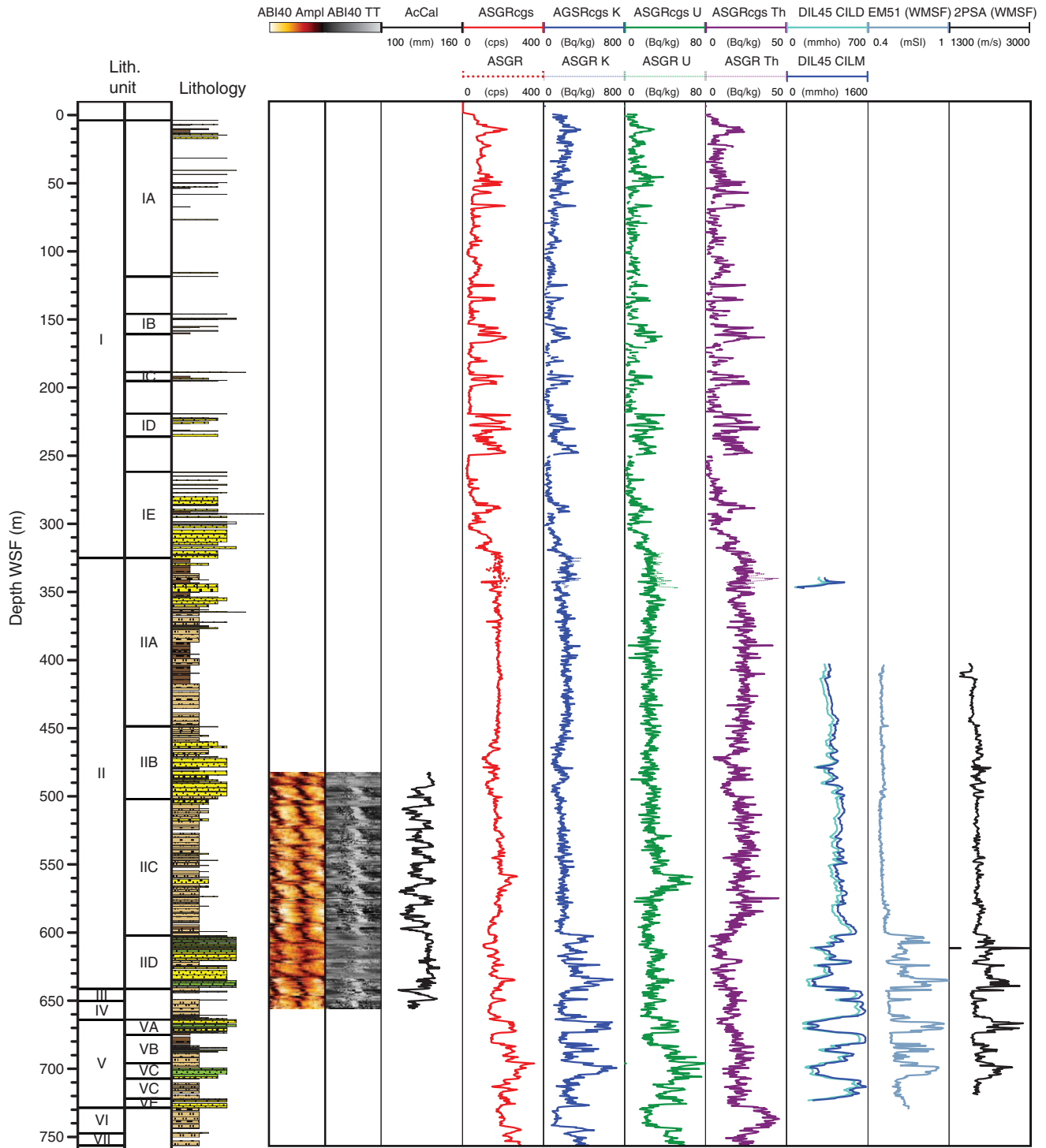
Figure F42. Total gamma ray (AGSRcgs; red curve) and Th/K ratio (green curve; logarithmic scale) with tentative lithological interpretation in the upper part of Hole M0029A (poor recovery).
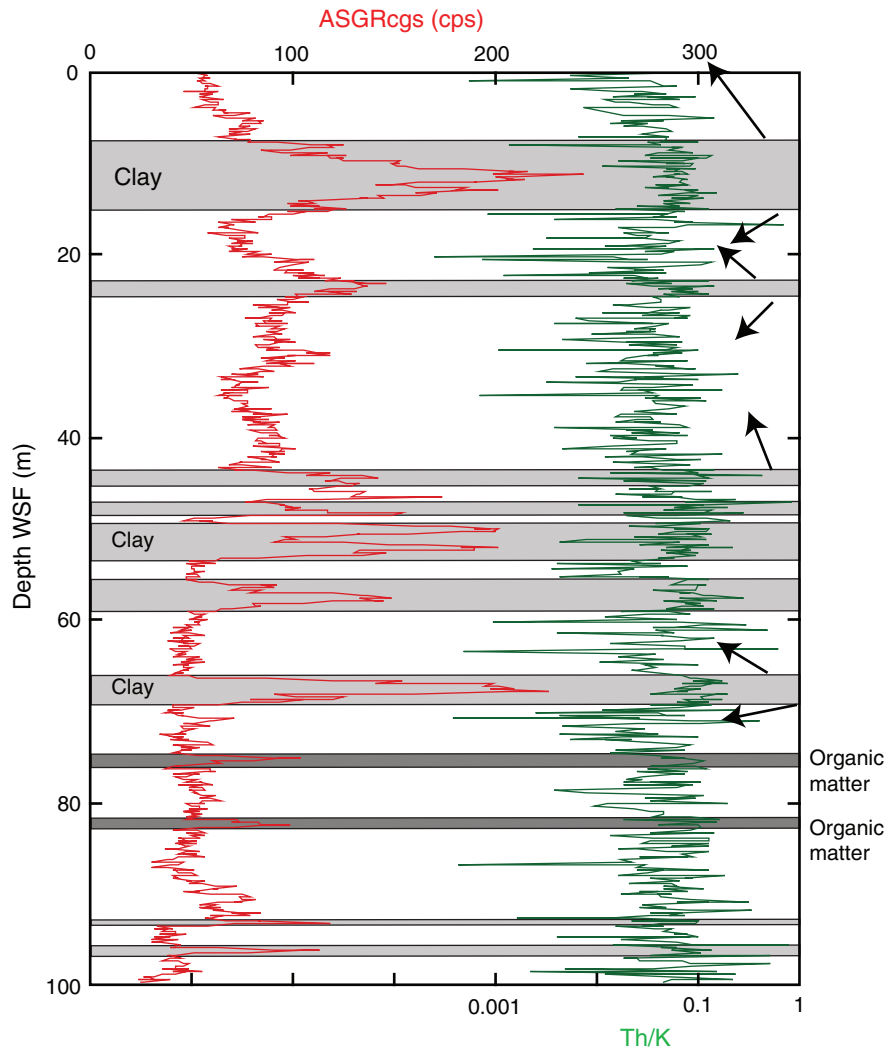
Figure F43. Composite of petrophysical and downhole logging data between 596 and 626 m WSF, Hole M0029A, to show two key surfaces (yellow lines) identified from the petrophysical data, both corresponding to a subunit boundary and the upper to the m5.2 surface. Normalized amplitude and traveltime acoustic images (ABI40 Ampl and ABI40 TT), hole diameter (AcCal), total gamma ray through pipe (AGSRcgs), Th/K ratio (from ASGR), conductivity (DIL45), magnetic susceptibility (EM51 and multisensor core logger [MSCL]), and *P*-wave (2PSA) in m WSF. Density and P-wave (MSCL), P-wave discrete, and resistivity from MSCL measurements on cores are in mbsf. See Figure **F4** in the "Methods" chapter for lithology legend.
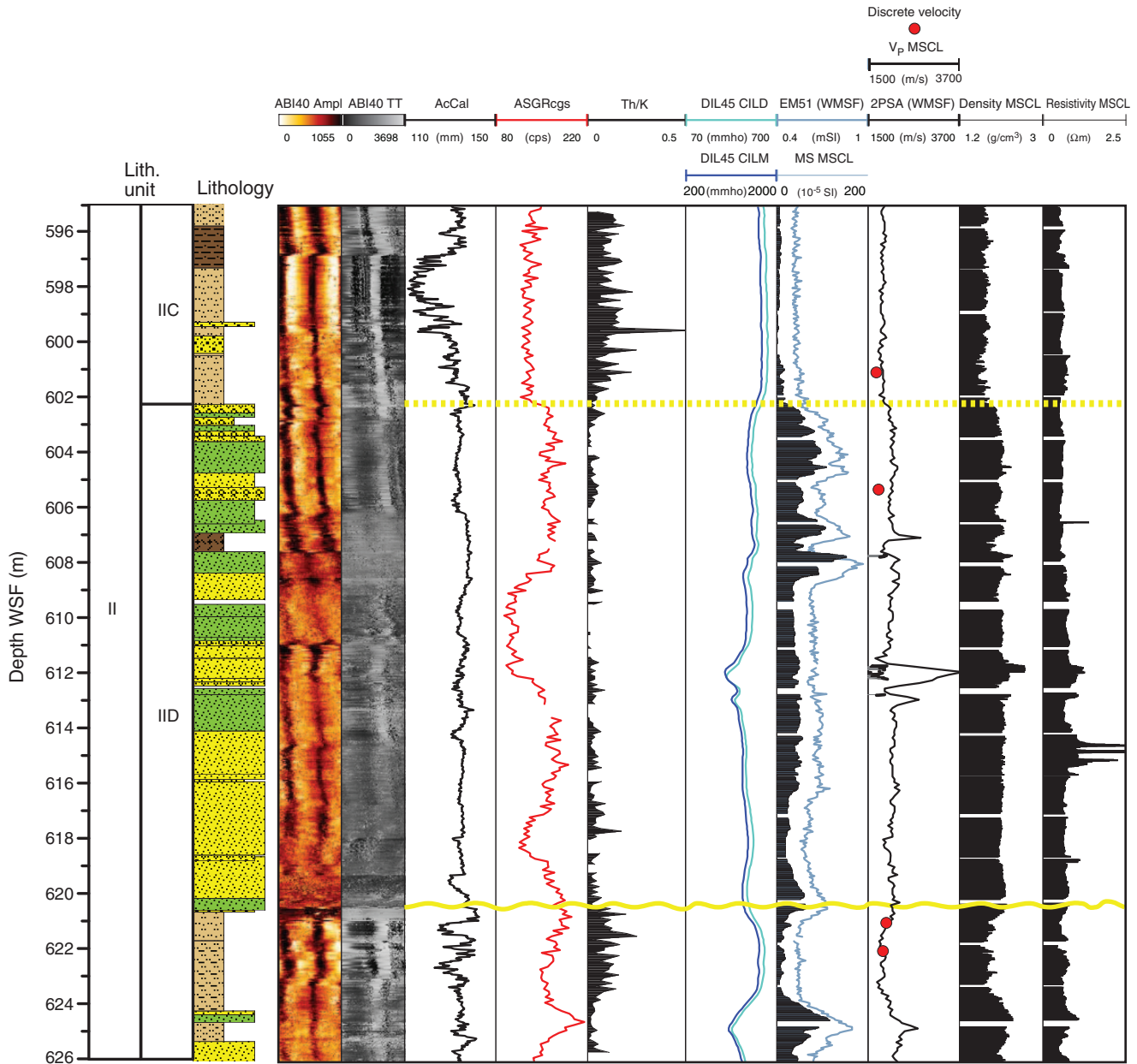
Figure F44. Detailed composite of selected downhole log data, petrophysical measurements, and derived calculations, Hole M0028A; normalized amplitude acoustic image (ABI40 ampl); acoustic caliper (ACCAL); total gamma ray through pipe (ASGRcgs) and on cores (NGR core); potassium, uranium, and thorium contents (ASGRcgs K, U, and Th, respectively); U-Th/3 ratios; clay volume estimate; magnetic susceptibility from cores (MagSus MSCL) and downhole logging (EM51); P-wave velocities on core (V_P MSCL) and from log (V_P 2PSA); density from whole core (density MSCL) and filtered signal; porosity from discrete measurements (porosity) and filtered signal; and impedance calculated from MSCL P-wave data (impedance MSCL) and sonic P-wave log (impedance 2PSA). Stratigraphic surfaces are added to the left (SB = sequence boundary, FS = flooding surface, HFS = maximum flooding surface, TS = transgressive surface). Petrophysical boundaries are drawn in pink. See text for discussion and Table T11 for boundary descriptions. See Figure F4 in the "Methods" chapter for lithology legend. **A.** 740–760 m WSF. (**Continued on next seven pages.**)
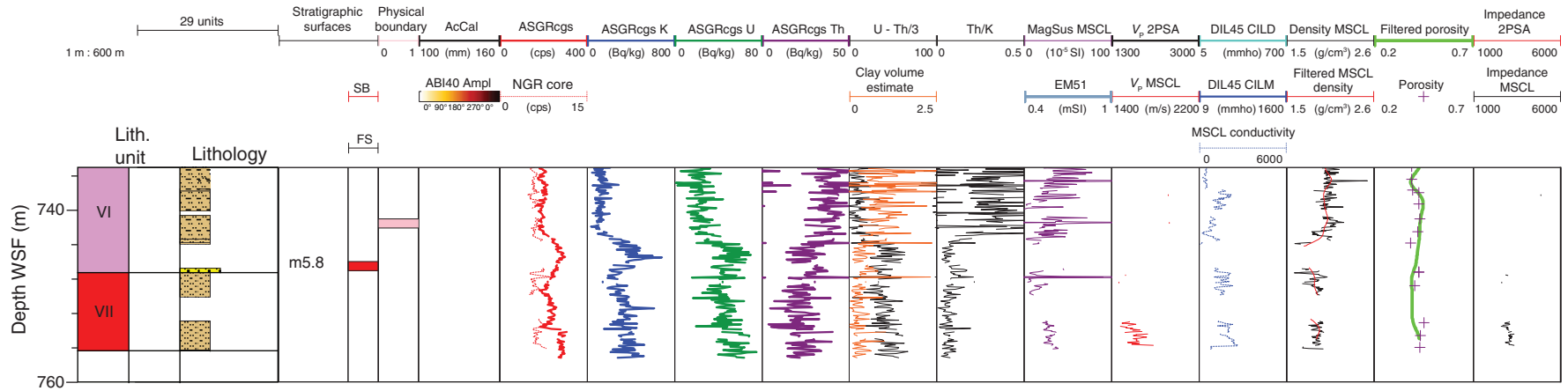
Figure F44 (continued). B. 640–720 m WSF. (**Continued on next page.**)
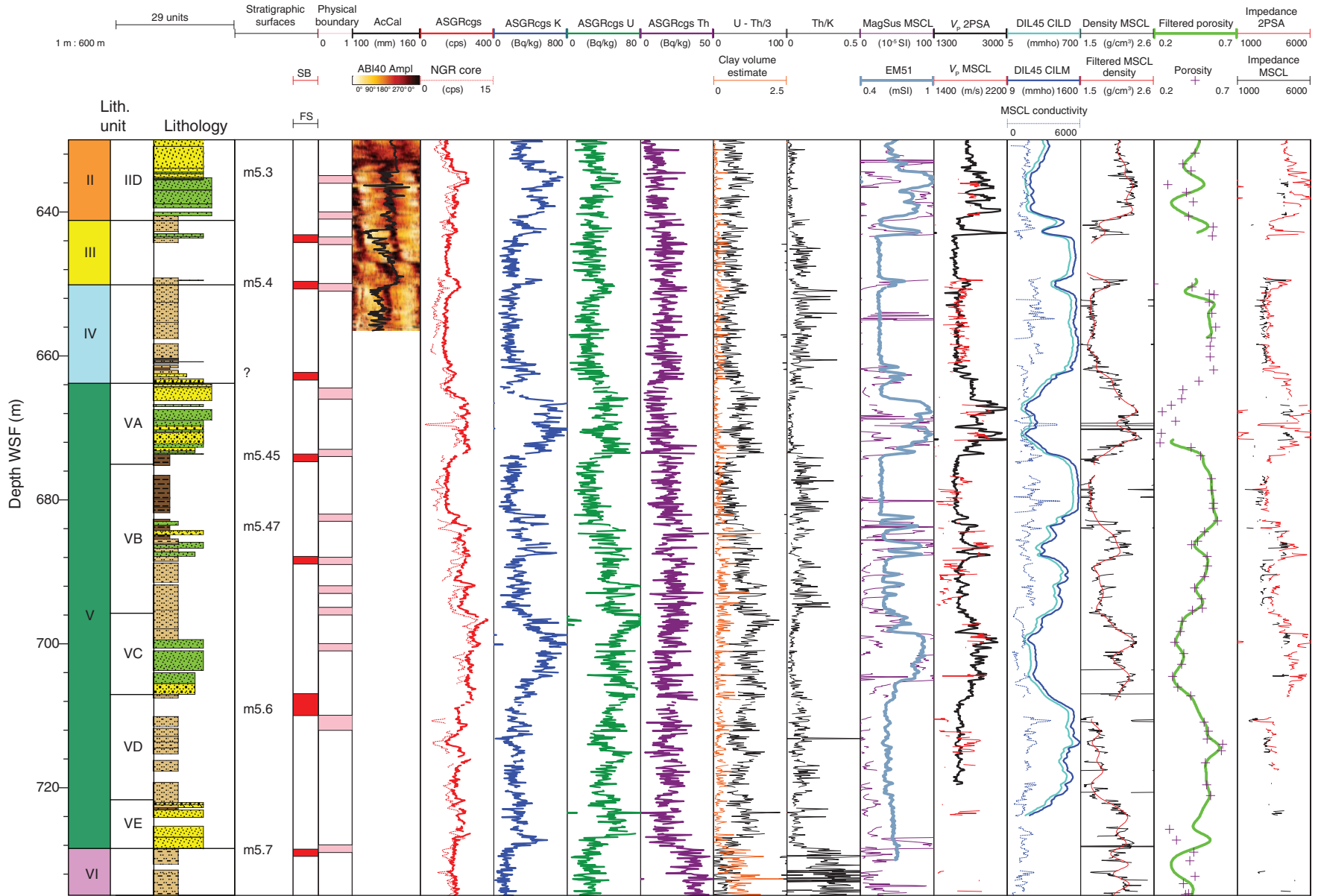
Figure F44 (continued). C. 540–620 m WSF. (Continued on next page.)
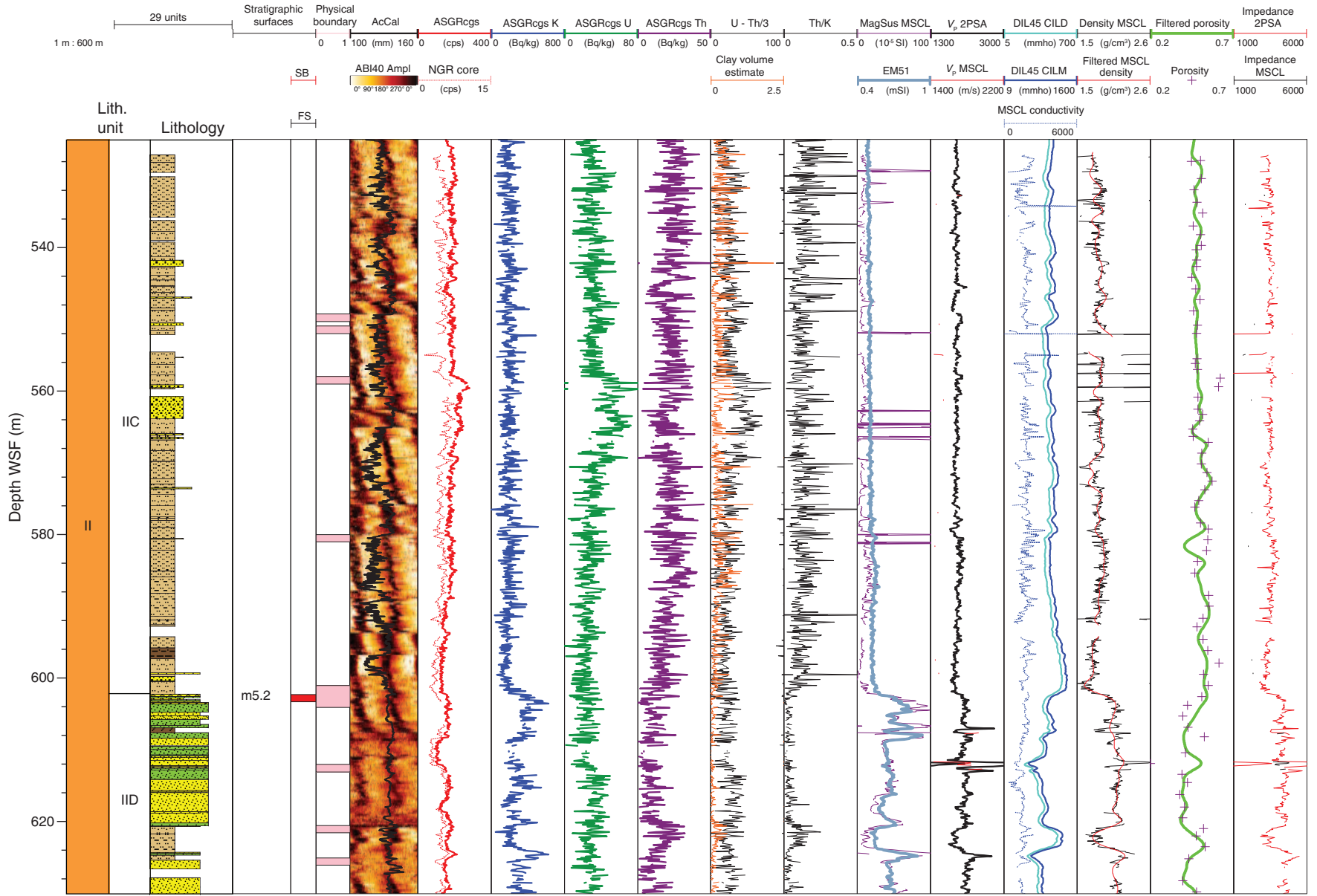
Figure F44 (continued). D. 420–520 m WSF. (Continued on next page.)
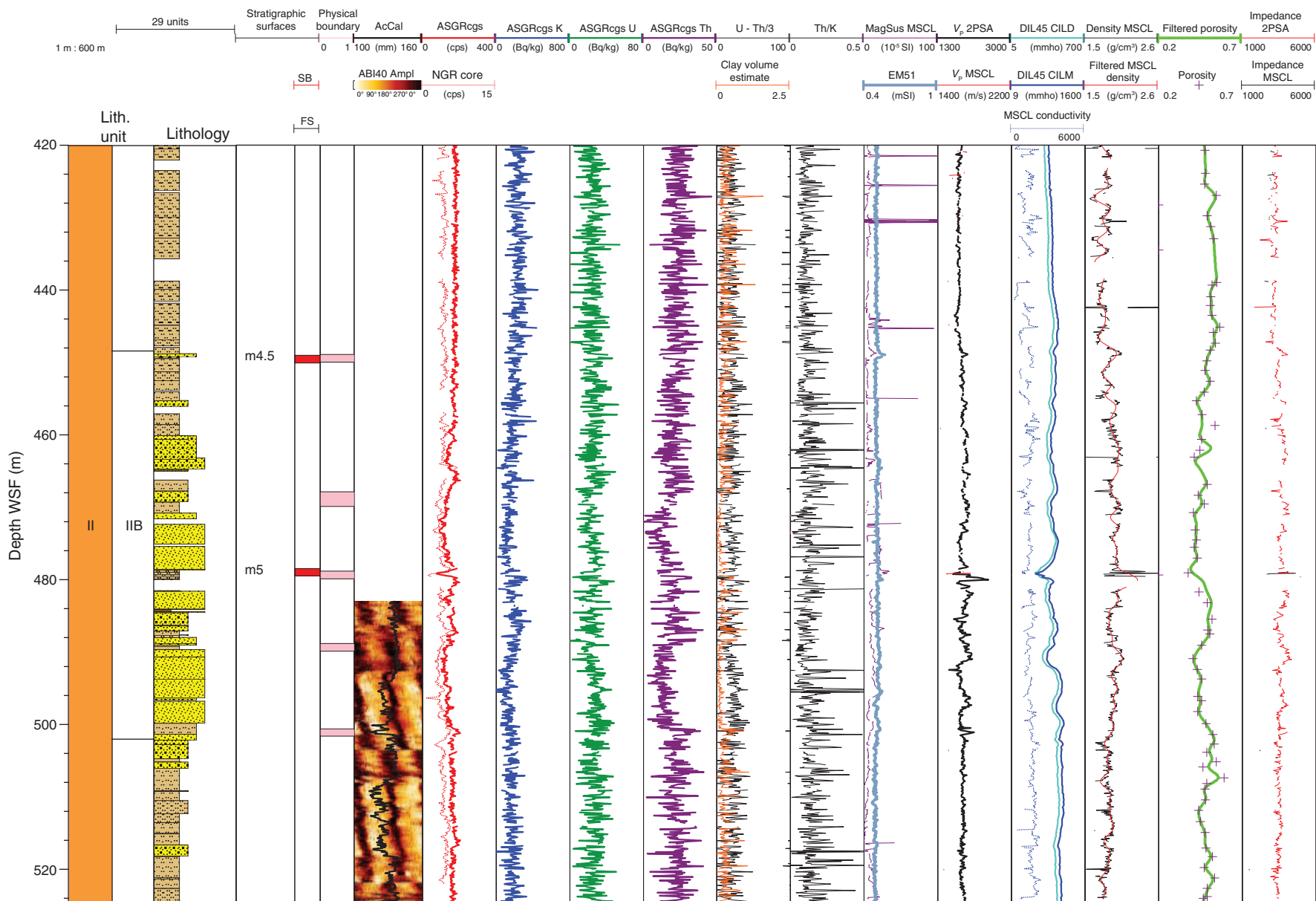
Figure F44 (continued). E. 320–420 m WSF. (Continued on next page.)
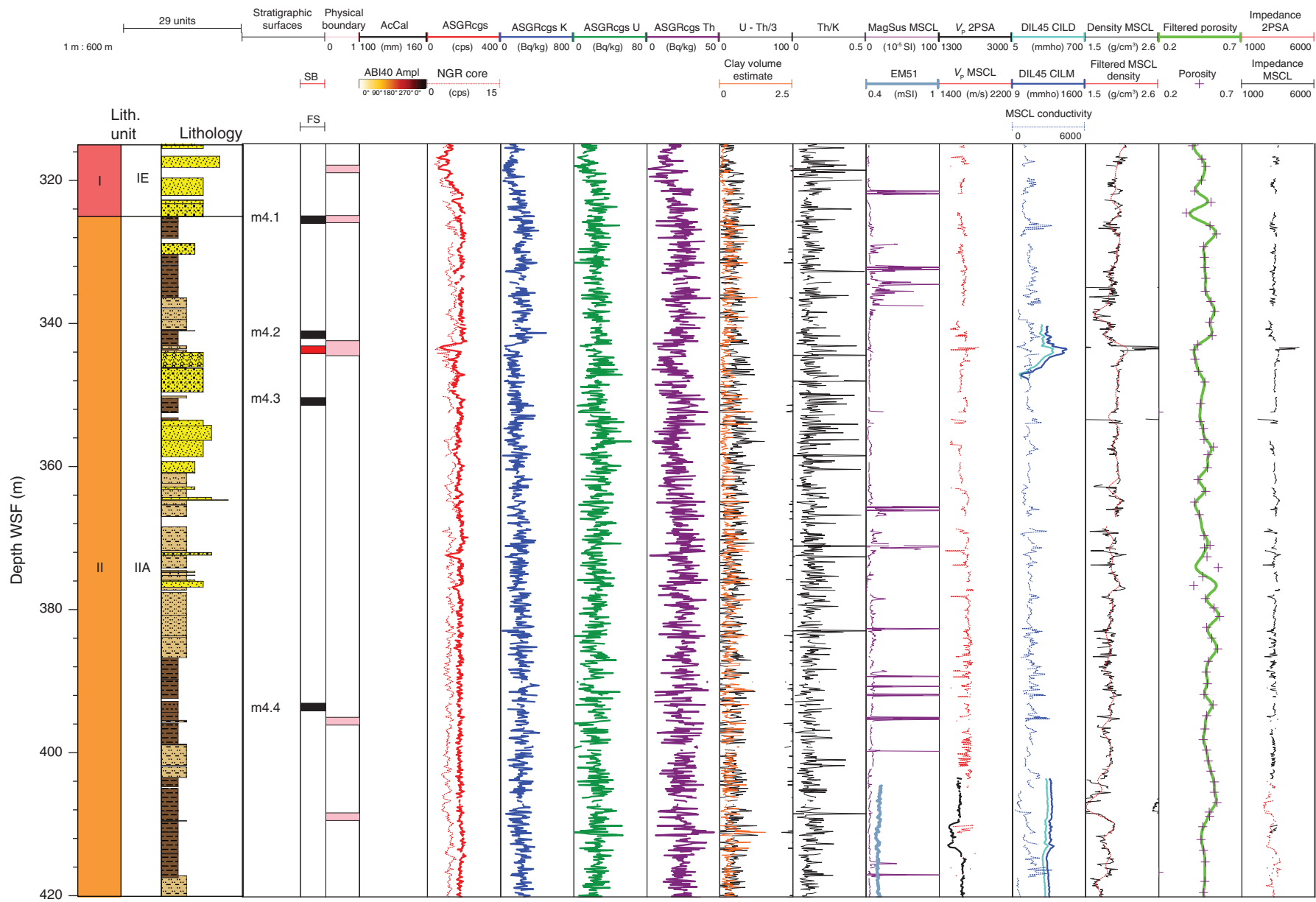
Figure F44 (continued). F. 220–300 m WSF. (Continued on next page.)
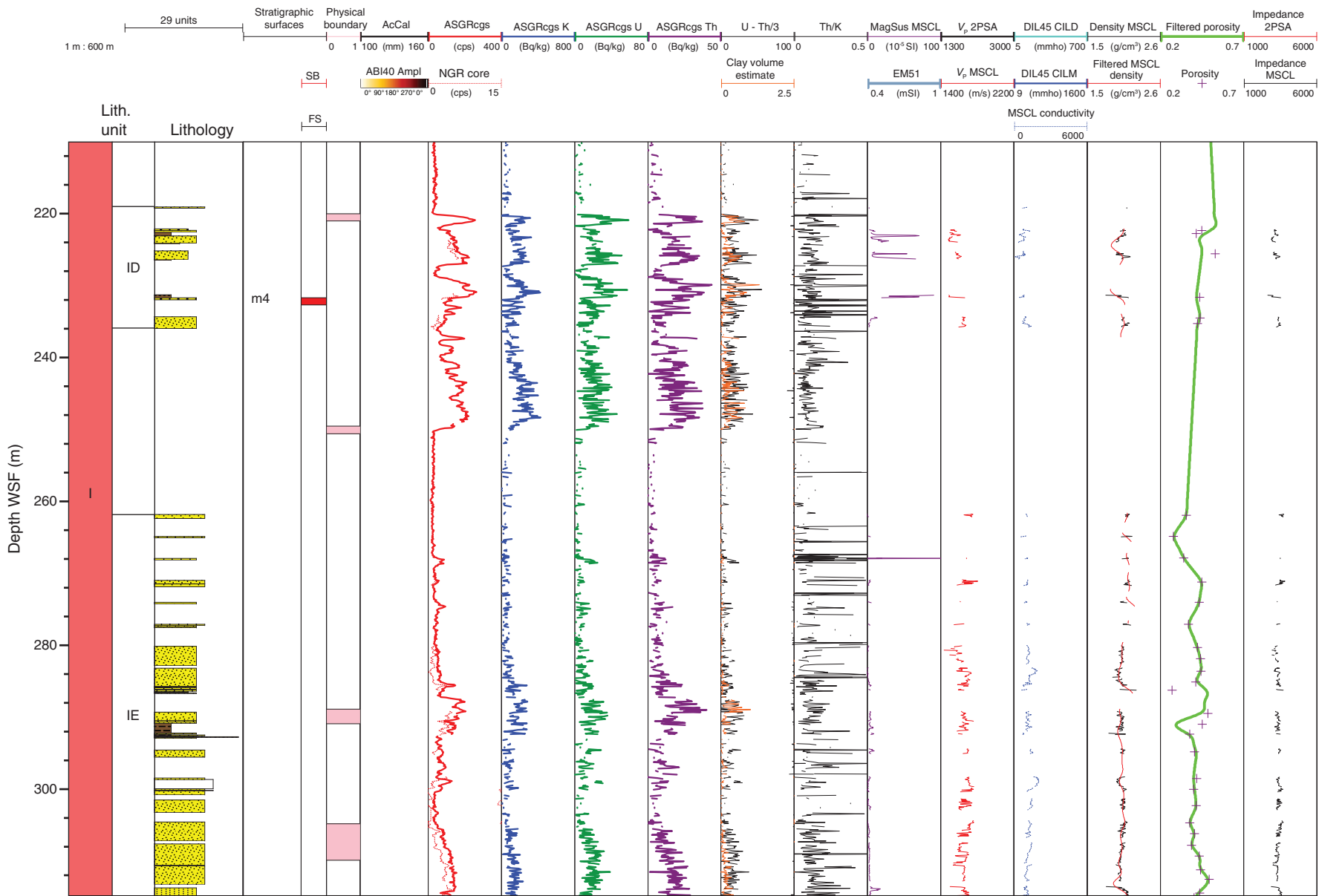
Figure F44 (continued). G. 120–200 m WSF. (Continued on next page.)
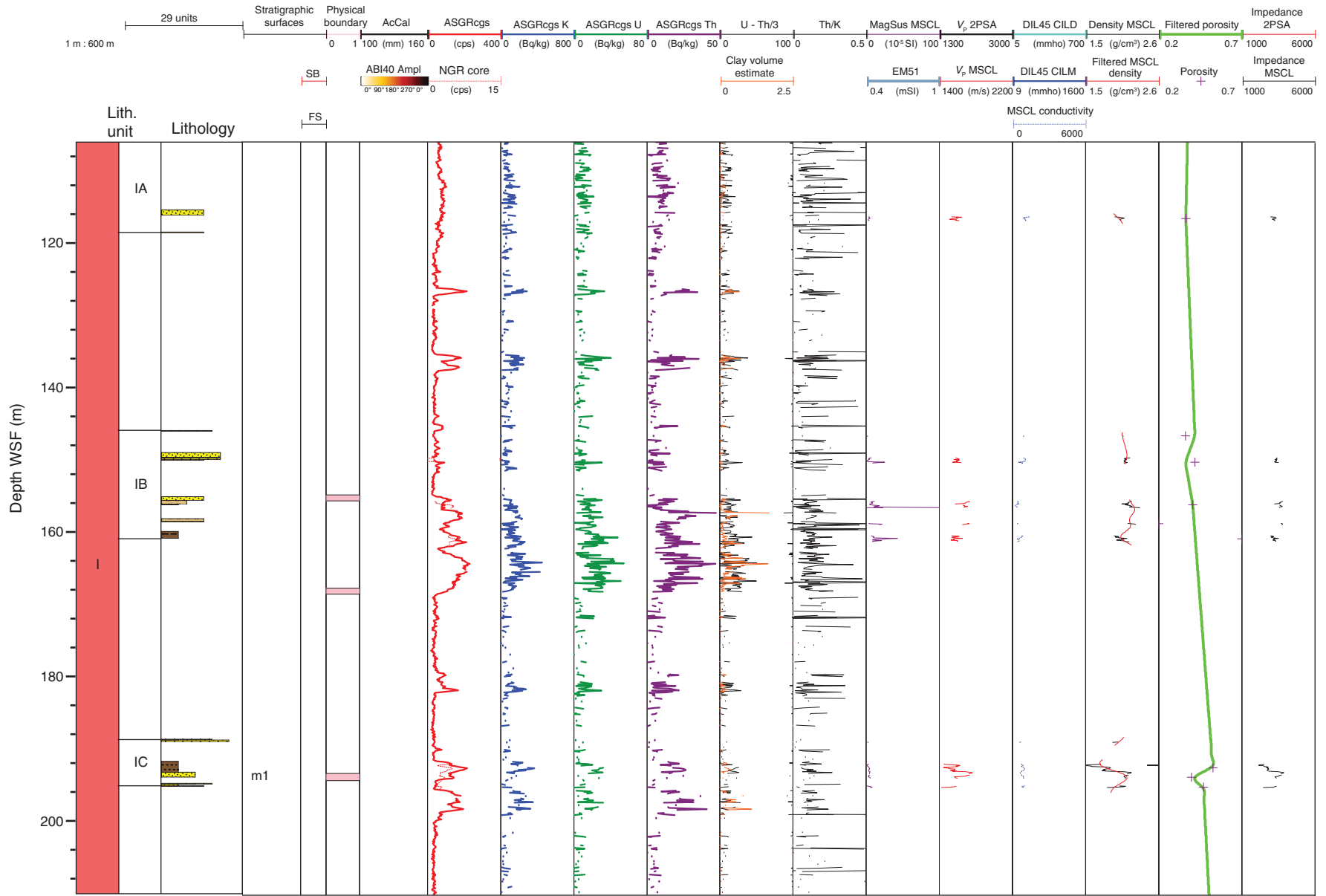
Figure F44 (continued). H. 0–100 m WSF.
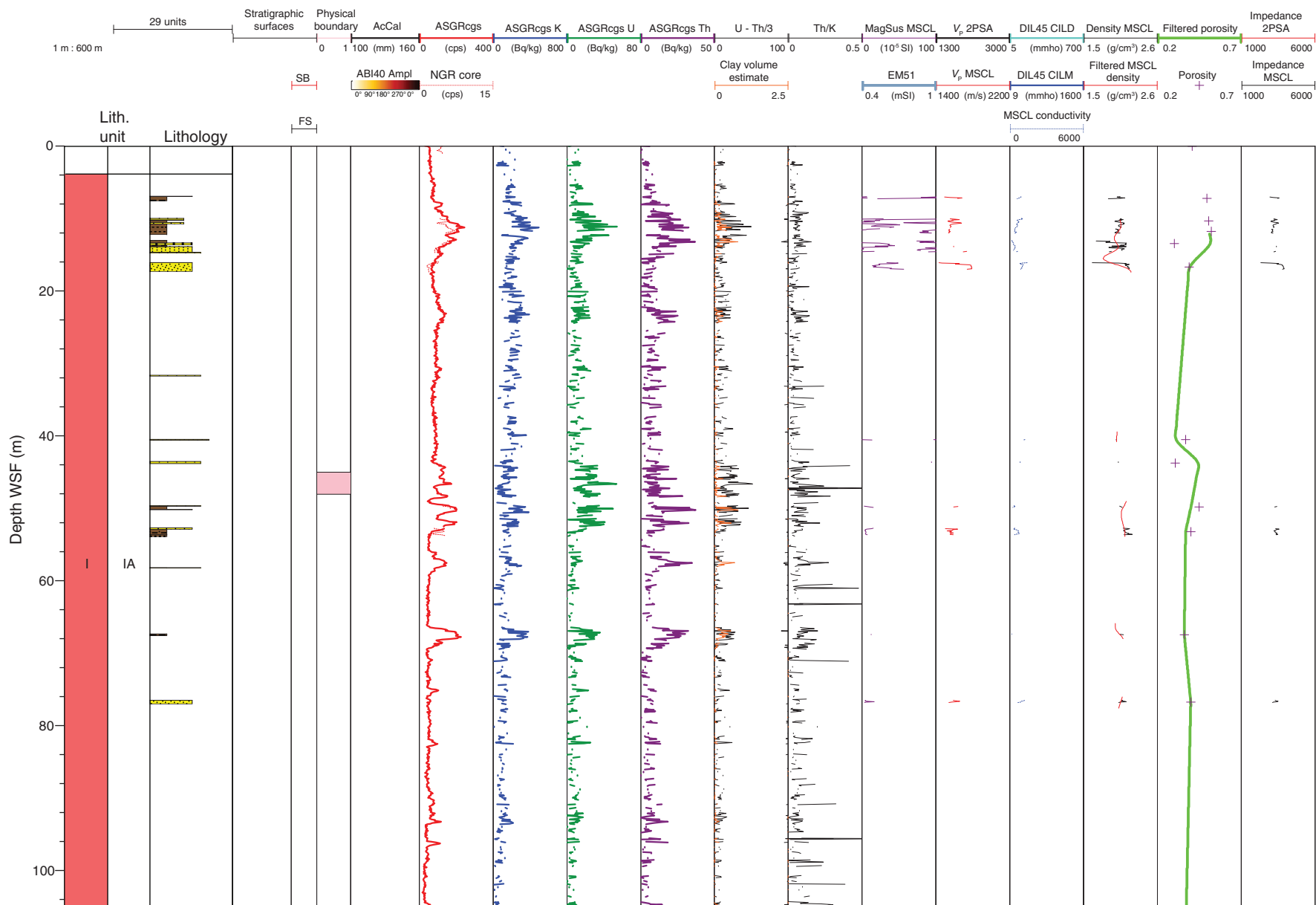
Figure F45. Composite of petrophysical and downhole logging data between 645 and 694 m WSF, Hole M0029A. Logs toward the left (total and spectral gamma ray and magnetic susceptibility) increase in an interval from ~660 to 666 m WSF. These logs respond to the lithological change at the Unit IV/V boundary. Sonic and conductivity logs display a broad low from 661 to 673 m WSF as lithologies become coarser grained. Between 682 and 668 m WSF the comparison between log and core magnetic susceptibility shows four clear peaks that correlate with coarser more glauconitic lithologies. They also show that there is a shift between core and logs as the upper two peaks observed in the core data should be shifted up to match the logs, consistent with the observation of a gap in core recovery here. The sonic log, multisensor core log (MSCL) velocity, and conductivity show clear correspondence, particularly between 667 and 674 m WSF with indurated intervals within the core.
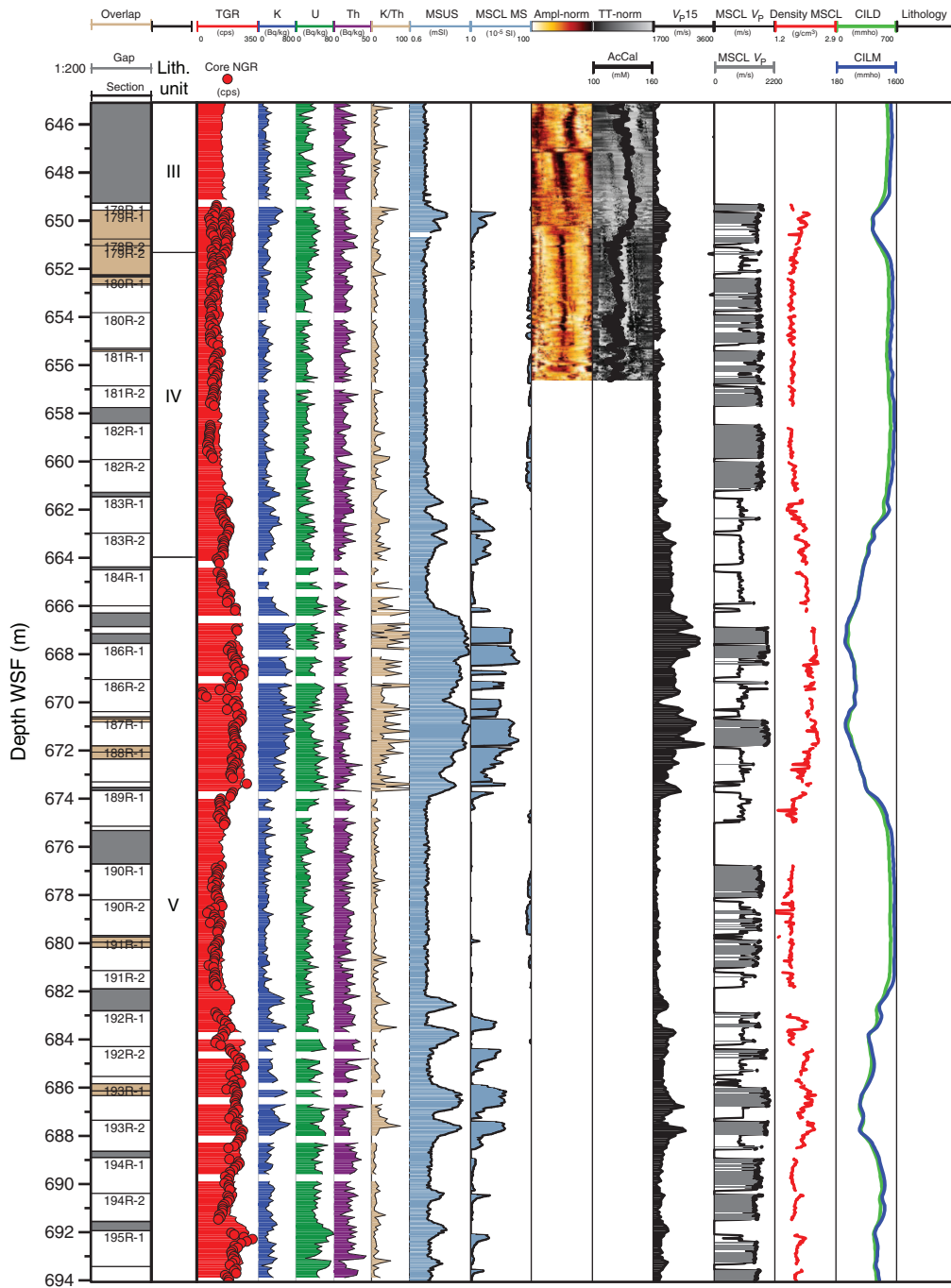
Figure F46. VSP two-way traveltime vs. depth, Hole M0029A.
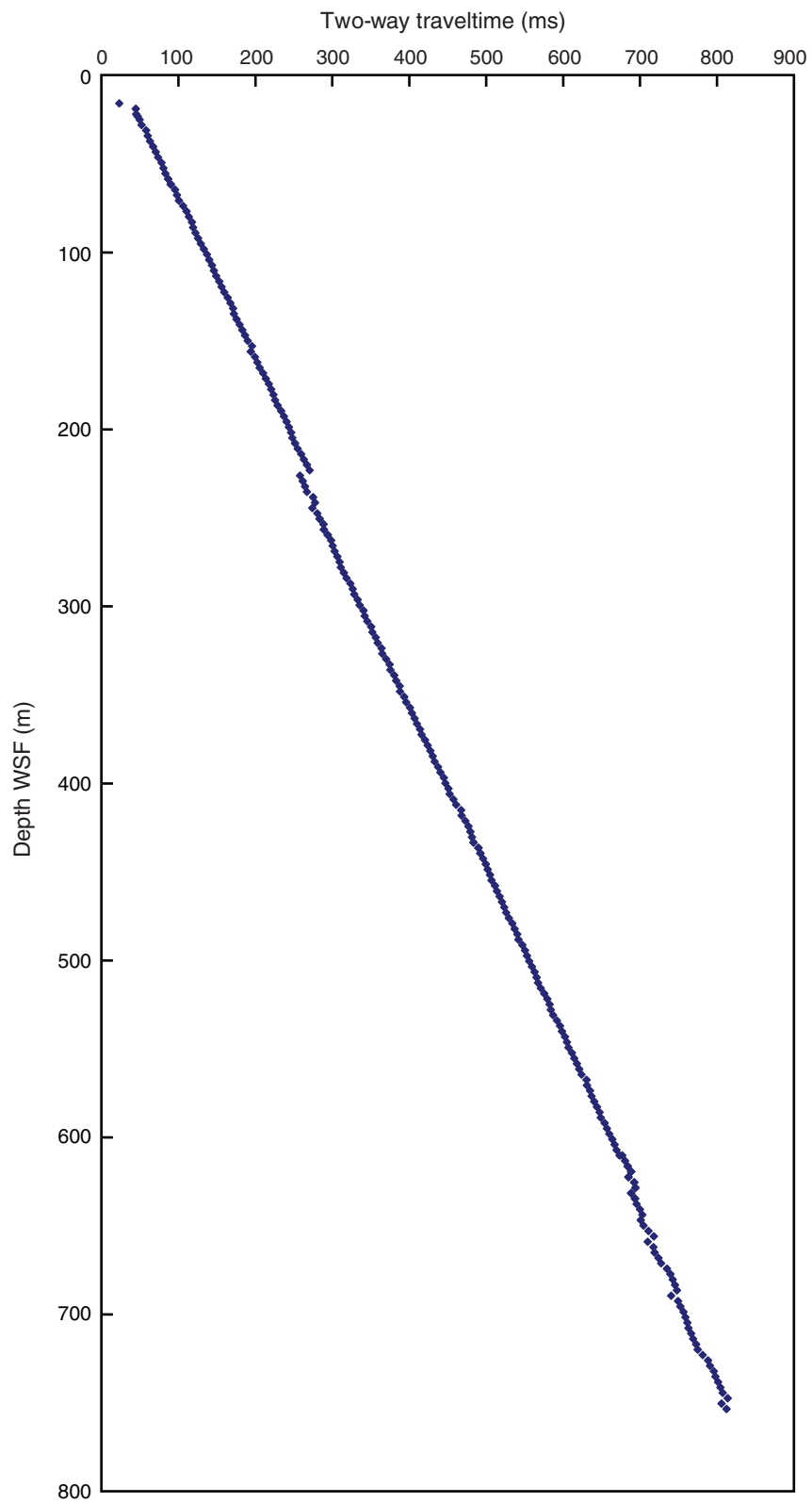
Figure F47. Interpretation of seismic surfaces on dip line Oc270 profile 529. CDP = common depth point.
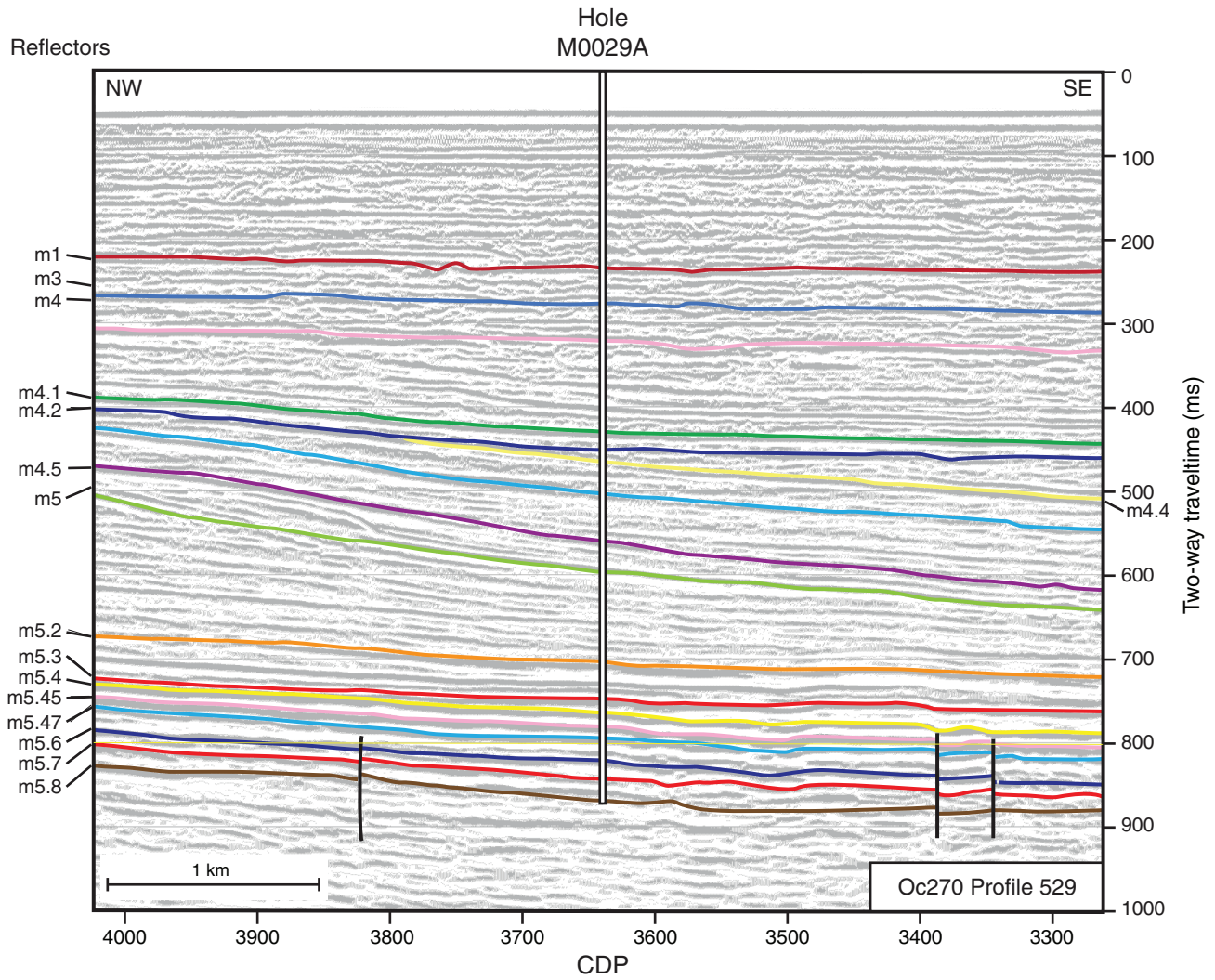
Figure F48. Interpretation of seismic surfaces on strike line CH0698 profile 310. CDP = common depth point.
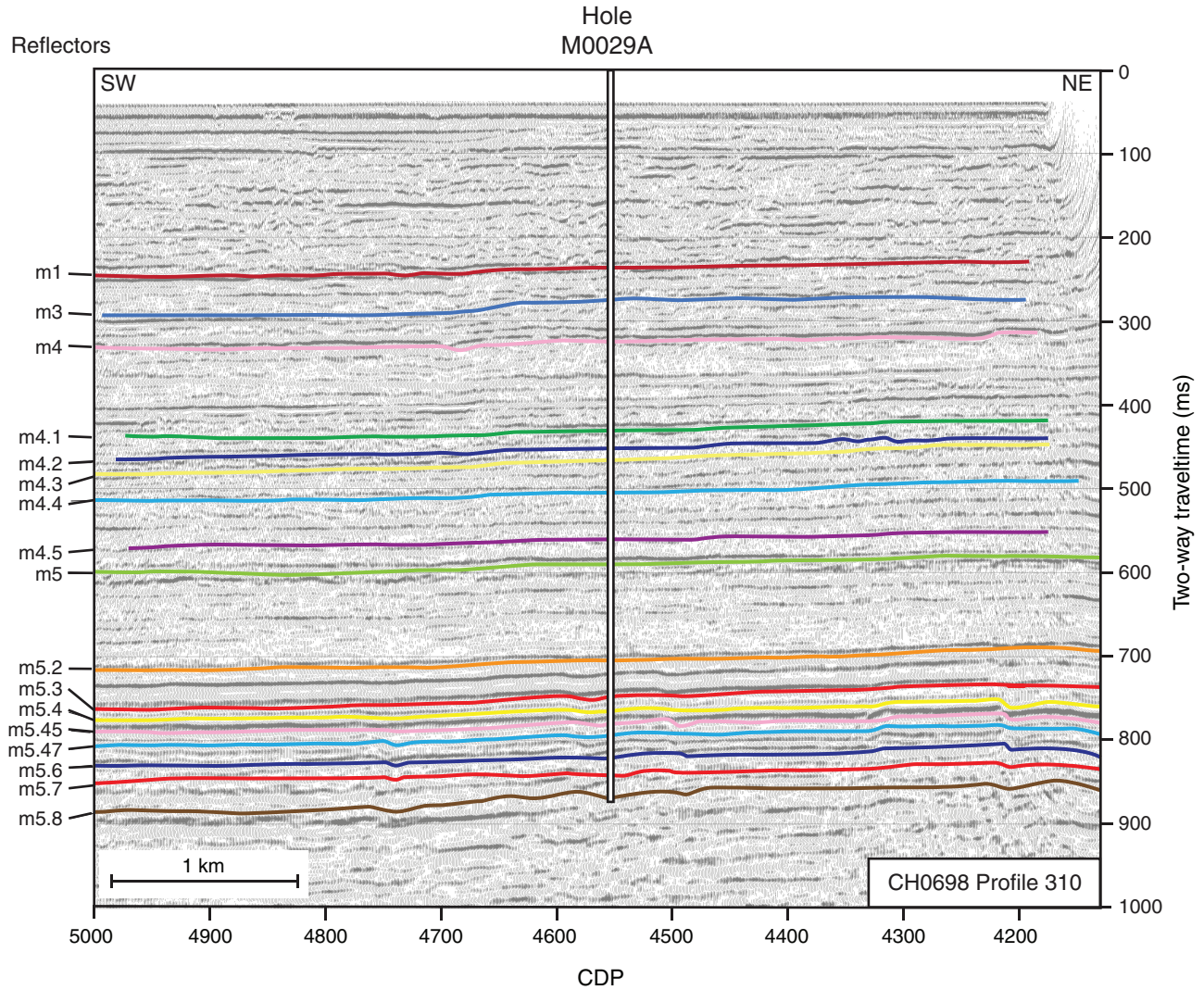
Figure F49. Summary of lithology, lithostratigraphy, well (TGR, K, U, and Th), and MSCL data (natural gamma radiation [NGR] and bulk density); acoustic impedance calculated using MSCL bulk densities; depositional environments and correlating core surfaces; and predicted depth ranges based on Hole M0029A velocity between 0 and 150 mbsf. Blue dots = NGR, red line = TGR. See Figure F1 for lithology legend.
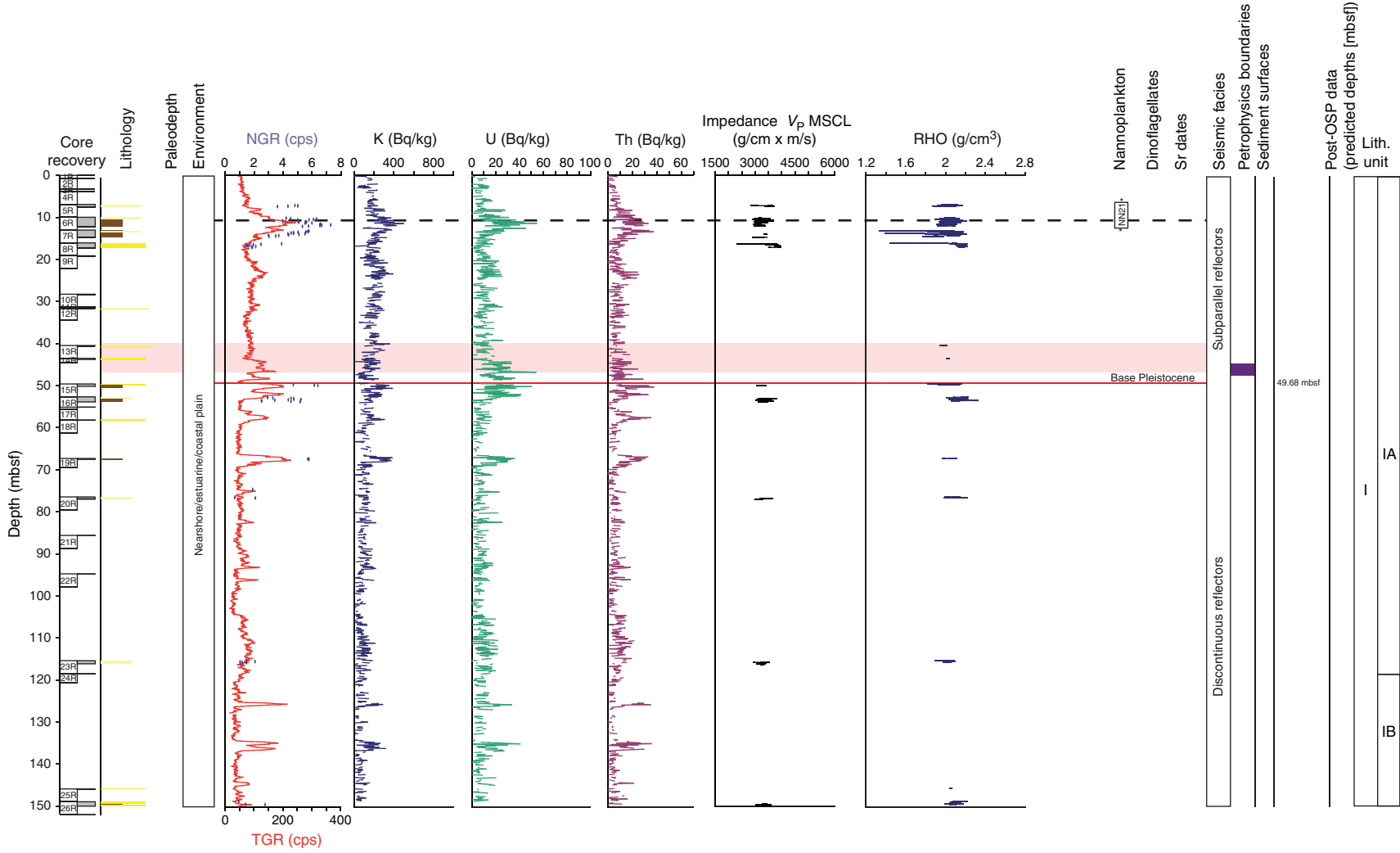
Figure F50. Correlation of core image with interpretation of deposition and age, 49.2–50.1 mbsf.
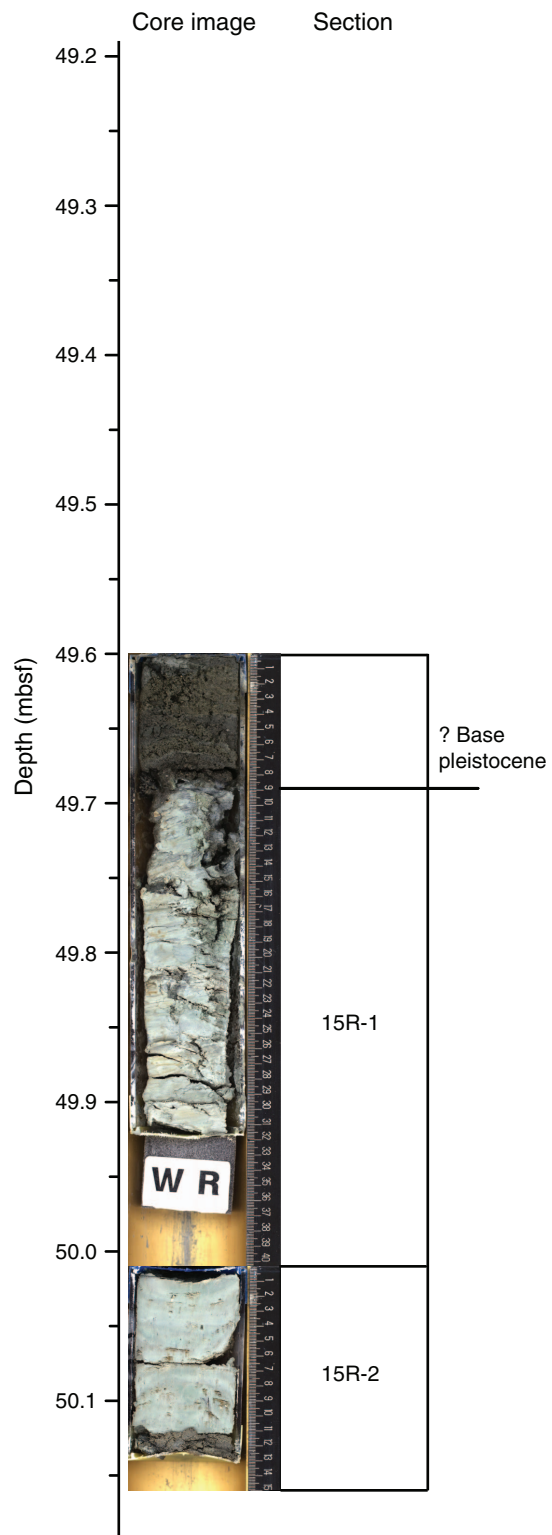
Figure F51. Summary of lithology, lithostratigraphy, well (TGR, K, U, and Th), and MSCL data (natural gamma radiation [NGR] and bulk density); acoustic impedance calculated using MSCL bulk densities; depositional environments and correlating core surfaces; and predicted depth ranges based on Hole M0029A velocity between 150 and 280 mbsf. SF = shoreface, SOT = shoreface–offshore transition. Blue dots = NGR, red line = TGR. See Figure **F1** for lithology legend.
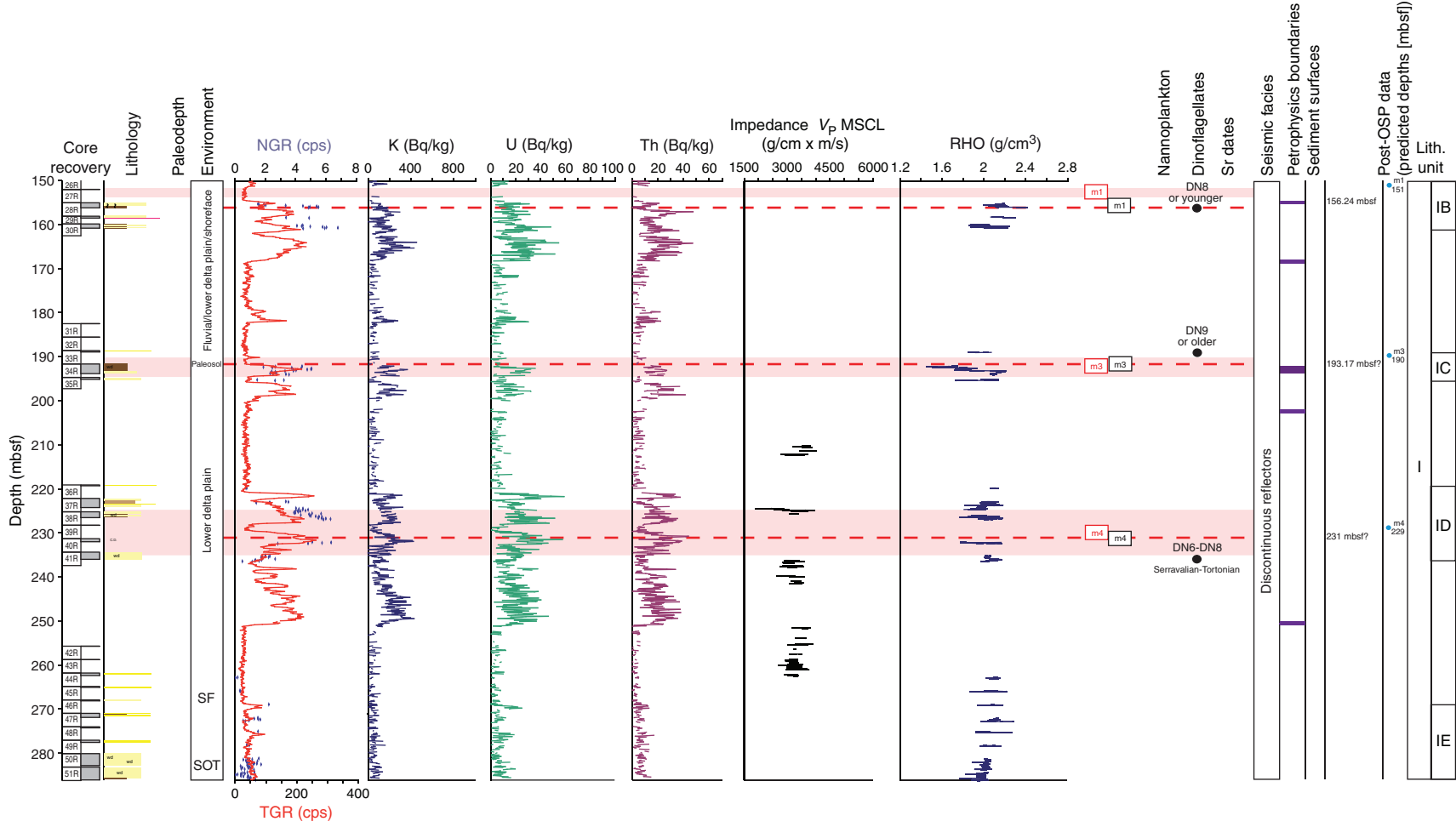
Figure F52. Correlation of core image with interpretation of deposition and age, 192.7–193.6 mbsf.
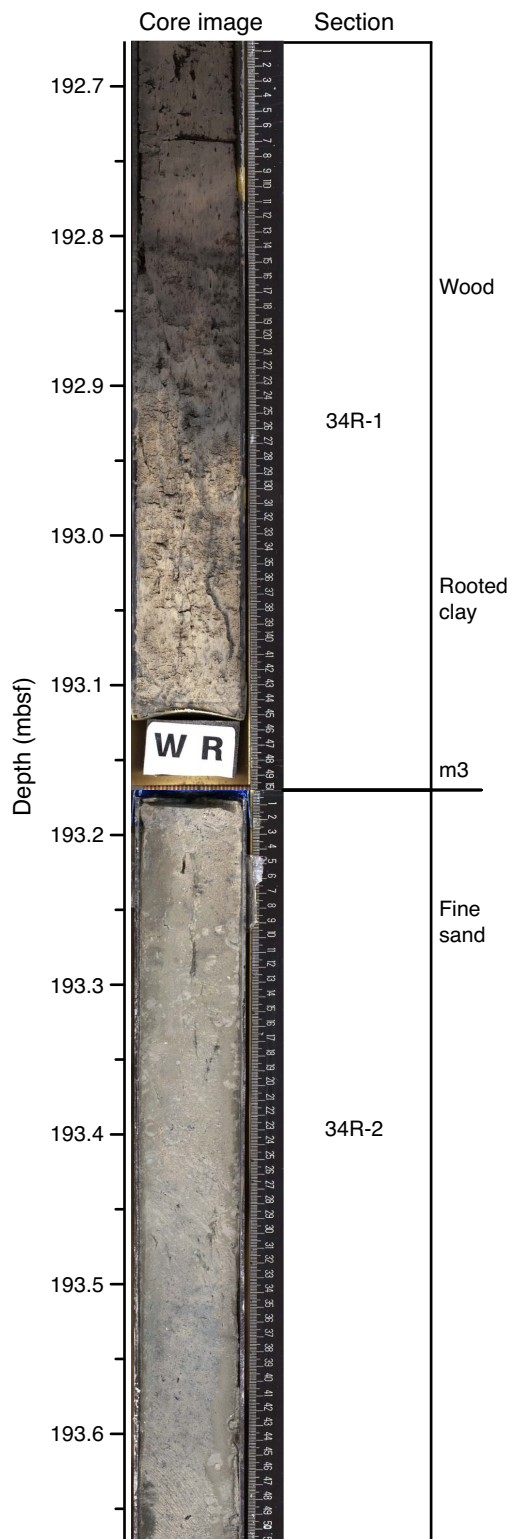
Figure F53. Summary of lithology, lithostratigraphy, well (TGR, K, U, and Th), and MSCL data (natural gamma radiation [NGR] and bulk density); acoustic impedance calculated using MSCL bulk densities; depositional environments and correlating core surfaces; and predicted depth ranges based on Hole M0029A velocity between 280 and 430 mbsf. OFF = offshore, SF = shoreface. Blue dots = NGR, red line = TGR. See Figure F1 for lithology legend.
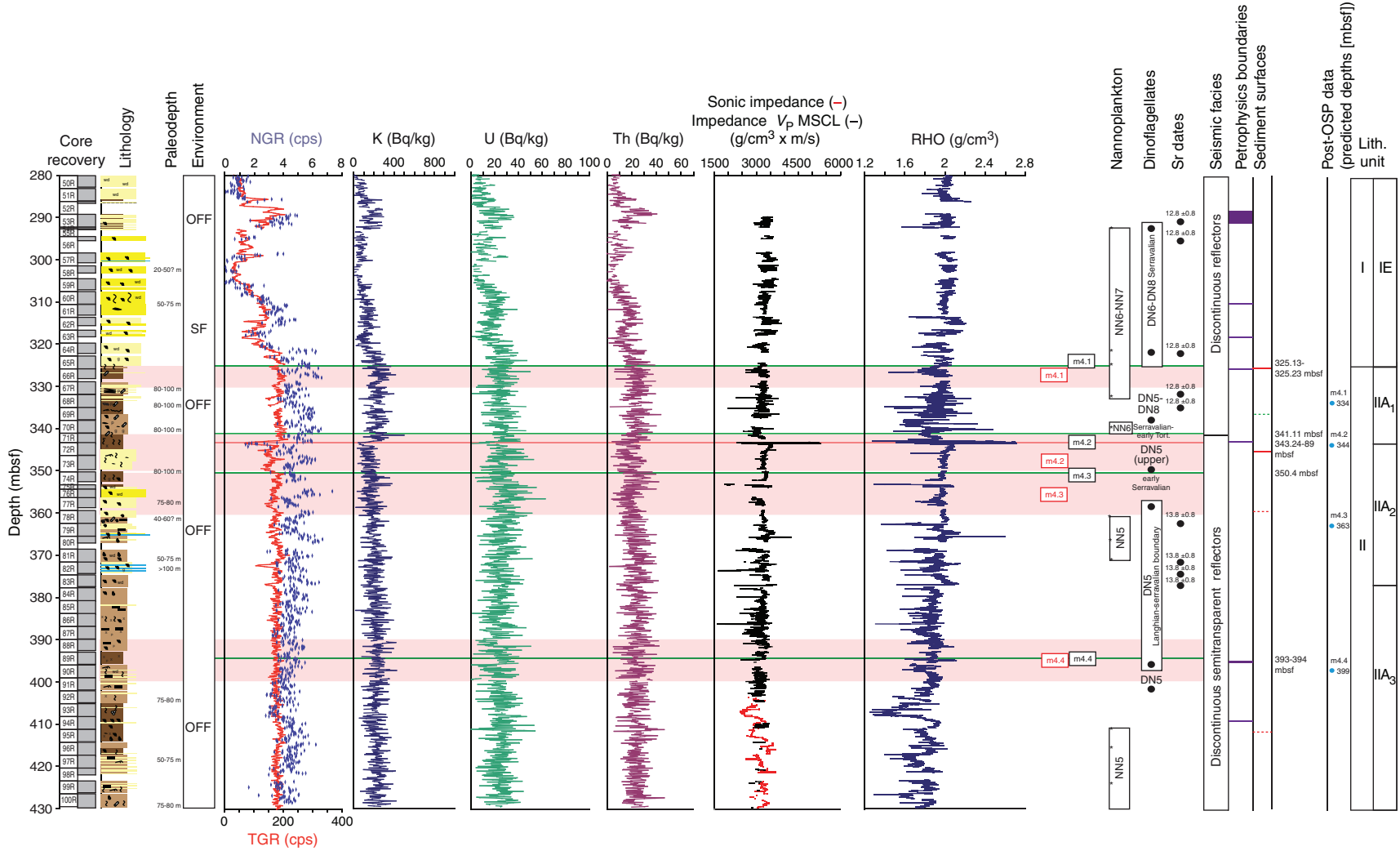
Figure F54. Correlation of core image with interpretation of deposition and age, 448.6–449.5 mbsf.
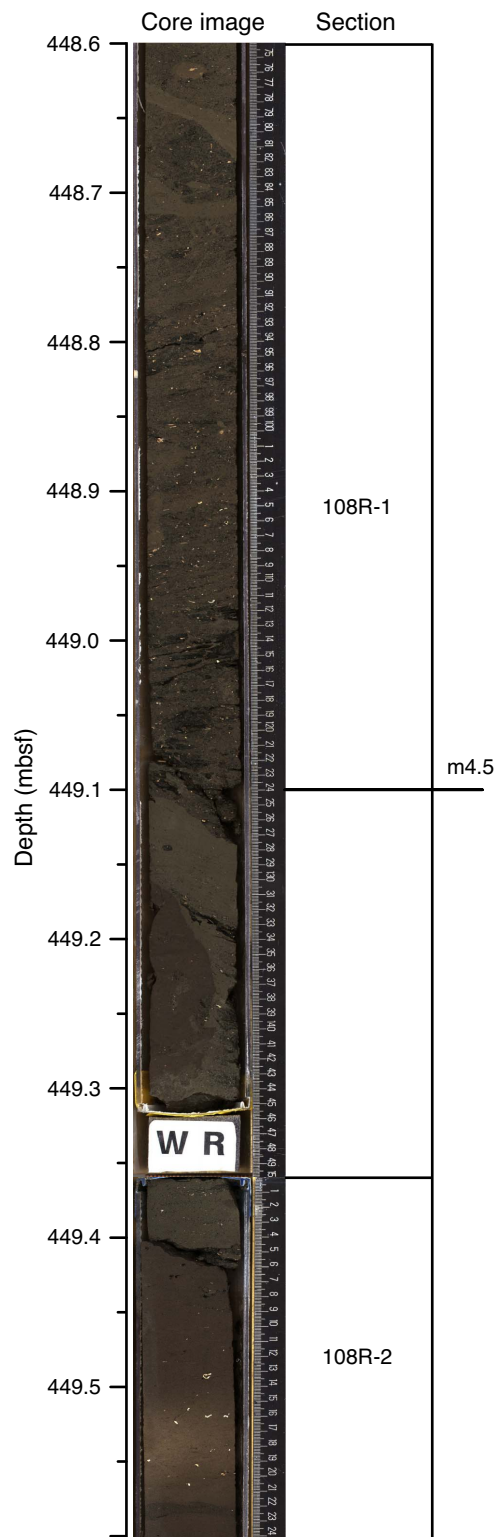
Figure F55. Summary of lithology, lithostratigraphy, well (TGR, K, U, and Th), and MSCL data (natural gamma radiation [NGR] and bulk density); acoustic impedance calculated using MSCL bulk densities; depositional environments and correlating core surfaces; and predicted depth ranges based on Hole M0029A velocity between 420 and 570 mbsf. OFF = offshore. Blue dots = NGR, red line = TGR. See Figure F1 for lithology legend.
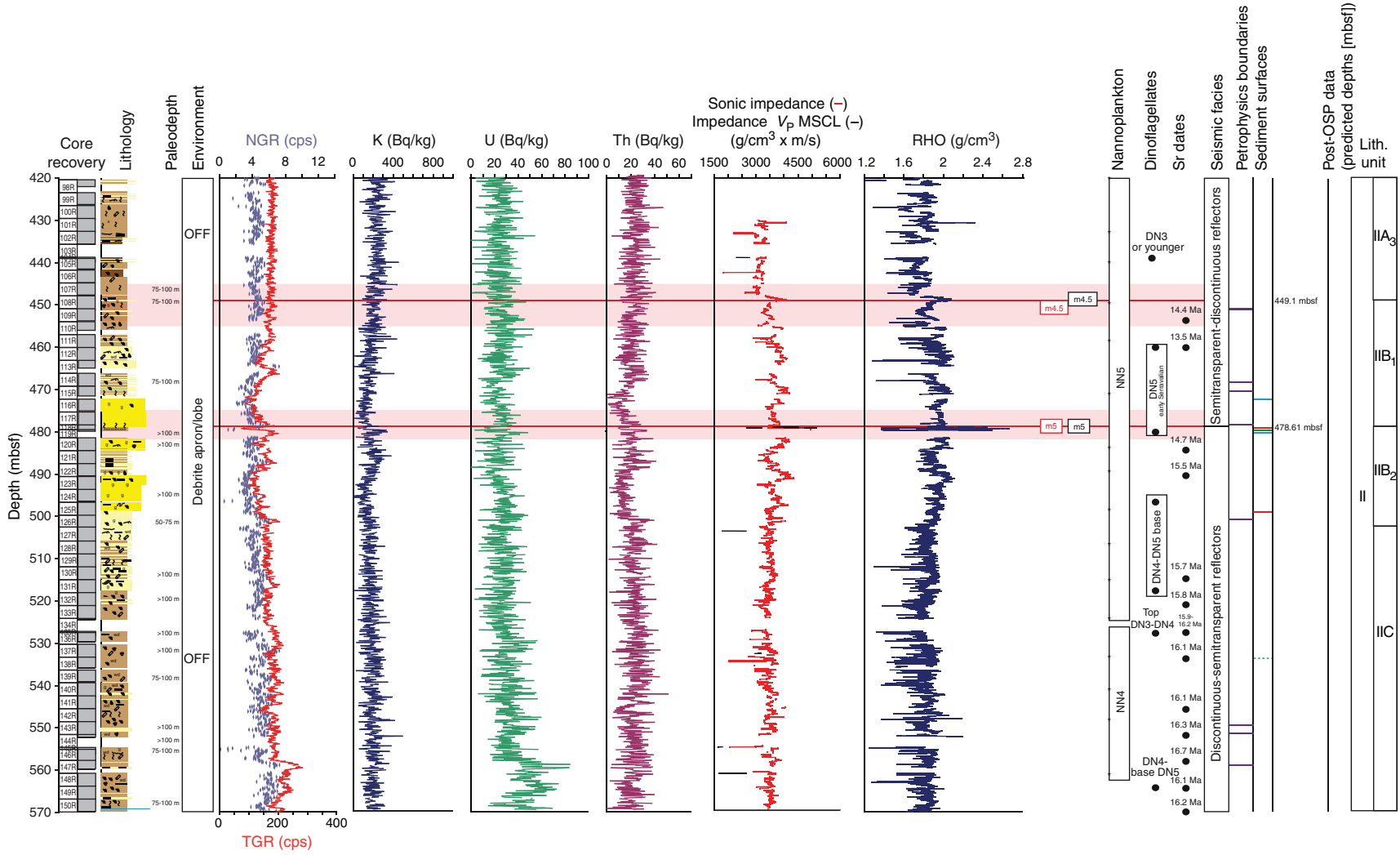
Figure F56. Correlation of core image with interpretation of deposition and age along with density, 478.2–479.1 mbsf.
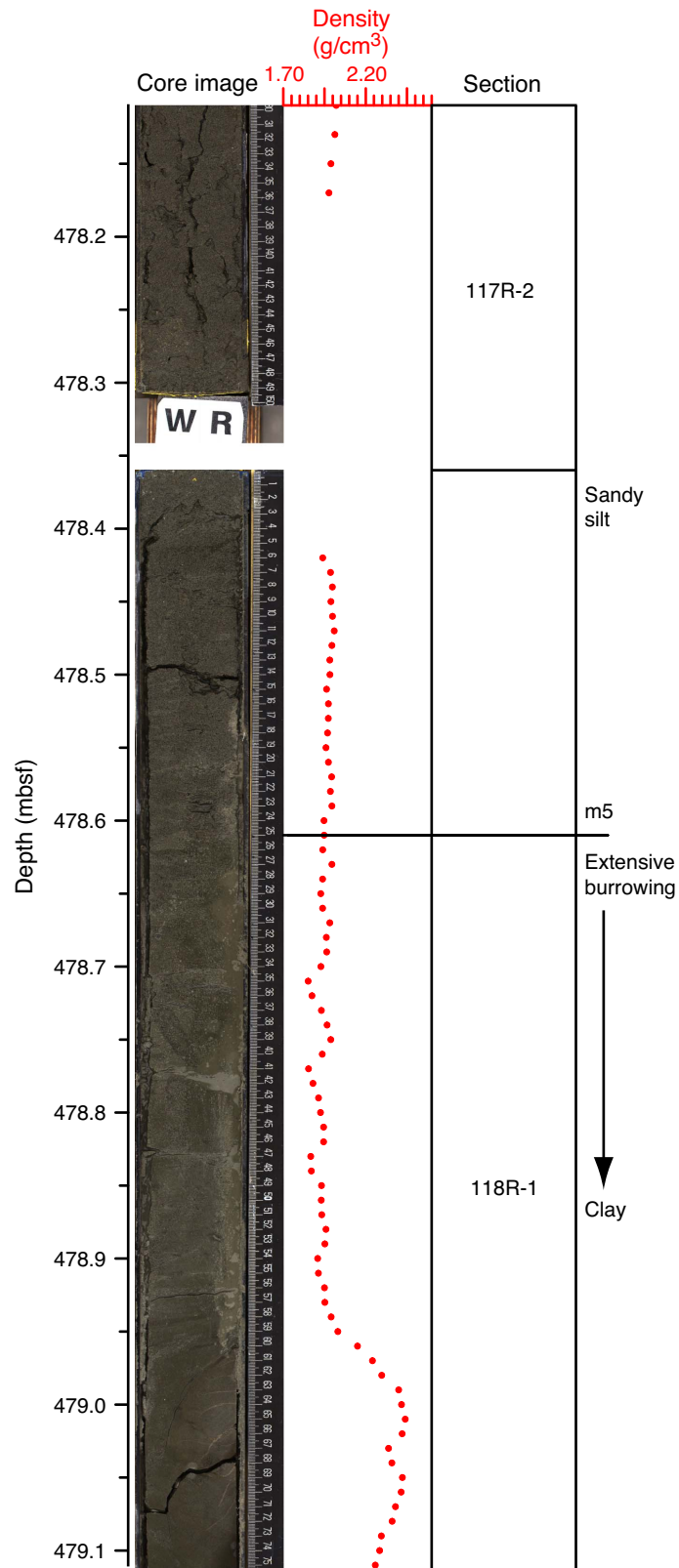
Figure F57. Summary of lithology, lithostratigraphy, well (TGR, K, U, and Th), and MSCL data (natural gamma radiation [NGR] and bulk density); acoustic impedance calculated using MSCL bulk densities; depositional environments and correlating core surfaces; and predicted depth ranges based on Hole M0029A velocity between 560 and 700 mbsf. OFF = offshore. Blue dots = NGR, red line = TGR. See Figure F1 for lithology legend.
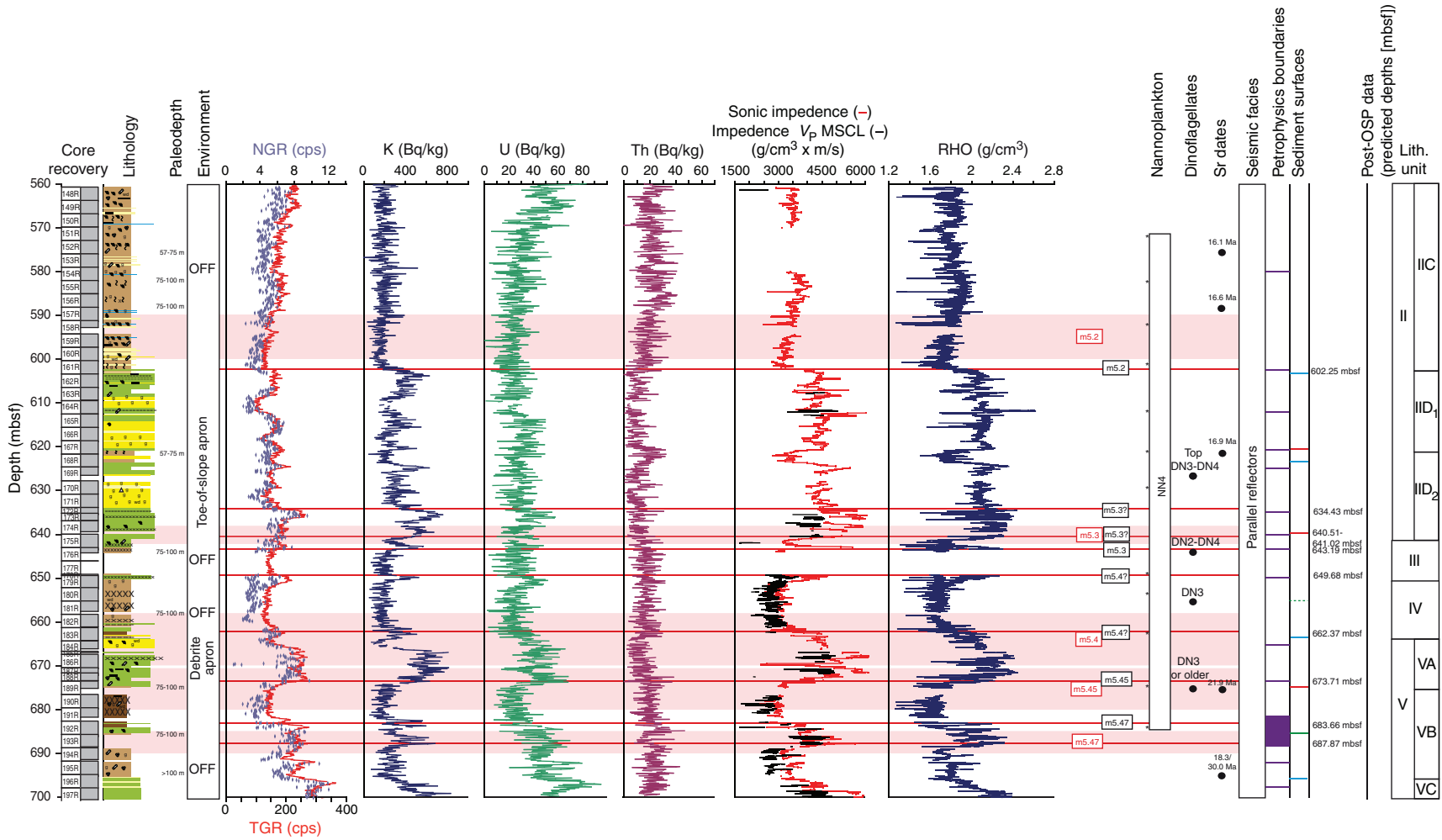
Figure F58. Correlation of core image with interpretation of deposition and age along with density, 601.8–602.7 mbsf.
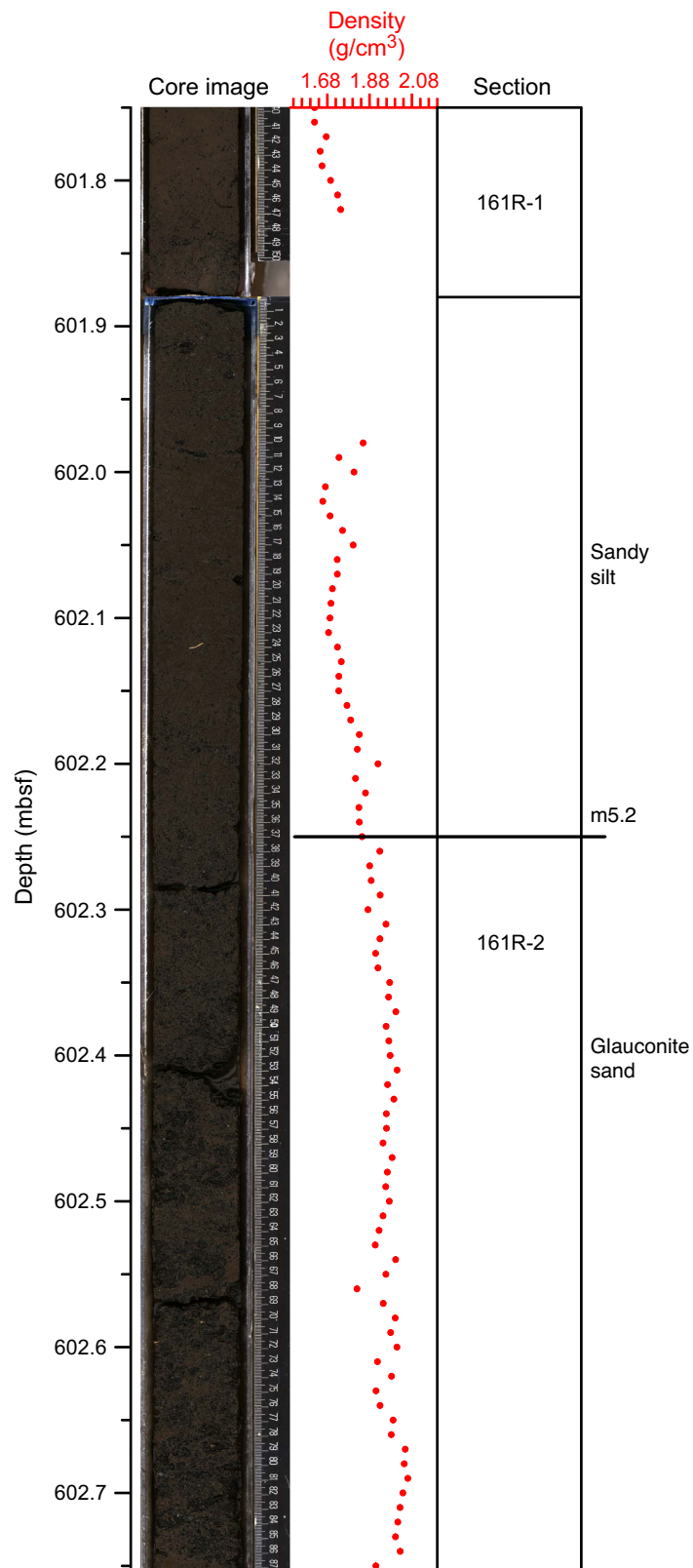
Figure F59. Correlation of core image with interpretation of deposition and age along with density, 642.7–643.6 mbsf.
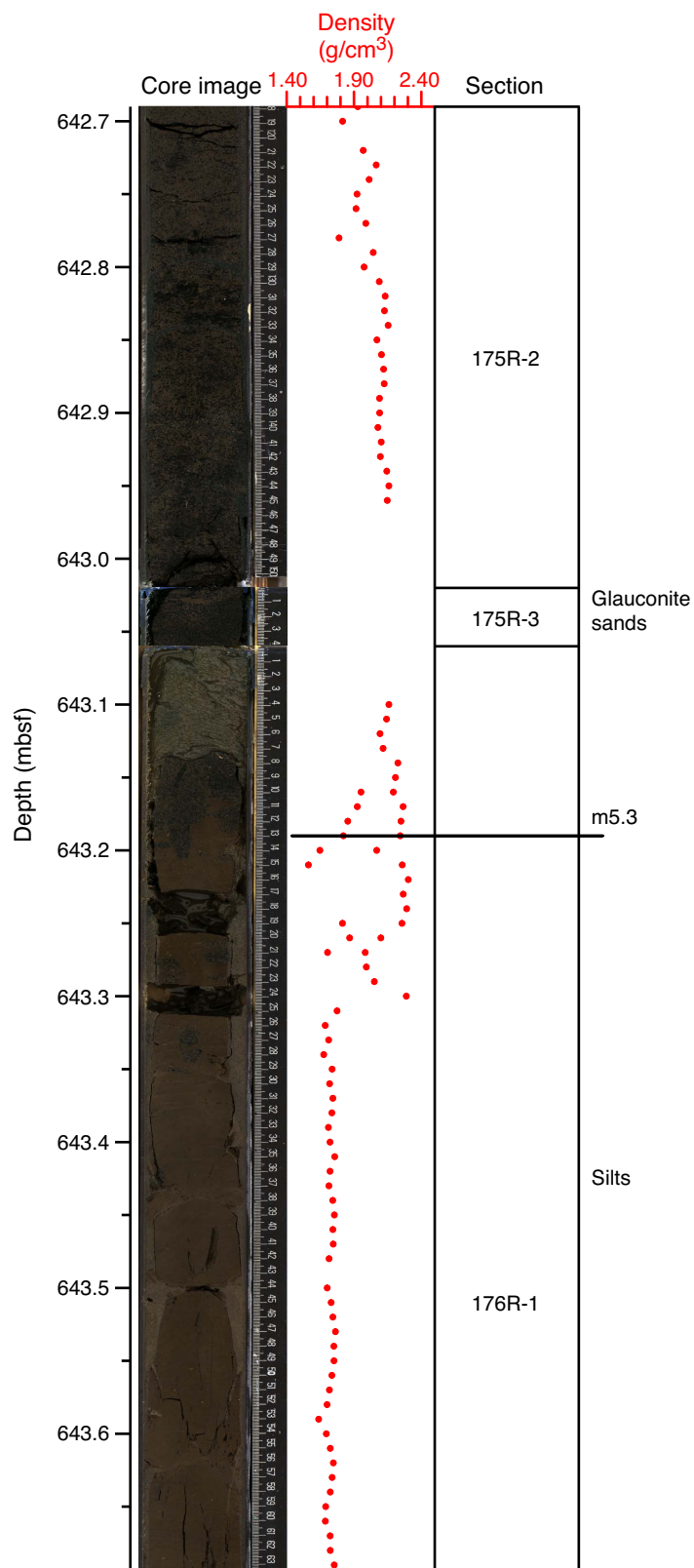
Figure F60. Correlation of core image with interpretation of deposition and age, 661.9–662.8 mbsf.
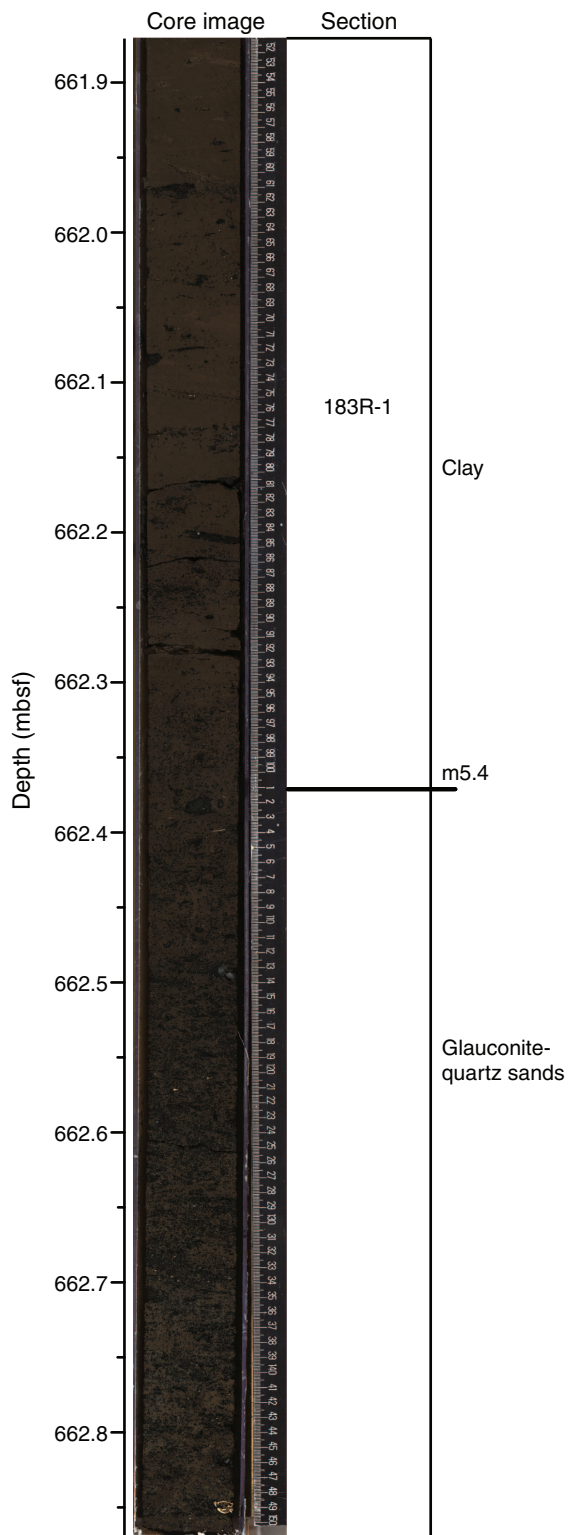
Figure F61. Correlation of core image with interpretation of deposition and age along with density, 673.3–674.2 mbsf.
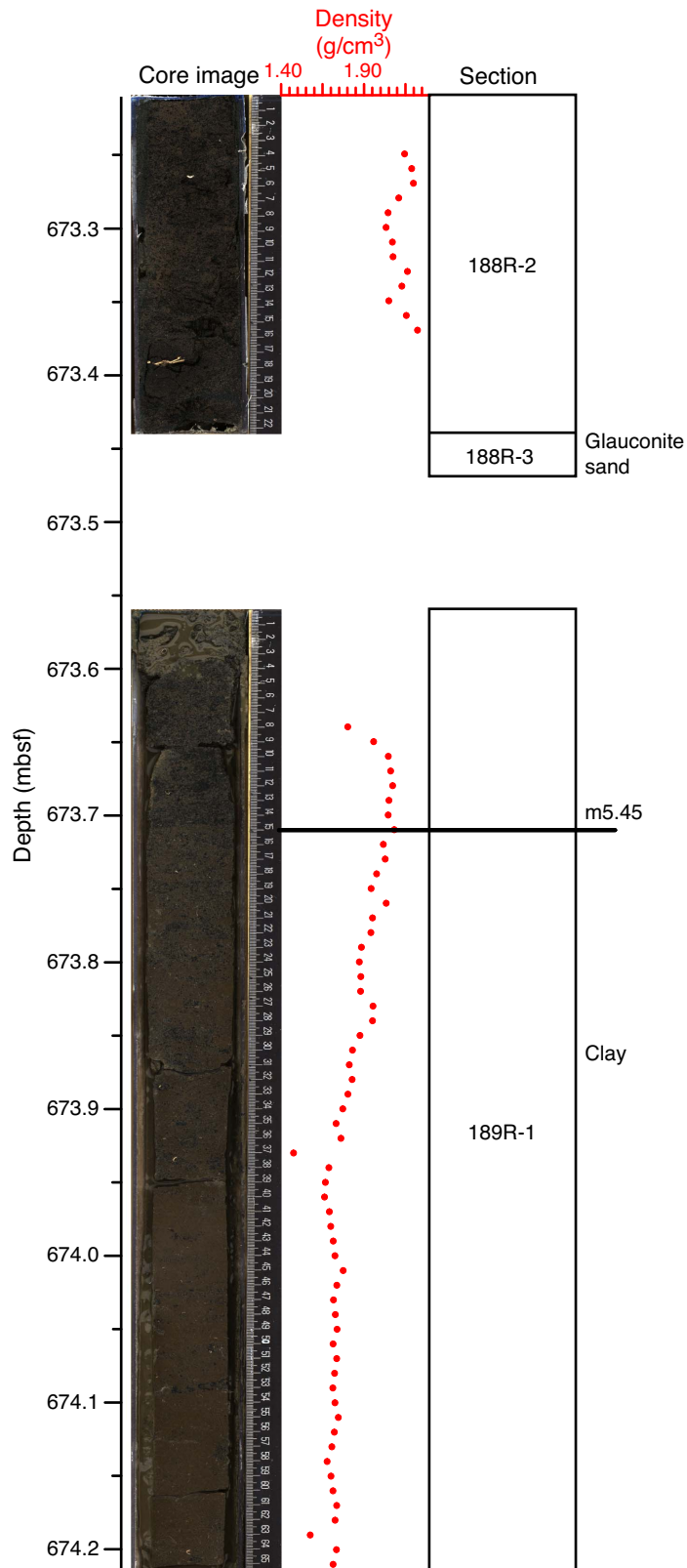
Figure F62. Correlation of core image with interpretation of deposition and age along with density, 687.4–688.2 mbsf.
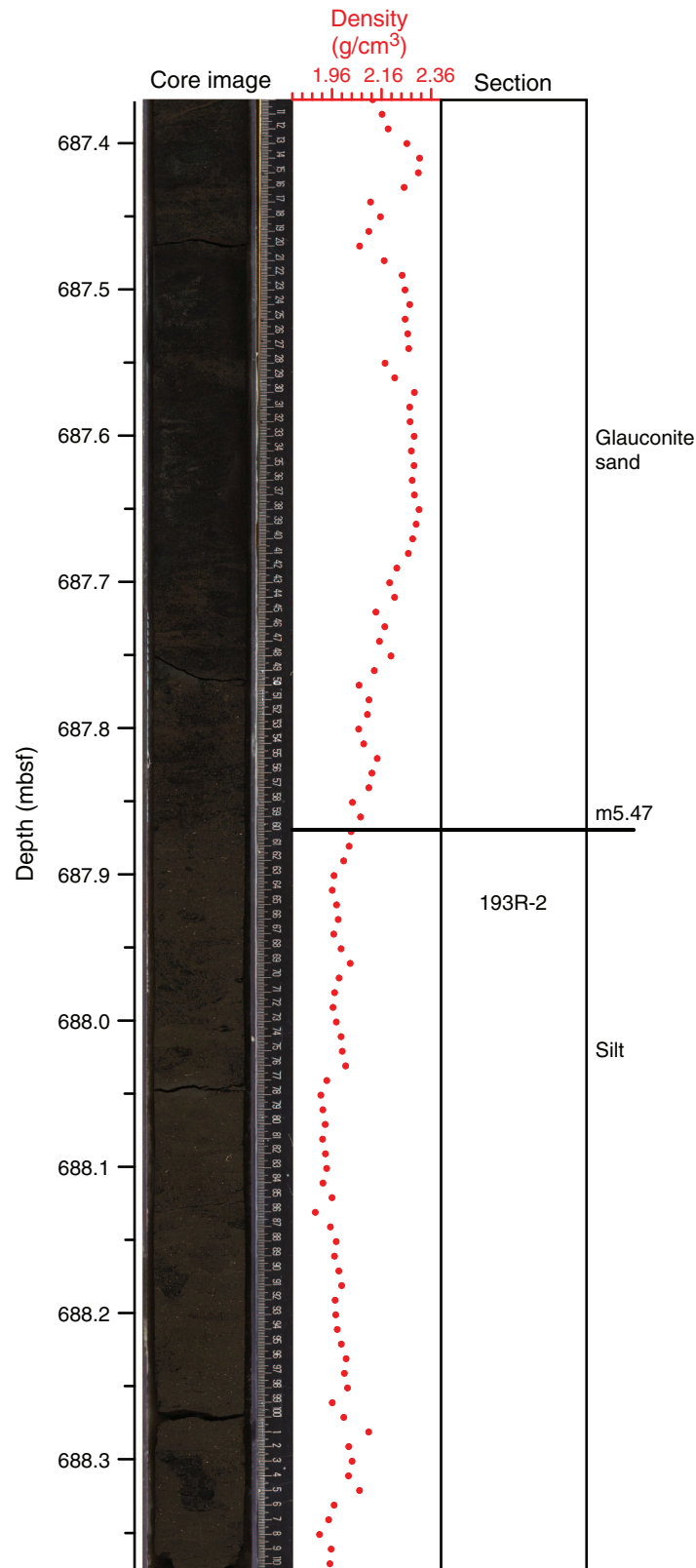
Figure F63. Summary of lithology, lithostratigraphy, well (TGR, K, U, and Th), and MSCL data (natural gamma radiation [NGR] and bulk density); acoustic impedance calculated using MSCL bulk densities; depositional environments and correlating core surfaces; and predicted depth ranges based on Hole M0029A velocity between 690 and 760 mbsf. OFF = offshore, dOFF = distal offshore. Blue dots = NGR, red line = TGR. See Figure **F1** for lithology legend.
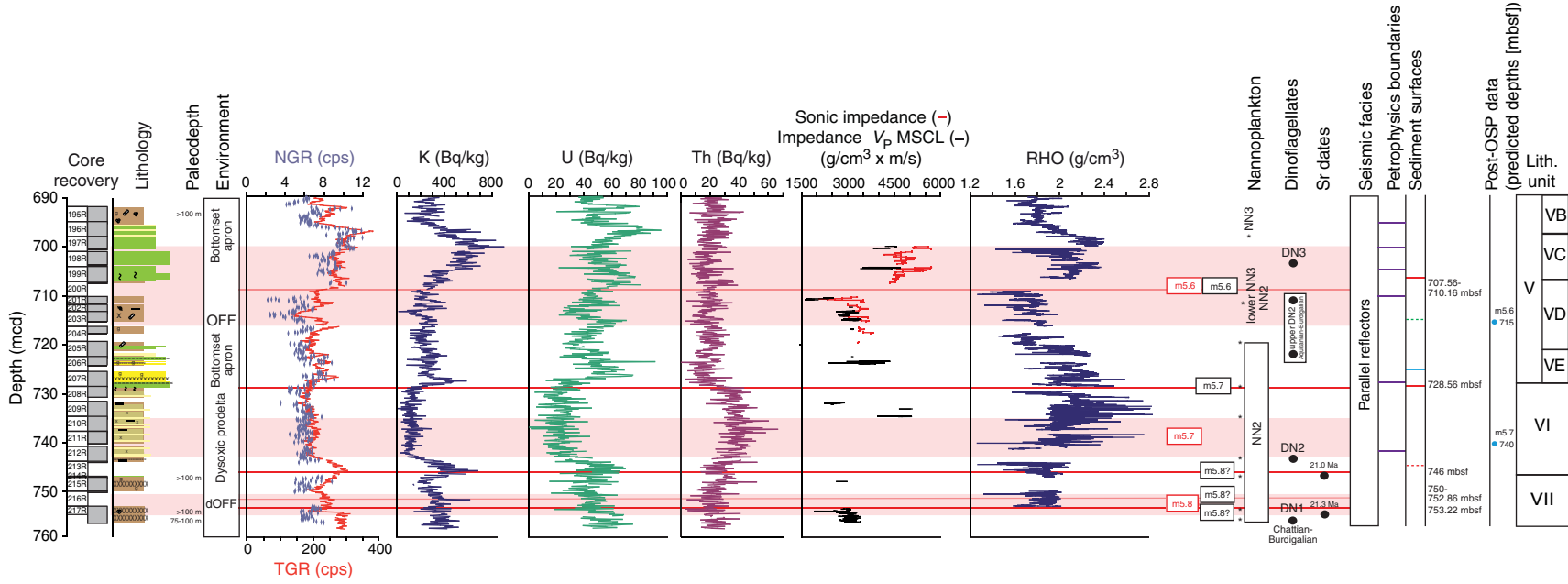
Figure F64. Correlation of core image with interpretation of deposition and age along with density, 728.1–729.0 mbsf.
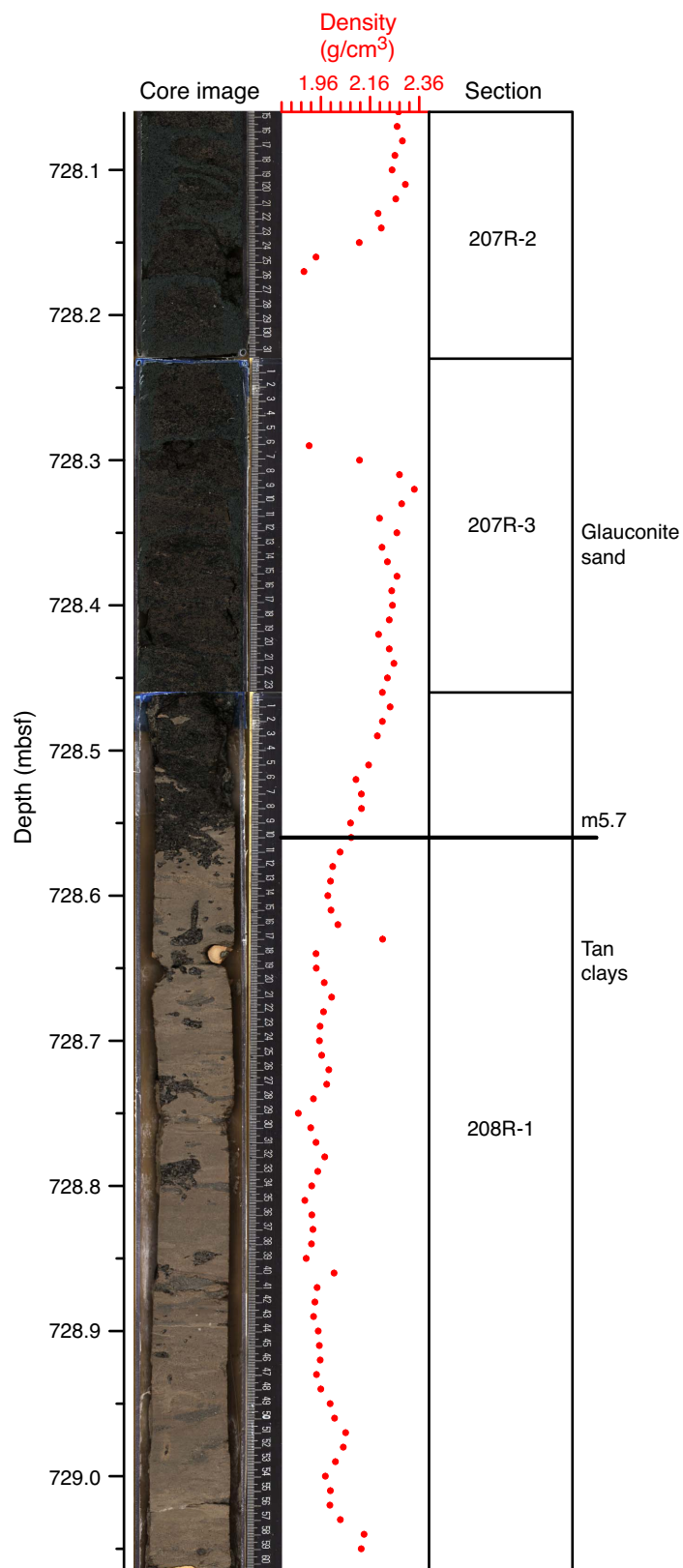
Figure F65. Synthesis of Hole M0029A, including lithology; lithostratigraphy; lithology, lithostratigraphy, well (total gamma ray [TGR], K, U, and Th), and multisensor core logger (MSCL) data (natural gamma radiation [NGR]); acoustic impedance from MSCL bulk density; depositional environments and correlating surfaces; and predicted depth ranges based on velocity. SF = shoreface, SOT = shoreface–offshore transition, OFF = offshore, dOFF = distal offshore. See Figure F1 for lithology legend.
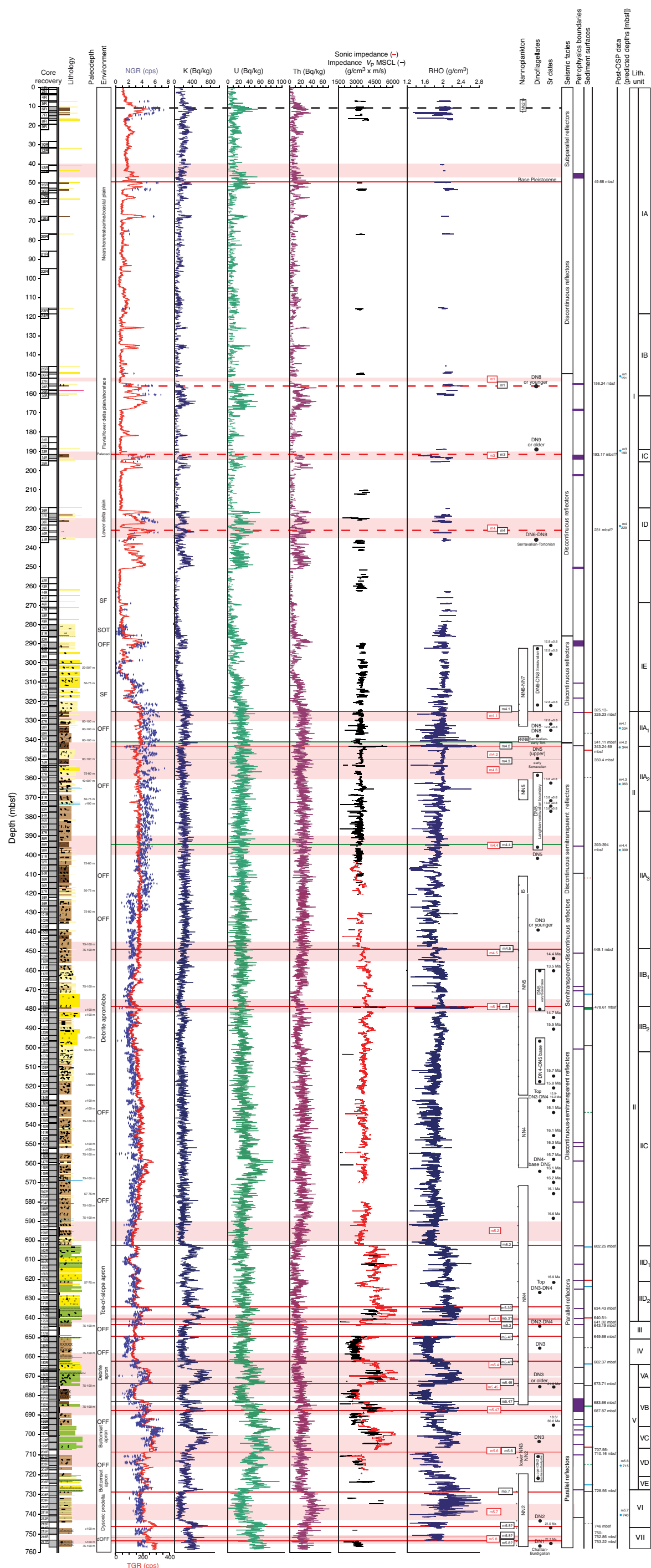
Table T1. Coring summary, Hole M0029A. (**Continued on next three pages.**)

Hole M0029A
  Latitude: 39°31.170500'N
  Longitude: 73°24.792500'W
  Seafloor (drill pipe measurement from rig floor, mbrf): 52.46
  Distance between rig floor and sea level (m): 16.49
  Water depth (drill pipe measurement from sea level, m): 35.97
  Total penetration (mbsf): 754.55
  Total drilled interval (m): 609.44

Core	Date (2009)	Time (UTC)	Depth (mbsf) Top	Depth (mbsf) Bottom	Length (m) Cored	Length (m) Recovered	Recovery (%)	Comments
313-M0029A-								
1R	21 June	1705	0.00	0.80	0.80	0.00	0.0	Fluorescent microspheres—bag did not burst
2R	21 June	1730	0.80	3.30	2.50	0.00	0.0	Fluorescent microspheres—bag did not burst
3R	21 June	1803	3.30	3.85	0.55	0.00	0.0	Fluorescent microspheres—bag did not burst
4R	21 June	1900	3.85	6.90	3.05	0.06	2.0	Fluorescent microspheres
5R	21 June	1915	6.90	9.95	3.05	0.62	20.3	Fluorescent microspheres
6R	21 June	1950	9.95	13.00	3.05	2.25	73.8	Fluorescent microspheres
7R	21 June	2020	13.00	16.05	3.05	1.77	58.0	Fluorescent microspheres
8R	21 June	2045	16.05	19.10	3.05	1.22	40.0	Fluorescent microspheres
9R	21 June	2120	19.10	22.15	3.05	0.07	2.3	Fluorescent microspheres
								*****Drilled from 22.15 to 28.25 mbsf***** Circulated for 30 minutes
10R	21 June	2330	28.25	31.30	3.05	0.03	1.0	Fluorescent microspheres—bag did not burst
11R	22 June	0005	31.30	31.60	0.30	0.01	3.3	Fluorescent microspheres
12R	22 June	0045	31.60	34.35	2.75	0.12	4.4	Fluorescent microspheres—bag did not burst
								*****Drilled from 34.35 to 40.45 mbsf*****
13R	22 June	0155	40.45	43.50	3.05	0.14	4.6	Fluorescent microspheres
14R	22 June	0310	43.50	44.50	1.00	0.29	29.0	
								*****Drilled from 44.5 to 49.6 mbsf*****
15R	22 June	0450	49.60	52.65	3.05	0.56	18.7	Fluorescent microspheres
16R	22 June	0535	52.65	55.70	3.05	1.22	40.0	Fluorescent microspheres
17R	23 June	0815	55.11	58.16	3.05	0.00	0.0	
18R	23 June	0855	58.16	61.21	3.05	0.06	2.0	
								*****Drilled from 61.21 to 67.31 mbsf*****
19R	23 June	1150	67.31	69.36	2.05	0.23	11.2	Twist off bit and reamer
								*****Drilled from 69.36 to 76.46 mbsf*****
20R	24 June	0650	76.46	79.51	3.05	0.48	15.7	Plastic catcher inside liner
								*****Drilled from 79.51 to 85.61 mbsf*****
21R	24 June	1020	85.61	88.66	3.05	0.03	1.0	Mud polymer patches causing barrels to stick together
								*****Drilled from 88.66 to 94.76 mbsf*****
22R	24 June	1330	94.76	97.81	3.05	0.04	1.3	
								*****Drilled from 97.81 to 115.41 mbsf*****
23R	25 June	1425	115.41	118.46	3.05	0.74	24.3	
24R	25 June	1530	118.46	120.63	2.17	0.10	4.6	Bit blocked off
								*****Drilled from 120.63 to 145.91 mbsf*****
25R	25 June	2120	145.91	148.96	3.05	0.12	3.9	
26R	25 June	2230	148.96	152.01	3.05	1.04	34.1	
27R	26 June	0000	152.01	155.06	3.05	0.03	1.0	
28R	26 June	0100	155.06	158.11	3.05	1.15	37.7	
29R	26 June	0210	158.11	159.87	1.76	0.42	23.9	Bit blocked off
30R	26 June	0325	159.87	162.54	2.67	0.96	36.0	Bit blocked off
								*****Drilled from 162.54 to 182.51 mbsf*****
31R	26 June	1020	182.51	185.56	3.05	0.00	0.0	Difficulties latching core barrel
32R	26 June	1150	185.56	188.61	3.05	0.00	0.0	
33R	26 June	1330	188.61	191.66	3.05	0.32	10.5	
34R	26 June	1450	191.66	194.71	3.05	2.18	71.5	
35R	26 June	1700	194.71	197.26	2.55	0.43	16.9	
								*****Drilled from 197.26 to 219.11 mbsf*****
36R	27 June	0100	219.11	222.16	3.05	0.19	6.2	
37R	27 June	0330	222.16	225.21	3.05	2.09	68.5	Some metal leaves of basket catcher twisted off and inside core
38R	27 June	0430	225.21	228.26	3.05	1.32	43.3	Some metal leaves of basket catcher twisted off and inside core
39R	27 June	0530	228.26	231.31	3.05	0.02	0.7	
40R	27 June	0815	231.31	234.36	3.05	0.70	23.0	
41R	27 June	1043	234.36	237.41	3.05	1.63	53.4	
								*****Drilled from 237.41 to 255.71 mbsf*****
42R	27 June	1745	255.71	258.76	3.05	0.01	0.3	
43R	27 June	1925	258.76	261.81	3.05	0.01	0.3	
44R	27 June	2055	261.81	264.86	3.05	0.57	18.7	
45R	27 June	2200	264.86	267.91	3.05	0.21	6.9	New tungsten carbide bit tried
46R	27 June	2310	267.91	270.96	3.05	0.22	7.2	
47R	28 June	0015	270.96	274.01	3.05	0.92	30.2	

Table T1 (continued). (Continued on next page.)

Core	Date (2009)	Time (UTC)	Depth (mbsf) Top	Bottom	Length (m) Cored	Recovered	Recovery (%)	Comments
48R	28 June	0145	274.01	277.06	3.05	0.24	7.9	
49R	28 June	0255	277.06	280.11	3.05	0.50	16.4	
50R	28 June	0415	280.11	283.16	3.05	2.71	88.9	Core undersized with spiral scoring
51R	28 June	0530	283.16	286.21	3.05	2.92	95.7	
52R	28 June	0800	286.21	289.26	3.05	0.46	15.1	
53R	28 June	1010	289.26	292.31	3.05	3.04	99.7	
54R	28 June	1215	292.31	292.70	0.39	0.46	118.0	
55R	28 June	1435	292.70	294.52	1.82	0.20	11.0	
56R	28 June	1700	294.52	298.41	3.89	0.99	25.5	
57R	28 June	1940	298.41	301.46	3.05	2.33	76.4	
58R	28 June	2050	301.46	304.51	3.05	1.71	56.1	
59R	28 June	2200	304.51	307.56	3.05	2.63	86.2	
60R	28 June	2315	307.56	310.61	3.05	2.96	97.1	
61R	29 June	0035	310.61	313.66	3.05	2.53	83.0	
62R	29 June	0150	313.66	316.71	3.05	1.98	65.0	
63R	29 June	0310	316.71	319.76	3.05	1.56	51.2	
64R	29 June	0425	319.76	322.81	3.05	2.46	80.7	
65R	29 June	0545	322.81	325.86	3.05	3.05	100.0	
66R	29 June	0825	325.86	328.91	3.05	2.32	76.1	Core oversized with cuttings packed around
67R	29 June	1035	328.91	331.96	3.05	2.95	96.7	Lost core in shoe
68R	29 June	1235	331.96	335.01	3.05	3.14	103.0	
69R	29 June	1455	335.01	338.06	3.05	2.90	95.1	
70R	29 June	1735	338.06	341.11	3.05	3.00	98.4	
71R	29 June	1955	341.11	343.32	2.21	2.53	114.5	Bit blocked off
72R	29 June	2140	343.32	346.37	3.05	2.99	98.0	
73R	29 June	2315	346.37	350.26	3.89	3.37	86.6	
74R	30 June	0040	350.26	353.31	3.05	2.33	76.4	Core lifter missing—assumed in core, ~70 cm core slipped on retrieval
75R	30 June	0210	353.31	354.35	1.04	1.07	102.9	Bit blocked off trying to recover slipped core
76R	30 June	0345	354.35	356.36	2.01	2.09	104.0	Basket catcher and lifter twisted
77R	30 June	0500	356.36	359.41	3.05	2.38	78.0	
78R	30 June	0655	359.41	362.46	3.05	3.11	102.0	
79R	30 June	0840	362.46	365.51	3.05	3.04	99.7	
80R	30 June	1025	365.51	368.56	3.05	1.60	52.5	Basket catcher broke—bottom half of core slipped on retrieval
81R	30 June	1215	368.56	371.61	3.05	3.29	107.9	
82R	30 June	1420	371.61	374.66	3.05	2.72	89.2	Core undercut by basket catcher at top
83R	30 June	1600	374.66	377.71	3.05	2.77	90.8	
84R	30 June	1725	377.71	380.76	3.05	3.22	105.6	
85R	30 June	1905	380.76	383.81	3.05	3.27	107.2	
86R	30 June	2025	383.81	386.86	3.05	3.03	99.3	Core undercut by basket catcher at top
87R	30 June	2150	386.86	389.91	3.05	2.98	97.7	Basket catcher ripped out of shoe and into core
88R	30 June	2320	389.91	392.96	3.05	2.67	87.5	Basket catcher ripped out of shoe and into core
89R	1 July	0050	392.96	396.01	3.05	2.88	94.4	Core lifter spring ripped out of shoe and into core
90R	1 July	0235	396.01	399.06	3.05	3.01	98.7	Basket catcher leaves in core
91R	1 July	0415	399.06	402.11	3.05	2.85	93.4	Core undersized
92R	1 July	0720	402.11	405.16	3.05	2.83	92.8	
93R	1 July	0925	405.16	408.21	3.05	3.18	104.3	Core undersized
94R	1 July	1125	408.21	411.26	3.05	3.01	98.7	
95R	1 July	1305	411.26	414.31	3.05	2.92	95.7	
96R	1 July	1450	414.31	417.36	3.05	3.31	108.5	
97R	1 July	1620	417.36	420.41	3.05	3.15	103.3	
98R	1 July	1915	420.41	423.46	3.05	1.62	53.1	Core liner jammed—damage to bottom of core on extraction
99R	1 July	2100	423.46	426.51	3.05	2.80	91.8	Basket catcher leaves in core
100R	1 July	2230	426.51	429.56	3.05	3.34	109.5	Compression to liner
101R	2 July	0025	429.56	432.61	3.05	3.25	106.6	Core lifter missing from shoe
102R	2 July	0200	432.61	435.66	3.05	3.03	99.3	Core lifter and basket catcher missing from shoe—metal leaves may remain in core
103R	2 July	0355	435.66	438.71	3.05	0.00	0.0	Slipped core on retrieval
104R	2 July	0535	438.71	439.01	0.30	1.16	386.7	
105R	2 July	0835	439.01	441.76	2.75	2.50	90.9	
106R	2 July	1035	441.76	444.81	3.05	2.97	97.4	
107R	2 July	1205	444.81	447.86	3.05	2.85	93.4	
108R	2 July	1345	447.86	450.91	3.05	3.41	111.8	
109R	2 July	1510	450.91	453.96	3.05	2.85	93.4	
110R	2 July	1705	453.96	457.01	3.05	2.05	67.2	
111R	2 July	1950	457.01	460.06	3.05	3.51	115.1	Basket catcher leaves in core
112R	2 July	2115	460.06	463.11	3.05	3.23	105.9	Basket catcher leaves in core
113R	2 July	2235	463.11	466.16	3.05	1.82	59.7	Basket catcher leaves in core
114R	3 July	0001	466.16	469.21	3.05	3.00	98.4	Basket catcher leaves in core

Table T1 (continued).

Core	Date (2009)	Time (UTC)	Depth (mbsf)		Length (m)		Recovery (%)	Comments
			Top	Bottom	Cored	Recovered		
115R	3 July	0115	469.21	472.26	3.05	2.31	75.7	
116R	3 July	0230	472.26	475.31	3.05	2.78	91.2	
117R	3 July	0335	475.31	478.36	3.05	3.17	103.9	Basket catcher leaves in core
118R	3 July	0505	478.36	479.50	1.14	1.17	102.6	
119R	3 July	0700	479.50	481.41	1.91	0.37	19.4	
120R	3 July	0910	481.41	484.46	3.05	3.03	99.3	
121R	3 July	1100	484.46	487.51	3.05	3.14	103.0	
122R	3 July	1250	487.51	490.56	3.05	3.03	99.3	
123R	3 July	1440	490.56	493.61	3.05	3.09	101.3	
124R	3 July	1635	493.61	496.66	3.05	2.86	93.8	
125R	3 July	1830	496.66	499.71	3.05	3.05	100.0	
126R	3 July	2035	499.71	502.51	2.80	2.92	104.3	Basket catcher leaves in core
127R	3 July	2205	502.51	505.81	3.30	3.40	103.0	Basket catcher leaves in core
128R	3 July	2335	505.81	508.86	3.05	3.30	108.2	Basket catcher leaves in core
129R	4 July	0055	508.86	511.91	3.05	3.35	109.8	
130R	4 July	0215	511.91	514.96	3.05	2.99	98.0	
131R	4 July	0335	514.96	518.01	3.05	3.19	104.6	Basket catcher leaves in core
132R	4 July	0450	518.01	521.06	3.05	3.20	104.9	
133R	4 July	0640	521.06	524.11	3.05	3.28	107.5	
134R	4 July	0905	524.11	527.16	3.05	0.30	9.8	Core slipped on retrieval
135R	4 July	1035	527.16	527.46	0.30	1.06	353.3	Short run to collect slipped core
136R	4 July	1220	527.46	530.21	2.75	2.14	77.8	
137R	4 July	1445	530.21	533.26	3.05	3.51	115.1	
138R	4 July	1625	533.26	536.31	3.05	2.56	83.9	
139R	4 July	1845	536.31	539.31	3.00	2.78	92.7	
140R	4 July	2030	539.31	542.41	3.10	3.55	114.5	Core lifter and basket catcher in cores
141R	4 July	2155	542.41	545.46	3.05	3.00	98.4	
142R	4 July	2355	545.46	548.51	3.05	3.33	109.2	Core lifter spring in core
143R	5 July	0150	548.51	551.56	3.05	3.06	100.3	
144R	5 July	0345	551.56	554.61	3.05	0.65	21.3	
145R	5 July	0500	554.61	555.06	0.45	1.78	395.6	
146R	5 July	0635	555.06	557.66	2.60	2.69	103.5	
147R	5 July	1030	557.66	560.71	3.05	2.07	67.9	
148R	5 July	1215	560.71	563.76	3.05	3.17	103.9	
149R	5 July	1400	563.76	566.81	3.05	3.19	104.6	
150R	5 July	1535	566.81	569.86	3.05	3.01	98.7	
151R	5 July	1715	569.86	572.91	3.05	3.13	102.6	
152R	5 July	2015	572.91	575.96	3.05	3.13	102.6	Basket catcher leaves twisted—possible metal in core
153R	5 July	2215	575.96	579.01	3.05	3.07	100.7	
154R	5 July	2345	579.01	582.06	3.05	3.20	104.9	Basket catcher leaves twisted—possible metal in core
155R	6 July	0155	582.06	585.11	3.05	3.00	98.4	
156R	6 July	0320	585.11	588.16	3.05	3.11	102.0	Basket catcher leaves twisted—possible metal in core
157R	6 July	0505	588.16	591.21	3.05	3.22	105.6	
158R	6 July	0655	591.21	594.26	3.05	1.59	52.1	
159R	6 July	0855	594.26	597.31	3.05	3.05	100.0	
160R	6 July	1050	597.31	600.36	3.05	3.18	104.3	
161R	6 July	1245	600.36	603.41	3.05	3.04	99.7	
162R	6 July	1450	603.41	606.46	3.05	3.18	104.3	
163R	6 July	1700	606.46	609.51	3.05	2.91	95.4	
164R	6 July	1905	609.51	612.56	3.05	3.01	98.7	
165R	6 July	2050	612.56	615.61	3.05	3.10	101.6	
166R	6 July	2250	615.61	618.66	3.05	3.24	106.2	
167R	7 July	0100	618.66	621.71	3.05	3.04	99.7	
168R	7 July	0300	621.71	624.66	2.95	2.95	100.0	
169R	7 July	0500	624.66	627.81	3.15	1.90	60.3	
170R	7 July	0715	627.81	630.86	3.05	3.03	99.3	
171R	7 July	0945	630.86	633.91	3.05	3.06	100.3	
172R	7 July	1145	633.91	635.23	1.32	1.62	122.7	Stabilizing ring deterioration—replaced
173R	7 July	1435	635.23	636.96	1.73	1.64	94.8	
174R	7 July	1830	636.96	640.01	3.05	2.49	81.6	
175R	7 July	2040	640.01	643.06	3.05	3.58	117.4	
176R	7 July	2255	643.06	646.11	3.05	1.22	40.0	
177R	8 July	0050	646.11	649.16	3.05	0.00	0.0	Core slipped on retrieval
178R	8 July	0250	649.16	649.45	0.29	3.39	1169.0	Core undersized
179R	8 July	0440	649.45	652.21	2.76	2.73	98.9	Basket catcher leaves twisted—possible metal in core
180R	8 July	0620	652.21	655.26	3.05	3.11	102.0	
181R	8 July	0840	655.26	658.31	3.05	2.40	78.7	
182R	8 July	1040	658.31	661.36	3.05	2.88	94.4	
183R	8 July	1230	661.36	664.41	3.05	2.93	96.1	

Table T1 (continued).

Core	Date (2009)	Time (UTC)	Depth (mbsf) Top	Bottom	Length (m) Cored	Recovered	Recovery (%)	Comments
184R	8 July	1445	664.41	666.76	2.35	1.79	76.2	
185R	8 July	1640	666.76	667.46	0.70	0.30	42.9	
186R	8 July	1940	667.46	670.51	3.05	3.26	106.9	
187R	8 July	2135	670.51	671.71	1.20	1.75	145.8	
188R	8 July	2335	671.71	673.56	1.85	1.76	95.1	
189R	9 July	0130	673.56	676.61	3.05	1.68	55.1	
190R	9 July	0250	676.61	679.66	3.05	3.29	107.9	
191R	9 July	0425	679.66	682.71	3.05	2.16	70.8	Basket catcher leaves twisted—possible metal in core
192R	9 July	0625	682.71	685.76	3.05	3.52	115.4	
193R	9 July	0945	685.76	688.81	3.05	2.82	92.5	
194R	9 July	1200	688.81	691.86	3.05	2.69	88.2	
195R	9 July	1410	691.86	694.91	3.05	3.45	113.1	
196R	9 July	1645	694.91	697.96	3.05	3.04	99.7	
197R	9 July	2015	697.96	701.01	3.05	2.70	88.5	
198R	9 July	2245	701.01	704.06	3.05	2.79	91.5	Basket catcher leaves twisted—possible metal in core
199R	10 July	0100	704.06	707.11	3.05	3.17	103.9	
200R	10 July	0235	707.11	710.16	3.05	0.44	14.4	Core slipped on retrieval
201R	10 July	0425	710.16	711.78	1.62	1.36	84.0	Short run to collect slipped core
202R	10 July	0535	711.78	713.21	1.43	1.90	132.9	
203R	10 July	0910	713.21	716.26	3.05	2.13	69.8	
204R	10 July	1130	716.26	719.31	3.05	1.47	48.2	
205R	10 July	1330	719.31	722.36	3.05	3.51	115.1	
206R	10 July	1530	722.36	725.41	3.05	1.82	59.7	
207R	10 July	1740	725.41	728.46	3.05	3.12	102.3	Hole caved at end of run and pipe became stuck
208R	10 July	2020	728.46	731.51	3.05	2.21	72.5	Basket catcher leaves twisted—possible metal in core
209R	10 July	2225	731.51	734.56	3.05	3.58	117.4	
210R	11 July	0050	734.56	737.61	3.05	3.27	107.2	
211R	11 July	0310	737.61	740.66	3.05	2.55	83.6	
212R	11 July	0535	740.66	743.71	3.05	3.16	103.6	
213R	11 July	0900	743.71	746.76	3.05	0.26	8.5	
214R	11 July	1100	746.76	746.96	0.20	0.53	265.0	
215R	11 July	1330	746.96	749.81	2.85	3.12	109.5	
216R	11 July	1600	749.81	752.86	3.05	0.00	0.0	Core slipped on retrieval
217R	11 July	1820	752.86	754.55	1.69	3.49	206.5	Bit blocking off—probably due to recovery of slipped core from previous run

Table T2. Summary of lithostratigraphic units, Hole M0029A.

Units	Interval	Depth (m DSF)	Depositional environment	Age
Unit I	4R-1, 0 cm, to 65R-2, 80 cm	3.85–325.12	Nearshore, estuarine, coastal plain	late Pleistocene to late Miocene
Subunit IA	4R-1, 0 cm, to 24R-1, 10 cm	3.85–118.56	Nearshore, estuarine, coastal plain	
Subunit IB	25R-1, 0 cm, to 30R-1, 94 cm	145.91–160.81	Fluvial, lower delta plain, shoreface	
Subunit IC	33R-1, 0 cm, to 35R-2, 8 cm	188.61–195.12	Fluvial, lower delta plain (paleosol)	
Subunit ID	36R-1, 0 cm, to 41R-3, 8 cm	219.11–235.97	Lower delta plain	
Subunit IE	44R-1, 0 cm, to 65R-2, 80 cm	261.81–325.12	Shoreface–offshore transition to shoreface	
Unit II	65R-2, 80 cm, to 175R-1, 50 cm	325.12–640.51	Offshore	middle Miocene (Langhian)
Subunit IIA	65R-2, 80 cm, to 108R-1, 63 cm	325.12–448.49	Offshore	
IIA$_1$	65R-2, 80 cm, to 72R-1, 49 cm	325.12–343.81	Offshore	
IIA$_2$	72R-1, 49 cm, to 83R-2, 99 cm	343.81–377.15	Offshore	
IIA$_3$	83R-2, 99 cm, to 108R-1, 63 cm	377.15–448.49	Offshore	
Subunit IIB	108R-1, 63 cm, to 126R-2, 80 cm	448.49–502.01	Debrite apron	
IIB$_1$	108R-1, 63 cm, to 118R-1, 25 cm	448.49–478.61	Debrite apron/lobe	
IIB$_2$	118R-1, 25 cm, to 126R-2, 80 cm	478.61–502.01	Debrite apron/lobe	
Subunit IIC	126R-2, 80 cm, to 161R-2, 37 cm	502.01–602.25	Offshore	
Subunit IID	161R-2, 37 cm, to 175R-1, 50 cm	602.25–640.51	Toe-of-clinoform-slope apron	
IID$_1$	161R-2, 37 cm, to 167R2, 42 cm	602.25–620.59	Toe-of-slope apron	
IID$_2$	167R-2, 42 cm, to 175R-1, 50 cm	620.59–640.51	Toe-of-slope apron	
Unit III	175R-1, 50 cm, to 179R-2, 28 cm	640.51 –650.13	Offshore	early Middle to late Early Miocene (early Langhian to late Burdigalian)
Unit IV	179R-2, 28 cm, to 183R-2, 101 cm	650.13–663.88	Offshore	middle early Miocene (mid-Burdigalian)
Unit V	183R-2, 101 cm, to 208R-1, 9 cm	663.88–728.55	Stacked seaward of toe-of-slope aprons	middle early Miocene (early to mid-Burdigalian)
Subunit VA	183R-2, 101 cm, to 189R-1, 15 cm	663.88–673.61	Debrite apron	
Subunit VB	189R-1, 15 cm, to 196R-1, 93 cm	673.61–695.84	Offshore	
Subunit VC	196R-1, 93 cm, to 199R-CC, 11 cm	695.84–707.17	Debrite apron	
Subunit VD	199R-CC, 11 cm, to 205R-2, 75 cm	707.17–721.74	Offshore	
Subunit VE	205R-2, 75 cm, to 208R-1, 9 cm	721.74–728.55	Debrite apron	
Unit VI	208R-1, 9 cm, to 214R-1, 52 cm	728.55–747.27	Dysoxic prodelta	middle early Miocene (late Aquitanian to early Burdigalian)
Unit VII	214R-1, 52 cm, to 217R-CC, 11 cm	747.27–756.33	Distal offshore	Aquatanian

Table T3. Distribution of calcareous nannofossils, Hole M0029A. This table is available in an **oversized format.**

Table T4. Planktonic foraminifer occurrences and zonation. (**See table note.**) (**Continued on next two pages.**)

Core, section, interval (cm)	Depth (mbsf)	Planktonic foraminifer zone	Stage	Planktonic foraminifer abundance	Catapsydrax parvulus	Dentoglobigerina altispira altispira	Fohsella peripheroronda	Globigerina connecta	Globigerina praebulloides praebulloides	Globigerina woodi	Globigerinita glutinata	Globigerinoides mitra	Globigerinoides obliquus	Globigerinoides quadrilobatus	Globigerinoides sacculifer	Globigerinoides subquadratus	Globigerinoides triloba	Globoquadrina baroemoenensis	Globoquadrina dehiscens	Globoquadrina langhiana	Globoquadrina venezuelana	Globorotalia archeomenardii	Globorotalia continuosa	Globorotalia obesa	Globorotalia praescitula	Globorotaloides suteri	Paragloborotalia mayeri	Praeorbulina sicana	Sphaeroidinellopsis disjuncta	Comments
313-M0029A-																														
21R-CC, 0–3	85.61			B																										
22R-CC, 0–4	94.76			B																										
23R-CC, 0–2	116.13			B																										
24R-CC, 8–10	118.54			B																										
25R-CC, 0–2	146.01			B																										
26R-CC, 13–15	149.98			B																										
27R-CC, 0–3	152.01			B																										
28R-CC, 14–17	156.18			B																										
29R-CC, 13–15	158.51			B																										
30R-CC, 0–2	160.81			B																										
33R-CC, 0–2	188.72			B																										
35R-CC, 8–10	195.12			B																										
36R-CC, 0–2	219.28			B																										
37R-CC, 13–15	224.23	Unzoned	Unzoned	B																										
40R-CC, 12–14	231.99			B																										
44R-CC, 0–1	262.37			B																										
46R-CC, 0–1	268.12			B																										
48R-CC, 0–1	274.24			B																										
50R-CC, 0–1	282.81			B																										
52R-CC, 16–18	286.65			B																										
53R-CC, 11–14	292.27			B																										
56R-CC, 15–17	295.49			B																										
58R-CC, 7–8	303.16			B																										
60R-CC, 0–3	310.49																X														Globigerinoides subquadratus
62R-CC, 0–3	315.61			B																										
63R-CC, 0–2	318.25			B																										
64R-CC, 0–2	322.20			B																										
67R-CC, 0–2	331.84	N14 (M11) or older				X		X	X	X																			
68R-1, 145–150	333.41	M10–M11/N13–N14								X			X					X	X								X			LO Paragloborotalia mayeri (11.4 Ma)
70R-CC, 0–2	341.04			B																										
74R-2, 84–86	352.59			B																										
75R-CC, 21–23	354.37	N14 (M11) or older		B																										
77R-CC, 18–20	358.72	Unzoned	Serravallian	B																										
78R-1, 148–153	360.89			B																										
78R-CC, 0–3	362.49			B																										
81R-CC, 0–2	371.83						X		X	X	X	X				X			X	X	X	X				X	X				LO Fohsella peripheroronda (13.8 Ma)
82R-CC, 13–15	374.31	M7/N10						X	X	X						X							X	X	X			X			LO Globorotalia archeomenardii (13.9 Ma)
84R-CC, 19–20	380.91			B																										
86R-CC, 17–19	386.82			B																										

Table T4 (continued). (Continued on next page.)

Core, section, interval (cm)	Depth (mbsf)	Planktonic foraminifer zone	Stage	Planktonic foraminifer abundance	Catapsydrax parvulus	Dentoglobigerina altispira altispira	Fohsella peripheroronda	Globigerina connecta	Globigerina praebulloides praebulloides	Globigerina woodi	Globigerinita glutinata	Globigerinoides mitra	Globigerinoides obliquus	Globigerinoides quadrilobatus	Globigerinoides sacculifer	Globigerinoides subquadratus	Globigerinoides triloba	Globoquadrina baroemoenensis	Globoquadrina dehiscens	Globoquadrina langhiana	Globoquadrina venezuelana	Globorotalia archeomenardii	Globorotalia continuosa	Globorotalia obesa	Globorotalia praescitula	Globorotaloides suteri	Paragloborotalia mayeri	Praeorbulina sicana	Sphaeroidinellopsis disjuncta	Comments
88R-CC, 12–14	392.56			B																										
90R-CC, 7–9	399.00			B																										
92R-CC, 0–2	404.92							X	X	X																		X		
94R-2, 149–151	411.20			B																										
97R-3, 13–15	420.49					X																						X		Reworking
100R-CC, 32–34	429.83				X	X			X		X									X										
102R-3, 13–15	435.62			B																										
104R-CC, 0–4	439.83			B																										
107R-3, 64–66	447.64			B																										
108R-CC, 0–5	451.22																	X	X				X		X	X				
109R-CC, 0–3	453.73			B																										
110R-CC, 0–2	455.99			B																										
111R-CC, 14–17	460.49	M7/N10	Serravallian	B																										
112R-CC, 0–3	463.27			B																										
114R-CC, 0–5	469.11																		X						X					
116R-CC, 0–5	474.99			B																										
119R-CC, 10–12	479.85															X	X	X	X								X			
120R-CC, 13–15	484.42			LO			X		X						X		X			X			X			X			X	LO Fohsella peripheroronda (13.8 Ma)
122R-CC, 0–2	490.52			B																										
124R-2, 133–135	496.45			B																										
126R-CC, 17–19	502.61					X			X								X													
128R-CC, 10–12	509.09			B																										
130R-CC, 0–2	514.88															X														
132R-CC, 0–4	521.17								X	X			X		X		X								X					
135R-CC, 0–2	528.20								X									X									X			
137R-CC, 14–16	533.70								X	X			X		X	X	X	X					X		X			X	X	LO Praeorbulina sicanus (14.8 Ma)
139R-CC, 0–2	539.07								X									X					X		X					
141R-CC, 0–5	545.36			B																										
143R-CC, 8–10	551.55				X					X					X	X	X	X					X		X		X	X		
144R-1, 64–65	552.20				X				X	X					X	X	X								X		X			
145R, 0–4	556.35				X					X																				
146R-CC, 7–9	557.73			B																										
148R-CC, 0–4	563.84	M5–M6/N8–N9	Langhian	B																										
150R-2, 149–151	569.80				X	X			X	X					X	X	X	X	X						X					
152R-CC, 0–2	576.02			B																										
154R-CC, 14–16	582.19				X				X	X					X	X	X	X	X						X		X	X		
156R-CC, 0–3	588.19				X				X					X		X	X	X	X	X	X						X	X	X	
158R-CC, 20–22	592.78			B																										
161R-2, 150–152	603.38			B																										
164R-CC, 0–5	612.47			B																										

Table T4 (continued).

Core, section, interval (cm)	Depth (mbsf)	Planktonic foraminifer zone	Stage	Planktonic foraminifer abundance	Catapsydrax parvulus	Dentoglobigerina altispira altispira	Fohsella peripheroronda	Globigerina connecta	Globigerina praebulloides praebulloides	Globigerina woodi	Globigerinita glutinata	Globigerinoides mitra	Globigerinoides obliquus	Globigerinoides quadrilobatus	Globigerinoides sacculifer	Globigerinoides subquadratus	Globigerinoides triloba	Globoquadrina baroemoenensis	Globoquadrina dehiscens	Globoquadrina langhiana	Globoquadrina venezuelana	Globorotalia archeomenardii	Globorotalia continuosa	Globorotalia obesa	Globorotalia praescitula	Globorotaloides suteri	Paragloborotalia mayeri	Praeorbulina sicana	Sphaeroidinellopsis disjuncta	Comments
166R-CC, 0–4	618.81	M5–6/N8–9	Langhian	B																									
167R-2, 151–153	621.68					X										X	X								X			X		FO Proeorbulina sicanus (16.4 Ma)
169R-CC, 9–11	626.54	M3–4/N6–7		B																									
170R-2, 150–152	630.82			B																									
173R-1, 153–156	636.76			B																									
176R-CC, 30–32	644.26																								X					Globorotalia praescitula
178R-CC, 0–3	652.52		Burdigalian	B																									
179R-CC, 0–4	652.14			B																									
181R-2, 88–89	657.64								X	X														X		X				
183R-CC, 0–2	664.27			B																									
189R-CC, 16–18	675.22																						X		X					Reworking
192R-CC, 15–17	686.21			B																									
195R-CC, 10–12	695.29				X	X				X									X	X			X		X					
198R-CC, 0–4	703.76	Unzoned		B																									
201R-CC, 0–4	711.48			B																									
203R-2, 79–81	715.32			B																									
205R-CC, 13–15	722.80			B																									
208R-3, 14–16	730.65			B																									
209R-1, 0–4	731.51			B																									
210R-3, 25–27	737.81			B																									
214R-1, 51–53	747.73																		X											Reworking Turborotalia cerroazulensis
217R-1, 0–4	752.86			B																									
217R-CC, 11–13	756.33			B																									

Note: LO = last occurrence, FO = first occurrence.

Table T5. Dinocyst occurrences and zonation. This table is available in an **oversized format.**

Table T6. Benthic foraminifer occurrences and paleobathymetric interpretations. (**See table notes.**) (**Continued on next two pages.**)

Core, section, interval (cm)	Depth (mbsf)	Benthic foraminifer taxa	Preservation	Comments	Paleodepth estimate (m)
313-M0029A-					
21R-CC, 0–3	85.61	Barren			?
22R-CC, 0–4	94.76	Barren			?
23R-CC, 0–2	116.13	Barren			?
24R-CC, 8–10	118.54	Barren			?
25R-CC, 0–2	146.01	Barren			?
26R-CC, 13–15	149.98	Barren			?
27R-CC, 0–3	152.01	Barren			?
28R-CC, 14–17	156.18	Barren			?
29R-CC, 13–15	158.51	Barren			?
30R-CC, 0–2	160.81	Barren			?
33R-CC, 0–2	188.72	Barren			?
35R-CC, 8–10	195.12	Barren			?
36R-CC, 0–2	219.28	*Lenticulina* (1); polymorph (1); *Cibicidoides* (2); *Alabamina* (1); lots of *Stilostomella* fragments	P–G	Shells and foraminifers to Sr; rare foraminifers (none >250)	?
37R-CC, 13–15	224.23	Barren			?
39R-CC, 0–2	228.26	Barren			?
40R-CC, 12–14	231.99	Barren			?
44R-CC, 0–1	262.37	Barren			?
46R-CC, 0–1	268.12	Barren			?
48R-CC, 0–1	274.24	Barren			?
50R-CC, 0–1	282.81	Barren			?
52R-CC, 16–18	286.65	Barren			?
53R-CC, 11–14	292.27	Barren			?
56R-CC, 15–17	295.49	Barren			?
58R-CC, 7–8	303.16	*Pullenia bulloides* (1); agglutinants (1); *Cibicidoides* (1); *Stilostomella* fragments, *Nonionella pizarrensis* (1); *Nonionella* sp. (1)	P–G	Rare foraminifers	??25–50??
60R-CC, 0–3	310.49	*Hanzawaia* (15); *Buliminella gracilis* (very good preservation) (3); *Stilostomella* (1); *Gyroidinoides* or *Cibicidoides* (1)	P–VG		50–75
62R-CC, 0–3	315.61	Barren			?
63R-CC, 0–2	318.25	Barren			?
64R-CC, 0–2	322.20	Barren			?
67R-CC, 0–2	331.84	R: marginulinid; A: *Uvigerina juncea, Nonionella pizarrensis, Bolivina alazanensis*; F–C: *Buliminella gracilis, Hanzawaia*; Pan: A: *Buliminella gracilis, Bolivina*	P–G	Abundant foraminifers	80–100
68R-1,145–150	333.41	A: *Uvigerina juncea, Bolivina*; R–F: *Hanzawaia, Nonionella pizarrensis*; R: marginulinid	P–G	Abundant foraminifers	80–100
70R-CC, 0–2	341.04	A: *Lenticulina, Uvigerina juncea*; C–A: *Nonionella pizarrensis, Bolivina alazanensis*; R: *Dentalina*	P–VG	Some pyritized *Lent, Bol*, and *Uvig*	80–100
74R-2, 84–86	352.59	*Nonionella pizarrensis* (9); marginulinid (1); *Buliminella gracilis* (4); *Rectuvigerina lamelata* (1)	P–G	Very small sample	80–100
75R-CC, 21–23	354.37	Barren			?
77R-CC, 18–20	358.72	*Uvigerina juncea* (4); *Bolivina alazanensis* (4); *Buliminella gracilis* (2); *Lenticulina* (2); *Nonionella pizarrensis* (15)	P–G		75–80
78R-1, 148–153	360.89	Barren			?
78R-CC, 0–3	362.49	A: *Nonionella pizarrensis*; C: *Lenticulina*; F: *Hanzawaia*, R: *Bolivina, Buliminella gracilis, Uvigerina juncea*	P–G	Abundant foraminifers	40–60 (to ?75)
81R-CC, 0–2	371.83	A: *Nonionella pizarrensis*; R: *Lenticulina, Buliminella gracilis, Fissurina*; C: *Hanzawaia*	P–E	Abundant foraminifers	50–75
82R-CC, 13–15	374.31	A: *Lenticulina, Hanzawaia concentrica, Nonionella pizarrensis, Bolivina paula*; C: *Buliminella gracilis, Uvigerina juncea*; R: *Cibicidoides*, polymorph, *Stilostomella, Fissurina, Pararotalia*	P–E		>100 (shallow end)
84R-CC, 19–20	380.91	Barren			?
86R-CC, 17–18	386.82	Barren			?
88R-CC, 12–14	392.56	Barren			?
90R-CC, 7–9	399.00	Barren			?
92R-CC, 0–2	404.92	*Lenticulina,* (7); *Dentalina* (1); *Nonionella pizarrensis* (2); *Bolivina* (3); *Buliminella gracilis* (5); *Uvigerina juncea* (2)	P–E		75–80

Core, section, interval (cm)	Depth (mbsf)	Benthic foraminifer taxa	Preservation	Comments	Paleodepth estimate (m)
94R-2, 149–151	411.20	Barren			?
97R-3, 13–15	420.49	Pan: A: *Bolivina paula, Bolivina* sp., *Buliminella elegantissima, Buliminella gracilis* (good preservation); *Anomalinoides* (1); *Pararotalia* (1); *Buliminella gracilis* (1)	P–G		50–75
99R-2, 128–130	426.24	Barren			?
100R-CC, 32–34	429.83	*Buliminella gracilis* (2); *Uvigerina juncea* (1); *Nonionella pizarrensis* (1); Pan: *Bolivina, Buliminella gracilis*	E	Rare foraminifers	75–80
102R-CC, 13–15	435.26	Barren			?
104R-CC, 0–4	439.83	Barren			?
107R-3, 64–66	447.64	Pan: *Buliminella gracilis*; A: *Lenticulina, Nonionella pizarrensis, Buliminella gracilis, Uvigerina juncea*; R: *Fissurina*, polymorph, *Quinqueloculina, Pararotalia, Hanzawaia*	P–E	Abundant foraminifers	75–100
108R-CC, 0–5	451.22	Pan: *Buliminella gracilis, Bolivina*; A: *Uvigerina juncea, Buliminella gracilis, Bolivina floridana, Nonionella pizarrensis*; C: *Lenticulina*; R: *Bulimina mexicana*	P–E	Abundant foraminifers	75–100
109R-CC, 0–3	453.73	Barren			?
110R-CC, 0–2	455.99	Barren			?
111R-CC, 14–17	460.49	Barren			?
112R-CC, 0–2	463.27	Barren			?
114R-CC, 0–5	469.11	*Lenticulina, Hanzawaia concentrica/Hanzawaia hughesi* (poor/good); Exc: *Buliminella gracilis, Uvigerina juncea, Nonionella pizarrensis*; *Cibicidoides* (poor)	P–E		75–100 (dash 50–75)
116R-CC, 0–5	474.99	Barren			?
119R-CC, 10–12	479.85	A: *Lenticulina, Hanzawaia concentrica, Uvigerina juncea, Bolivina floridana*; F–C: *Cibicidoides pachyderma*; R: *Cancris sagra, Nonionella pizarrensis, Oridorsalis, Cassidulina, Rectuvigerina lamelata*, polymorph, *Nonion*	P–E		>100
120R-CC, 13–15	484.42	F–C: *Cibicidoides pachyderma, Cibicidoides* spp., *Uvigerina juncea, Buliminella gracilis, Lenticulina, Hanzawaia mantaensis*; R: agglutinants, *Nonionella pizarrensis*	P–G	Abundant foraminifers	>100
122R-CC, 0–2	490.52	Barren			?
124R-2, 133–135	496.45	P–G: *Hanzawaia concentrica, Cibicidoides pachyderma, Uvigerina juncea*; VG: *Nonionella pizarrensis, Lenticulina*	P–VG	Few to rare foraminifers	>100 or transported deepwater
126R-CC, 17–19	502.61	A: *Hanzawaia concentrica* (poor), *Buliminella gracilis* (exc); F: *Nonionella pizarrensis* (exc); R: *Pararotalia, Uvigerina juncea* (exc), *Bolivina alazanensis*, agglutinants, *Cibicidoides* (poor–good)	P–E		50–75
128R-CC, 10–12	509.09	Barren			?
130R-CC, 0–2	514.88	A: *Lenticulina, Hanzawaia concentrica/Hanzawaia hughes*i, *Uvigerina juncea* and *Buliminella gracilis* (exc pres); C: *Nonionella pizarrensis*; R: *Cassidulina, Stilostomella*; C–A: *Cibicidoides* (mod)	P–E		100
132R-CC, 0–4	521.17	C–A: *Lenticulina, Nonionella pizarrensis, Uvigerina juncea, Buliminella gracilis, Hanzawaia*; E: *Bolivina floridana, Cibicidoides pachyderma, Cibicidoides* sp., agglutinants, miliolids, *Pararotalia, Textularia, Stilostomella, Globobulimina* sp.	E	Abundant foraminifers	>100
135R-CC, 0–2	528.20	C–A: *Lenticulina, Nonionella pizarrensis, Uvigerina juncea, Hanzawaia*; F–C: *Bolivina paula, Cibicidoides* sp., polymorph, *Stilostomella*	E	Abundant foraminifers	>100
137R-CC, 14–16	533.70	C–A: *Lenticulina, Uvigerina juncea, Hanzawaia*; C: *Nonionella pizarrensis, Bulimina mexicana, Buliminella gracilis*; F: *Cibicidoides pachyderma, Cibicidoides* sp., *Cassidulina crassa*, miliolid; Pan: *Bolivina paula*	E		>100
139R-CC, 0–2	539.07	A: *Lenticulina, Uvigerina juncea, Nonionella pizarrensis, Hanzawaia*; R: *Buliminella gracilis, Rectuvigerina lamelata*, polymorph	P–E		75–100
141R-CC, 0–5	545.36	Barren			?
143R-CC, 8–10	551.55	A: *Rectuvigerina lamelata, Nonionella pizarrensis, Bolivina paula, Bolivina tectiformis, Buliminella gracilis*; C: *Lenticulina, Hanzawaia concentrica*; R–F: *Spiroloculina, Hanzawaia mantaensis*; R: *Globocassidulina subglobosa, Bulimina mexicana, Uvigerina*; Pan: *Buliminella gracilis*	P–E		>100
144R-1, 64–65	552.20	A-*Bolivina paula, Bolivina tectiformis*; C–A: *Rectuvigerina lamelata, Buliminella gracilis*; R–F: *Hanzawaia mantaensis, Uvigerina, Spirosigmoilina, Bulimina mexicana, Cibicidoides pachyderma*	E	Very small sample	>100
145R-CC, 0–4	556.35	A *Nonionella pizarrensis, Uvigerina juncea*; C: *Buliminella gracilis, Lenticulina, Hanzawaia*	P–E		75–100
146R-CC, 7–9	557.73	Barren			?
148R-CC, 0–4	563.84	Barren			?
150R-2, 149–151	569.80	C–A: *Lenticulina, Uvigerina, Nonionella pizarrensis, Buliminella gracilis, Cassindulina laevigata*; R: *Pararotalia*, polymorph, *Cibicidoides pachyderma*; Pan: planktonic foraminfer, *Buliminella gracilis*		Abundant foraminifers	75–100 (deeper than 145R-CC)

Table T6 (continued).

Core, section, interval (cm)	Depth (mbsf)	Benthic foraminifer taxa	Preservation	Comments	Paleodepth estimate (m)
152R-CC, 0–2	576.02	A: *Lenticulina, Cassidulina laevigata*; C: *Nonionella pizarrensis*; F–C: *Buliminella gracilis*; R–F: polymorph, *Bulimina mexicana, Hanzawaia mantaensis, Hanzawaia concentrica/hughesi, Spirosigmoilina, Textularia, Cibicidoides* spp.	P–E	Abundant planktonics and benthics	50–75, dash to 100
154R-CC, 14–16	582.19	Pan: A: *Hanzawaia concentrica, Bolivina tectiformis*; A: *Uvigerina juncea, Bolivina paula, Buliminella gracilis*; C: *Nonionella pizarrensis*; R: *Rectuvigerina lamelata, Cassidulina laevigata, Hanzawaia concentrica*		Abundant foraminifers	75–100
156R-CC, 0–3	588.19	A: *Uvigerina juncea, Bolivina paula*; C: *Buliminella gracilis, Nonionella pizarrensis, Lenticulina*; R–F: *Rectuvigerina lamelata, Bulimina mexicana*, polymorph	G–E		75–100
158R-CC, 20–22	592.78	Barren			?
161R-2, 150–152	603.38	Barren			?
164R-CC, 0–5	612.47	Barren			?
166R-CC, 0–4	618.81	Barren			?
167R-2, 151–153	621.68	A-*Bolivina paula, Bolivina tectiformis*; C: *Buliminella gracilis, Hanzawaia concentrica* (mod pres); F: *Uvigerina*; R: *Globocassidulina subglubosa; Cassidulina laevigata*	M–E	Abundant foraminifers	50–75
169R-CC, 9–11	626.54	Barren			?
170R-2, 150–152	630.82	Barren			?
173R-1, 153–156	636.76	Barren			?
176R-CC, 30–32	644.26	Pan: *Bolivina tectiformis, Buliminella gracilis, Uvigerina juncea, Stilostomella, Cibicidoides pachy*derma; A: *Uvigerina juncea*; R: *Buliminella gracilis, Textularia, Rectuvigerina lamelata*; F–R: *Hanzawaia concentrica/hughesi*	G–E	Very small sample	75–100 (deep end)
178R-CC, 0–3	652.52	C–A: *Lenticulina, Nonionella pizarrensis, Hanzawaia concentrica/hughesi, Uvigerina juncea, Buliminella gracilis*; F–C: *Cibicidoides pachyderma, Textularia, Gyroidinoides, Pararotalia, Chilostomella, Fursenkoina*	P–G		100 with downslope tranport; low O2 porewater
179R-CC, 0–4	652.14	Barren			?
181R-2, 88–90	657.64	A: *Uvigerina juncea*, F–C: *Hanzawaia, Nonionella pizarrensis, Buliminella gracilis;* few foraminifers in pan: *Nonionella pizarrensis, Buliminella gracilis, Bolivina tectiformis*	E	Very small sample	75–100
183R-CC, 0–2	664.27	Barren			?
189R-CC, 16–18	675.22	*Uvigerina juncea* (3); *Nonionella pizarrensis* (3); *Hanzawaia* (2); *Lenticulina* (3); *Cibicidoides pachyderma* (2); *Bolivina* (5); *Buliminella gracilis* (1); *Buliminella* sp. (2); *Spirosigmoilina* (2); *Tritaxia* (1)	G–E	Very small sample	75–100 (deep end)
192R-CC, 15–17	686.21	*Uvigerina juncea* (5); *Cibicidoides pachyderma* (4); *Nonionella pizarrensis* (1)	E		75–100 (deep end)
195R-CC, 10–12	695.29	*Lenticulina*, marginulinids, polymorph, *Bulimina mexicana, Buliminella gracilis*, agglutinants, A: *Cibicidoides pachyderma, Pullenia bulloides, Rectuvigerina lamelata, Cibicidoides crebbsi, Oridorsalis, Melonis pompilioides*	P–E	Abundant planktonics and benthics, especially in pan; diverse, dw assemblage	>100
198R-CC, 0–4	703.76	Barren			?
201R-CC, 0–4	711.48	Barren			?
203R-CC, 79–81	715.32	Barren			?
205R-CC, 13–15	722.80	Barren			?
208-CC, 14–16	730.65	Barren			?
209R-1, 0–4	731.51	Barren			?
210R-3, 25–27	737.81	Barren			?
214R-1, 51–53	747.73	*Cibicidoides pachyderma, Oridorsalis, Hanzawaia mantaensis, Bolivina, Gyroidinoides, Uvigerina, Buliminella gracilis, Lenticulina*, polymorph; Pan: quartz and glauconite with foraminifers	P–M; a few exc (*Orid, Bol*)		>100
217R-1, 0–4	752.86	A: *Uvigerina juncea*, C: *Lenticulina, Bigenerina, Buliminella gracilis, Hanzawaia mantaensis, Bolivina, Cibicidoides pachyderma, Cibicidoides crebbsi*; R: *Fissurina, Plectofrondicularia*; Pan: *Buliminella, Bolivina, Stilostomella*	P–VG		>100 shallower than 214
217R-CC, 11–13	756.33	*Plectofrondicularia*, polymorph, *Uvigerina juncea, Buliminella gracilis*; Pan: *Buliminella gracilis*, rare foraminifers	P–G		75–100

Notes: Abundance: A = abundant; C = common; Fr = frequent, R = rare; F = few, P = present. Polymorph = *Guttulina austriaca, Guttulina candata,* undifferentiated *polymorphinids. Nonionella pizarrensis* includes possible *Nonionella grateloupi. Buliminella gracilis = Caucasina elongata? Gyroidinoides* includes possible *Gyroidinoides nipponica.* Preservation: E = excellent; G = good; M = moderate; P = poor; VG = very good.

Table T7. Palynomorph data and remarks on dominant tree taxa. (**See table note.**)

Core, section, interval (cm)	Depth (mbsf)	Nonsaccate arboreal pollen	Herbal pollen	Cyperaceae and Poaceae pollen	Pollen spores	Fungal spores	Dinocysts	Foraminifer combined	All bisaccates including reworked	Nonsaccate arboreal pollen + herbal pollen	Dinocyst + foraminifer test linings	(Dinocysts + foraminifer test linings)/(nonsaccate aboreal pollen + herbal pollen)	Remarks
28R-CC, 14–17	156.18	93	9	3	1	0	6	3.3	13	102	9.3	0.0915	
33R-CC	188.72	92	12	3	1	1	0	0.7	19.5	104	0.7	0.0064	Rather high amount of herb pollen, probably steppic areas in the hinterland
38R-CC, 16–18	226.51	45	6	0	1	0	3	1.0	24	51	4.0	0.0784	Probably hickory-oak forest, but also rather some open landscapes as indicated by herbal pollen, no beech pollen, generally low amount of pollen/sample
54R-CC, 14–16	292.75	94	6	7	0	0	12	0.3	12	100	12.3	0.1233	Presence of grass pollen 100% sure, oak pollen dominating
64R-CC	322.20	99	6	2	1	0	34	6.7	79	105	40.7	0.3873	Extraordinarily high abundance of beech pollen, hickory less abundant
73R-CC	349.70	95	11	5	1	2	9	4.0	19	106	13.0	0.1226	Probably hickory-oak forest, but also rather some open landscapes as indicated by herbal pollen
85R-CC, 12–15	384.00	97	7	3	1	0	26	11.0	15.5	104	37.0	0.3558	Oak pollen dominating (>half of total non-saccate pollen)
91R-CC	401.90	115	4	4	0	2	15	6.0	12	119	21.0	0.1765	Hickory pollen very frequent
104R-CC	439.83	121	5	4	0	0	13	5.7	49	126	18.7	0.1481	Hickory pollen very frequent
111R-CC, 14–17	460.49	97	3	0	0	0	10	0.0	58.5	100	10.0	0.1	Hickory pollen very frequent
119R-CC, 10–12	479.85	98	7	0	0	1	40	4.7	9.5	105	44.7	0.4254	
124R-2, 133–135	496.45	106	4	0	0	0	11	2.3	10.5	110	13.3	0.1212	
131R-CC, 14–16	518.13	100	1	0	0	0	18	5.0	14.5	101	23.0	0.2277	Very low amount of herb pollen
148R-CC	563.84	106	3	1	0	0	5	0.0	38	109	5.0	0.0459	Hickory pollen rare, high amounts of beech and elm pollen, very low amount of herb pollen
158R-CC, 20–22	592.78	108	1	1	0	0	8	2.7	49	109	10.7	0.0979	Very low amount of herb pollen
169R-CC, 9–11	626.54	91	3	1	1	0	13	0.3	26.5	94	13.3	0.1418	
176R-CC, 30–32	644.26	101	9	1	1	0	10	0.0	23	110	10.0	0.0909	Hickory pollen very frequent
180R-CC, 11–13	655.30	100	3	0	0	0	14	1.3	53	103	15.3	0.1489	Extraordinarily high amount of elm pollen
189R-CC, 16–18	675.22	95	8	0	0	0	15	0.0	90	103	15.0	0.1456	Hickory pollen very frequent
198R-CC	703.76	98	4	0	0	0	13	0.0	9.5	102	13.0	0.1275	
208R-CC, 14–16	730.65	95	7	0	1	1	24	6.3	101	102	30.3	0.2974	Pollen of different hemlock species abundant, extraordinarily high amount of bisaccate pollen and marine palynomorphs
209R-CC, 18–19	735.07	103	5	1	1	1	49	9.0	132.5	108	58.0	0.5370	Pollen of different hemlock species abundant, extraordinarily high amount of bisaccate pollen and marine palynomorphs
212R-CC, 22–25	743.79	122	7	4	1	0	44	4.0	52	129	48.0	0.3721	Hickory pollen very abundant, hickory/quercus 1/2: large hickory colonies, presence of eastern hemlock
217R-CC, 11–13	756.33	101	2	0	0	0	18	2.3	26	103	20.3	0.1974	

Note: Remarks concerning nonsaccate pollen like "high percentages" are always in relation to the production and transport potential of the different pollen types.

Table T8. Composition of interstitial water, Hole M0029A. This table is available in an **oversized format.**

Table T9. Total carbon, total organic carbon, total inorganic carbon, and total sulfur in sediment, Hole M0029A.

Core, section, interval (cm)	Depth (mbsf)	Carbon (wt%)			Total Sulfur (wt%)
		Total	Organic	Inorganic	
313-M0029A-					
5R-1, 37.0–38.0	7.28	1.81	0.66	1.15	0.23
8R-1, 97.0–98.0	17.03	0.30	0.07	0.23	0.09
15R-2, 3.0–4.0	50.05	0.60	0.22	0.38	0.31
15R-2, 3.0–4.0	50.05	0.57	0.23	0.34	0.31
67R-2, 60.0–61.0	331.02	1.81	1.08	0.73	0.33
68R-1, 36.0–37.0	332.33	2.09	1.93	0.15	1.43
68R-1, 36.0–37.0	332.33	2.08	1.99	0.09	1.45
69R-2, 48.0–49.0	337.01	2.07	1.74	0.33	1.70
69R-2, 48.0–49.0	337.01	2.29	1.77	0.53	1.78
71R-1, 28.0–29.0	341.40	2.47	2.42	0.06	3.34
74R-1, 6.0–7.0	350.33	1.27	1.11	0.16	2.22
78R-1, 0.0–1.0	359.42	0.76	0.66	0.10	0.67
81R-1, 0.0–1.0	368.57	2.05	1.84	0.21	2.16
83R-2, 116.0–117.0	377.33	—	1.30	—	—
86R-2, 100.0–101.0	386.32	2.34	1.86	0.48	2.06
89R-1, 70.0–71.0	393.67	2.22	1.46	0.76	0.96
89R-1, 70.0–71.0	393.67	2.25	1.47	0.78	1.04
90R-2, 45.0–46.0	397.96	2.05	1.63	0.42	1.70
90R-2, 45.0–46.0	397.96	2.03	1.66	0.37	1.81
93R-2, 47.0–48.0	406.97	2.73	2.45	0.28	2.18
96R-2, 18.0–19.0	416.00	2.79	2.73	0.06	2.90
104R-1, 10.0–11.0	438.82	2.83	2.35	0.48	2.14
104R-1, 10.0–11.0	438.82	2.82	2.42	0.40	2.21
144R-1, 21.0–22.0	551.78	8.23	7.93	0.30	4.20
150R-1, 80.0–81.0	567.62	2.86	2.53	0.33	2.40
156R-2, 112.0–113.0	587.78	2.69	2.07	0.62	1.98
160R-2, 80.0–81.0	599.69	2.78	2.69	0.09	1.97
172R-1, 29.0–30.0	634.21	1.05	0.65	0.41	0.96
180R-2, 68.0–69.0	654.41	3.33	2.84	0.49	1.82
187R-1, 28.0–29.0	670.80	1.65	0.72	0.92	1.53
196R-1, 80.0–81.0	695.72	4.99	3.41	1.57	2.03
208R-2, 43.0–44.0	730.40	1.15	0.66	0.49	2.60
211R-1, 60.0–61.0	738.22	0.50	0.40	0.10	0.14

Table T10. Summary of sediment mineralogy from X-ray diffraction, Hole M0029A. (**See table notes.**)

Intensity ratios	Mean	Max
Clay minerals	14.0	26.9
Kaolinite	5.6	12.8
Micas and Illite	4.1	7.4
Mixed layered clays	3.1	4.1
Smectite	1.2	2.6
Carbonates	7.1	23.1
Mg-rich calcite	0.9	2.5
Calcite	2.0	6.4
Siderite	1.2	4.2
Rhodochrosite	1.4	4.0
Dolomite and ankerite	0.6	3.6
Aragonite	1.1	2.6
Detrital minerals	70.6	103.1
Quartz	58.9	70.3
Plagioclase	3.8	13.4
Chlorite	2.3	4.6
K-Feldspar	2.0	4.7
Pyroxene	1.5	5.3
Zeolites	0.8	2.1
Gibbsite	0.3	1.2
Epidote	0.6	1.1
Amphibole	0.3	0.5
Authigenic minerals	8.4	16.3
Pyrite	2.8	5.4
Glauconite	1.4	3.5
Goethite	1.8	2.9
Apatite	1.0	2.2
Magnetite	0.9	1.5
Barite	0.5	0.8
Total	100.0	169.3

Notes: The original sum for the mean of all measured peak intensity ratios was 93.2%. After elimination of all clay minerals (4.55–4.4 Å, 4.1%), gypsum (1.0%), and halite (2.0%), this sum became 86.1%, which was then renormalized to 100% above.

Table T11. Downhole surfaces and trends from petrophysical and downhole measurements, Hole M0029A. (**See table note.**)

Depth (mbsf)	Depth Top	Depth Bottom	Total gamma ray	Th/K	U	Th	Conductivity	Sonic	V_p	Density	Resistivity	Magnetic susceptibility	Surface correspondence	Comments/Interpretation
	45	48	2 small peaks							Decrease			Base of Pleistocene 1 m below bottom of interval	
155.0	154.2	155	Increase										Predicted m1 depth 2 m above	
168.0	167.2	168	Decrease										No corresponding surface	Within core recovery gap
193.0	194	—	Low between two peaks						Peak	Peak			m3	
220.0	220	221	Increase										Subunit ID top 1 m above	
250.0	249.6	250.3	Decrease										No corresponding surface	Within core recovery gap
289.0	291	—	Peaks							Small changes			No corresponding surface	Just below a cemented horizon
310.0	305	310	Increase						Decrease				No corresponding surface	
318.0	—	—								Peak			No corresponding surface	
326.0	325	326								Decrease			Unit I/II boundary and m4.1	
343.5	—	—	Hole				Peak			Peak			m4.2 FS 3 m above and SB	Cemented horizon
395.0	—	—								Low		High zone	m4.4 surface 2 m above	
410.0	408.3	409.8								Increase			No corresponding surface	
449.0	—	—		Increase			Small low	Small peak		Small peak			Subunit IIA/IIB boundary and m4.5 surface	Small impedance peak
470.0	468	480				Hole							See below	
479.0	—	—					Hole	Peak		Peak			Subunit IIB$_1$/IIB$_2$ boundary and m5 surface	Cemented horizon
490.0	489	490				Decrease	Decrease			Increase			No corresponding surface	
500.8	—	—				Increase							No corresponding surface	
549.3	—	—						Increase	Increase				No corresponding surface	
551.0	—	—			Peak		Decrease		Decrease				Subunit IIB/IIC boundary 1 m below	
	558	559	Increase		Increase								No corresponding surface	Cemented horizon just below
580.0	—	—					Decrease	Increase					No corresponding surface	Cemented horizon
604.0	601	604		Increase			Decrease	Increase		Increase		Increase	Subunit IIC/IID boundary and m5.2 surface in interval	Cemented horizon just below
612.0	—	—					Hole			Peak			No corresponding surface	Cemented horizon
620.5	—	—					Small peak			Small peak		Small peak	Subunit IID$_1$/IID$_2$ boundary and recognized surface	Clear surface in acoustic image
625.0	—	—					Hole	Peak				Peak	Recognized surface just above	Cemented horizon
635.0	—	—	Increase				Decrease	Increase				Increase	m5.3 surface 0.5 m above	
640.0	—	—					Increase	Decrease		Decrease		Decrease	Unit II/III boundary <1 m below	Cemented horizons
643.2	—	—						Decrease	Decrease	Decrease		Decrease	Unnamed sequence boundary recognized	Cemented horizons
650.0	—	—	Peaks				Low	Peak				Peak	Unit III/IV boundary and m5.4 surface	Cemented horizons
666.0	664.5	666		Increase			Decrease	Increase	Increase	Increase		Increase	Unit IV/V boundary and ?SB 2 m above	
674.0	673	674		Decrease			Increase	Decrease	Decrease	Decrease		Decrease	m5.45 surface 1.5 m below	
682.0	—	—	Increase				Decrease			Increase		Increase	m5.47 surface at top and SB at base	
688.0	—	—	Decrease				Increase			Decrease		Decrease	SB	Impedance decrease
692.0	—	—			Peak					Peak			No corresponding surface	
695.0	—	—	Increase				Decrease	Increase	Increase	Increase	Increase		Subunit VB/VC boundary at top of interval	Cemented horizon at base
700.0	—	—		Low			Low			High			No corresponding surface	Cemented horizon
710.0	—	—					Increase	Decrease	Decrease	Decrease	Decrease		m5.6 at base of interval	
700.0	695	700					Decrease	Increase	Increase	Increase	Increase			
710.0	700	710					Increase	Decrease	Decrease	Decrease	Decrease			
728.0	—	—		Decrease	Decrease	Increase				Increase		Peak	Unit V/VI boundary and m5.7 surface <1 m below	Cemented horizon
742.0	—	—		Increase	Increase	Decrease				Decrease			m5.8 4 m below	Surface located at peak, petrophsyical interval at start of increase

Note: — = not applicable. All descriptions (increase/decrease) downhole. No petrophysical picks have been made using gamma ray in the top 200 m of the hole with no core recovery. Hole = sharp confined low in measurement. Peak = sharp confined high in measurement. FS = flooding surface. SB = surface boundary.

Table T12. Preliminary magnetostratigraphic age-depth tie points, Hole M0029A. (**See table note.**)

Depth (mbsf)	Interpretation A	Age (Ma)
327.95–327.53	C5AAr–C5AAn	13.139
331.11–330.91	C5ABn–C5AAr	13.302
733.49–733.29	C6An.2n–C6An.1r	20.996

Note: All ages according to Cande and Kent (1995).

Table T13. Correlations of seismic sequence boundaries to core surfaces, Hole M0029A. (**See table notes.**)

Predicted age BKSA95 (Ma)	Seismic sequence boundaries	Seismic picks (ms)	Predicted depth (mbsf)		Predicted core	Actual depth (mbsf)	Actual core, section, interval (cm)	Notes	Age (Ma)	Age error (Ma)
			Monteverde	Seismic and velocity function core						
					313-M0029A-		313-M0029A-			
—	Base Pleistocene	—	—	40–48	—	49.68	15R-1, 8		?	—
11.5	m1	192	154	152–153	26R	—			?	—
12.8	m2	—	—	NR	—				?	—
13.6	m3	236	192	190–195	32R–34R	?193.17	Base of ?31R-1		?	—
?14.1	m4	280	230	225–235	37R–40R	?231.70	?40R-1, 39	SB; clay over silty fine sand	<13.2	—
—	m4.1	387	326	325–330	65R–66R	325.13–325.23	65R-2, 80–90	FS silty glauconite fine sand over silty clay	—	—
—	m4.2	403	341	345–350	72R–73R	341.11	Top of 71R-1	FS burrowed surface; clay with sands into clay	—	—
—	—	—	—	—	—	343.24–343.89	71R-2, 64R–72R-1, 57	SB indurate contact; clays over claystones over muddy fine sand	?13.4	12.6–13.7
—	m4.3	423	360	350–360	73R–77R	350.40	74R-1, ~14	FS burrowed surface; sands over silty clay; coarsen up above	—	—
—	m4.4	460	395	390–400	87R–90R	~393.00–394.00	89R-1	FS clayey interval with nodules	—	—
—	m4.5	517	449	445–455	106R–109R	449.10	108R-1, 124–128	SB irregular contact; glauconitic silty sand over siliceous silt	?14.6?	13.5–14.6
14.8–15.8	m5	547	479	475–482	117R–118R	478.61	118R-1, 25	SB very fine sand/sandy silt, 57 cm thick burrowed zone; indurated siltstone to top of 20-1, medium–fine sand	15.0–15.4	14.6–15.4
16–16.5	m5.2	664	597	590–600	155R–160R	602.25	161R-2, 37	SB clayey silt over glauconite sand	16.1–16.2	15.6–16.3
—	m5.2	—	—	—	—	—	—		—	—
—	m5.2	—	—	—	—	—	—		—	—
17.2	m5.3	708	642	638–642	173R–174R	634.43	171R-2, 57	Large density peak; glaucontiic quartz sand over glauconite sand	16.2–16.9	16.2–16.9
—	m5.3	—	—	—	—	640.51–641.20	175R-1, 50–120 (slurry between)	Silty glauconite sand over siltstone	—	—
—	m5.3	—	—	—	—	643.19	176R-1, 13	SB glauconite sand over silt; density max; sharp decrease density at base	16.9–18.3	16.9–18.3
17.8–18.2	m5.4	723	658	660–670	182R–186R	649.68	179R-1, 23	SB? top indurated zone, clay with burrowed gluaconite above; glauconite sand to 23 cm; clay below; density peak; this is the likely core sequence boundary	—	—
—	m5.7	—	—	—	—	662.37	183R-1, 102	SB? slightly glauconitic clay over glauconite sand; density peak; V_p increase 662, V_p maximum 667.5; this is the seismic sequence boundary	—	—
19.5	m5.45	739	676	670–680	186R–190R	673.71	189R-1, 15	SB glauconite bed on clay	16.9–18.3	16.9–18.3
19.7	m5.47	752	690	685–690	193R–194R	683.66	192R-1, 46	Top of glauconite; density increase	—	—
—	m5.47	—	—	—	—	684.33	192R-2, 11	Clay on glauconite; density increase	—	—
—	m5.47	—	—	—	—	687.87	193R-2, 60	SB glauconite on clay; base of density high	16.9–18.3	16.9–18.3
20.1	m5.5	—	—	NR	—	—			—	—
20.2	m5.6	777	716	700–710	197R–200R	707.56/710.16	Base of 200R-1/top of 201R-1	SB in coring gap; glauconite sand above; clay below	?18.5	18.3–19.0
20.4	m5.7	802	743	735–742	210R–212R	728.56	208R-1, 9–11	SB dramatic burrowed contact glauconite sands over tan clays; large decrease in density across boundary	19.6–20.2	19.6–20.2
21.5–22.0	m5.8	—	—	750–755	215R/TD	?746.00	213R-1/214R-1–215R-1 top	?SB base of TGR peak; glauconitic clay over coring gap over clay	?21.3	20.4–21.6
—	—	—	—	—	—	750.00–752.86	Base of 215R–top of 217R	Clay over coring gap over glauconitic clay	—	—
—	—	—	—	—	—	753.80 mcd/753.22 mbsf	217R-1, 36	Core gamma peak, top glauconite	<21.5?	—

Notes: BKSA95 from Cande and Kent (1995). Seismic picks from Seisworks. Predicted depth and ages for seismic sequence boundaries m1 to m5.8 from Monteverde et al. (2008). Two predicted depths in two way travel time (TWT) and depth (mbsf) are given, the first from Monteverde et al. (2008) and the second from Mountain et al. (prospectus). Actual depth and actual core are the best fit to surfaces or other contacts noted in the cores. * = where multiple surfaces potentially fit predicted sequence boundaries, preferred placement is in bold. Preliminary age and age error are derived from **"Chronology."** NR = none recovered. SB = sequence boundary, FS = flooding surface, TGR = total gamma ray.